Numéro d'ordre NNT: 2019LYSEC45 Année: 2019

THESE de DOCTORAT DE L'UNIVERSITÉ DE LYON
OPÉRÉE AU SEIN DE L'ÉCOLE CENTRALE DE LYON

ÉCOLE DOCTORALE MEGA

Mécanique, Enegétique, Génie civil et Acoustique

Spécialité: Mécanique

Soutenue le 19/12/2019 par

Guang ZHU

Wave Propagation Analysis in Complex Media based On Second Strain Gradient Theory

---

Devant le jury composé de:

Walid Larbi	Professeur, LMSSC, CNAM	Rapporteur
Mohamed Amine Ben Souf	Professeur, L2MP, ENIS	Rapporteur
Michelle Salvia	Maître de Conférence, ECL	Examinatrice
Catherine Marquis-Favre	Directrice de recherche, LGCB, ENTPE.	Présidente
Mohamed Ichchou	Professeur, LTDS, ECL	Directeur
Abdelmalek Zine	Maître de Conférence, ICJ, ECL	Co-directeur

Acknowlegements

Pursuing a Ph. D. is a both difficult and enjoyable experience. It's accompanied by bitterness, hardships, frustrations along with encouragements, and appreciations. After three year's Ph.D. pursuing, I finally find myself at the top enjoying the beautiful scenery. Here I would like to express my gratitude to all the people who helped me in these three years.

First of all, I would like to thank the professors of the defense committee, especially the two reviewers, for their valuable amendments to this thesis. Then I would like to give my sincere thanks to my supervisors Mohammed Ichchou, for creating such a good research team for me, guiding me in my research step by step, giving me the trust and encouragement when I was frustrated. Your constant help to my doctor for three years makes me grateful for life. I would like also thank my associate supervisor, Abdelmalek Zine, for his mathematical guidance and enthusiastic care. Thanks for your tutorial in the last three years. I would like also to express my thanks to Christophe Droz. Although he is not my supervisor, we discuss issues frequently, and he gave me many valuable opinions. I also want to thanks Pascal Fossat who is always patient for my endless questions, worked with me on very detailed issues.

I would like to express my thanks to many colleagues in our laboratory LTDS in these three years. When I started the thesis, Yi Kaijun and Liu Jiuzhou helped me much in Vibro-acoustics. Zakaria worked with me on literature survey and program coding, Yang Yifan taught me a lot about elasticity mechanical analysis. Régis is an expert in mathematics. I have so many amazing friends in these three years, Huang Xingrong, Zheng Fei, Meng Han, Ding Haohao, Li Muchen, Lou Mingyang, Chai Wenqi, Hui Yi, Shen Zihan, Giulia, Nassardin, Fabrizio, Giovanni, Wu Qiche. I'd like to express my gratitude to all these friends.

A particular acknowledgement is made to my dear families. They trust me, encourage me, and support me during the last three years. The most profound gratitude is for my husband, Mr. Liu. I am so lucky to meet you here in France, to be your friend, and then to be your wife. You are the best thing that ever happens to me. Thanks for your unconditional support, understand and encouragement. The rest of the life please enlighten.

At last, I would like to acknowledge China Scholarship Council (CSC) for providing the funding source of my Ph. D. research.

ZHU Guang
Ecully, France
14 December 2019

Abstract

In this work, two enriched models respectively describing non-classical longitudinal motion in rods, and non-classical bending and shear motion in beams, are established based on Mindlin's Second Strain Gradient (SSG) theory. The latter can describe local behaviors of heterogeneity caused by complex micro-structure interaction in the frame of continuum mechanics. The multi-scale modelling starts with expressing the SSG theory-based strain energy, kinetic energy and virtual work done by external forces, then the governing equations and the associated boundary conditions are derived with the utilization of Hamilton principle. Lattice model corresponding to 1D longitudinal motion is proposed to map the long range interactions to higher order material constants in SSG theory.

Wave propagation features in complex continua are significantly different due to the local behavior of heterogeneity caused by complex micro-structure interaction. With the formulated SSG theory-based rod model, dispersion relation of non-classical longitudinal wave accompanied with two evanescent waves are investigated. Meanwhile, non-classical bending wave and shear wave together with four evanescent waves are also investigated with the SSG theory-based Timoshenko beam model. The investigations are developed on the modal density of the propagating waves, energy flow, mobility of the complex structures, transfer of vibrating power, and frequency response analysis of complex rod as well as complex beam. The frequency response results are validated by FEM approach resulting from COMSOL.

With employing the proposed enriched models, vibration transmission and reflection characteristics through planar interface between two complex structures are studied. The study is conducted on transmission and reflection coefficients of longitudinal wave in complex rod, and bending wave in complex Timoshenko beam, upon which energy distribution and attenuation in reflected waves as well as in transmitted waves are discussed. Transmission and reflection of longitudinal wave through a certain length of complex rod is also investigated.

With utilization of the derived enriched beam model, wave radiation from infinite vibrating surface is analyzed. Radiation characteristics including square velocity, radiation impedance and radiated pressure field are achieved. These acquired enriched characteristics are interpreted combining with wave propagation characters in complex beam. Wave radiation from baffled finite beam is investigated using the Kirchhoff-Helmholtz integral equation. The influences of local behavior caused by complex micro-structure interactions are discussed and well interpreted based on results of SSG theory based-model and classical model.

Keywords: Second strain gradient theory, Multi-scale modelling, Wave propagation features, Energy flow, Reflection and transmission, Wave radiation.

Résumé

Dans le cadre de la mécanique des milieux continus, la théorie du Second Gradient de Déformation (Second Strain Gradient, SSG) de Mindlin permet de décrire le comportement local d'hétérogénéité causé par l'interaction complexe des microstructures. Dans ce travail, nous établissons deux modèles enrichis basés sur la théorie SSG. Ces deux modèles décrivent respectivement un mouvement longitudinal non classique dans des tiges et un mouvement de flexion et de cisaillement non classiques dans des poutres. Cette modélisation multi-échelle permet d'exprimer l'énergie de déformation, l'énergie cinétique et le travail virtuel effectué par des forces externes. Le principe d'Hamilton nous a permis ensuite de déduire les équations du mouvement ainsi que les conditions aux limites associées. Un modèle discrétisé du type réseau d'oscillateurs monodimensionnels est proposé afin de représenter les interactions mécaniques de la grande échelle au comportement lié aux constantes d'ordre supérieur dans la théorie SSG.

En raison du comportement local d'hétérogénéité provoqué par l'interaction complexe des micro-structures, la théorie SSG met en évidence des caractéristiques de propagation très différentes de celles constatées pour la théorie classique. Pour le modèle de tige basé sur la théorie SSG, en plus de l'onde longitudinale, la relation de dispersion fait apparaître deux ondes évanescentes, apparaissant exclusivement pour cette théorie. Et, pour le modèle de poutre de Timoshenko basé sur la théorie SSG, en plus des ondes de flexion et de cisaillement non classiques, nous constatons l'apparition de quatre ondes évanescentes. Les recherches sont développées à la fois pour la densité modale des ondes propagées, le flux d'énergie concernant des paramètres cinétiques d'ordre supérieur, la mobilité de structure complexe, le transfert de puissance de vibration et l'analyse de la réponse en fréquence pour des structures complexes à excitation forcée ponctuelle. Les résultats de réponse en fréquence sont validés par la méthode FEM dans COMSOL.

En utilisant le modèle enrichie, les caractéristiques de transmission et de réflexion des vibrations via une interface plane entre deux structures complexes sont étudiées. Les coefficients de transmission et de réflexion de l'onde longitudinale dans une tige complexe et de l'onde de flexion dans une poutre complexe sont calculés. Basée sur ces coefficients, la distribution et l'atténuation de l'énergie dans les ondes réfléchies et dans les ondes transmises sont discutées. Nous étudions ensuite, la transmission et la réflexion des ondes longitudinales classiques à travers une certaine longueur de tige complexe.

En utilisant le modèle de poutre enrichie, le rayonnement d'onde provenant d'une surface vibrante infinie est étudié. Les caractéristiques enrichies, y compris le carré de la vitesse, l'impédance de rayonnement et le champ de pression rayonné, sont calculées et interprétées en les combinant au caractère de propagation des ondes dans une poutre complexe. Ensuite, le rayonnement d'onde provenant d'une poutre simplement supportée est étudié en utilisant l'équation intégrale de Kirchhoff-Helmholtz. Les influences du comportement local causé par des interactions complexes des micro-structures sont discutées et bien interprétées sur la base

des résultats du modèle SSG et du modèle classique.

Mots-clés: Théorie du second gradient de déformations, Modélisation multi-échelle, Caractéristiques de propagation des ondes, Flux d'énergie, Réflexion et transmission, Rayonnement des ondes

Contents

Introduction

Complex media is one kind of media in which local behavior and global behavior can be observed conjointly. For general materials, the internal structure of the materials possess heterogeneity on various scales. In most cases the material can be considered as a continuum and described by conventional elasticity theory. When the external characteristic wavelength is comparable to characteristic size of major heterogeneous features, the classical continuum theory loses its accuracy, and heterogeneity caused by internal micro-structures is required to be considered in structure vibration analysis as well as wave dispersion and propagation analysis.

Due to the great performance of complex media in both static and dynamic aspects, complex media is widely used in many industries. Typical examples include composite structure applied in aerospace, automotive industries and civil engineering, micro-/nano- structure in MEMS/NEMS, biological material in medical machinery, etc. Investigation of such complex media has been proceed for decades for both static and dynamic characters. Wave propagation analysis in complex structure is of great interest in understanding the structural vibration behavior and forced response in frequency domain and further more in structure optimization and wave active control.

Modeling and characteristic study of complex structures has been done by various methods. Some of the investigations are carried out by the experimental methods, it is the most accurate yet difficult to apply especially when the specimen is in micro-scale. Some of the investigations are proceeded with numerical approach. To describe shorter wave propagation feature in complex media by numerical approach, it is in principle possible to explicitly resolve the details of the heterogeneous internal structure. Typical numerical method includes Finite Element Method (FEM), Wave Finite Element Method (WFEM) (for periodic structure), Boundary Element Method (BEM). This approach often leads to high demands on the computational resources and sometimes ill-condition problem. For complex media in micro-scale, many scientists and engineers resorted to atomistic level simulation techniques. The behavior of graphene at atomistic levels are simulated via the molecular dynamics (MD) simulation, but it refers to expensive computer simulations depicting physical movements of atoms and molecules at the nano-scale. Numerous homogenization techniques are proposed as an alternative analytical approach to study the complex media (particularly the periodic structures), including the equivalent strain energy method, mode-based method, wave-based method, asymptotic homogenization method. The main idea of homogenization methods is to find an continuous homogeneous structure which gives the equivalent behavior. With including the character at micro-scale into a macroscopic model, it gives relevant information on the relation between the local and global behaviours. Thus homogenization method can predict dynamic behavior of complex media on some frequency range, but with the assumption that the size of the cell is much short with respect to the wavelength,

the internal interaction in the cell on higher frequency can still not be predicted.

Generalized continuum theory is adopted in the presented research. Generalized continuum theory, or non-local continuum theory, non-classical continuum theory, have been developed to capture the long range of applicability or to increase the accuracy of the theories of the classical Cauchy continua. It is suggested with incorporating the non-local effects in different forms. Generalized continuum theory can be classified into mangy catalogues, such as higher order theory, higher gradient theory, non-local elasticity theory,etc. The essence of the generalized continuum theory is that the stress field at a point in an elastic continuum depends not only on strain at that point but also on the strain or history strain of a certain neighborhood of that point or even of the entire body.

Generalized continuum theory are mainly applied in analysis of nano-scale structure behavior in the past with defining the instinct length in lattice scale, for example the size effect. Recently, more researches are conducted with employing the non-classical continuum theories in modelling of general complex media with considering the internal micro-structure effect. In the presented research, the 'second strain gradient theory' (SSG theory) is employed to establish enriched structural models describing the non-classical motion in complex media. SSG theory is a powerful generalized continuum theory suggested by Mindlin, in which the non-local effects is described by enriching the strain energy density with the contributions of higher order strain tensors. The constitutive equation for a linearly isotropic elastic material in SSG theory has more than ten additional higher-order constants. These higher order constants reflect some terms involving the characteristic lengths of the material which are capable of capturing the long range interaction between the underlying micro-structures. Upon the enriched models, wave propagation features in complex medias, wave reflection and transmission on the interface between complex medias are analyzed, and sound radiation from complex Timoshenko beam are also investigated with the SSG theory-based model.

Thesis Contribution

The main contributions of the work in this thesis are:

1. Establish 1D multi-scale continuous models for rods and beams based on SSG theory, which are capable of capturing the long range interaction caused by internal micro-structures. Develop one discreet lattice model for SSG theory-based rod model and relate the long range interaction coefficients in the lattice model with higher order material constants in continuous rod model.

2. Investigate free wave propagation features in complex rod and complex Timoshenko beam based on the proposed enriched models. The dispersion relation,

modal density, and size effect are discussed. Establish the energy flow expressions for non-classical wave propagation in complex rod and complex Timoshenko beam, which is a combination of work involving both the regular forces and higher order forces.

3. Study the frequency response of complex rod and complex beam with some proper boundary conditions. Confirm the analytical results of wave approach with numerical results in COMSOL.

4. Apply the SSG theory-based model into wave transmission and reflection characteristics analysis. The investigation are conducted respectively in term of wave transmission on a planner interface and wave transmission through a certain length of SSG theory-based media. Based on the obtained results, potential applications of SSG theory model are discussed in complex media designing with certain internal scale parameters.

5. Apply the SSG theory-based model into wave radiation characteristics analysis. Investigate near field effect in the radiated fluid domain originated with microstructure interactions in the solid structure.

Thesis Outline

Chapter 1 presents the research background of complex media. The survey starts with an interpretation on the failure of conventional continuum theory and on the origination of complex behavior. Then a review of existing methods in studying complex media, including general heterogeneous media, periodic medium, and nanosize structures is given. Upon which, generalized continuum elasticity theories are introduced with detailed historical review, development, fundamental equations. Length scale parameter existing in SSG theory-based model and its capability of capturing the long range interaction are illustrated. Different approaches to identify the length scale parameters are discussed in end of this chapter.

Chapter 2 develops SSG theory-based rod model to describe non-classical longitudinal motion in complex rod. Upon which, free wave propagation features and forced structural behavior of complex rod are studied with considering the underlying micro-structure interactions. The results are compared with results of classical homogeneous rod model and the influence of heterogeneity are discussed with several numerical examples.

Chapter 3 develops SSG theory-based Timoshenko beam model to describe the bending and shear motion in a complex Timoshenko beam. Free wave proroga-

tion features and forced structural behavior with considering the micro-structure interactions are studied. The results are also compared with results of classical homogeneous Timoshenko beam model and the influence of heterogeneity on behavior of complex beam are discussed with several numerical examples.

In chapter 4, the proposed SSG theory-based rod and Timoshenko beam models are utilized to study wave transmission and reflection through a planar interface between complex medias, and to study the wave transmission characteristic through a certain length of complex media. Some potential application of the proposed model are presented.

Chapter 5 employs the proposed SSG theory based-Timoshenko beam model to study the infinite wave radiation characteristics, and to study finite wave radiation from simply supported beam structure. Attention has been paid to study the radiated pressure field and radiation impedance in low and high frequency. Numerical cases are carried out to illustrate the capability of the proposed model, especially in reflecting the influence of heterogeneity on radiation pressure in near field.

Finally, the conclusions and perspectives are drawn in chapter 6.

Chapter 1

Literature survey

Contents

1.1 Introduction

Almost all materials used in contemporary life and in industrial field, acquired from nature or manufactured artificially, are heterogeneous material which possess rich and complicated internal structures characterized by micro-structural details whose size typically ranges over many orders of magnitude. In classical continuum mechanics, material is generally been assumed as an homogeneous mass rather than as discrete particles. However in some other circumstance, one has found that the constitutive models conceived for the conventional continuum theory become increasingly insufficient, and this is particularly true for micro-/nano-size structures in

which local behavior of discrete particles plays a major role to material propriety [1]. Local behavior caused by complex interactions between underlying micro-structures significantly affect the global behavior of the material and furthermore properties of the macro-scale material. The media in which local behavior and global behavior can be observed conjointly is defined as complex media.

This chapter begins with the introduction of micro-structures of different material and the influence of micro-structures on material properties. Then the phenomenon that conventional continuum theory fails to describe material behavior is illustrated, and the interpretation is conducted subsequently with lattice dynamic approach. Afterwards, some representative complex medias are presented in Sec 1.2, among the others, periodic complex structure and nano-structure are introduced in details. These two types of structures are respectively considered as two representatives of complex media with visible-size micro-structure and atomic-size micro-structure. Then a literature survey of existing methods to study periodic media is presented. Throughout out the survey, attention is led to the analytical method of multi-scale modelling. Local behavior of complex media can be successfully described with multi-scale modelling based on generalized continuum theory in frame of continuous model. One review on generalized continuum is conducted in terms of its classification, application, recent development. At last, methods for identification of length scale parameter are briefly referred.

1.1.1 Micro-structures

In material research, different levels of observation can be distinguished, and the micro-level indicates the internal structure of the material can be recognised. To construct a material model, one must also firstly select a certain resolution level below which the micro-structural details are not explicitly 'visible' to the model, this resolution level can also be regarded as a standard length scale to define the micro-structure. To be noted, the expression 'micro-structure' in this research will be used as a generic denomination for any type of internal material structure, not necessarily on the level of micrometers.

For most materials as long as it is not monocrystal material, they all have complicated internal structures, such as alloy material, composite material, porous material, Polymer, biological materials, etc. The internal structures are characterized by micro-structural details whose size can varies from atomic scale to visible scale. Examples of micro-structures in different size scale is shown in figure 1.1 [2].

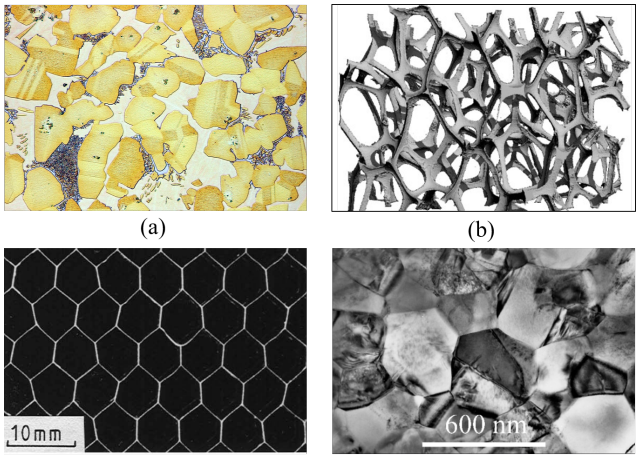

Figure 1.1: Material consisting of heterogeneous internal structures. (a) Aluminium-bronze; (b) Open-cell foams; (c) Aluminium honeycomb; (d) Micro-structure of ceramic

For granular materials, micro-level corresponds to the observation level at which individual particles are considered. For cellular composite material, micro-level corresponds to the structure of each cell which constructing the whole structure. For ceramics, micro-level means the small crystals called grains. For metallic material, micro-level corresponds to a large number of irregularly shaped crystals with a variety of shape, size, arrangement, and orientation, which depend on the conditions of their formation. Generally speaking, the micro-level is the size at which no internal material structure can be recognized anymore. and the material in macro-scale can be regarded as an assembly of individual micro-structures. Behavior of micro-structures can be transited from micro-scale to macro-level unequivocally. Actually, there is a large class of problems for which the local discrete micro-level properties may considerably influence the behaviour of an assembly of micro-structures, resulting in a heterogeneous material response. These heterogeneous can be generated either via strong time variations in the displacement (rotation) field, during which the generated wave lengths become of the same order of magnitude as the particle size, or via strong spatial variations in the displacement (rotation) field, which appear when narrow failure zones are manifested over a small amount of grains, i.e. shear bands [3].

1.1.2 The failure of conventional continuum theory

For conventional continuum elasticity theory, material is modeled to be a continuous mass rather than as discrete particles. The continuous mass can be decomposed into a set of idealized, infinitesimal material volumes, each of which can be described independently as far as the constitutive behavior is concerned. During a deformation process, the global behavior of classical continuum can be defined as the level where

an assembly of particles acts as a continuum with an homogeneous strain distribution. Thus the classical continuum formulation can only capture the first gradient of the displacement field, which is known as the strain[3]. The stress in one point only depends on the strain at that point ONLY for classical material.

Based on the classical continuum theory, propagation of longitudinal waves in an homogeneous rod is described by the hyperbolic partial differential equation as

$$\rho\ddot{u} - Eu'' = 0 \tag{1.1}$$

in which ρ is the mass density, E is the elastic modulus, $u(x,t)$ is the displacement. Over-dots represents derivatives with respect to time t, and primes denotes derivatives with respect to the spatial coordinate x. The solution is in form of

$$u\left(x,t\right) = u_0 e^{i(kx-\omega t)} = u_0 e^{i(kx-ct)} \tag{1.2}$$

in which ω is the circular frequency, k is the wavenumber, and $c = \omega/k$ is the wave velocity. Substitution of Eq. (1.2) into Eq. (1.1) yields the relation

$$\omega = \pm k\sqrt{\frac{E}{\rho}}$$

The sign $\pm$ represent wave propagation direction. Then phase velocity

$$c = \frac{\omega}{k} = \sqrt{\frac{E}{\rho}} \tag{1.3}$$

is a constant, only determined by material properties, independent of the wavenumber k.

This situation is different in a discrete lattice model, which is one valid method to study continue structure in discrete way. The approach would have consisted in discretizing the continuous media supporting the propagation of wave into a series of lumped masses connected by a lumped spring as shown in figure 1.2.

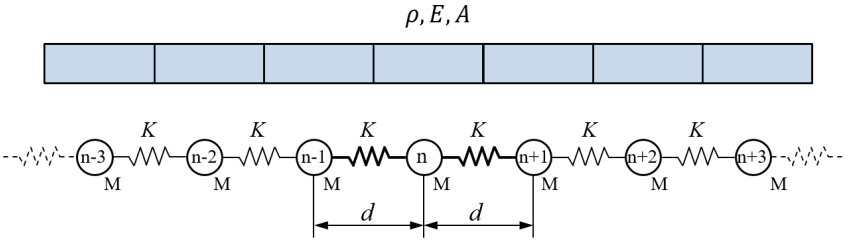

Figure 1.2: Discretization of a rod into a spring mass lattice

In absence of an external load, the equation of motion for the nth mass is

$$M\ddot{u}_n + 2Ku_n - K\left(u_{n-1} + u_{n+1}\right) = 0,$$

where $M = \rho Ad$ is the mass of each mass point, $K = EA/d$ is the spring stiffness, A represents the cross section of the rod, u_n is the displacement of mass point number n, and the position of nth mass within the chain is at $x_n = nd$. A solution is sought in form of a harmonic plane wave as

$$u\left(x_n, t\right) = u_n\left(t\right) = \hat{u}_n\left(\omega\right) e^{-i\omega t} = \tilde{u}_n\left(k\left(\omega\right)\right) e^{i(kx_n - \omega t)}. \tag{1.4}$$

The spatial part of the solution $\hat{u}_n\left(\omega\right)$ is expressed as

$$\hat{u}_n\left(\omega\right) = \tilde{u}_n\left(k\left(\omega\right)\right) e^{ikx_n} = \tilde{u}_n\left(\bar{k}\right) e^{i\bar{k}n}, \qquad \bar{k} = kd. \tag{1.5}$$

$\tilde{u}$ is a complex quantity that defines the amplitude of wave motion, while the exponential term describes the phase changes as the wave propagates from one mass to the next. The amplitude $\tilde{u}$ is expressed as a function of wavenumber, and therefore of frequency. $\bar{k}$ is the 'propagation constant', $\bar{k}$ is introduced by considering the interatomic distance as the characteristic length scale of the problem, and the definition of the spatial period of the system.

Equation (1.5) is an expression of the Floquet–Bloch theorem, which governs the propagation of plane waves in a periodic medium [4]. Bloch's theorem implies that the change in wave amplitude occurring from cell to cell does not depend on the cell location within the lattice, insofar as the unit cell is merely a component of an infinite lattice. Accordingly, the wave propagation characteristics of the periodic assembly can be fully identified through the analysis of the reference unit cell, provided the system does not present any dissipation, as in the case of the lattice presented here. In addition, a real wave propagation constant $\bar{k}$ corresponds to a wave propagating without attenuation, while an imaginary component to $\bar{k}$ defines the spatial decay in amplitude as the wave progresses through the lattice [5].

Substitution of Eq. (1.4) into governing equation gives

$$\left[-\omega^2 M + 2K - K(e^{-ikd} + e^{ikd})\right] \tilde{u}\left(\bar{k}\right) e^{i\left(\bar{k}n - \omega t\right)} = 0.$$

As $\tilde{u}\left(\bar{k}\right) \neq 0$, the plane wave solution for arbitrary location as

$$-M\omega^2 + 2K - K\left(e^{-ikd} + e^{ikd}\right) = -M\omega^2 + 2K\left(1 - \cos kd\right) = 0. \tag{1.6}$$

This equation represents the dispersion relation for the considered lattice model. The circular frequency corresponding to wavenumber k is thus

$$\omega = \sqrt{\frac{2K}{M}\left(1 - \cos kd\right)} = 2\sqrt{\frac{K}{M}}\left|\sin\frac{kd}{2}\right|. \tag{1.7}$$

The dispersion relation of the normalized wavenumber kd/π against normalized frequency $\bar{\omega} = \omega\sqrt{M/K}$ is illustrated in figure1.3[5],

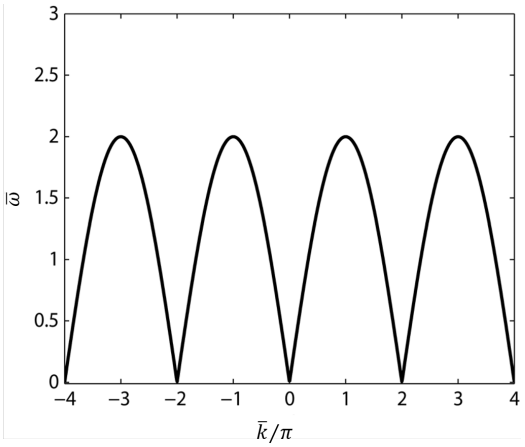

Figure 1.3: Dispersion relation for 1D spring mass lattice [5]

The nonlinearity of the dispersion relation indicates that the periodic lattice is dispersive in contrast to the continuous rod. Phase velocity in the lattice is far from constant as

$$c_{ph} = \frac{\omega}{k} = d\sqrt{\frac{K}{M}}\frac{\left|\sin\frac{kd}{2}\right|}{\frac{kd}{2}}.$$

The dispersion relation only behaves linearly in long wavelength limit ($\bar{k} \to 0$). In that case both the phase velocity and group velocity $c_g = \frac{dk}{d\omega}$ of lattice approximate to the constant

$$c_{ph} \approx d\sqrt{\frac{K}{M}} = \sqrt{\frac{E}{\rho}}.$$

Figure 1.3 also indicates the propriety of low band filter of periodic lattice. The dispersion relation solved in terms of frequency provides solutions in a limited range, i.e., for $\bar{\omega} \in [0, 2]$. Plane wave propagation occurs only in the range of $\bar{\omega} \in [0, 2]$. When $\bar{\omega} > 2$, there are no corresponding real-valued wavenumbers, and harmonic plane waves do not propagate. If certain mass point is externally excited with a circular frequency larger than $\bar{\omega}_{max}$, the vibration does not propagate through the entire chain and only remains localized to the neighborhood of the excited mass point. The range of $\bar{\omega} > 2$ therefore corresponds to an attenuation range, also denoted in the literature as a "stop band" or, when this phenomenon occurs over a limited frequency range, a "bandgap."

Another distinct property exhibited by the lattice model in Eq. (1.7) is that the dispersion relation is symmetric about $\bar{k} = 0$ and periodic with period 2π. Consequently, the behavior of the relation in the fundamental period $\bar{k} \in [-\pi, +\pi]$ fully describes the characteristics of harmonic plane waves in terms of the relation between their wavelength and the frequency of wave motion. This range of wavenumbers defining the fundamental period of the dispersion relation is called

the first Brillouin zone (FBZ) [4], which is generally defined by period of the dispersion relation, the dual of the direct lattice describing the geometry of the periodic domain. Combined with the symmetric property, dispersion relation of the lattice can be characterized within half of FBZ $\bar{k} \in [0, +\pi]$, which is called Irreducible Brillouin Zone (IBZ). The wavenumber with respect to frequency along the contour of IBZ forms the band structure. In physics, this diagram represents the backbone of electronic structure theory, credited for forming a basis for the classification of all crystals into metals, semiconductors and insulators [5]. In mechanics, a band structure is precisely a representation of dispersion relation describing the nature of free wave propagation in an elastic (or acoustic) medium. For 1D periodic structures, the term 'dispersion relation' is employed, and for 2D periodic structures, 'band structure' is used.

For a given value $\bar{\omega}$, the wavenumber is verified for $\bar{k} + 2m\pi$, where m can be any integer. When $m = 0$, the maximum wavenumber $k = \pi d$, correspondingly, the minimum wavelength is $\lambda = 2d$, which defines a wave where two neighboring masses move out of phase. Conceptually, all waves of wavelength $\lambda = 2d/(2m + 1)$ satisfy this condition. However, for this particular case of the discrete 1D lattice model, the cases for $|m| > 0$ describe wave motion with several inter-mass oscillations, which are not justified by the lumped parameter model and the associated degrees of freedom (DOF). This issue is, however, of great importance and introduces complexity in the analysis of periodic structures defined by unit cells with multiple degrees of freedom or of continuous periodic structures.

In the long wave limit, the velocity of the continuous rod matches the velocity in lattice model. For short elastic wave (i.e.$\bar{k} \to \pi$), they differ substantially as shown in figure 1.4 [5].

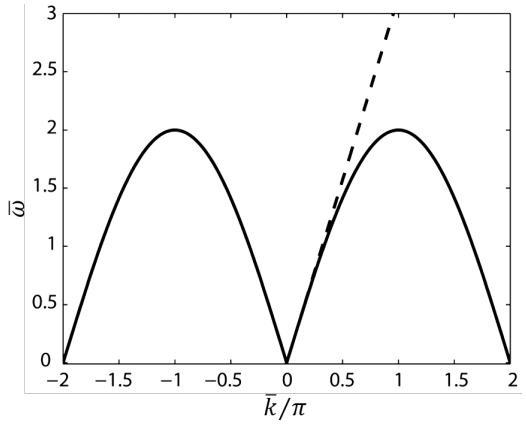

Figure 1.4: Comparison of dispersion relation for 1D spring mass lattice (solid line) and continuous rod (dashed line) [5]

The nonlinearity of the dispersion relation resulting from lattice model become

more prominent, and the mismatch of continuous rod model based on conventional continuum theory become increasingly obvious. In addition, the dispersion relation of elastic wave in crystal is a real physical phenomenon that can be observed and studied experimentally. In reference [6], dispersion curve for phonons propagation in aluminum in one specific direction is illustrated as in figure 1.5.

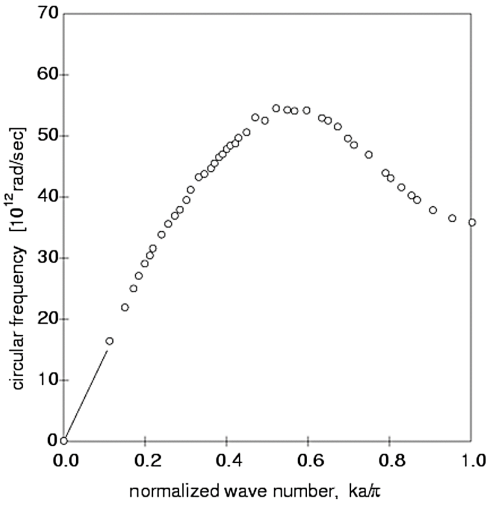

Figure 1.5: Dispersion curve for aluminum

We can see the real dispersion relation in crystal matches neither the classical continuous model nor the simple spring-mass lattice model. In other words, even lattice model consisting of discrete mass-spring system is quite a realistic model to study continue structure in discrete way, the above lattice is still not capable of fully describing material behavior. This incapability should attributed to the insufficiency of local behavior description, which is governed by the interaction forces arising not only between immediate neighbors but also at longer distance. The real crystal lattice model should be capable of modelling all the interaction forces as [7]

$$-M\omega^2 + \sum_{n=1}^{N} K_n \left(1 - e^{-knd}\right) - \sum_{n=1}^{N} K_n \left(e^{-knd} - 1\right) = 0, \tag{1.8}$$

where the stiffness K_2, $K_3 ... K_3$ represent the long range interactions between the studied atom and mass points in distance of $2d$, $3d$,...,Nd. The deficiency of describing material behavior is more evident in short wave limit because long range interaction between adjacent particles in a local field (instead of immediate neighboring) play an important role in characterising the behavior of particle.

From this section, we understand that the continuum equations for elasticity can be considered as a long-wave approximation of the lattice dynamics, where the deformation length scale of continuum elements are much greater than the inter-particle distances in the lattice. The classical continuum theory can only provides a simplified result applying to long wave deformation, and can not be used to describe

the material behavior when wavelength is not much longer the length of internal micro-structures.

Secondly, the classical lattice approximate the inter-particle force only with the interactions between immediate neighboring particle, thus it is not capable of describing more complex interactions occurring in crystalline materials, which is particularly true for the long-range interactions.

Combined with what has been discussed in section 1.1.1, if the characteristic wavelength of the deformation field remains much above the resolution level of the material model, the long wave approximation is valid, so the conventional continuum theory is adequate in modelling. On the other hand, if the characteristic wavelength of the deformation field is comparable to characteristic size of internal micro-structures, namely, for the short wave propagation ($\bar{k} \to \pi$), long rang interaction between micro-structures should be considered for each individual particle, then the local behavior of heterogeneity caused by complex micro-structure interactions will be significantly affected, so will the global behavior of the material. It is worth mentioning that the notion of characteristic wavelength should be interpreted in a broad sense, not only as the spatial period of a dynamic phenomenon, but also as the length on which the value of strain changes substantially in static problems from the given type of geometry and loading.

1.2 Complex media

Material consisting of heterogeneous internal structures falls into many categories. Appropriate examples can be cited from all branches of industries, such as alloy material, porous material, composite structure, ceramic material etc. Common to all of them is they consist of internal structures characterized by micro-structures as shown in figure 1.1. Even though the size of the micro-structure varies from nanometer scale to visible scale, micro-structures in all cases lay an important factor in the final property of the material in many respect. Micro-structure of material (such as metals, polymers, ceramics or composites) can strongly influence physical properties such as strength, toughness, ductility, hardness, corrosion resistance, high/low temperature behaviour or wear resistance. For ceramics, the micro-structure is made up of small crystals called grains. The smaller the grain size, the stronger and denser is the ceramic material. For composite material, a composite unit cell can be regarded as its micro-structure, and it represents not only the representative volume element in the composite structure, but also an entity to carry the information of composite constituent materials, heterogeneous structures and effective properties. These information essentially determine the propriety exhibiting by composite structure, such as the high specific bending stiffness, good shear and fracture strength, lightweight.

Complex media is defined as on kind of heterogeneous media in which local behavior and global behavior can be observed conjointly. This phenomenon usually happens when the characteristic size of deformation field is comparable to charac-

teristic size of heterogeneity in analysis of static and dynamic behaviors. In that case, long rang interaction between micro-structures plays an important role in governing each individual particle. Local behavior of heterogeneity caused by long rang interactions becomes more and more distinct, and the co-dynamic behavior of local character and global material becomes increasingly significant in describing the material behavior . Therefore, material modelling requires suitable incorporation of the discrete material behavior governed by the individual particles.

1.2.1 Composite material and periodic structure

As one kind of complex media, composite materials are widely used in many engineering field especially in aerospace industries duo to its high performance. As shown in figure 1.6, the proportion of composite used in Boeing 787 has reached fifty percent [8].

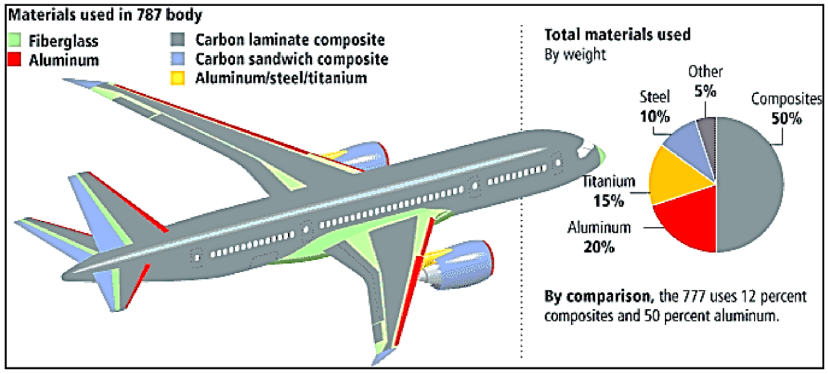

Figure 1.6: Use of material in Boeing 787

Consider the special requirements in aerospace industries, high heterogeneity design within different components is widely employed in composite material to acquire lightweight and high performance in mechanics and acoustics. In this catalogue, periodic designed structures are preferred by many engineers. Examples can be referred to composite sandwich panels, ribbed plates, truss beams, perforated plate used in mechanic industries as shown in figure 1.7.

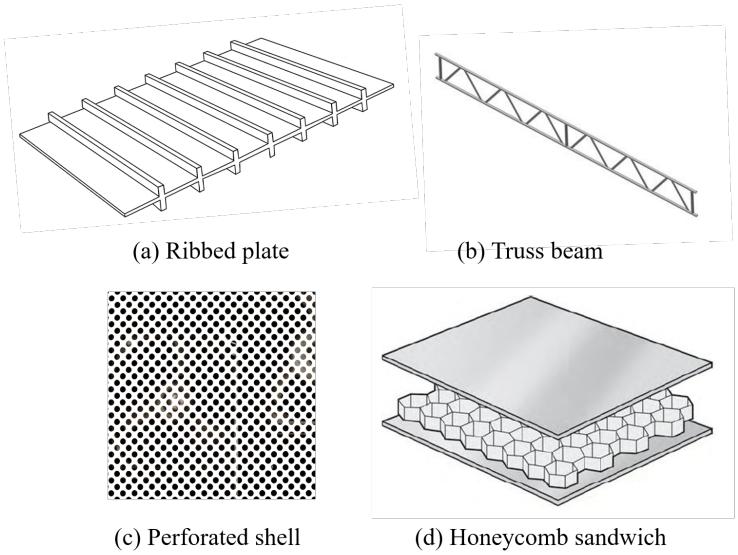

Figure 1.7: Engineering periodic structure

As one important kind of complex media, periodic structures not only process high performance of static features, but also process high quality in dynamic behavior and acoustics. The periodic distribution of heterogeneity is significant to its dynamic property and wave propagation features (section1.2.1). The study of wave propagation characteristic and dynamic behaviours of periodic structures is of big concern in mechanics community.

For general complex media with abundant and irregular internal structures, the complex interaction will affect the material properties undoubtedly, but the description and modelling of material with irregular micro-structures is almost unable to achieve. Whereas, the periodic designed internal structures lends itself to the development of analytical models which has certain effective material properties and local fluctuations arising from the heterogeneity.

For better understanding, although the size scale of micro-structure in different materials varies significantly, the phenomenon that material property is affected by long rang interactions between internal structures follows the similar principle, the only discrepancy lays in the size of representative volume element.

Wave filtering property can also be observed in periodic structures. That means elastic waves cannot propagate freely within some frequency ranges. There are two types of stop bands (or band gaps) mechanisms in the periodic medium: Bragg Scattering and Local Resonance. Bragg scattering stop band appears when wavelengths are on the same order as the period length, and it is due to the spatial periodicity of the impedance mismatch. Local resonance stop band depends on the properties of the local resonator instead of on the structural periodic property (the period length, the geometric arrangement within the unit cell), it can even appear in structures without periodicity.

To have a physical understanding of wave propagating and band gap in periodic

structure, one lattice model of spring mass system is illustrated in figure 1.8, which features two different masses m_1 and m_2.

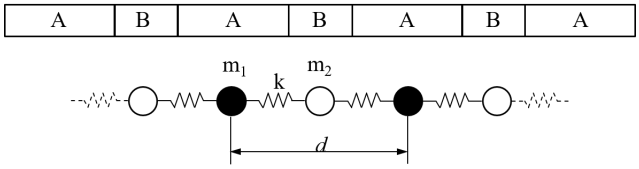

Figure 1.8: 1D diatomic lattice

The analysis of wave motion relies on the expressions of the equations of motion for two neighboring masses ($2n$ and $2n+1$), in the absence of external forcing and under the assumption of harmonic motion.

$$\begin{aligned} \left(-\omega^2 m_2 + 2K\right) u_{2n} - K\left(u_{2n-1} - u_{2n+1}\right) = 0 \\ \left(-\omega^2 m_1 + 2K\right) u_{2n+1} - K\left(u_{2n} - u_{2n+2}\right) = 0 \end{aligned} \tag{1.9}$$

For simplicity, Eq. (1.9) is expressed in the following matrix form

$$\left(\mathbf{K} - \omega^2 \mathbf{M}\right) \mathbf{u}_{2n} + \mathbf{K}_{n-1}\mathbf{u}_{2n-1} + \mathbf{K}_{n+1}\mathbf{u}_{2n+1} = 0 \tag{1.10}$$

where $\mathbf{u}_n = [u_{2n}, u_{2n+1}]^{\mathrm{T}}$ represents the degrees of freedom of the nth unit cell of the lattice. With the periodicity assumption, the notation can be simplified by letting $\mathbf{K}_n = \mathbf{K}_0$, where $\mathbf{K}_m, m = -1, 0, +1$ are matrices defining the spring interactions within a representative unite cell and with its neighbors. These matrices are identical for all the cells because of periodicity, and are thus independent of the cell location within the lattice.

The dispersion properties for the diatomic lattice system can be obtained by generalizing the approach for the spring-mass system presented in Sec. 1.1.2. The derivation of the dispersion properties for the system of (1.4) consists of imposing a plane-wave solution $\hat{u}_n(\omega)$, as

$$\hat{u}_n(\omega) = \tilde{u}_n\left(k(\omega)\right) e^{ikx_n} = \tilde{u}_n\left(\bar{k}\right) e^{i\bar{k}n}, \qquad \bar{k} = kd. \tag{1.11}$$

$\tilde{u}$ is a complex quantity that defines the amplitude of wave motion. For the presented diatomic lattice model, a plane-wave solution can be expressed in forms of

$$\mathbf{u}_n(\omega) = \tilde{\mathbf{u}}_n\left(\bar{k}\right) e^{i\bar{k}n}, \qquad \bar{k} = kd \tag{1.12}$$

where $\tilde{\boldsymbol{u}}$ is a complex vector that defines the amplitude of wave motion, The propagation constant $\bar{k}$ is imposed to solve the resulting expression in terms of frequency. Substituting equation (1.12) into Eq. (1.9) gives

$$\left[\boldsymbol{\mathcal{K}}\left(\bar{k}\right) - \omega^2 \mathbf{M}\right] \tilde{\mathbf{u}}\left(\bar{k}\right) e^{i\bar{k}n} = 0 \tag{1.13}$$

where $\boldsymbol{\mathcal{K}}\left(\bar{k}\right) = \sum_{m=-1,0,1} \left(e^{im\bar{k}} \mathbf{K}_m\right)$. Equation (1.13) for any value of n represents a linear eigenvalue problem in terms of ω^2 that can be solved for assigned values of

$\bar{k}$ in the FBZ. For the studied diatomic lattice, the eigenvalues correspond to the various dispersion branches in IBZ. while the eigenvectors $\tilde{\mathbf{u}}\left(\bar{k}\right)$ represent the wave modes, and describe the relative motion of the unit-cell degrees of freedom, or in general the polarization of the various wave modes. The two dispersion branches for the diatomic lattice are shown in figure 1.9 [5] for the case of $m_2 = 2m_1$, $m_1 = 1$, $K = 1$.

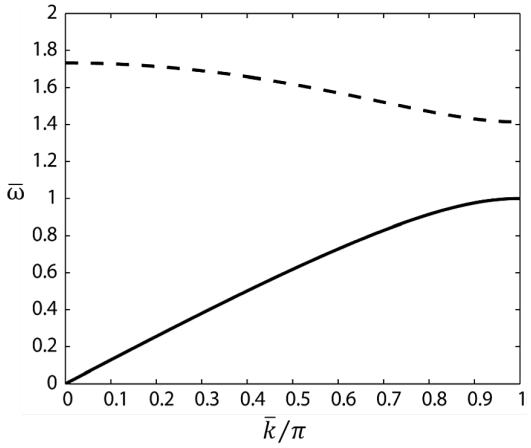

Figure 1.9: Dispersion curves of the 1D diatomic spring-mass lattice [5]

The lower branch, which in the long wavelength coincides with the dispersion branch of an acoustic wave in an homogeneous medium, is called as the 'acoustic mode', while the top branch is called the 'optical mode'. Similar with 1D monatomic case, one stop band appears above the optical mode. Meanwhile another band gap appears separating the acoustical and optical mode, whose width is defined by the mass ratio m_2/m_1, and becomes equal to zero in the limiting case of $m_2 = m_1$.

With comparing of these the two lattice models, we can have some conclusions. Firstly, the monatomic lattice model is established by considering the interatomic distance as the characteristic length scale. It can also be considered as periodic model with interatomic distance being the spatial period of the system. Secondly, the deficiency existing in monatomic lattice, lack of capturing long rang interaction, will also exist in the diatomic lattice model. When wavelength is approaching the order of the spatial period length, the mechanic behavior in each cell will be significantly affected by long rang interactions.

The same situation appears in periodic structure corresponding to the diatomic lattice in figure 1.8. As a piece-wise homogeneous structure, when the wavelength of the deformation field is comparable to the spatial period length, namely at the edge of 'Bragg scatting', the micro-structure effect will significantly affect the behavior of each cell.

1.2.2 Nano-structures

Material engineering has recently advanced at an ever increasing pace, and nowadays one has reached to engineer materials at scales approaching the micro, nano, and even atomic scale. A nano-structure is a small object of intermediate size between molecular and microscopic structures. Nano-structures possess superior mechanical, thermal, electrical and electronic properties, they are lighter, stronger, cleaner, less expensive, and durable products. Therefore, they are increasingly employed in the emerging field of nanotechnology. And the understanding of the mechanical response of nano-scale structures (small-scale structures of nanometer dimension), such as bending, vibration and buckling, is indispensable for the development and accurate design of nano-structures such as carbon nanotubes (CNTs), nanowires, nanobeams, nanorings, nanoribbons, and nanoplates(graphene sheets), etc. A single-walled CNT and single-walled graphene sheets is shown in figure 1.10, The dots in the figure represent carbon atoms[9].

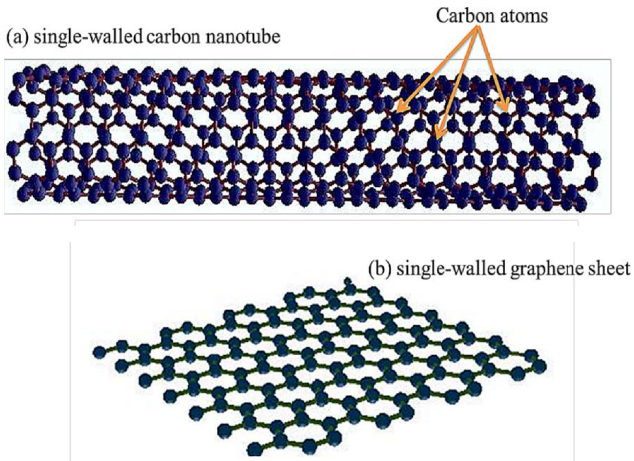

Figure 1.10: Schematic diagrams of (a) single walled carbon nanotube and (b)single walled graphene sheet[9]

As we can see in figure 1.10 nano-structure can be regarded as one kind of complex media possessing periodicity (atoms) spaced in atomic distance. At such a small scale, material's micro-structure becomes increasingly significant for material deformation behavior. The behavior of the atoms and molecules governed by complex interatomic forces in nano-materials plays a major role in governing its property, therefore nano-structure are observed to show complex properties in many situations [1]. An important consequence of this is the occurrence of size effects, which means nano-structure's property display a strong size-dependence. The term "size effect" designates the effect of the macroscopic size, relative to the cell size, on the mechanical behaviour. The deformation behavior of nano-structures cannot be model with simple conventional continuum model.

As to the other kinds of investigation approach for nano-structure, an experimental approach at the nano-scale is obviously a better way as it is more realistic.

However, in experimental study, controlling every parameter in nano-scale is a difficult task. Besides, the behavior of graphene at atomistic levels can be also simulated via the molecular dynamics (MD). MD simulation refers to expensive computer simulations depicting physical movements of atoms and molecules at the nano-scale. In an MD simulation, the motion of individual atoms within an assembly of N atoms or molecules is modeled on the basis of either a Newtonian deterministic dynamic or a Langevin-type stochastic dynamic, given the initial position coordinates and velocities of the atoms. Applying Newton's equations of motion, the trajectories of molecules and atoms are determined. In MD simulations, the forces between the particles and potential energy are defined by molecular mechanics force fields. Molecular simulation methods can provide accurate results but suffer from the disadvantage that these are sophisticated, require larger computational resources, require solving large number of equations and are highly expensive and time-consuming [9]. Thus it usually be employed as a validation method to results from other modelling approaches.

As nano-structure can be regarded as one type of periodic media which possess spatial periodicity in atomic scale, they can be described with homogenized models having additional effective material properties and the local fluctuations arising from the heterogeneity. In the following research of generalized continuum theory, a number of literature and applications are devoted to nano-scale structures as nano-structure is essentially one branch of scope of this research.

1.3 Existing methods for periodic complex media modelling

Modelling of simple homogeneous elastic solids is easy to achieve, and the analytical expression of dispersion relation can be found in [10]. Examples include one-dimensional continuous structures such as rods and thin beams and two-dimensional continuous structures such as thin plates. Long wave approximation is utilized in these classical cases. For general heterogeneous structures, the analysis becomes more difficult or even impossible, and the dispersion equation is usually transcendental. For the periodic medias, a number of methods can be utilized in study of propagation of elastic waves. The analytical method, such as plane-wave expansion method and Transfer Matrix Method (TMM), are available. The numerical methods can be marked as, among others, Finite Difference Method (FDM) is usually defined on regular grids and efficient for large scale simulations, but insufficient of handling wave simulation when there are changes in material property and geometry of the structures. Finite Element Method (FEM)[11, 12] is extensively used in modelling complex geometries. However, it is computationally expensive for wave propagation simulations. Spectral Finite Element (SFEM)[13, 14] is a combination of FEM and higher-order interpolations with specific quadrature formulae, it is capable of simulating wave propagation in complex structure with better convergent rate than FEM and reduced computational cost. Wave Finite Element Method (WFEM)[15, 16] is

a combination of conventional FEM and the Floquet-Bloch theorem which converts the study of a periodic structure into a single unit cell, it is mainly used for periodic structure analysis. Boundary Element Method (BEM)[17] is employed in structure modelling with small surface/volume ratio, and not computational efficient for modelling large structures.

As for analytical methods, among the other analytical methods, higher order shear deformation theory method [18, 19, 20] has been developed to study the mechanic property of laminated Composite. Homogenization methods have been developed in different forms to study the heterogeneous materials or periodic structures. Plane-wave expansion method is often used for photonic crystal modelling[5]. Transfer matrix methods are an excellent tool for analysing the wave transmission in periodic and quasi-periodic multi-layer media with.

In this section, We are not intended to list all the approaches in details, instead WFEM and Homogenization method are illustrated in details as two exampled approach for periodic structure modelling. Then one new analytical method is proposed by establishing a multi-scale model incorporating with local behavior of heterogeneity based on generalized continuum mechanic theory.

1.3.1 Wave Finite Element Method

WFEM was developed to the investigation of periodic structures, and it is widely used in the analysis of periodic structure as well homogeneous structures in terms of different types of investigation. This method has been used in many situations, such as the thin-walled structures [15], fluid-filled pipes[21], curved members [22], Honeycomb sandwich panel [23]. The related investigations refer to free and forced vibration, transient wave scattering and damage detection. The method is initially developed based on periodic structures theory, with which the study of periodic structure can converted into the study a single unit cell or a small segment of the structure. In the modelling, the unite cell can be modelled with the conventional FE software packages, the dynamic stiffness and mass matrix of the unit cell can be built explicitly, then the whole structure with complex geometries or material distributions can be analysed with relative less computational cost.

Assuming no external forces acting on the structures except boundary force, and no damping existing in the system, motion equation of the unit cell for free wave propagation can be expressed as

$$\left(\mathbf{K}-\omega^2\mathbf{M}\right)\begin{pmatrix}\mathbf{q}_{\mathrm{bd}}\\ \mathbf{q}_{\mathrm{I}}\end{pmatrix}=\begin{pmatrix}\mathbf{f}_{\mathrm{bd}}\\ 0\end{pmatrix}, \tag{1.14}$$

where $\mathbf{q}_{\mathrm{bd}}$ and $\mathbf{f}_{\mathrm{bd}}$ represent the displacement and the force of the boundary nodes, and $\mathbf{q}_{\mathrm{I}}$ represents displacements of the internal nodes. With the dynamic stiffness matrix $\mathbf{D}=\mathbf{K}-\omega^2\mathbf{M}$, the equation of motion can be rewritten as

$$\begin{bmatrix}\mathbf{D}_{\mathrm{bd}} & \mathbf{D}_{\mathrm{bdI}}\\ \mathbf{D}_{\mathrm{Ibd}} & \mathbf{D}_{\mathrm{II}}\end{bmatrix}\begin{pmatrix}\mathbf{q}_{\mathrm{bd}}\\ \mathbf{q}_{\mathrm{I}}\end{pmatrix}=\begin{pmatrix}\mathbf{f}_{\mathrm{bd}}\\ 0\end{pmatrix}. \tag{1.15}$$

After dynamic condensation, it becomes

$$\mathbf{D}_{\mathrm{bd}}\mathbf{q}_{\mathrm{bd}} = \mathbf{f}_{\mathrm{bd}}, \tag{1.16}$$

with

$$\mathbf{D}_{\mathrm{bd}} = \mathbf{D}_{\mathrm{bdbd}} - \mathbf{D}_{\mathrm{bdI}}\mathbf{D}_{\mathrm{II}}{}^{-1}\mathbf{D}_{\mathrm{Ibd}}$$

For simplicity, equation (1.16) can be rewrite in forms of

$$\begin{bmatrix} \mathbf{D}_{\mathrm{LL}} & \mathbf{D}_{\mathrm{LR}} \\ \mathbf{D}_{\mathrm{RL}} & \mathbf{D}_{\mathrm{RR}} \end{bmatrix} \begin{pmatrix} \mathbf{q}_{\mathrm{L}} \\ \mathbf{q}_{\mathrm{R}} \end{pmatrix} = \begin{pmatrix} \mathbf{f}_{\mathrm{L}} \\ \mathbf{f}_{\mathrm{R}} \end{pmatrix}. \tag{1.17}$$

The subscript 'L' and 'R' represent right boundary and left boundary. Then Eq. (1.16) can be reformed into the following form:

$$\mathbf{u}_{\mathrm{R}} = \mathbf{S}\mathbf{u}_{\mathrm{L}} \tag{1.18}$$

where $\mathbf{u}_{\mathrm{L}} = \left((\mathbf{q}_{\mathrm{L}})^{\mathrm{T}}(-\mathbf{f}_{\mathrm{L}})^{\mathrm{T}}\right)^{\mathrm{T}}$ and $\mathbf{u}_{\mathrm{R}} = \left((\mathbf{q}_{\mathrm{R}})^{\mathrm{T}}(\mathbf{f}_{\mathrm{R}})^{\mathrm{T}}\right)^{\mathrm{T}}$ represent the left and fight state vectors for the unite cell. $\mathbf{S}$ is a symplectic matrix with the following expression [24]

$$\mathbf{S} = \begin{bmatrix} -\mathbf{D}_{\mathrm{LR}}{}^{-1}\mathbf{D}_{\mathrm{LL}} & -\mathbf{D}_{\mathrm{LR}}{}^{-1} \\ -\mathbf{D}_{\mathrm{RL}} + \mathbf{D}_{\mathrm{RR}}\mathbf{D}_{\mathrm{LR}}{}^{-1}\mathbf{D}_{\mathrm{LL}} & -\mathbf{D}_{\mathrm{RR}}\mathbf{D}_{\mathrm{LR}}{}^{-1} \end{bmatrix}.$$

According to the Bloch theorem, free wave propagation characteristic can be represented by wavenumbers and wave basis, which are associated to the eigenvalues and eigenvectors of the following eigen-problem.

$$\mathbf{S}\mathbf{\Phi}_i = \lambda_i \mathbf{\Phi}_i, \qquad |\mathbf{S} - \lambda_i \mathbf{\Phi}_{2n}| = 0. \tag{1.19}$$

The eigenvalues are related to wavenumbers by $\lambda = \exp(-ikd)$, where d is the period of the periodic structure. Then the wavenumber and the frequency are associated with the eigenvalue problem in Eq. (1.19), and the dispersion relation in first Brillouin zone can be obtained. The above formulation is referred as the direct form of WFEM in 1D model. The direct form of WFEM1D is also the most applied among the forms of WFEM. It can be used in investigations of not only the propagating wave shapes but also the decaying wave shapes, therefore it has be employed to study the damped structure and the frequency response of the structure [25, 26]. For complex structures with cross-sections, the eigenvalue problem may be poor conditioned. In these case, there are other form of WFEM proposed [27].

To achieve the dispersion relation of periodic structures, it involves solving the eigenvalue problem as many times as the value of wavenumber k or frequency f is varied. The size of the eigenvalue problem and the number of modes are determined by the number of degrees of freedom of the unit cell. When the DOFs are enormous the required computational effort is usually extremely high. To overcome this deficiency, several techniques have been developed to speed up band structure calculation [28, 29], based on which Model Order Reduction technique are proposed based on wave basis [30, 31] or modal basis, then the Condensed Wave Finite Element [32] can be established as a combination of WFEM and the model order reduction techniques. Here we are not going to explain all of those method in detail. An excellent review are given in article of [5].

1.3.2 Homogenization method

Homogenization method is to develop the macroscopic scale model with passing from the description at the heterogeneity scale (microscopic scale or the local scale). A variety of homogenization methods have been developed to study the heterogeneous materials or periodic structures. The equivalent strain energy method is initially proposed by Nemat-Nasser [33] in estimating the overall elastic moduli of a composite with an isotropic elastic matrix containing periodically distributed (anisotropic) inclusions. Then the application are expanded to sensitivity analysis and topology optimization of micro-structures in composite materials [34], and to evaluate the effective elastic stiffness of periodic masonry structure [35]. The asymptotic homogenization method is also widely used to find equivalent model of composite structures [36, 37]. Based on which, high frequency homogenization [38] is proposed which can be used to investigate the wave propagation behaviour of a periodic structure in situation when the wavelength and micro-structural length scales. Besides that, there are also the mode-based method [39] and the wave-based method [40] for analysing the equivalent model. The essential principle pf homogenization method is establishing an homogeneous structure with equivalent material properties.

1.3.2.1 Equivalent strain energy method

Based on equivalent strain energy method, the periodic structure can be replaced by an equivalent homogenized model with the same volume. Besides, the stress and the strain tensors of the homogeneous medium are equivalent to the average stress and strain of the unit cell as

$$\frac{1}{V}\int \boldsymbol{\sigma} dV = \bar{\sigma}; \qquad \frac{1}{V}\int \varepsilon dV = \bar{\varepsilon}$$

V denotes the volume of the unit cell. The average stress and strain of the homogenized model follow the Hooke's law as

$$\bar{\sigma} = \mathrm{D}^{\mathrm{H}}\bar{\varepsilon}$$

where D^{H} is the effective elastic tensor of the material. The effective elastic tensor of 2D orthotropic material under plane-stress can be written in matrix form as

$$\mathrm{D}^{\mathrm{H}} = \begin{bmatrix} \mathrm{D}^{\mathrm{H}}_{1111} & \mathrm{D}^{\mathrm{H}}_{1122} & 0 \\ \mathrm{D}^{\mathrm{H}}_{1122} & \mathrm{D}^{\mathrm{H}}_{2222} & 0 \\ 0 & 0 & \mathrm{D}^{\mathrm{H}}_{1212} \end{bmatrix} \tag{1.20}$$

The strain energy stored in the periodic structure and the homogenized model have to be equal as

$$U(\varepsilon) = \frac{1}{2V}\int_{\Omega} (\sigma_{11}\varepsilon_{11} + \sigma_{22}\varepsilon_{22} + \sigma_{12}\varepsilon_{12})\, d\Omega = \frac{1}{2}(\bar{\sigma}_{11}\bar{\varepsilon}_{11} + \bar{\sigma}_{22}\bar{\varepsilon}_{22} + \bar{\sigma}_{12}\bar{\varepsilon}_{12}) = U(\bar{\varepsilon}) \tag{1.21}$$

With some specific boundary conditions, the effective elastic tensor can be identified from the strain energies of unit cell.

1.3.2.2 Mode-based method

Jhung [41] proposed the mode-based method to determine equivalent Young's Modulus of solid plate to match the frequencies of the perforated plate. The following steps are conducted in his research. Firstly, develop a finite element model for homogeneous solid plate and perforated plate. Secondly, perform the modal analysis for perforated plate and the solid plate with original properties. Thirdly, compare the frequencies and determine the ratio of frequencies for the perforated plate to those of homogeneous solid plate. At last, find the multipliers of Young's modulus of homogeneous solid plate in order to match the frequencies of the perforated plate with original properties using the relationship between the frequency and Young's modulus. This investigation approach can be expand in applications. However, with mode-based approach, one may find different equivalent parameters if the modal analysis is carried out under different boundary conditions. Moreover, one may find different equivalent parameters if the modal analysis is carried out under different boundary conditions.

1.3.2.3 Wave-based method

Chronopoulos [40] proposed a wave-based method to calculate a dynamic stiffness matrix for the modeled laminate. The wave dispersion relation of propagating flexural and shear waves in solid structure can be easily found associated with the mechanical characteristics of the structure. Meanwhile the wave dispersion characteristics of 2D periodic medium can be numerically predicted using a Wave Finite Element Method (WFEM) for a wide frequency range. The computed dispersion characteristics are used in order to update the classical plate theories and calculate a dynamic stiffness matrix for the modeled laminate. The derived equivalent dynamic mechanical characteristics are in expressions of

$$\begin{aligned} D_{eq,i} &= \frac{\omega^2 \rho_s}{k_{f,i}^4}, \\ B_{eq,xy} &= \frac{\omega^2 \rho_s}{k_{s,xy}^4}, \end{aligned} \tag{1.22}$$

where ρ_s represent the mass per unit area. $D_{eq,i}$ is the equivalent flexural stiffness of the structure towards direction i, and $B_{eq,i}$ is equivalent shear stiffness in the $x-y$ plane. The resulting updated Equivalent Single Layer (ESL) modeling proves to be time efficient and accurate for a wide frequency range.

1.3.2.4 Asymptotic homogenization method

Here a brief overview of the steps involved in the development of classical asymptotic homogenization method under the long wavelength approximation is introduced [42]. Consider a periodic structure occupying domain Ω with boundary $\partial\Omega$. The first step is to define the microscopic variables y_i in the domain of the unit cell Y,

$$y_i = \frac{x_i}{\varepsilon}, \qquad i = 1, 2, 3, \tag{1.23}$$

where $\varepsilon = l/L$, where l is the period of the structure and L is the length of the structure. Then the derivatives with respect to $x_i$can be transformed according to

$$\frac{\partial}{\partial x_i} \rightarrow \frac{\partial}{\partial x_i} + \frac{1}{\varepsilon}\frac{\partial}{\partial y_i} \tag{1.24}$$

so the boundary-value problem which describes the elastic deformation of the periodic structure can be written as:

$$\frac{\partial {\sigma_{ij}}^{\varepsilon}}{\partial x_i} + \frac{1}{\varepsilon}\frac{\partial {\sigma_{ij}}^{\varepsilon}}{\partial y_i} = f_i \quad in \quad \Omega, \quad {u_i}^{\varepsilon} = 0 \quad on \quad \partial\Omega \tag{1.25a}$$

$${\sigma_{ij}}^{\varepsilon}(\mathbf{x},\mathbf{y}) = C_{ijkl}(\mathbf{y})\frac{\partial u_k}{\partial x_l}(\mathbf{x},\mathbf{y}) \tag{1.25b}$$

The next step is to consider the asymptotic expansions in terms of the small parameter ε:

i) Asymptotic expansion for the displacement field:

$$\mathbf{u}^{\varepsilon}(\mathbf{x},\mathbf{y}) = \mathbf{u}^{(0)}(\mathbf{x},\mathbf{y}) + \varepsilon\mathbf{u}^{(1)}(\mathbf{x},\mathbf{y}) + \varepsilon\mathbf{u}^{(2)}(\mathbf{x},\mathbf{y}) + ... \tag{1.26}$$

ii) Asymptotic expansion for the stress field:

$${\sigma_{ij}}^{\varepsilon}(\mathbf{x},\mathbf{y}) = {\sigma_{ij}}^{(0)}(\mathbf{x},\mathbf{y}) + \varepsilon{\sigma_{ij}}^{(1)}(\mathbf{x},\mathbf{y}) + \varepsilon^2{\sigma_{ij}}^{(2)}(\mathbf{x},\mathbf{y}) + ... \tag{1.27}$$

All functions in $\mathbf{y}$ are collectively periodic with the unit cell Y. By substituting equation (1.23), (1.24) and (1.25b) into Eq. (1.25a) and considering at the same time the periodicity of $\mathbf{u^{(i)}}$ in $\mathbf{y}$ in the asymptotic displacement field expansion to show that it depends only on the macroscopic variable $\mathbf{x}$. Subsequently, by substituting Eq. (1.27) into Eq. (1.25a) and considering terms with like powers of ε, one obtains a series of differential equations the first two expressions of which are

$$\frac{\partial \sigma_{ij}^{(0)}}{\partial y_j} = 0 \tag{1.28a}$$

$$\frac{\partial \sigma_{ij}^{(1)}}{\partial y_j} + \frac{\partial \sigma_{ij}^{(0)}}{\partial x_j} = 0 \tag{1.28b}$$

where

$$\sigma_{ij}^{(0)} = C_{ijkl}\left(\frac{\partial u_k^{(0)}}{\partial x_l} + \frac{\partial u_k^{(1)}}{\partial y_l}\right) \tag{1.29a}$$

$$\sigma_{ij}^{(1)} = C_{ijkl}\left(\frac{\partial u_k^{(1)}}{\partial x_l} + \frac{\partial u_k^{(2)}}{\partial y_l}\right) \tag{1.29b}$$

Combination of Eqs. (1.28a) and (1.29a) leads to the following expression

$$\frac{\partial}{\partial y_j}\left(C_{ijkl}\frac{\partial u_k^{(1)}(\mathbf{x},\mathbf{y})}{\partial y_l}\right) = -\frac{\partial C_{ijkl}(\mathbf{y})}{\partial y_j}\frac{\partial u_k^{(0)}(\mathbf{x})}{\partial x_l} \tag{1.30}$$

The separation of variables on the right-hand-side of Eq. (1.30) gives us to write down the solution for $\mathbf{u}^{(1)}$

$$u_m^{(1)}(\mathbf{x},\mathbf{y}) = V_m(\mathbf{x}) + \frac{\partial u_k^{(0)}(\mathbf{x})}{\partial x_l} N_m^{kl}(\mathbf{y}) \tag{1.31}$$

where functions N_m^{kl} are periodic in $\mathbf{y}$ and satisfy

$$\frac{\partial}{\partial y_j}\left(C_{ijmn}(\mathbf{y})\frac{\partial N_m^{kl}(\mathbf{y})}{\partial y_n}\right) = -\frac{\partial C_{ijkl}}{\partial y_j} \tag{1.32}$$

while the function $V_m(x)$ is the homogenous solution of Eq. (1.31) and satisfies

$$\frac{\partial}{\partial y_j}\left(C_{ijmn}(\mathbf{y})\frac{\partial N_m^{kl}(\mathbf{y})}{\partial y_n}\right) = 0 \tag{1.33}$$

We can see that Eq. (1.32) depends entirely on the fast variable $\mathbf{y}$ and is thus solved on the domain Y of the unit cell, remembering at the same time that both C_{ijkl} and N_m^{kl} are Y-periodic in $\mathbf{y}$. Consequently, Eq. (1.32) is appropriately referred to as the unit cell problem.

The next important step in the model development is the homogenization procedure. This is carried out by first substituting (1.31) into Eq. (1.29a), and combining the result with Eq. (1.28a). The resulting expression is eventually integrated over the domain Y of the unit cell (with volume $|\mathbf{Y}|$) remembering to treat x_i as a parameter as far as integration with respect to y_j is concerned. This yields

$$\frac{1}{|Y|}\int_Y \frac{\partial \sigma_{ij}{}^{(1)}(\mathbf{x},\mathbf{Y})}{\partial y_i} dv + \tilde{C}_{ijkl}\frac{\partial u_k{}^{(0)}(\mathbf{x})}{\partial x_j \partial x_i} = f_i \tag{1.34}$$

where the homogenized or effective elastic coefficients $\tilde{C}_{ijkl}$ can be expressed as follows:

$$\tilde{C}_{ijkl} = \frac{1}{|Y|}\int_Y \left(C_{ijkl}(\mathbf{y}) + C_{ijmn}(\mathbf{x})\frac{\partial N_m^{kl}}{\partial y_n}\right) dv$$

It is noticed that the effective elastic coefficients are free from the inhomogeneity complications that characterize their actual rapidly varying material counterparts, C_{ijkl}, and as such, are more amenable to analytical and numerical treatment. The effective coefficients shown above are universal in nature and can be used to study a wide variety of boundary value problems associated with a given composite structure.

1.4 Generalized continuum theory method

From section 1.1 and 1.2, developing the model with the combination of discrete material governed by the individual particles can be a solution to capture the microstructures effect when the wavelength is approaching the length of spatial period of the system. However, modelling each inner individual micro-particle separately

requires enormous time and computational resource. Another solution is enrich the conventional continuum theory with the micro-scale behavior explicitly included in the modelling. Accordingly, macroscopic constitutive models can be employed that capture the local micro-scale properties by an appropriate definition of non-local parameters. This theory is know as 'generalized continuum theory' or, 'non-local continuum theory'. The basic idea of the generalized continuum theory is to establish a relationship between macroscopic mechanical quantities and microscope physical quantities within the framework of continuum mechanics.

In this section, a review is presented for the origination, development of different kind of generalized continuum theory. Among these theories, three types are illustrated in details. Then the application of generalized continuum theory are presented for both nano-size structures and general periodic structure.

1.4.1 The origination and development of generalized continuum theory

The origination of generalized continuum theories can be traced back to 1909, when Cosserat brothers developed a non-linear theory for bars, surfaces and bodies with an independent couple-stresses in an elastic continuum [43]. In 'Cosserat continuum', a 'rigid triad' is introduced at every point which can rotate independently from the local rotation of the medium in the course of deformation, then the effect of couple stresses can be fully accounted in the deformation process.

The work of the Cosserat brothers did not get much attention until early 1960s, the elasticity theory with couple stresses was discussed and expanded to different branches by several authors. In general, these branches can be categorized into three different classes namely the higher gradient theory, the higher order theory and non-local elasticity theories.

Among the strain gradient theories, Truesdell and Toupin [44, 45], Mindlin and Tiersten [46], Eringen [47] initially suggested a special case for the Cosserat continuum theory, in which the rotation of the rigid Cosserat triad is not an independent kinematic variable. This theory is referred as 'Couple Stress theory' (CS theory). In CS theory, the gradient of the rotation vector is introduced into the strain energy density function, that is eight of the eighteen components of the first gradient of strain. Subsequently, the 'Strain Gradient theory' (SG theory) was developed by introducing all the components of strain gradient into the strain energy density function [48]. Based on the concept of expansion to higher order gradient, 'multipolar theory' is established with including all higher-order gradients of the strain [49]. In 1965, Mindlin [50] established the 'Second Strain Gradient theory' (SSG theory), in which the strain energy density is considered to depend on the second and third derivatives of the displacement, along with classical strain tensor. In this work, the stress-equation of equilibrium and the constitutive equations are both established in general form. All these above theories which associate potential energy to spatial gradients of strain, are referred as 'higher gradient theories' in the literature. Recently, in 2002, 'Modified Couple Stress theory' (MCS theory) and 'Modified Strain

Gradient theory' (MSG) theory [51, 52] are developed by modifying Mindlin's theory with an additional equilibrium relation to govern the behavior of the 'couple' and less material length scale parameters are involved in the corresponding constitutive equation.

Another direction of generalizing classical continuum theory is by supplying additional degrees of freedom to a material point to describe effects of the underlying micro-structure deformation, which is referred as 'higher order theories' in literature. The micromorphic theory by Eringen [47][53], the micro-structure theory of Mindlin [54] falls into this category. In classical classical continuum mechanics, a material body is considered as a continuous collection of material points, each with infinitesimal size and no inner structure. By contrast, in Micromorphic theory [47], a material body is considered as a continuous collection of deformable particles and each possesses finite size and inner structure. The deformable particle is represented by a geometric point and some vectors attached to that point, which denote the orientations and intrinsic deformations of all the material points in the deformable particle. Two special cases of the micromorphic theory are the microstretch [55] theory and the micropolar theory [56]. In the microstretch continuum, four additional degrees of freedom including three for the rotation and one for the stretch, is introduced. In the case of the micropolar continuum, the directors are rigid and there are only three rotational degrees of freedom besides the three classical displacement degrees of freedom.

The third branch of generalized continuum theory is non-local elasticity theory, which was initially proposed in 1960s by Kroner [57], Kunin [58] and Krumhansl [59]. The early formulations of non-local elastic constitutive equation are based on lattice dynamics. Then the non-local elastic theory is improved by Eringen who formulate the constitutive equation of non-local material via the vehicles of global balance laws and the second law of thermodynamics for the first time [60, 61, 62], and determine the non-local material moduli to fit the obtained dispersion relations with the acoustical branch of elastic waves within the first Brillouin zone in one dimensional periodic lattices [63]. On the basis of the nonlocal continuum field theory developed by Eringen, Gao developed an asymmetric theory of nonlocal elasticity with nonlocal body couple in 1999 [64], in which the antisymmetric stress is caused by nonlocal effect of local rotation and anisotropy, and the higher gradient theory can be regarded as first order approximation of nonlocal theory. Non-local elasticity theory was initially formulated in an integral form and later reformulated by Eringen [65] in a differential form by considering a specific kernel function. When it expresses the stress at a point of a material domain as a weighted value of the entire strain field, the non-local elasticity theory approach can be qualified as 'integral' or 'strongly' non-local. It can be qualified as 'gradient' or 'weakly' non-local when the stress is expressed as a function of the strain and its gradients at the same points [9].

In the last few decades, a bunch of hybrid method has been developed in the frame of generalized continuum theory, for example non-local strain gradient theory [66, 67], which is proposed based on a combination of the non-local elasticity theory

and the strain gradient theory. Chen et al. [68] provides an atomic viewpoint to examine the physical foundations of the generalized continuum theories and to justify their applicability through lattice dynamics and molecular dynamics.

1.4.2 Fundamental equations of generalized continuum theories

The fundamental equations are different for different types of generalized continuum theory as they describe micro-structure effect in different forms. For development of generalized models associated with different problems and applications, proper generalized continuum theory should be selected. In the following subsections, we will briefly state the fundamental equations of these theories.

1.4.2.1 Non-local elasticity theory

Non-local elasticity theory has been widely applied in the field of nano-structures analysis. It has great potential applications in closing the gap between the classical continuum limit and the atomic theory of lattices. The following assumptions are considered for the non-local elasticity equation: elastic, linear, homogenous and isotropic solid. The basic concept of non-local elasticity [9] without body forces is represented in integral form by Eq. (1.35)

$$\begin{aligned}
&\sigma_{ij,i} + \rho\left(f_i - \ddot{u}_j\right) = 0 \\
&\sigma_{ij}(\mathbf{x}) = \int_{\mathbf{V}} H\left(\left|\mathbf{x}' - \mathbf{x}\right|, \phi\right) \sigma_{ij}^{c}\left(\mathbf{x}'\right) dV\left(\mathbf{x}'\right) \\
&\sigma_{ij}^{c}\left(\mathbf{x}'\right) = \lambda \varepsilon_{rr}\left(\mathbf{x}'\right) \delta_{ij} + 2\mu \varepsilon_{kl}\left(\mathbf{x}'\right) \\
&\varepsilon_{kl}\left(\mathbf{x}'\right) = \frac{1}{2}\left(\frac{\partial u_i(\mathbf{x}')}{\partial {x'}_j} + \frac{\partial u_j\left(\mathbf{x}'\right)}{\partial {x'}_i}\right)
\end{aligned} \tag{1.35}$$

The term σ_{ij} is non-local stress; σ_{ij}^{c} is classical stress; ε_{kl} is classical strain; C_{ijkl} is fourth-order elasticity tensors. The terms λ and μ are Lame's first and second parameters, respectively. The volume integral is over the region $\mathbf{V}$ occupied by the body. The kernel function $H\left(\left|\mathbf{x}' - \mathbf{x}\right|, \phi\right)$ is known as the non-local modulus or influencing kernel function. The non-local modulus acts as an attenuation function incorporating into the constitutive equations the non-local effects at the reference point $\mathbf{x}$ produced by local strain at the source $\mathbf{x}'$. The term $\left|\mathbf{x}' - \mathbf{x}\right|$ is the distance in the Euclidean form and ϕ is a material constant that depends on the internal (e.g. lattice parameter, granular size and distance between the C-C bonds) and external (e.g. crack length and wave length) characteristic lengths. The non-local modulus reaches its maximum at $\mathbf{x} = \mathbf{x}'$ attenuating with $\mathbf{x}' - \mathbf{x}$.

The single parameter ϕ based on non-local elasticity is expressed as:

$$\phi = \frac{e_0 l_c}{l_e},$$

where e_0 is the constant appropriate to each material; l_c denotes the internal characteristic length, and l_e denotes external characteristic length. For the internal

characteristic length, examples can be referred to lattice parameter, granular size and distance between C-C bonds. While the external characteristic length includes crack length, wave length and sample size of the nano-structure, length of CNTs and graphene sheets (sample size) is generally used as external characteristic length. In other size-dependent continuum mechanics such as MCS theory, thickness of the structure is considered as external characteristic length. Value of e_0 can be obtained by matching the dispersion curves from Born-Karman model of lattice dynamics and non-local theory. One such example can be cited in [69] of determining the value of e_0 for the free vibration of non-local beams.

For a given material, the non-local modulus H can be determined by matching the dispersion curves of plane waves with those of atomic lattice dynamics or experiments. By defining different forms of non-local modulus, various approximate models of non-local elasticity can be obtained. One such example is implemented in [70] for the free vibration of single-walled carbon nanotubes by comparing the predictions from the nonlocal first-order shear deformation theory shell model with MD simulations. Another example refers to free vibration of double-walled carbon nanotube based on non-local elasticity theory (see e.g. Kaddour et al. [71]). If the non-local term (parameter) approaches zero, i.e $\phi \to 0$, the non-local modulus H reverts to the Dirac delta measure. Consequently, classical elasticity is included in the limit of vanishing internal characteristic length. When $\phi \to 1$, non-local theory approximates atomic lattice dynamics.

Since the governing relation of non-local elasticity (1.35) is an integro-partial differential equation, it is generally difficult to solve. To simplify the governing non-local relation, the non-local modulus $H\left(\left|x'-x\right|,\phi\right)$ is assumed as Green's function of linear differential operator:

$$L_o H\left(\left|x'-x\right|,\phi\right)=\delta\left(\left|x'-x\right|\right). \tag{1.36}$$

where L_o is the linear differential operator and δ is the Dirac-delta function. Green's function is chosen in conjunction with the properties of non-local modulus. Applying L_o to Eq. (1.35) gives

$$L_o\sigma_{ij}={\sigma_{ij}}^c \tag{1.37}$$

The differential operator L_o can have different forms for different expressions of non-local modulus. For the non-local modulus depicted in Eq. (1.36), combining with Eq. (1.37), linear differential operator can be given as

$$L_o=1-{l_e}^2\phi^2\nabla^2, \tag{1.38}$$

where ∇^2 is the Laplace operator. According to equations (1.37) and (1.38), the non-local constitutive relation can be expressed in differential form as:

$$[1-(e_0l_c)^2\nabla^2]\sigma_{ij}=\lambda\varepsilon_{rr}\delta_{ij}+2\mu\varepsilon_{kl} \tag{1.39}$$

For simplicity, Eq. (1.39) can be written as

$$[1-(e_0l_c)^2\nabla^2]\sigma_{ij}=C_{ijkl}\varepsilon_{kl} \tag{1.40}$$

where C_{ijkl} is the fourth-order elasticity tensor.

Non-local elasticity theory has been widely employed in many cases. Among other applications, Zhang et al. developed non-local beam model for the free transverse vibrations of double-walled carbon nanotubes, and investigate the influence of small length scale to the natural frequencies and the associated amplitude ratios of the inner to the outer tubes [72]. Reddy et al. reformulate various beam theories using nonlocal differential constitutive relations of Eringen, deduce the analytical solutions of bending, vibration and buckling, and investigated the effect of the nonlocal behavior on deflections, buckling loads, and natural frequencies[73, 74]. Silling proposed the 'peridynamic' formulation based on non-local elasticity theory to study the discontinuities in materials, with which the wave dispersion relation linear stress waves and material stability is studied. The reformulated approach permits the solution of fracture problems using the same equations either on or off the crack surface or crack tip [75].

1.4.2.2 Modified couple stress theory

The Modified Couple Stress theory (MCS) was proposed by Yang et al. [51] by modifying the classical couple stress theory of Toupin [45], Mindlin and Tiersten [46] with introducing an additional equilibrium condition for moments of couples to enforce the couple stress tensor to be symmetric. Then the number of additional material length scale parameters in the modified couple stress theory is reduced from two to one. The strain energy $\bar{u}$ is a function of both strain and curvature as 1.41,

$$\bar{u} = \frac{1}{2}\left(\sigma_{ij}\varepsilon_{ij} + m_{ij}\chi_{ij}\right), \qquad (i,j = 1,2,3), \tag{1.41}$$

where

$$\begin{aligned}
\sigma_{ij} &= \lambda\varepsilon_{mm}\delta_{ij} + 2\mu\varepsilon_{ij},\\
\varepsilon_{ij} &= \tfrac{1}{2}(u_{i,j} + u_{j,i}),\\
m_{ij} &= 2l^2\mu\chi_{ij},\\
\chi_{ij} &= \tfrac{1}{2}\left((\nabla\theta)_{ij} + (\nabla\theta)_{ij}{}^{T}\right).
\end{aligned}$$

σ_{ij} represents the component of the symmetric part of stress tensor $\boldsymbol{\sigma}$, $\boldsymbol{\varepsilon}$ represents the strain tensor, m_{ij} is the deviatoric part of the couple stress tensor and $\boldsymbol{\chi}$ is the symmetric part of the curvature tensor. $\mathbf{u}$ and $\boldsymbol{\theta}$ are the displacement vector and the rotation vector. The two Lame constants and the material length scale parameter are represented by λ and μ and l respectively. The components of the infinitesimal rotation vector θ_i are related to the components of the displacement vector field u_i as

$$\theta_i = \frac{1}{2}(curl\,(\mathbf{u}))_i$$

MCS theory has been widely employed to establish generalized continuum models for different types of structures. To be specific, in modelling Euler-Bernoulli beam to study its large deflections and nonlinear forced-vibration by Kahrobaiyan et al. [76].

Trinh [77] investigated the static deflection and free vibration of functionally graded microbeams based on MCS theory. Ma and Reddy [78] also developed a modified couple stress theory-based Timoshenko beam model with considering both bending and axial deformations as well as the Poisson effect. The resulting static bending and free vibration agree with those observed experimentally. Asghari studied the nonlinear deformation of Timoshenko microbeam based on MCS theory, in which the nonlinear behavior of the proposed model is due to the present of induced mid-plane stretching, a prevalent phenomenon in beams with two immovable supports. MCS theoy has also been used in modelling and property analysis of plate structure. For instance, non-classical Kirchhoff plate model and Mindlin plate model are developed by Tsiatas [79] and Tsiatas[80] based on MCS theory with material length scale parameter, nonlinear deformation of bending, buckling, and vibration responses of microplates are investigated based on the proposed models.

1.4.2.3 Second strain gradient theory

According to Mindlin's research [50], in SSG theory, the potential energy density $\bar{u}$ is assumed to be a function of three tensors $\boldsymbol{\varepsilon}$, $\boldsymbol{\eta}$ and $\boldsymbol{\xi}$, in which $\boldsymbol{\varepsilon}$ is the classical symmetric strain tensor, $\boldsymbol{\eta}$ and $\boldsymbol{\xi}$ are respectively the second gradient of the displacement vector and the third gradient of the displacement vector,

$$\boldsymbol{\varepsilon} = \frac{1}{2}\left(\nabla\mathbf{u} + \mathbf{u}\nabla\right), \quad \boldsymbol{\eta} = \nabla\nabla\mathbf{u}, \quad \boldsymbol{\xi} = \nabla\nabla\nabla\mathbf{u}. \tag{1.42}$$

Since the media is composed of numerous crystals with random orientation, the material can be considered homogeneous and isotropic, then strain energy density of the material is expressed as,

$$\begin{aligned}\bar{u} =& \frac{1}{2}\lambda\varepsilon_{ii}\varepsilon_{jj} + \mu\varepsilon_{ij}\varepsilon_{ij} + a_1\eta_{ijj}\eta_{ikk} + a_2\eta_{iik}\eta_{kjj} + a_3\eta_{iik}\eta_{jjk} + a_4\eta_{ijk}\eta_{ijk} + a_5\eta_{ijk}\eta_{kji} \\ &+ b_1\xi_{iijj}\xi_{kkll} + b_2\xi_{ijkk}\xi_{ijll} + b_3\xi_{iijk}\xi_{jkll} + b_4\xi_{iijk}\xi_{llkj} + b_5\xi_{iijk}\xi_{lljk} + b_6\xi_{ijkl}\xi_{ijkl} \\ &+ b_7\xi_{ijkl}\xi_{jkli} + c_1\varepsilon_{ii}\xi_{jjkk} + c_2\varepsilon_{ij}\xi_{ijkk} + c_3\varepsilon_{ij}\xi_{kkij} + b_0\varepsilon_{iijj},\end{aligned} \tag{1.43}$$

where λ and μ are the usual Lame's constants. Parameters a_i, b_i and c_i are higher-order material constants which particularly appear in SSG theory. ε_{ij}, η_{ijk} and $\xi_{ijkl}\,(i,j,k,l=1,2,3)$ are the components of tensors $\boldsymbol{\varepsilon}$, $\boldsymbol{\eta}$ and $\boldsymbol{\xi}$, and their expressions can be written in terms of the components of displacement vector as

$$\begin{aligned}\varepsilon_{ij} &= \frac{1}{2}\left(\frac{\partial u_j}{\partial x_i} + \frac{\partial u_i}{\partial x_j}\right) = \frac{1}{2}\left(\partial_j u_i + \partial_i u_j\right), \\ \eta_{ijk} &= \frac{\partial^2 u_k}{\partial x_i \partial x_j} = \partial_i\partial_j u_k, \\ \xi_{ijkl} &= \frac{\partial^3 u_l}{\partial x_i \partial x_j \partial x_k} = \partial_i\partial_j\partial_k u_l.\end{aligned} \tag{1.44}$$

If the potential energy density is assumed to depend on the strain and the gradient of the strain, setting $b_i = 0$ and $c_i = 0$, then it results the strain gradient theory. The conjugate stresses are defined by differentiating the strain energy density $\bar{u}$ with respect to the corresponding strain components,

$$\boldsymbol{\sigma} = \frac{\partial \bar{u}}{\partial \boldsymbol{\varepsilon}}, \quad \boldsymbol{\tau} = \frac{\partial \bar{u}}{\partial \boldsymbol{\eta}}, \quad \boldsymbol{\pi} = \frac{\partial \bar{u}}{\partial \boldsymbol{\xi}}. \tag{1.45}$$

It should be noted here, even though the stress tensors $\boldsymbol{\sigma}$, $\boldsymbol{\tau}$ and $\boldsymbol{\pi}$ are respectively named with the classical stress, the first higher-order stress and the second higher-order stress, their values could be related with all three order strains as,

$$\begin{aligned}
\sigma_{pq} =& \lambda \varepsilon_{ii} \delta_{pq} + 2\mu \varepsilon_{pq} + c_1 \xi_{iijj} \delta_{pq} + c_2 \xi_{pqii} + \frac{1}{2} c_3 \left(\xi_{iipq} + \xi_{iiqp} \right), \\
\tau_{pqr} =& a_1 \left(\eta_{pii} \delta_{qr} + \eta_{qii} \delta_{pr} \right) + \frac{1}{2} a_2 \left(\eta_{iip} \delta_{qr} + 2\eta_{rii} \delta_{qp} + \eta_{iiq} \delta_{pr} \right) \\
& + 2a_3 \eta_{iir} \delta_{pq} + 2a_4 \eta_{pqr} + a_5 \left(\eta_{rqp} + \eta_{rpq} \right), \\
\pi_{pqrs} =& \frac{2}{3} b_1 \xi_{iijj} \delta_{pqrs} + \frac{2}{3} b_2 \xi_{jkii} \delta_{jkpqrs} + \frac{1}{6} b_3 \left[\left(\xi_{iijk} + \xi_{iikj} \right) \delta_{jkpqrs} + 2\xi_{jsii} \delta_{jpqr} \right] \\
& + \frac{2}{3} b_4 \xi_{iisj} \delta_{jpqr} + \frac{2}{3} b_5 \xi_{iijs} \delta_{ipqr} + 2b_6 \xi_{pqrs} + \frac{2}{3} b_7 \left(\xi_{qrsp} + \xi_{rspq} + \xi_{spqr} \right) \\
& + \frac{1}{3} c_1 \varepsilon_{ii} \delta_{pqrs} + \frac{1}{3} c_2 \varepsilon_{ij} \delta_{ijpqrs} + \frac{1}{3} c_3 \varepsilon_{is} \delta_{ipqr},
\end{aligned} \tag{1.46}$$

in which δ_{ij} is the Kronecker delta and

$$\delta_{pqrs} = \delta_{ij}\delta_{kl} + \delta_{ik}\delta_{jl} + \delta_{jk}\delta_{il}, \quad \delta_{ijklmn} = \delta_{ik}\delta_{jl}\delta_{mn} + \delta_{ik}\delta_{jm}\delta_{ln} + \delta_{il}\delta_{jm}\delta_{kn}.$$

Mindlin's SSG theory is considered as one of the most effective gradient elasticity theory, even though the lack of available experimental measurement techniques for second gradient elastic moduli, and being short of the physical interpretation of the higher-order constants yield some criticisms. One can note that the CS theory and SG theory are particular cases of the SSG theory with less higher-order constants. Therefore, this theory is more general than the CS and SG theories.

SSG theory already has some successful applications, namely, being capable of capturing the scale effects of experimentally observed mechanics behaviors where the specimen characteristic length or the wavelength of the disturbance are comparable to the lengths of the major heterogeneity in the media [81]. Among other applications, Karparvarfard et al. [82] developed nonlinear governing differential equation for small-scale Euler–Bernoulli beams and investigated nonlinear size-dependent static bending and free vibration behaviors. SSG theory-based Timoshenko beam model has been established by Asghari [83] to study the static and free-vibration behaviors, and to capture the size effects in micro-scale and nano-scale structures. One can also cite the SSG theory-based modelling by Momeni [84]) for functionally graded beam structures (FGMs) with Hamilton principle, the size-dependent response of FG beams in free-vibration and static behavior is numerically investigated.

1.4.2.4 Strain gradient theory

Strain gradient theory, or first strain gradient theory, was developed by introducing all the components of strain gradient into the strain energy density function, and it can be regarded as one special case of SSG theory. If the potential energy density is assumed to depend on the strain and the gradient of the strain, then it results the strain gradient theory. The strain and stress tensors of SG theory share the same expression as the first two equations in (1.44) and (1.45), and the strain energy density of SG theory can be be obtained by setting the higher oreder constants $b_i = 0$ and $c_i = 0$ as

$$\bar{u} = \frac{1}{2}\lambda\varepsilon_{ii}\varepsilon_{jj} + \mu\varepsilon_{ij}\varepsilon_{ij} + a_1\eta_{ijj}\eta_{ikk} + a_2\eta_{iik}\eta_{kjj} + a_3\eta_{iik}\eta_{jjk} + a_4\eta_{ijk}\eta_{ijk} + a_5\eta_{ijk}\eta_{kji} \tag{1.47}$$

Duo the simplicity, SG theory and the related gradient theory models have been employed to analyze various problems. Among other areas. Kong et al. [85] assessed the static and dynamic problems of Bernoulli–Euler beams based on SG theory model, with which the beam deflections are found to decrease and natural frequencies increase remarkably when the thickness of the beam becomes comparable to the material length scale parameter. Wang et al. [86] analyzed the static bending and free vibration problems of a simply supported micro-scale Timoshenko beam, the new model incorporated three material length scale parameters and can consequently capture the size effect. A cantilever beam model was developed by Joseph based on strain gradient elasticity theory [87] to investigate its large deformation behavior, and this model is further employed to study the fracture behavior of a flexoelectric double cantilever beam (DCB) under large deformation [88]. The effect of uncracked part of the DCB is found to be substantial in determining the strain energy release rate and it must not be ignored even for the slender beams. A dielectric nanobeam is investigated based on strain gradient theory by Zhou [89] with incorporating three length-scale parameters, which shows that the strain gradient elasticity and flexoelectricity have apparent size effects and significant influence on the electromechanical response. This work may be helpful in understanding the mechanism of flexoelectricity at the nano-scale and sheds light on the flexoelectricity energy harvesting. In the work of Ansari [90], a size-dependent functionally graded (FGM) Timoshenko microbeam model is developed based on the strain gradient theory, the effects of the length scale parameter, gradient index and slenderness ratio on the vibrational behavior of FGM microbeams are explored. Various beam theories including the classical, modified couple stress, strain gradient theories are compared.

In addition to these four type of generalized continuum theory, the other kinds are also has been developed and applied in many cases. For example the micro-polor theory has been used in cantilevered plate modelling by McFarland and Colton [91] to study its bending stiffness. The Modified Strain Gradient Theory theory (MSG theory) has been used in Euler beam formulation[92], based on which the finite element implementation are presented.

1.4.3 Application of generalized continuum theory in wave propagation analysis

Generalized continuum theories introduce not only different deformation behaviors for the particles but also complex behavior in wave propagation. A known consequence is the existence of new wave modes which could not be observed in the classical elastic solids. Recent work by Suiker et al. [3, 93] predicted dispersive body waves based on the proposed second-gradient micro-polar formulation. When the wavelength reaches the order the particle size, the dispersion becomes more prominent. Li et al. [94] investigate the flexural wave propagation in small-scaled functionally graded (FG) beams with non-local strain gradient theory model, based on which an asymptotic phase velocity of both the acoustical and optical branches can be observed. The asymptotic phase velocity can be increased by decreasing the nonlocal parameter or increasing the material characteristic parameter. Wave propagation characteristics are also investigated by Gopalakrishnan [95] using the Erigen's stress gradient model and Mindlin's strain gradient model with atomistic length scale parameters brought into the continuum governing equations. These scale parameter are proven to significantly affect the wave propagation referring to not only the dispersion relation, but also the escape frequency, phase speeds and group speeds in the structures, and the prediction results match very well with those predicted using atomistic simulation.

Generalized models based on various non-classical continuum theories have been modified by many research in dynamic modelling to have a better performance in approximation of dynamic behavior and wave propagation in non-classical continuum. In particular, Mindlin's theory model is improved in the research by De Domenico et al. [96] with an additional micro-inertia term. The dispersion behavior produced by the improved models fit better with experimental results. Lim et al. [67] introduced a higher order strain tensor with non-locality into the stored energy function to integrate non-locality into the higher-order strain gradient model. By doing so, the new dispersion relations agree better with MD simulation and matches experimental observations, which could not be matched either the classical non-local stress theory or the pure strain gradient theory. Nonlocal dispersive model for wave propagation in heterogeneous media is derived by Fish [97] from the higher order mathematical homogenization theory with multiple spatial and temporal scales. In this model, a fast spatial scale and a slow temporal scale are introduced to account for rapid spatial fluctuations of material properties as well as to capture the long term behaviour of the homogenized solution.

The unification of micro-structure models are achieved in the work of Berezovski [98] with the concept of dual internal variables. He derived the wave propagation with micro-elastic and micro-inertial characteristics in physically acceptable models. In 2011, Askes and Aifantis [99] gave a comprehensive overview of gradient elasticity theories which are applicable to statics as well as dynamics. They suggested that inclusion of the inertia-related length scale in acceleration gradients theory is essential in describing wave dispersion in dynamics. In like manner, these results are

confirmed with the research by Askes [100] and Metrikine [101]. They suggested a dynamically consistent model from a discrete micro-structure in which each higher-order stiffness term is accompanied by a higher order inertia term. The resulting dispersion equation is of the sixth order with respect to the wavenumber, hence one harmonic vibration of a point can excite three 'waves' on every side of this point. One is a propagating wave and the other two are non-propagating oscillations decaying with the distance from the excitation point. Li et al. [102] also pointed out that the dipolar gradient elastic solid creates one additional evanescent mode with consideration of the size effects and thermal effects.

The micro-structure effects not only also cause different waves reflection and transmission on a discontinuous surface of generalized continua. In the context of generalized continua, Placidi et al. [103] studied compression and shear wave propagation in second-gradient continua. They noticed that the effect of the second-gradient parameter are important for the reflection and transmission coefficients at surfaces of discontinuity. Dell'Isola et al. [104] deduced the mechanical energy equilibrium for second gradient material, based on which they estimated that the reflection and transmission coefficients at plane displacement discontinuity surfaces are significantly frequency-dependent. According to the research of Li et al.[102, 105], the reflection and transmission coefficients at the interface of two generalized medias are not only dependent of the micro-structure's parameters, but also of the incident angular frequency. This phenomenon is owing to the dispersive nature of the reflected and transmitted waves, and also to the two additional surface waves resulting from the micro-structural effects. This phenomenon only becomes pronounced when the incident wavelength is close to the characteristic length of the micro-structure.

1.5 Identification of length scale parameters

In material with a lattice micro-structure and heterogeneous media wherein the external characteristic length-scales are of the same order as those of the dominant heterogeneity, classical continuum elasticity theory fails to describe the physical phenomena in these materials because non-local (long-range) interactions play a major role in the deformation process.

Roughly speaking, the incapability of classical continuum mechanics theories is due to the absence of an internal length, which can characterize the underlying micro-structure from the constitutive equations. One obvious solution could be modeling every single micro-structural component individually, which represents the basis of molecular/atomistic models. Nevertheless, such models may be computationally prohibitive or extremely demanding on memory resources, thus unfeasible to cope with real engineering problems.

1.5.1 Length scale parameter

The proposed generalized continuum theories in section 1.3 including higher-gradient continuum theories, high order continuum theories and non-local elasticity theory,

are proven to be capable of bridging the gap between atomistic models and classical continuum mechanics theory. For example, the SSG theory formulations enrich the field equations of classical elasticity theory by means of 16 additional higher-order spatial derivative components of relevant state variables. These higher-order terms are accompanied by length scale parameters, which can reflect the underlying material micro-structure. To explicit the length scale parameters related with higher order material constants, the equation of force equilibrium for the media is developed in work of Mindlin [50] with variational method. In the presence of a body force $\mathbf{f}$ the equation of equilibrium for the media has the following form,

$$\nabla \cdot (\boldsymbol{\sigma} - \nabla \cdot \boldsymbol{\tau} + \nabla\nabla : \boldsymbol{\pi}) + \mathbf{f} = 0. \tag{1.48}$$

and the traction boundary conditions are in forms of

$$\begin{aligned}
\mathbf{t}_1 &= \mathbf{n} \cdot (\boldsymbol{\sigma} - \nabla \cdot \boldsymbol{\tau} + \nabla\nabla : \boldsymbol{\pi}) + \mathbf{L} \cdot \left[\mathbf{n} \cdot (\boldsymbol{\tau} - \nabla \cdot \boldsymbol{\pi}) + \mathbf{L} \cdot (\mathbf{n} \cdot \boldsymbol{\pi}) - \left(\overset{\mathbf{s}}{\nabla} \right) \cdot (\mathbf{nn} : \boldsymbol{\pi}) \right], \\
\mathbf{t}_2 &= \mathbf{nn} : (\boldsymbol{\tau} - \nabla \cdot \boldsymbol{\pi}) + \mathbf{n} \cdot [\mathbf{L} \cdot (\mathbf{n} \cdot \boldsymbol{\pi})] + \mathbf{L} \cdot (\mathbf{nn} : \boldsymbol{\pi}) \\
\mathbf{t}_3 &= \mathbf{nnn} \vdots \boldsymbol{\pi},
\end{aligned} \tag{1.49}$$

in which the vector $\mathbf{n}$ denotes the unit outward normal to the surface of the media, and $\overset{\mathbf{s}}{\nabla}$ and $\mathbf{L}$ are defined as

$$\overset{\mathbf{s}}{\nabla} = (\mathbf{I} - \mathbf{nn}) \cdot \nabla, \qquad \mathbf{L} = \mathbf{n} \overset{\mathbf{s}}{\nabla} \cdot \mathbf{n} - \overset{\mathbf{s}}{\nabla}.$$

The role of multiple scalar multiplication of dyads and trids are given as

$$\mathbf{ab} : \mathbf{cd} = (\mathbf{a} \cdot \mathbf{b})(\mathbf{b} \cdot \mathbf{d}); \qquad \mathbf{abd} \vdots \mathbf{def} = (\mathbf{a} \cdot \mathbf{d})(\mathbf{b} \cdot \mathbf{e})(\mathbf{c} \cdot \mathbf{f}).$$

Combination of Eq. (1.48), (1.46) and (1.43), the motion equation only in terms of displacement u is obtained as

$$(\lambda + 2\mu) D_{11}^2 D_{12}^2 \nabla\nabla \cdot \mathbf{u} - \mu D_{21}^2 D_{22}^2 \nabla \times \nabla \times \mathbf{u} + \mathbf{f} = 0, \tag{1.50}$$

where

$$D_{ij}^2 = 1 - l_{ij}^2 \nabla^2,$$

and

$$\begin{aligned}
2(\lambda + 2\mu) l_{1j}^2 &= \bar{a} - 2\bar{c} \pm \left[(a - 2c)^2 - 4\bar{b}(\lambda + 2\mu) \right]^{\frac{1}{2}}, \\
2\mu l_{2j}^2 &= \bar{a}' - c_3 \pm \left[(\bar{a} - c_3)^2 - 4\bar{b}'\mu \right]^{\frac{1}{2}}.
\end{aligned}$$

And

$$\begin{aligned}
&\bar{a} = 2(a_1 + a_2 + a_3 + a_4 + a_5); \\
&\bar{b} = 2(b_1 + b_2 + b_3 + b_4 + b_5 + b_6 + b_7); \\
&\bar{c} = c_1 + c_2 + c_3; \quad \bar{a}' = 2(a_3 + a_4); \quad \bar{b}' = (b_5 + b_6).
\end{aligned}$$

It can observed that the displacement equilibrium in Eq. (1.50) contains some terms involving the characteristic lengths of the material. The capability of the

SSG theory in capturing the size effect is the direct manifestation of involvement of these characteristic lengths. In fact, not only the SSG theory, but also all the other types of generalized continuum theory include such kind of intrinsic length scale parameters in theory that allows us to model physical phenomena where the micro-structure clearly exhibits specific features with particular length scales. The response of a material point depends not only on the strain at that point but also on the strain or history strain of a certain neighborhood of that point or even of the entire body. This is the reason that generalized continuum theories can be used to capture the complex multi-scale behaviors exhibited by complex media.

As we know, the CS theory and SG theory are particular cases of the SSG theory with less higher-order constants. Thus theoretical basis of Mindlin's SSG theory is more completed, and Mindlin's SSG theory is considered as one of the most effective gradient elasticity theories. In the following chapters of this thesis, SSG theory will be employed to establish generalized continuum models for both rod and beam structure with considering the local behaviors of the intrinsic heterogeneity in the complex media, and non-classical structural dynamic behavior and wave propagation features in complex media will be thoroughly investigated based on the proposed models.

To implement the investigation, the first step is choosing the correct length scale parameters, namely, higher order material constants for SSG theory. Certainly, the intrinsic length parameters of the periodic structure and the nano-structure are not the same, and the length scale parameters should be chosen corresponding with its intrinsic length.

To the present, the general length scale parameter identification method is matching the structural property, including but not limited to the fundamental frequencies, dispersion curves of plane waves, resulting from analytical model with those calculated by the MD simulations or experiments. For example, in the research of Kandaz [92], MSG theory and MCS theory are employed in Euler Bernoulli beam formulation, and the size effect for micro beams is demonstrated with the length scale parameters of gold micro-beams for MSGT and MCST identified for the first time form the existing experimental data of load-displacement curves in literature [106]. In the same manner, material length scale parameters are determined by Liebold [107] by analyzing experimental data obtained from force-displacement measurements using extremely small cantilever beams. In the research of Ansari [108], vibrational characteristics of single-walled carbon nanotubes (SWCNTs) based on the gradient elasticity theories are investigated with material length scale parameter l_m, and the appropriate values of l_m/l related to different beam theories are extracted by matching the fundamental frequencies obtained from the continuum models with those calculated by the MD simulations.

1.5.2 Length scale parameter identification for fcc metals

Mindlin (1964, 1965) presented the exact analytical formulations for the displacement fields pertinent to both first and second strain gradient theories. But due

to lack of the knowledge of the characteristic lengths, quantitative study was not possible. In the work of Shodja [109], the additional material constants and the characteristic lengths are evaluated for fcc metals in the framework of first and second strain gradient theories, and subsequently demonstrate their applications in two different types of problems.

Consider a lattice of interacting atoms, in which $\mathbf{r}^{\alpha}$ is the position vector of the αth atom, and $\mathbf{r}^{\alpha\beta}$ is defined as: $\mathbf{r}^{\alpha\beta} = \mathbf{r}^{\beta} - \mathbf{r}^{\alpha}$. The total energy density of the lattice can be written as:

$$E_v = \frac{U}{V}, \tag{1.51}$$

where V is the total volume of the lattice and U is the total inter-atomic potential energy. The inter-atomic potential energy can be represented by an appropriate empirical potential function. In the research of Shodja, the many body Sutton-Chen potential is chosen as a suitable potential function for fcc metals. This potential function serves to describe both cohesion in metals and the long range van der Waals interaction between atoms. This potential function has the following form:

$$\begin{aligned} U &= \varepsilon \left[\sum_{\alpha} \sum_{\alpha \neq \beta} U_2 \left(r^{\alpha\beta} \right) - c \sum_{\alpha} \sqrt{\rho^{\alpha}} \right], \\ U_2 &= \left(\frac{b}{r^{\alpha\beta}} \right)^{n}, \\ \rho^{\alpha} &= \sum_{\beta \neq \alpha} \left(\frac{b}{r^{\alpha\beta}} \right)^{rn}. \end{aligned} \tag{1.52}$$

where ε has the dimension of energy, c is a positive dimensionless parameter calculated from equilibrium condition. m and n are positive integer with $n > m$, ρ_{α} is the local electron density, and b is the equilibrium lattice parameter with the dimension of length. The above mentioned parameters for ten fcc metals are calculated by Sutton and Chen (1990) [110]. The analytical expression for the total energy density of an fcc lattice can be derived by setting the total energy density in the framework of SSG theory equivalent to Sutton-Chen interatomic potential function. Then the analytical formulations for the additional material constants corresponding to fcc metals are given in terms of the parameters of Sutton-Chen interatomic potential function.

1.5.3 Scale parameter identification for engineering periodic structure

In the research of Domenico [96], an extension of Mindlin's model is proposed with incorporating three internal length scale parameters corresponding to one micro-stiffness and two micro-inertia terms. Length scale identification is carried out based on higher-order homogenization to link the constitutive coefficients of the gradient theory directly to micro-structural properties of the layered composite. According

this research, the constitutive equation of the new model is expressed as

$$\sigma_{ij} = C_{ijkl}\left(\varepsilon_{kl} - {l_1}^2\varepsilon_{kl,mn} + {l_2}^2\ddot{\varepsilon}_{kl} - {l_2}^2\ddot{\varepsilon}_{kl,mn}\right) \tag{1.53}$$

We can see three gradient terms are accompanied by three length scale parameters l_1, l_2 and l_3 relating essentially to internal lengths and internal times (i.e. expanding ε_{kl} in Taylor series not only in space but also in time). For one-dimensional media

$$\sigma_{ij} = E\left(\varepsilon - {l_1}^2\varepsilon'' + {l_2}^2\ddot{\varepsilon} - {l_3}^2\ddot{\varepsilon}''\right), \tag{1.54}$$

where E is the Young's modulus. Over-dots and primes represent derivatives with respect to time and to the spatial coordinate x. Considering the equilibrium equation $\sigma' - \rho\ddot{u} = 0$, and rearranging the terms, the following motion equation in terms of displacement is expressed as

$$\rho\left(\ddot{u} - \frac{E}{\rho}{l_2}^2\ddot{u}'' + \frac{E}{\rho}{l_3}^2\ddot{u}''''\right) = E\left(u'' - {l_1}^2u''''\right), \tag{1.55}$$

which can be also rewritten as

$$\rho\left(\ddot{u} - \alpha l^2\ddot{u}'' + \beta l^2\ddot{u}''''\right) = E\left(u'' - \gamma l^2u''''\right). \tag{1.56}$$

The three length scales l_1, l_2, and l_3 are reported in terms of just a single length scale parameter l, characterizing the underlying material micro-structure. The three dimensionless coefficients α, β, γ adjust the relative magnitudes between the various length scales appearing in the strain gradient term and in the micro-inertia contributions.

To identify the corresponding length scale coefficients α, β, γ existing in the motion equation, the research work of by Domenico [111] is referred. A composite laminate is studied based on higher-order asymptotic homogenization schemes with multiple length scales and time scales. In that case, the internal micro-structure is known a prior as shown in figure 1.11

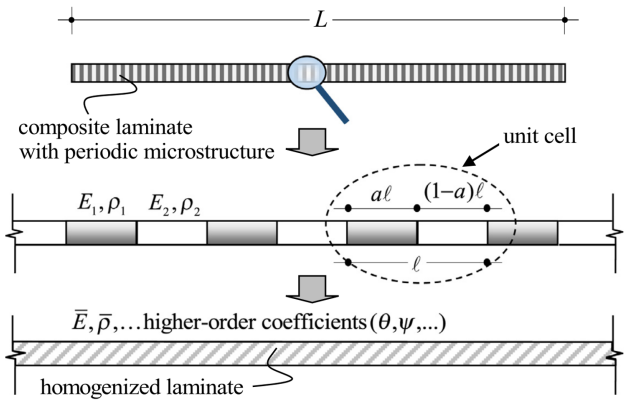

Figure 1.11: Two-component composite laminate with periodically heterogeneous micro-structure [111]

The composite laminate can be modeled as a one-dimensional rod with a periodic internal micro-structure, and the internal micro-structure is composed of two layers alternating periodically along the rod length L, namely, the composite laminate has piecewise homogeneous material characteristics, with layer 1 being characterized by mass density ρ_1 and Young's modulus E_1, and layer 2 being defined by ρ_2 and E_2. In each unit cell, materials 1 and 2 are assigned a volume fraction a and $1-a$, respectively, with $0 \leq a \leq 1$. The composite rod is considered to be long enough that the wave propagation in its periodic layer can be studied by analyzing the behavior of each unit cell of length l. The underlying assumption is that the microscopic size l of heterogeneity is significantly smaller than the macroscopic length L, at the limit $\varepsilon = l/L \to 0$. The homogenized equation of motion in the limit case as $\varepsilon = 0$ is given as

$$\bar{\rho}\ddot{u} = \bar{E}u'', \tag{1.57}$$

with $\bar{\rho}$ and $\bar{E}$ represent the effective mass density and the effective Young's modulus that are related to the component properties through the following relations

$$\begin{aligned} \bar{\rho} &= a\rho_1 + (1-a)\,\rho_2, \\ \bar{E} &= \frac{E_1 E_2}{(1-a)\,E_1 + aE_2}. \end{aligned} \tag{1.58}$$

In order to account for local variations of the displacements on the scale of heterogeneity, higher-order asymptotic homogenization schemes with multiple length scales and time scales is adopted, an asymptotic expansion including terms up to $\mathcal{O}(\varepsilon^4)$ is developed as

$$\bar{\rho}\ddot{u} = \bar{E}\left(u'' - \frac{1}{12}\theta^2 l^2 u'''' + \frac{1}{360}\theta^2\psi^2 l^4 u''''''\right) + \mathcal{O}\left(\varepsilon^6\right), \tag{1.59}$$

where

$$\theta = \frac{a\,(1-a)\,(E_1\rho_1 - E_2\rho_2)}{\bar{\rho}\,[(1-a)\,E_1 + aE_2]};$$

$$\psi = \frac{1}{\bar{\rho}\,[(1-a)\,E_1 + aE_2]} \left\{ \begin{array}{l} a^2 {E_2}^2 \left[2a^2 {\rho_1}^2 - (1-a)^2 {\rho_2}^2 + 6a\,(1-a)\,\rho_1\rho_2\right] \\ +2a\,(1-a)\,E_1E_2\left[3a^2{\rho_1}^2 + 3(1-a)^2{\rho_2}^2 + 11a\,(1-a)\,\rho_1\rho_2\right] \\ -(1-a)^2{E_1}^2\left[a^2{\rho_1}^2 - 2(1-a)^2{\rho_2}^2 - 6a\,(1-a)\,\rho_1\rho_2\right] \end{array} \right\}^{\frac{1}{2}}. \tag{1.60}$$

After performing some mathematical manipulations, Eq. (1.60) can be written in forms of

$$\bar{\rho}\left(\ddot{u} - \frac{1}{12}\left(\theta^2+1\right)l^2\ddot{u}'' + \frac{1}{720}\theta^2\left(5\left(\theta^2+1\right) - 2\psi^2\right)l^4\ddot{u}''''\right) = \bar{E}\left(u'' - \frac{1}{12}l^2u''''\right) + \mathcal{O}\left(\varepsilon^6\right). \tag{1.61}$$

By comparing motion equation resulting from generalized continuum theory modal (1.56) and the equation resulting from higher order homogenization method (1.61), a one-to-one correspondence of the three length scale material parameters is attained as follows

$$\alpha = \frac{1}{12}\left(\theta^2 + 1\right), \quad \beta = \frac{1}{720}\left(5\left(\theta^2 + 1\right) - 2\psi^2\right), \quad \gamma = \frac{1}{12}. \tag{1.62}$$

As l is set equal to the size of the unit cell, all the scale parameters of the proposed three-length-scale gradient elasticity formulation are identified from the microstructural mechanical and physical properties of the periodic composite laminate. In the latter analysis, the scale parameters is proven be the effective in predicting wave dispersion against experimental and micro-mechanical data from the literature.

1.6 Conclusion

The literature review in this chapter is presented in four aspects:

At the beginning of this chapter, the definition of micro-structures is presented. The investigations on failure of conventional continuum theory as well as the interpretation of complex behavior are given, upon which, complex media in general along with periodic media and nano-media are introduced for latter analysis.

Secondly, a review of numerous methods is given for periodic structure modelling. Among them, the wave finite element method, the homogenization method, including equivalent strain energy method, mode-based method, wave-based method and asymptotic homogenization method, are presented with details.

In the third part, generalized continuum elasticity theory is introduced with historical review, in which the origination and development of generalized continuum elasticity theories are thoroughly explained. Then the fundamental equations and applications for four types of generalized continuum theory are explained in detail, including the non-local elasticity theory, modified couple stress theory, second strain gradient theory and strain gradient theory.

In the last part, length scale parameter existing in the generalized theory-based models are discussed, and different approaches to identify the length scale parameter are investigated. Method based on equality of potential energy and method based on equality of correspondence coefficients are interpreted in detail.

Chapter 2

Wave propagation analysis of SSG theory-based Rod

Contents

2.1 Introduction

In this chapter, SSG theory-based rod model is developed to study the free wave propagation features and forced vibration behavior of rod structure with considering the underlying complex micro-structure interactions. The governing equation and associated boundary conditions are derived based on Hamilton's principle, then the non-classical longitudinal wave together with the extra-waves appearing exclusively in SSG theory model are investigated. The investigation are conducted based on dispersion relation, modal density of propagating wave mode and energy flow in non-classical rod. With the free wave propagation features, the structural mobility and impedance, the forced vibration of finite rod with certain boundary conditions

are analyzed. The results of the enriched model are validated by numerical results in COMSOL, then well interpreted by comparing with the classical theory results. Some useful conclusions are derived with respect to wave propagation characteristics in complex media based SSG theory-based model.

2.2 The formulation of SSG theory rod and wave propagation features

The multi-scale modeling begins with establishing the motion equation of the rod for free vibration. The coordinate system and kinematic parameters of the model are illustrated in Figure 2.1. The rod is assumed to be uniform, homogeneous and initially straight along the x-direction with length L. r denotes the radius of the circular cross section, and $q(x,t)$ denotes the resultant of the tractions and body forces acting on the structure in x direction as force per unit axial length.

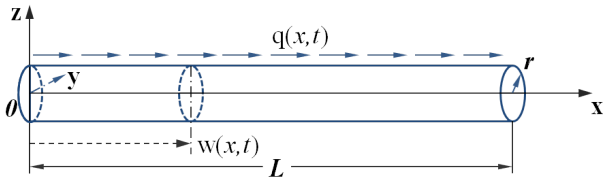

Figure 2.1: Coordinate system and kinematic parameters of the rod

The displacement field in a rod model is written as,

$$\begin{aligned} u_x(x,y,z,t) &= w(x,t), \\ u_y(x,y,z,t) &= 0, \\ u_z(x,y,z,t) &= 0, \end{aligned} \tag{2.1}$$

where u_x, u_y, and u_z denote the displacement components of the particles along x, y, and z directions respectively.

2.2.1 The derivation of governing equation and boundary conditions

According to the definition in Sec.1.4.2.3, nonzero components of the strain tensor $\boldsymbol{\varepsilon}$, $\boldsymbol{\eta}$, and $\boldsymbol{\xi}$ can be depicted as

$$\varepsilon_{11} = \frac{\partial w}{\partial x}, \quad \eta_{111} = \frac{\partial^2 w}{\partial x^2}, \quad \xi_{1111} = \frac{\partial^3 w}{\partial x^3}. \tag{2.2}$$

Substituting the nonzero components of strain tensors $\boldsymbol{\varepsilon}$, $\boldsymbol{\eta}$, and $\boldsymbol{\xi}$, as mentioned in equations (2.2) into the general expression of strain energy density Eq. (1.43), the

strain energy density $\bar{u}$ for the SSG theory rod can be simplified as

$$\begin{aligned}\bar{u} =& \frac{1}{2}\lambda {\varepsilon_{11}}^2 + \mu {\varepsilon_{11}}^2 + (a_1 + a_2 + a_3 + a_4 + a_5)\,{\eta_{111}}^2 + (b_1 + b_2 + b_3 + b_4 \\ &+ b_5 + b_6 + b_7)\,{\xi_{1111}}^2 + (c_1 + c_2 + c_3)\,\varepsilon_{11}\xi_{1111}.\end{aligned} \tag{2.3}$$

In this expression, lame's constants λ and μ are related to the Young's modulus E and the Poisson's ratio ν, as $\lambda = \nu E/(1+\nu)\,(1-2\nu)$, $\mu = E/2\,(1+\nu)$, so the Lame's constants here can be determined with experimentally tested E and ν. However, there are still not yet standard experiments to determine the higher-order material constants a_i, b_i, and c_i. Instead of experimentation method, atomistic simulation method are resorted in many researches to calculate the higher order material constants. In present model, the higher-order material constants of different materials refer to the results in the research of Shodja et al. (2012) [109] with method shown in Sec. 1.5.2.

The strain energy of the rod can be calculated by integrating its density over its volume. Combination of equations (2.2) and (2.3) yields the strain energy of the whole volume for the SSG theory-based rod as

$$U = \int_0^L \int_A \bar{u} dA dx = \frac{1}{2}\int_0^L \left[\chi EA\left(\frac{\partial w}{\partial x}\right)^2 + B_1\left(\frac{\partial^2 w}{\partial x^2}\right)^2 + B_2\left(\frac{\partial^3 w}{\partial x^3}\right)^2 + B_3\frac{\partial w}{\partial x}\frac{\partial^3 w}{\partial x^3}\right] dx, \tag{2.4}$$

in which,

$$\begin{aligned} B_1 &= 2A\,(a_1 + a_2 + a_3 + a_4 + a_5)\,, \\ B_2 &= 2A\,(b_1 + b_2 + b_3 + b_4 + b_5 + b_6 + b_7)\,, \\ B_3 &= 2A\,(c_1 + c_2 + c_3)\,, \end{aligned}$$

with parameter A as the area of the rod cross section, and $\chi = (1-\upsilon)/(1+\upsilon)\,(1-2\upsilon)$. To avoid the Poisson effect, the research in the present work will be proceeded with setting the Poisson's ratio $\upsilon = 0$, namely $\chi = 1$.

From the displacement field presented in Eq. (2.1), the kinetic energy of the rod can be written as,

$$T = \frac{1}{2}\int_0^L \int_A \rho\left(\frac{\partial w}{\partial t}\right)^2 dA dx = \frac{1}{2}\int_0^L m_0\left(\frac{\partial w}{\partial t}\right)^2 dx, \tag{2.5}$$

where $m_0 = \rho A$ represents the mass per unit length.

The variation of virtual work done by available loads on the rod, including body loads q and boundary surface loads P_i (i=0,1,2), can be expressed as

$$\delta W = \int_0^L (q\delta w) dx + \left[P_0\delta w + P_1\delta\left(\frac{\partial w}{\partial x}\right) + P_2\delta\left(\frac{\partial^2 w}{\partial x^2}\right)\right]\Bigg|_{x=0}^{x=L}, \tag{2.6}$$

in which P_i are the end-sectional loads dual to corresponding kinematic parameters, and these loads are resultants of not only classical stresses but also higher-order stresses on the surface of an section, including the P_1 which is the classical force in unit of N.

To derive the governing equation and the associated boundary conditions of the SSG theory-based rod, the Hamilton principle is employed as

$$\int_{t_1}^{t_2} (\delta T - \delta U + \delta W) dt = 0 \tag{2.7}$$

where δT and δU are the variation of kinetic energy and the variation of strain energy which both have been described. Substituting equations (2.4) (2.5) and (2.6) into Eq. (2.7), and doing some mathematical operations in accordance with the variation calculus, the governing equation of the enriched rod model can be expressed as,

$$EA\frac{\partial^2 w}{\partial x^2} + (B_3 - B_1)\frac{\partial^4 w}{\partial x^4} + B_2\frac{\partial^6 w}{\partial x^6} + q - m_0\frac{\partial^2 w}{\partial t^2} = 0, \tag{2.8}$$

and the associated boundary conditions at the rod ends (i.e.$x = 0, L$) as

$$\begin{aligned}
P_0 &= EA\frac{\partial w}{\partial x} + (B_3 - B_1)\frac{\partial^3 w}{\partial x^3} + B_2\frac{\partial^5 w}{\partial x^5} \quad or \quad \delta w = 0, \\
P_1 &= \left(B_1 - \frac{B_3}{2}\right)\frac{\partial^2 w}{\partial x^2} - B_2\frac{\partial^4 w}{\partial x^4} \quad or \quad \delta\left(\frac{\partial w}{\partial x}\right) = 0, \\
P_2 &= \frac{B_3}{2}\frac{\partial w}{\partial x} + B_2\frac{\partial^3 w}{\partial x^3} \quad or \quad \delta\left(\frac{\partial^2 w}{\partial x^2}\right) = 0.
\end{aligned} \tag{2.9}$$

In each boundary condition, there are two kinds: a loading type or an geometric type, only one type need to be considered at an end-section of the rod in each case. From the expressions of the governing equation and boundary conditions, we can also see if we set the higher-order material constants $a_i = 0$, $b_i = 0$ and $c_i = 0$, all the components composed of B_i vanish, and the classical theory rod governing equation and classical boundary condition can be achieved[83].

For further exploration and parametric study of the enriched properties for SSG theory-based rod, normalization of the governing equation and the associated boundary conditions is necessary. Thus the following normalization parameters are defined,

$$\bar{x} = \frac{x}{L}, \quad \bar{w} = \frac{w}{L}, \quad \bar{\omega} = \frac{\omega}{\omega_k}, \quad \tau = \frac{t}{t_k}. \tag{2.10}$$

The term ω_k represents the normalization parameter for angular frequency ω with expression in form of

$$\omega_k = \sqrt{\frac{E}{\rho}}\frac{\kappa}{L},$$

κ is a constant determined by the boundary conditions in the model. In the presented case, and it is set to be π, namely, the first nature frequency of rod with fixed-fixed

boundary condition. The normalization parameter for time t is expressed as

$$t_k = \frac{1}{\omega_k} = \sqrt{\frac{\rho}{E}}\frac{L}{\kappa}.$$

Substituting the newly defined variables into the governing equation and boundary conditions, we can have the normalized model as

$$\frac{E}{\mu}\frac{\partial^2 \bar{w}}{\partial \bar{x}^2} + \frac{(B_3 - B_1)}{\mu AL^2}\frac{\partial^4 \bar{w}}{\partial \bar{x}^4} + \frac{B_2}{\mu AL^4}\frac{\partial^6 \bar{w}}{\partial \bar{x}^6} + \bar{q} - \frac{m_0 L^2}{\mu A k_t^2}\frac{\partial^2 \bar{w}}{\partial \tau^2} = 0, \tag{2.11}$$

in which $\bar{q} = qL/\mu A$ is the dimensionless body load intensity. The term μA can be regarded as the normalization parameter for force in unit of N. With the same method, dimensionless boundary conditions can be obtained as,

$$\begin{aligned}
\bar{P}_0 &= \frac{P_0}{\mu A} = \frac{E}{\mu}\frac{\partial \bar{w}}{\partial \bar{x}} + \frac{B_3 - B_1}{\mu AL^2}\frac{\partial^3 \bar{w}}{\partial \bar{x}^3} + \frac{B_2}{\mu AL^4}\frac{\partial^5 \bar{w}}{\partial \bar{x}^5} \quad or \quad \delta \bar{w} = 0, \\
\bar{P}_1 &= \frac{P_1}{\mu AL} = \frac{2B_1 - B_3}{2\mu AL^2}\frac{\partial^2 \bar{w}}{\partial \bar{x}^2} - \frac{B_2}{\mu AL^4}\frac{\partial^4 \bar{w}}{\partial \bar{x}^4} \quad or \quad \delta\left(\frac{\partial \bar{w}}{\partial \bar{x}}\right) = 0, \\
\bar{P}_2 &= \frac{P_2}{\mu AL^2} = \frac{B_3}{2\mu AL^2}\frac{\partial \bar{w}}{\partial \bar{x}} + \frac{B_2}{\mu AL^4}\frac{\partial^3 \bar{w}}{\partial \bar{x}^3} or \quad \delta\left(\frac{\partial^2 \bar{w}}{\partial \bar{x}^2}\right) = 0
\end{aligned} \tag{2.12}$$

2.2.2 Dispersion relation

Wave propagating in structures could be defined as a phenomenon in which the physical quantity propagates in a supporting medium, without net transport of the medium. It may be characterized kinematically by the form of relative displacements from their positions of equilibrium of the particles–that is to say the form of distortion–together with the speed and direction of propagation of this distortion [112]. In a linear wave propagating system, a simple harmonic disturbance generated at one point in space will propagate away and travel at a phase velocity c_{ph}, which is determined by the kinematic form of the disturbance, the properties of the medium, and any external forces on the medium. Dispersion relation describes how the oscillation in time is related with the oscillation in space.

For the medium with heterogeneity caused by internal micro-structures, long range interaction has great influences on the deformation process as well as the mechanical properties of the structure, especially when the wavelength is of the same order with the heterogeneity. The classical elasticity theory is clearly not capable of describing these physical properties. In this section, free wave dispersion relation with considering long-rang interactions will be investigated based on the proposed SSG theory model.

Simple harmonic variations in time and space can be described mathematically by means of a complex exponential,

$$w = w_0 \cdot e^{i(\omega t - kx)}, \tag{2.13}$$

in which ω depicts angular frequency (rad/s), and 'wavenumber' k denotes the phase change spatially per unit distance.

$$k = \frac{\omega}{c_{ph}} = \frac{2\pi}{\lambda_k}. \tag{2.14}$$

λ_k is the wavelength representing the spatial period of a simple harmonic wave.

The form of relationship between k and ω is termed the dispersion relation. It is a property of the type of wave, as well as the type of wave-supporting medium. For classical rod theory, the dispersion relation is expressed as $k = \sqrt{\frac{\rho}{E}} \cdot \omega$. In this relationship k and ω is linear with each other, which indicates an arbitrary spatial form of disturbance will not be subject to change as it propagates. If the dispersion relation is not linear, the wave is said to be dispersive, which indicates a disturbance generated by a process that is not simple harmonic in time will not propagate through a medium unaltered in its basic spatial form.

Assuming the external loading $q = 0$, the dispersion relation of the wave modes in the proposed enriched SSG model can be achieved by injecting the general exponential form of wave propagation (2.13) into the governing equation. One 6th-order dispersion relation can be obtained as

$$EAk^2 - (B_3 - B_1)\, k^4 + B_2 k^6 - m_0\omega^2 = 0. \tag{2.15}$$

For parametric study, wavenumber k is normalized as $\bar{k} = kL$, then the normalized dispersion relation can be achieved as

$$\frac{B_2}{L^4}\bar{k}^6 - \frac{B_3 - B_1}{L^2}\bar{k}^4 + EA\bar{k}^2 - \frac{m_0\bar{\omega}^2 L^2}{{t_k}^2} = 0. \tag{2.16}$$

This dispersion relation function is clearly different with the classical rod dispersion relation. According to the form of the equation, 6 solutions (k_i) can be achieved corresponding to each frequency (ω). Thus we can predict that three positive going modes and three negative going modes can be generated in complex rod structure based on SSG theory rod model.

To further study the wave dispersion properties, one numerical case is implemented. The rod structure is shown as in Figure 2.1. The radius of the circular cross section $r = 3a_0$, and length $L = 5r$ with lattice parameter $a_0 = 4.04$Å. The material is aluminum with $\mu = 26\,\text{GPa}$ and $\rho = 2.7 \times 10^3 \text{kg/m}^3$, and the higher-order material constant values are given in Table 2.1. The external body force $q(x,t)$ is zero.

Employing the parameters above into the dispersion Eq. (2.16), one arrives six solutions. The results are shown as follows.

Table 2.1: High-order material constants for aluminum(Shodja et al.,2012).

a_1(eV/Å)	a_2(eV/Å)	a_3(eV/Å)	a_4(eV/Å)	a_5(eV/Å)		
0.1407	0.0027	−0.0083	0.0966	0.2584		
b_1(eV · Å)	b_2(eV · Å)	b_3(eV · Å)	b_4(eV · Å)	b_5(eV · Å)	b_6(eV · Å)	b_7(eV · Å)
0.7927	0.0644	−0.1943	−0.0009	−0.0009	16.1566	48.5291
c_1(eV/Å)	c_2(eV/Å)	c_3(eV/Å)				
0.5041	0.3569	0.1782				

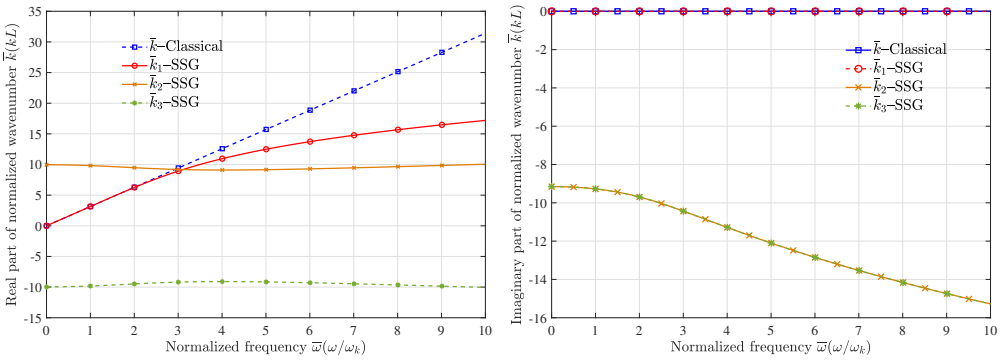

(a) Real part (b) Imaginary part

Figure 2.2: Dispersion relation of positive going waves k^+

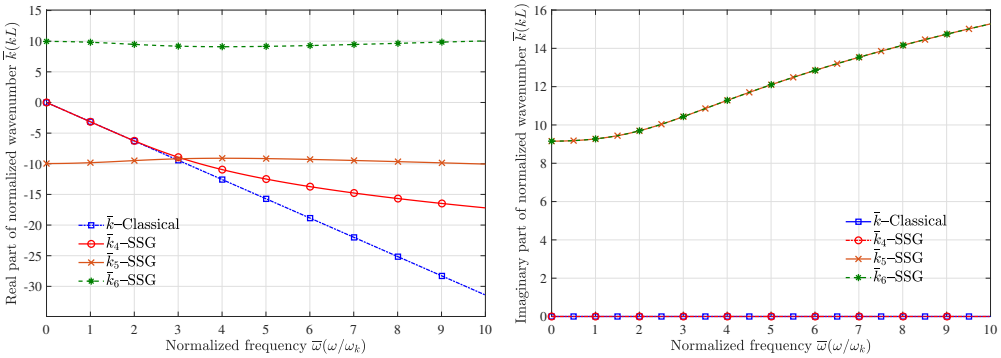

(a) Real part (b) Imaginary part

Figure 2.3: Dispersion relation of negative going waves k^-

Figure 2.2 and Figure 2.3 respectively illustrate the dispersion relation of positive going waves and negative going waves. It should be noticed here, the wavenumber k_3, with negative imaginary part and negative real part is considered as a positive-going wave, and k_6 with positive imaginary part and positive real part as a negative-going wave. In a periodic waveguide with unit-cell's dimension d, k is $2m\pi/d$ -periodic, the positive- or negative-going waves can have arbitrary Real(k) sign. The direction of propagation is defined by the Imag(k), which corresponds to the wave attenuation. For continuous waveguide, the cell periodicity d is arbitrary.

Although propagating to opposite directions, the positive-going wave k^+ and negative-going waves k^- share similar properties, so we will illustrate more detailed characteristics with focusing on k^+. Figure 2.2 has two sub-figures, fig.2.2(a) and fig.2.2(b), which display the real part and imaginary part of the dimensionless wavenumbers for all the positive-going waves in frequency range $0 \leq \overline{\omega} \leq 10$. Different from the linear dispersion relation of classical theory, three modes (k_1, k_2, k_3) can be generated by the SSG theory-based model, k_1 for the progressive wave, k_2 and k_3 for the evanescent waves. Compared with the classical longitudinal wave $k - Classical$, we can see the non-classical longitudinal wave k_1 is propagating in a dispersive manner. On each frequency, the spatial phase change for the non-classical longitudinal wave is less and the difference become wider with the increasing frequency. The other two evanescent waves k_2 and k_3 appear exclusively in SSG theory model. They decay to zero in a very close range and do not individually transport energy to long distance, so in many references they are referred as 'near fields'. The predictions agree with some references (see e.g.[3, 93, 100, 101]).

In order to confirm the size-effect of the dispersive feature, dispersion curves of non-classical longitudinal wave k_1 in rod structures of different size are investigated. The results are illustrated in Figure 2.4.

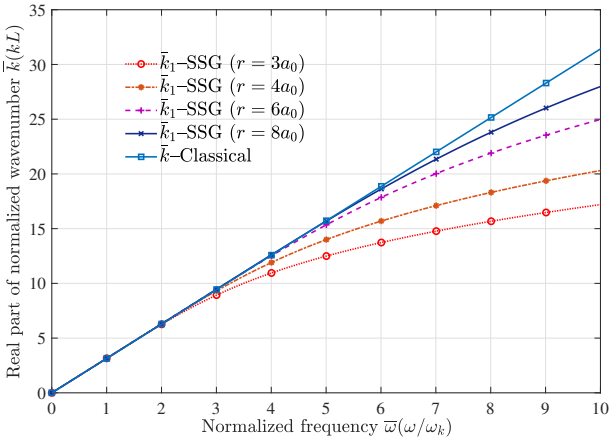

Figure 2.4: Wavenumber changing with rod dimension

Figure 2.4 display the comparison of dispersion curves for classical longitudinal wave and non-classical wave k_1 in rod structures with section radius increasing from $3a_0$ to $8a_0$. We should notice that the length to radius ratio of the structure is fixed as $L = 5r$, hence the resulting classical dispersion curve is constantly linear correlated with angular frequency by the same slop. Whereas the non-classical dispersion curves are observed to exhibit less dispersive feature as the dimension r goes up from $3a_0$ to $8a_0$. As the structural length increase and internal length be invariant., the influence of long range micro-structure interaction diminish evidently, hence we can expect that the non-classical dispersive curve will converge to the classical one eventually.

The above outcomes are all obtained without damping in the system, namely, without energy dissipation. In practical applications, there are always damping in the system. Energy dissipation can significantly affect wave propagation features. In the case of hysteretic damping, we can assume $E = 52\,(1+i\zeta)$ GPa with ζ indicating the loss factor of the system. The real part of the resulting dispersion curves will not be influenced, while the imaginary part representing energy dissipation will be affected significantly. To analyze the damping effect on wave propagation feature in complex rod structure, the imaginary part of longitudinal wave dispersion curves with $\zeta = 0.005$ is shown in Figure 2.5

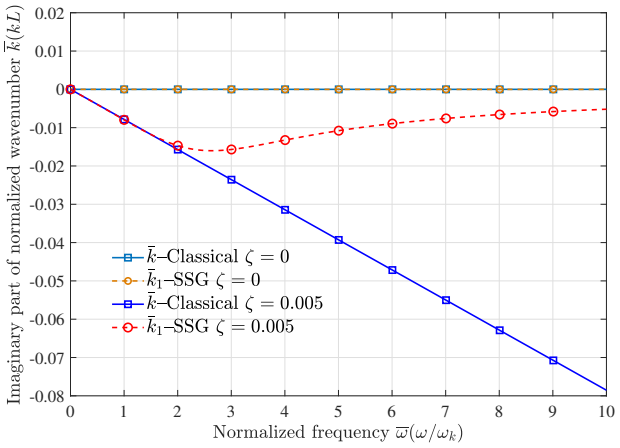

Figure 2.5: Wavenumber changing with damping

As can be seen, Im(k)-Classical is linear correlated with frequency in whole frequency range. In relatively low frequency range $0 \leq \overline{\omega} \leq 2$, Im($k_1$)-SSG match well with classical result. On higher frequency range $2 \leq \overline{\omega} \leq 10$, Im($k_1$)-SSG is clearly affected by the long range interactions captured by higher-order strain gradient. |Im(k_1)|-SSG decrease and draw near to zero; energy dissipation through viscous damping for non-classical longitudinal wave k_1 become negligible compared with the classical model.

2.2.3 Modal density

Modal density of one kind of vibration of a structure at any frequency ω is denoted as $n\,(\omega)$, which means the number of resonant frequencies in a neighborhood $\Delta\omega$ local to that frequency ω. It may also be interpreted as the expected number of natural frequencies per radiant per second. Based on this definition, modal density can be expressed as

$$n(\omega) = \frac{dN}{d\omega}, \tag{2.17}$$

in which N, the mode count, represents the number of resonant frequencies below that given frequency ω. The propagating wave at any frequency is characterized by

the wavenumber k $(= 2\pi/\lambda_k)$, which is the phase difference between two points in the continuous system per unit distance in the direction of wave propagation. It can be said that, as the wave propagates, its phase changes by k per unit length. Hence as it propagates from the left-end of the structure to the right-hand end, the total phase change is kL. The wave is reflected from the right-hand end, in the form of an identical but opposite-going wave, back towards the left-hand end, and the phase of the wave changes by another kL in the process. At each of the reflecting boundaries, a phase difference is introduced between the incoming and reflected wave. Let these be δ_R and δ_L at the right- and left- hand ends respectively. The total phase changes as the 'wave travels one complete circuit around the system' is therefore $2kL + \delta_R + \delta_L$. The 'phase-closure principle' states that if the total phase change is an integral number of $2\pi's$, the condition is satisfied for a natural mode, and the frequency at which it occurs is a natural frequency of the system. This principle can be written as

$$2kL + \delta_R + \delta_L = N \cdot 2\pi.$$

Assuming δ represent the total phase change introduced by reflecting boundaries which varies with different boundary conditions, then we have

$$2kL \pm \delta = N \cdot 2\pi \Rightarrow N(k) = \frac{kL \pm \frac{\delta}{2}}{\pi}.$$

As the structural mode order increases, the number of resonances $N(k)$ in frequency domain become increasingly less sensitive to the boundary conditions. Hence, we may consider the mode count as,

$$N(k) = \frac{kL}{\pi}, \tag{2.18}$$

so the Eq. (2.17) can be simplified as

$$n(\omega) = \frac{dN}{d\omega} = \frac{dN}{dk}\frac{dk}{d\omega} = \frac{L}{\pi}\frac{1}{c_g}, \tag{2.19}$$

in which, the term c_g denotes the group velocity of the studied wave

$$c_g = \frac{d\omega}{dk}.$$

It represents information and energy transported velocity by this wave mode. With the normalizing variables defined in Eq. (2.10), the normalized modal density can be expressed as

$$\overline{n}(\overline{\omega}) = \frac{1}{\pi}\frac{d\overline{k}}{d\overline{\omega}} = \frac{1}{\pi}\frac{1}{\bar{c}_g}. \tag{2.20}$$

As the evanescent waves dose not contribute to the structure resonance directly, modal density of non-classical longitudinal wave k_1-SSG are illustrated as follows,

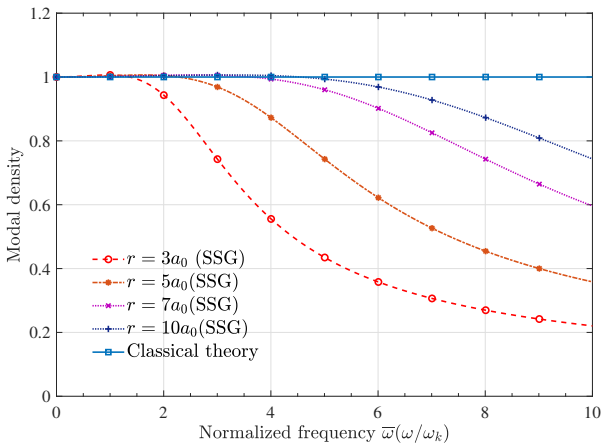

Figure 2.6: Modal density of non-classical longitudinal wave

Figure 2.6 depicts modal density of non-classical wave k_1 compared with classical result, which keeps constantly in frequency domain as expected. Modal density of k_1-SSG decrease distinctly as frequency increases, and the contrast becomes more serious as the section radius decreasing to $r = 3a_0$. Compared with the classical result which is size and frequency independent, the influence of long range interaction between underlying micro-structures is quite obvious, and the present SSG theory model can clearly capture the micro-structure effect.

2.2.4 Energy flux analysis

In this section, the approach to predict the energy velocity at one point in the SSG theory-based rod structure is presented. At one observation point M, with the classical elasticity theory, the instantaneous kinetic energy density $\mathrm{T(M,t)}$, potential energy density $\mathrm{U_0(M,t)}$ and the instantaneous active energy flow $\mathrm{P_0(M,t)}$ are defined [113][114] as

$$\mathrm{T_0} = \frac{\rho}{2}\mathrm{Re}\left(\mathbf{V}\right)\cdot\mathrm{Re}\left(\mathbf{V}\right), \quad \mathrm{U_0} = \frac{1}{2}\mathrm{Re}\left(\boldsymbol{\sigma}\right)\cdot\mathrm{Re}\left(\boldsymbol{\varepsilon}\right), \quad \mathrm{P_0} = -\mathrm{Re}\left(\boldsymbol{\sigma}\right)\cdot\mathrm{Re}\left(\mathbf{V}\right), \tag{2.21}$$

where $\mathbf{V}$ is the velocity vector, and $\boldsymbol{\sigma}$ and $\boldsymbol{\varepsilon}$ are the classical stress and strain tensors respectively. As the strain and stress tensor are defined differently in the SSG theory, instantaneous potential energy density and energy flow should be revised by the new definition. instantaneous potential energy is enriched with the higher order components as [50]

$$\mathrm{U} = \frac{1}{2}\left[\mathrm{Re}\left(\boldsymbol{\sigma}\right)\cdot\mathrm{Re}\left(\boldsymbol{\varepsilon}\right) + \mathrm{Re}(\boldsymbol{\tau}) :\ \mathrm{Re}\left(\boldsymbol{\eta}\right) + \mathrm{Re}\left(\boldsymbol{\pi}\right) \vdots \mathrm{Re}\left(\boldsymbol{\xi}\right)\right], \tag{2.22}$$

where $\boldsymbol{\tau}$ and $\boldsymbol{\eta}$ are the first higher order stress and strain tensor, $\boldsymbol{\pi}$ and $\boldsymbol{\xi}$ are second higher order stress and strain tensor. The sum of the kinetic and potential energy density is the instantaneous total energy density:

$$\mathrm{W_{total}} = \mathrm{T_0} + \mathrm{U}. \tag{2.23}$$

With a vibrating structure the time averaged value is more important than the instantaneous value. In the following investigations, the time will be removed. A physical quantity H, which represents here an energy or a power density, can generally be expressed as

$$H = f \cdot g,$$

where f and g are complex harmonic physical variables which denote stress, strain, or displacement in the formulation. Thus the time averaged of H is given by

$$\langle H \rangle = \frac{\omega}{2\pi} \int_0^{2\pi} \mathrm{Re}\,(f) \cdot \mathrm{Re}\,(g) dt = \frac{1}{2} \mathrm{Re}\,(f \cdot g^*)\,,$$

where '*' denotes conjugation, and '$\langle\ \rangle$' denotes time averaged. Therefore, the time averages of kinetic energy, potential energy through the observation cross section A are given as,

$$\begin{aligned} \langle \mathrm{T}_0 \rangle &= \frac{\rho}{4} \int_A \mathrm{Re}\,(\mathbf{V} \cdot \mathbf{V}^*) dA, \\ \langle \mathrm{U} \rangle &= \frac{1}{4} \int_A \mathrm{Re} \left(\boldsymbol{\sigma} \cdot \boldsymbol{\varepsilon}^* + \boldsymbol{\tau} \,:\, \boldsymbol{\eta}^* + \boldsymbol{\pi} \vdots \boldsymbol{\xi}^* \right) dA \end{aligned} \tag{2.24}$$

According to Eq. (2.4) and (2.5), the time averaged kinetic energy and enriched time averaged potential energy of the studied rod per unit length is defined as

$$\begin{aligned} \langle \mathrm{T}_0 \rangle &= \frac{\rho}{4} \int_A \mathrm{Re}\,(\dot{w} \cdot \dot{w}^*) dA, \\ \langle \mathrm{U} \rangle &= \frac{1}{4} \mathrm{Re} \left[EA \left(\frac{\partial w}{\partial x} \right) \left(\frac{\partial w}{\partial x} \right)^* + B_1 \left(\frac{\partial^2 w}{\partial x^2} \right) \left(\frac{\partial^2 w}{\partial x^2} \right)^* + B_2 \left(\frac{\partial^3 w}{\partial x^3} \right) \left(\frac{\partial^3 w}{\partial x^3} \right)^* + B_3 \frac{\partial w}{\partial x} \left(\frac{\partial^3 w}{\partial x^3} \right)^* \right]. \end{aligned} \tag{2.25}$$

When the higher-order components are taken into account, the expression of active energy flow and reactive power flow through the observation section A are revised as

$$\langle \mathrm{P} \rangle = -\frac{1}{2} \mathrm{Re} \left[P_0 \cdot \dot{w}^* + P_1 \cdot \left(\frac{\partial \dot{w}}{\partial x} \right)^* + P_2 \cdot \left(\frac{\partial^2 \dot{w}}{\partial x^2} \right)^* \right], \tag{2.26a}$$

$$\langle \mathrm{Q} \rangle = -\frac{1}{2} \mathrm{Im} \left[P_0 \cdot \dot{w}^* + P_1 \cdot \left(\frac{\partial \dot{w}}{\partial x} \right)^* + P_2 \cdot \left(\frac{\partial^2 \dot{w}}{\partial x^2} \right)^* \right], \tag{2.26b}$$

where '$\dot{w}$' denotes the time derivative of the displacement w, P_0, P_1, and P_2 are the resultant loads dual to the corresponding kinematic parameters at the observation section, produced by not only the classical strain but also the higher strain as

$$\begin{aligned} P_0 &= EA \frac{\partial w}{\partial x} + (B_3 - B_1) \frac{\partial^3 w}{\partial x^3} + B_2 \frac{\partial^5 w}{\partial x^5}, \\ P_1 &= \left(B_1 - \frac{B_3}{2} \right) \frac{\partial^2 w}{\partial x^2} - B_2 \frac{\partial^4 w}{\partial x^4}, \\ P_2 &= \frac{B_3}{2} \frac{\partial w}{\partial x} + B_2 \frac{\partial^3 w}{\partial x^3}. \end{aligned}$$

The energy velocity of the wave propagation equals the time averaged active energy flow $\langle P \rangle$ in x direction over the time averaged total energy $\langle W_{total} \rangle$, which can be expressed as

$$\mathrm{V}_e = \frac{\langle \mathrm{P} \rangle}{\langle W_{total} \rangle}. \tag{2.27}$$

With the normalizing variables defined in Eq. (2.10), the normalized energy and power flow through the observation cross section can be expressed as

$$\langle \overline{\mathrm{T}} \rangle = \frac{\langle \mathrm{T} \rangle}{\mu A}, \quad \langle \overline{\mathrm{U}} \rangle = \frac{\langle \mathrm{U} \rangle}{\mu A}, \quad \langle \overline{\mathrm{P}} \rangle = \frac{\langle \mathrm{P} \rangle \cdot k_t}{\mu A L}, \quad \overline{\mathrm{V}}_e = \frac{\mathrm{V}_e \cdot k_t}{L}, \tag{2.28}$$

The validation of the energy flux expression is important because energy equilibrium is employed based on Eq. (2.26a) in the following research. To implement the validation of the energy flux expression, energy velocity V_e and group velocity c_g of non-classical wave k_1 are calculated. If the formulation (2.25) and (2.26a) are validated, energy velocity V_e should be identical to group velocity c_g without damping in the system.

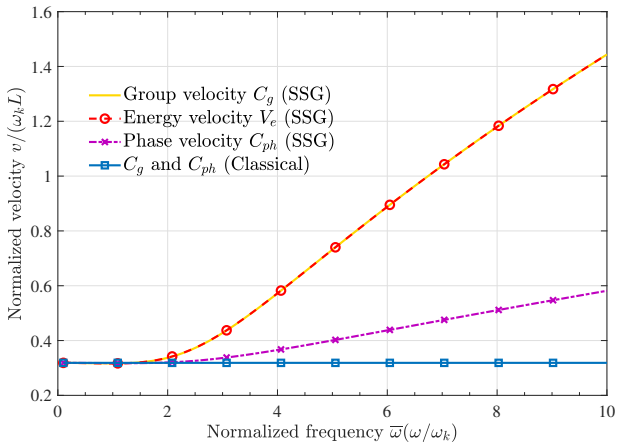

Figure 2.7: Energy velocity of the longitudinal wave

From Figure 2.7, as expected, ***The formulation of potential energy density*** (2.25) ***and energy flux*** (2.26a) ***in complex rod based on SSG theory-based rod model are proved to be correct with*** $c_g = V_e$ ***in whole frequency range.*** In addition, group velocity c_g and phase velocity C_{ph} of k_1 in SSG theory model are clearly different from each other, which confirms the dispersive property of non-classical longitudinal wave.

2.3 Mobility and impedance of infinite rod structure

To investigate the dynamic behaviors of complex rod structure, in this section, frequency response analysis of infinite rod to simple harmonic excitation is proceeded

based on the proposed SSG theory model. The impedance and mobility function of the complex rod are developed using the wave formulation method. Energy input, transfer and dissipation are also derived to have a proper interpretation for the obtained dynamic behaviours. Figure 2.8 shows an infinite rod subject to a harmonic point axial force $F(t) = \mathrm{Re}(q_0 \cdot e^{i\omega t})$ at $x = 0$.

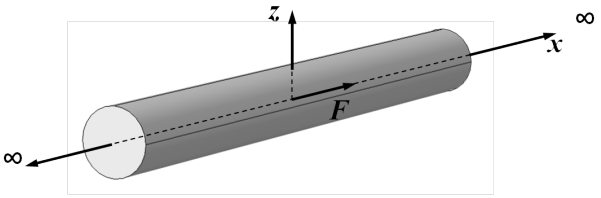

Figure 2.8: An infinite rod with force excitation.

2.3.1 Derivation of the displacement field based on SSG rod theory

According to Sec. 2.2, the governing equation of free longitudinal vibration 2.8 applies to all the points on the rod that are not subject to external forces, in this case the driving forces at $x = 0$. At the driving point, the axis force suffers a step change equal to the applied harmonic force $F(t)$. One Dirac delta function $\delta(x - 0)$ is employed to represent the concentrated force F applied at $x = 0$, hence the governing equation of infinite SSG theory rod subject to harmonic point axial force $F(t) = \mathrm{Re}(\mathrm{q_0} \cdot \mathrm{e}^{\mathrm{i}\omega \mathrm{t}})$ at $x = 0$ can be expressed as

$$EA\frac{\partial^2 w}{\partial x^2} + (B_3 - B_1)\frac{\partial^4 w}{\partial x^4} + B_2\frac{\partial^6 w}{\partial x^6} - m_0\frac{\partial^2 w}{\partial t^2} = -q_0 \cdot \delta(x) \cdot e^{i\omega t}. \tag{2.29}$$

The governing equation is insufficient to describe the behaviour of the rod subject to a point force, boundary conditions at the discontinuous point of the rod are also required. The solution to this in-homogeneous equation can be given by the superposition of the progressive and retrograde contribution from all wavenumbers (k_1, k_2 *and* k_3). Considering the assumption that the rod is infinitely extended, only waves propagating towards positive direction are taken into account in the region (x>0), and in the region (x<0), only negative going waves. The two complex solutions given in 2.30 represents all the physically possible forms of free longitudinal vibration of complex rod in the frame of SSG theory-based model

$$\begin{aligned} w(x^+, t) &= \widetilde{w}_{x^+} \cdot e^{i\omega t} = \left(\mathcal{A}e^{-ik_1 x} + \mathcal{B}e^{-ik_2 x} + \mathcal{C}e^{-ik_3 x}\right) e^{i\omega t}, \qquad (x \geq 0) \\ w(x^-, t) &= \widetilde{w}_{x^-} \cdot e^{i\omega t} = \left(\mathcal{D}e^{ik_1 x} + \mathcal{E}e^{ik_2 x} + \mathcal{F}e^{ik_3 x}\right) e^{i\omega t}. \qquad (x < 0) \end{aligned} \tag{2.30}$$

Since the system is symmetrical about the driving force position $x = 0$, the displacement $w(x_0, t)$ with arbitrary x_0 should equal $w(-x_0, t)$ on each frequency. Thus, based on the expression in Eq. (2.30), $\mathcal{A}$, $\mathcal{B}$, $\mathcal{C}$, that are the amplitudes of positive-going wave k_1, k_2 and k_3 in region $x \geq 0$, should be identical with $\mathcal{D}$, $\mathcal{E}$ and $\mathcal{F}$,

the amplitudes of negative-going wave $-k_1$,$-k_2$ and $-k_3$ in region $x < 0$ on each frequency, then the solution given in 2.30 is simplified as

$$\begin{aligned} w(x^+,t) &= \widetilde{w}_{x^+} \cdot e^{i\omega t} = \left(\mathcal{A}e^{-ik_1 x} + \mathcal{B}e^{-ik_2 x} + \mathcal{C}e^{-ik_3 x}\right) e^{i\omega t}, \qquad (x \geq 0) \\ w(x^-,t) &= \widetilde{w}_{x^-} \cdot e^{i\omega t} = \left(\mathcal{A}e^{ik_1 x} + \mathcal{B}e^{ik_2 x} + \mathcal{C}e^{ik_3 x}\right) e^{i\omega t}, \qquad (x < 0) \end{aligned} \tag{2.31}$$

According to Fig.2.8 and Eq.(2.29), the stress tensors $\boldsymbol{\sigma}$, $\boldsymbol{\tau}$, $\boldsymbol{\pi}$ on left-hand end of the section $x = 0$, produce a regular force of amplitude P_{0^-}, a first higher order force of amplitude P_{1^-}, and a second higher order force of amplitude P_{2^-}, that are the force respectively in unit of N, $N \cdot m$, and $N \cdot m^2$. Meanwhile forces of amplitude $-P_{0^+}$, $-P_{1^+}$,$-P_{2^+}$ are produced on the right-hand end of the section A. The equilibrium are illustrated in Figure 2.9.

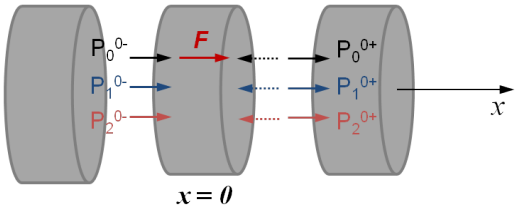

Figure 2.9: Illustration of force equilibrium

Assuming the applied force is positive, and the mass of the rod between $x = 0^+$ and $x = 0^-$ is infinitesimal, the force equilibrium can be developed at $x = 0$ as

$$-{P_0}^{0^+} + {P_0}^{0^-} + F = 0 \tag{2.32}$$

in which the force ${P_0}^{0^+}$ and ${P_0}^{0^-}$ respectively equal the loads at the $x = 0$ section dual to the kinematic parameter δw generated by the right-hand end deformation and left-hand end deformation.

$$\begin{aligned} {P_0}^{0^+} &= EA\frac{\partial w_{0^+}}{\partial x} + (B_3 - B_1)\frac{\partial^3 w_{0^+}}{\partial x^3} + B_2\frac{\partial^5 w_{0^+}}{\partial x^5} \\ {P_0}^{0^-} &= EA\frac{\partial w_{0^-}}{\partial x} + (B_3 - B_1)\frac{\partial^3 w_{0^-}}{\partial x^3} + B_2\frac{\partial^5 w_{0^-}}{\partial x^5} \end{aligned}$$

Besides the force equilibrium of regular force, the higher order force equilibrium can also been established. Since there exist no external higher-order forces applied on the section $x = 0$, the following equilibrium should be guarantied as,

$$-{P_1}^{0^+} + {P_1}^{0^-} = 0, \tag{2.33a}$$

$$-{P_2}^{0^+} + {P_2}^{0^-} = 0. \tag{2.33b}$$

${P_1}^{0^-}$ and ${P_2}^{0^-}$ represent the amplitude of first higher order force and second higher order force produced on the left-hand end of the section $x = 0$, $-{P_1}^{0^+}$ and $-{P_2}^{0^+}$

represent the forces produced on the right-hand end of the section, and they are in forms of expressions as follows

$$
\begin{aligned}
{P_1}^{0^+} &= \left(B_1 - \frac{B_3}{2}\right)\frac{\partial^2 w_{0^+}}{\partial x^2} - B_2\frac{\partial^4 w_{0^+}}{\partial x^4} \qquad {P_2}^{0^+} = \frac{B_3}{2}\frac{\partial w_{0^+}}{\partial x} + B_2\frac{\partial^3 w_{0^+}}{\partial x^3} \\
{P_1}^{0^-} &= \left(B_1 - \frac{B_3}{2}\right)\frac{\partial^2 w_{0^-}}{\partial x^2} - B_2\frac{\partial^4 w_{0^-}}{\partial x^4} \qquad {P_2}^{0^-} = \frac{B_3}{2}\frac{\partial w_{0^-}}{\partial x} + B_2\frac{\partial^3 w_{0^-}}{\partial x^3}
\end{aligned}
$$

In addition, displacement continuity and higher-order displacements continuity are required on the force applied section, which yields

$$w_{0^-} = w_{0^+}, \tag{2.34a}$$

$$\frac{\partial w_{0^-}}{\partial x} = \frac{\partial w_{0^+}}{\partial x}, \tag{2.34b}$$

$$\frac{\partial^2 w_{0^-}}{\partial x^2} = \frac{\partial^2 w_{0^+}}{\partial x^2}. \tag{2.34c}$$

Substitute solution (2.31) into the expressions of boundary conditions (2.32)(2.33) and (2.34), we find that Eq. (2.33a), (2.34a) and (2.34c) are naturally valid because of the symmetrical assumption, and the combination of the other three equations (2.32), (2.33b) and (2.34b) are sufficient to calculate the unknown variables $\mathcal{A}$, $\mathcal{B}$, $\mathcal{C}$ in solution (2.31). The amplitudes of wave k_1, k_2 and k_3 are obtained on each frequency, then we can easily find the complex amplitude $\widetilde{w}_{x^+}$ and $\widetilde{w}_{x^-}$ of displacement w on each frequency at arbitrary position by wave superposition.

2.3.2 Input mobility and transfer mobility

Mechanical impedance is the frequency-dependent relationship between forces and motions. It measures the resistance of the structure when subjected to a harmonic axis force. For a given frequency, the mechanical impedance is defined as the ratio of the force amplitudes q_0 and the resulting velocity $\dot{w}$. The inverse of impedance is termed as 'mobility', which represents how much velocity will be generated by a unit force at the point of interest. If the observed response point of the structure is at the same point and in the same direction as that of the applied force, it is termed as as 'driving point impedance' or 'driving point mobility', otherwise it is termed as 'transfer impedance' and 'transfer mobility'. By using the complex amplitude solution in Eq. (2.31), the complex mobility of the studied complex structure can be expressed with the ratio of the resulting velocity $\dot{w}$ and the applied force F and any interface for a given frequency as,

$$
\begin{aligned}
Y(x,\omega) = \frac{\dot{w}_x}{F} = \frac{i\omega \cdot \widetilde{w}_x}{q_0} &= \frac{\left(\mathcal{A}e^{-ik_1 x} + \mathcal{B}e^{-ik_2 x} + \mathcal{C}e^{-ik_3 x}\right)\cdot i\omega}{q_0} \qquad (x \geq 0) \\
&= \frac{\left(\mathcal{A}e^{ik_1 x} + \mathcal{B}e^{ik_2 x} + \mathcal{C}e^{ik_3 x}\right)\cdot i\omega}{q_0} \qquad .(x < 0)
\end{aligned} \tag{2.35}
$$

With the normalized variables defined in Eq. (2.10), the normalized mobility can be expressed as

$$\overline{Y} = \frac{\overline{\dot{w}}_x}{\overline{F}} = \frac{Y \cdot \mu A k_t}{L}. \tag{2.36}$$

Numerical analysis is proceeded based on the SSG theory formulation for the mobility of the complex rod studied in Sec. 2.2. Assuming no hysteretic damping in the system with $E = 52\,\text{GPa}$, and the amplitude of the harmonic axial force $q_0 = 0.05\mu A$ at $x = 0$ in Figure 2.8, the resulting normalized 'driving force mobility' is shown in Figure 2.10

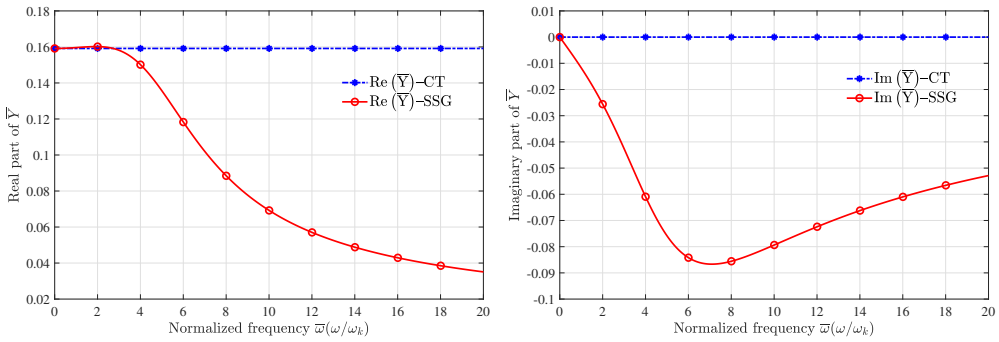

(a) Real part (b) Imaginary part

Figure 2.10: Force driving mobility of infinite rod

Figure 2.10 illustrate the comparison of complex force driving mobility $\overline{Y}$ of the point $\bar{x} = 0$ resulting from SSG theory rod model and the classical theory rod model. As we can see the classical mobility $\overline{Y}$ is completely frequency independent with unchanging positive real part and zero imaginary part, which means energy input will be carried away without any dissipation and the response is constantly in the same phase with the excitation. In contrast, both the real part and the imaginary part of complex mobility ($\overline{Y}$-SSG) are highly dependent of frequency. The real par decrease greatly in frequency domain especially in frequency range $\bar{\omega} > 2$. The complex rod structure with considering the long range interactions between microstructures shows more resistance to the driving force and the net energy transmitted into the structure diminish distinctly compared with the classical one even without damping dissipation. The none-zero $\text{Im}(\overline{\text{Y}}) - \text{SSG}$ indicates the resultant velocity has phase difference with the excitation force, and the value of imaginary reflects the input reactive power flow.

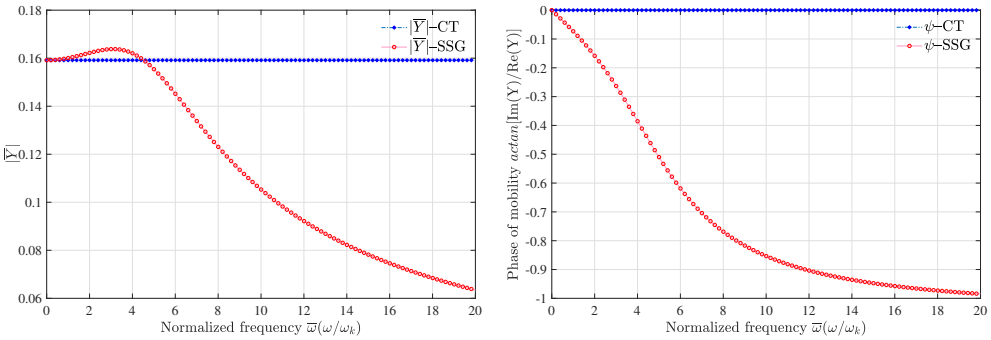

(a) Absolute value (b) Phase

Figure 2.11: Modulus and phase of driving mobility of infinite rod

To study more details of the complex mobility, we illustrate the absolute value and the phase changing of the mobility as follows as shown in Figure 2.11. The modulus of driving point mobility keeps dropping down in higher frequency and the phase difference ψ keeps increasing as frequency goes up. The more phase difference, the less proportion power can be transferred from the force to the structure. The driving point impedance certainly exhibit different characteristic of the complex rod medium.

Transfer mobility relates the complex amplitude of the longitudinal velocity at point of $x > 0$ or $x < 0$ and the amplitude of the exciting force. In the following, the transfer mobility $\overline{Y}_t$ between the force driving point $\bar{x} = 0$ and the point $\bar{x} = 1$ are analyzed on different frequency ($\overline{\omega} = 4, 6, 8$),

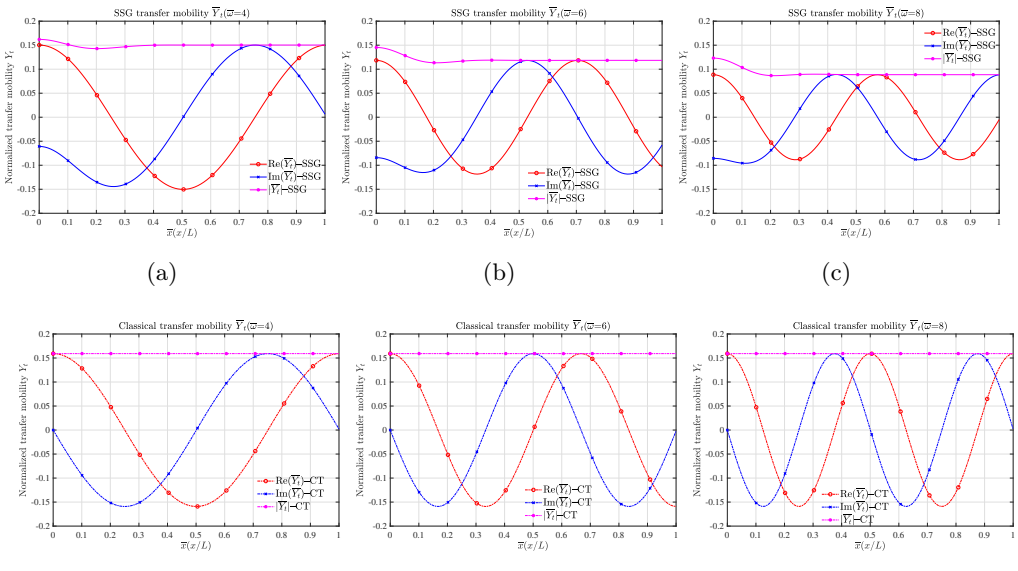

(a) (b) (c)

(d) (e) (f)

Figure 2.12: Comparison of transfer mobility

As we can see in Figure 2.12(d), 2.12(e), 2.12(f), the classical mobility $\overline{Y}$ are pure real at force driving point $\bar{x} = 0$, which indicates that the resultant velocity at that point is in phase with the excitation force. In contrast, as we can see in Figure 2.12(a), 2.12(b), 2.12(c), the input non-classical mobility is originated as a complex value at $\bar{x} = 0$ due to the near field effect generated by the force interaction at the force driving point, so the resultant velocity has phase difference with the excitation force.

The harmonic disturbance generated at $\bar{x} = 0$ propagate away to infinity. As the wave propagation field in homogeneous rod consist of only one pure propagating wave, and no damping is assumed in this case, the harmonic disturbance will propagate away spatially in simple sinusoidal form without amplitude decay. For the complex mobility of heterogeneous rod resulting from SSG theory formulation, the harmonic disturbance propagate away spatially in different form. Mobility modulus decays clearly from the excitation point in the field close to the force application point. The higher the frequency, the more distinct the decrease.

In addition, the spatial period in far field of SSG theory formulation is longer than the classical result for a given frequency. Spatial period is determined by $\lambda_k = c_{ph} \cdot T$ with c_{ph} representing phase speed at which the disturbance travels in the structure. For a given frequency, phase differences between the resultant velocities at the observation points and the excitation force due to the distance and the spatial period can be calculated with $\psi = \arctan[\mathrm{Im}(\overline{\mathrm{Y}})/\mathrm{Re}(\overline{\mathrm{Y}})]$, ψ-classical and ψ-SSG are clearly different caused by the driving point phase difference, the near field attenuation and different spatial period.

2.3.3 Input power and transfer power

When a structure is subjected to one load only, the input active and reactive power are governed by the driving point mobility at load application point. The active power is proportional to the real part of the direct mobility, while the reactive power is proportional to the imaginary part of the direct mobility [115]. To explore the influence of long range interactions on energy input into the heterogeneous rod structure, input active flow and reactive flow are analyzed based on the SSG theory model. The real and imaginary parts of Eq. (2.37) gives the active and reactive energy as

$$P_{in} = \frac{1}{2}\mathrm{Re}\left[q_0 \cdot (\dot{w})^*\right], \tag{2.37a}$$

$$Q_{in} = \frac{1}{2}\mathrm{Im}\left[q_0 \cdot (\dot{w})^*\right]. \tag{2.37b}$$

With the complex amplitude $\widetilde{w}$ expressed by wave superposition at $x = 0$ and $\dot{w} = i\omega \cdot \widetilde{w}$, input power flow can be easily obtained. By the normalizing expression in (2.28), the normalized power flow are achieved and shown as follows,

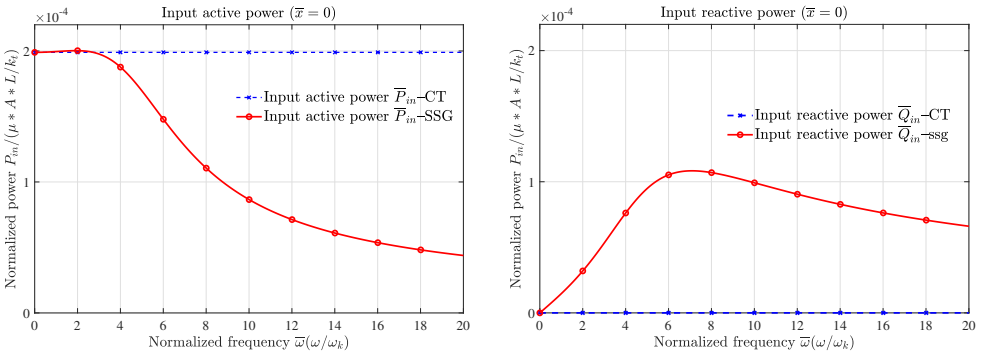

(a) Active power (b) Reactive power

Figure 2.13: Input active power and reactive power

Figure 2.13 display the dimensionless input active and reactive flow. The active power represents the apparent 'damping' effect of energy being carried away to infinity, and the reactive power does not transform power from force or dissipate power. For the classical theory rod, the active power is positive and invariant in frequency range $0 \leq \overline{\omega} \leq 10$, and the reactive power is constantly zero. This makes physical sense because the rod has been assumed to possess no damping. Different from the classical theory, the input active power and reactive power of complex rod show frequency dependence characteristics. The higher the frequency is, the less the injecting active power. Thus the structure is more resistant as the frequency goes up. The input reactive power is not zero even without damping effect, it is generated by the complex force interaction at the force driving point, and it reflects the local behavior of heterogeneity caused by long range interaction between micro-structures in the near field of the force driving point resulting from long range interactions.

To explore the near-field feature, transfer active power and reactive power on different frequency are analyzed. Expression of time averaged energy flow in complex rod based on SSG theory rod model has been derived in Eq. (2.26) in Sec .2.2.4, and the spatial variation results are illustrated in Figure 2.14,

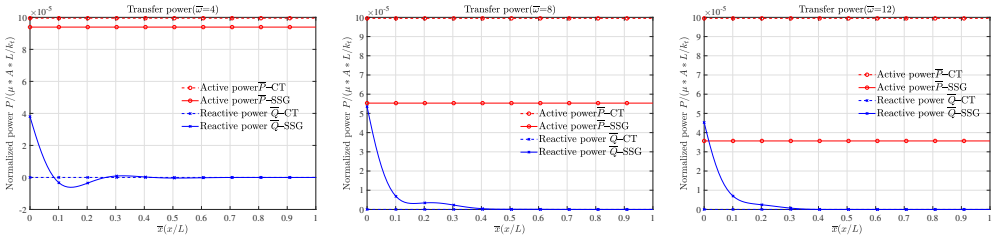

(a) (b) (c)

Figure 2.14: Transfer active power and reactive power

As shown in Figure 2.14, transfer active $\overline{P}$–CT and reactive power $\overline{Q}$–CT resulting from classical rod theory is completely frequency and spatial position independent. The classical input active powers at $\bar{x} = 0$ are identical regardless of frequency

($\overline{\omega} = 4, 8, 12$), and are transmitted to infinite along the propagation direction without dissipation. The time-averaged reactive power is constantly equal to zero as the field is purely propagating without wave attenuation. Whereas the propagation field of complex rod is of frequency dependence. The active power at $x = 0$ on each frequency equals to half of the input active power on each frequency shown in Figure 2.13, which are less than the classical input active power. The higher the frequency, the more distinct the difference. Without damping, the input active power can also be transmitted to infinite without variation. Near field effect does not affect spacial transfer of active power but affect transfer of reactive power. The reactive power at $x = 0$ also equals to half of the input reactive power shown in Figure 2.13. After been generated, $\overline{Q}$–SSG decreases rapidly to zero along the propagation direction in the field close to excitation force. The higher the frequency, the more rapidly the transfer reactive power $\overline{Q}$–SSG decay. For a given frequency, the greater the distance between the points of observation and force application, the smaller the near-field effect.

Considering the distinct character of the transfer reactive power exhibited by SSG theory-based model, it is necessary to validate the results with energy flow balance in wave propagation direction. In a region which is not loaded, the reactive energy flow balance should follow the principle [113]

$$\nabla \cdot \langle Q \rangle + 2\omega \left(\langle T \rangle - \langle U \rangle \right) = 0. \tag{2.38}$$

This expression shows the net reactive flow is proportional to time averaged Lagrangian energy density which equals the difference between time averaged kinetic energy and potential energy. To test that the proposed model follow the reactive power balance in Eq. (2.38), values of $-\nabla \cdot \langle Q \rangle$ and $2\omega \left(\langle T \rangle - \langle U \rangle \right)$ are calculated on one arbitrary frequency $\overline{\omega} = 3$ based on SSG theory formulation, and the results are shown in Figure 2.15,

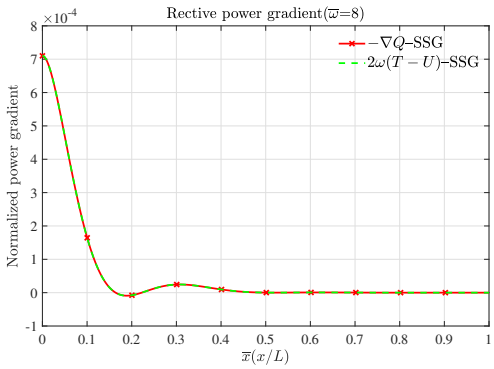

Figure 2.15: Reactive power flow balance

As shown in Figure 2.15, reactive power balance in Eq. (2.38) is validated for the proposed formulation. For the SSG theory-based model, the net reactive flow is proportional to the difference between time averaged kinetic energy and

potential energy. At the force excitation point, the time averaged potential energy has great difference with time averaged kinetic energy due to the description higher order deformation potential energy, and the near field effect is prominent. As wave propagate to the far field, evanescent waves decay to zero and near field effect become less obvious.

2.4 Frequency response of finite rod based on SSG theory model

As shown in Figure 2.16, a fix-free rod subject to a harmonic load $q = q_0 e^{i\omega t}$ at the free end is considered for frequency response function analysis. The observation point is at $x = 0.78L$. The radius of the cross-section $r = 3a_0$ and the length $L = 5r$.

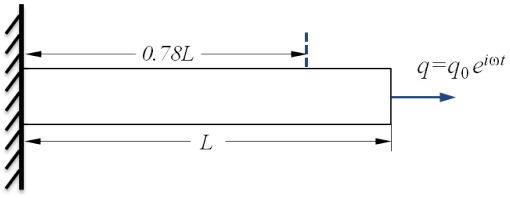

Figure 2.16: A fixed-free complex rod with loading in free end

The solution for the displacement can be given by the superposition of the progressive and retrograde contribution from all the wave modes($\pm k_1$, $\pm k_2$ *and* $\pm k_3$). The general expressions of the normalized displacement $\overline{w}$ can be expressed as

$$\overline{w}(\overline{x},\tau) = \left(\mathcal{A}e^{-i\overline{k}_1\overline{x}} + \mathcal{B}e^{i\overline{k}_1\overline{x}} + \mathcal{C}e^{-i\overline{k}_2\overline{x}} + \mathcal{D}e^{i\overline{k}_2\overline{x}} + \mathcal{E}e^{-i\overline{k}_3\overline{x}} + \mathcal{F}e^{i\overline{k}_3\overline{x}}\right) e^{i\overline{\omega}\tau}. \quad (2.39)$$

From the dispersion relation, which is obtained by the governing equation in Sec. 2.2.2, all the wavenumbers $\overline{k}_1$, $\overline{k}_2$ and $\overline{k}_3$ on each frequency can be obtained. Then the value of the displacement on each frequency only depends on the amplitudes of each wave ($\mathcal{A}$, $\mathcal{B}$, $\mathcal{C}$, $\mathcal{D}$, $\mathcal{E}$, $\mathcal{F}$). For the case in Figure 2.16, the boundary conditions should be set as

$$\begin{aligned}
&\bar{w}\,(0,\tau) = 0 \qquad at\ \ \bar{x} = 0,\\
&\bar{P}_1\,(0,\tau) = \frac{2B_1 - B_3}{2\mu AL^2}\frac{\partial^2\bar{w}}{\partial\bar{x}^2} - \frac{B_2}{\mu AL^4}\frac{\partial^4\bar{w}}{\partial\bar{x}^4} = 0 \quad at\ \ \bar{x} = 0,\\
&\bar{P}_2\,(0,\tau) = \frac{B_3}{2\mu AL^2}\frac{\partial\bar{w}}{\partial\bar{x}} + \frac{B_2}{\mu AL^4}\frac{\partial^3\bar{w}}{\partial\bar{x}^3} = 0 \qquad at\ \ \bar{x} = 0,\\
&\bar{P}_0\,(1,\tau) = \frac{E}{\mu}\frac{\partial\bar{w}}{\partial\bar{x}} + \frac{B_3 - B_1}{\mu AL^2}\frac{\partial^3\bar{w}}{\partial\bar{x}^3} + \frac{B_2}{\mu AL^4}\frac{\partial^5\bar{w}}{\partial\bar{x}^5} = -\frac{q_0}{\mu A}e^{i\omega t} \qquad at\ \ \bar{x} = 1,\\
&\bar{P}_1\,(1,\tau) = \frac{2B_1 - B_3}{2\mu AL^2}\frac{\partial^2\bar{w}}{\partial\bar{x}^2} - \frac{B_2}{\mu AL^4}\frac{\partial^4\bar{w}}{\partial\bar{x}^4} = 0 \quad at\ \ \bar{x} = 1,\\
&\bar{P}_2\,(1,\tau) = \frac{B_3}{2\mu AL^2}\frac{\partial\bar{w}}{\partial\bar{x}} + \frac{B_2}{\mu AL^4}\frac{\partial^3\bar{w}}{\partial\bar{x}^3} = 0 \qquad at\ \ \bar{x} = 1.
\end{aligned} \quad (2.40)$$

These boundary conditions physically means: at the fixed end $\bar{x} = 0$, the displacement equals zero, the first higher order force $\bar{P}_1$ and the second higher order force $\bar{P}_2$ equal zero; at the loading end $\bar{x} = 1$, the produced classical force follows the force equilibrium, the first higher order force $\bar{P}_1$ and the second higher order force $\bar{P}_2$ equal zero.

The interpretations of these boundary conditions are as follows, The extra kinematic parameters $\frac{\partial \bar{w}}{\partial \bar{x}}$ and $\frac{\partial^2 \bar{w}}{\partial \bar{x}^2}$ represent the micro-rotation and micro-curvature between the adjacent micro-structures, and the corresponding generalized loads $\bar{P}_2$ and $\bar{P}_3$ represent the inner interaction dual to the kinetic variables $\frac{\partial \bar{w}}{\partial \bar{x}}$ and $\frac{\partial^2 \bar{w}}{\partial \bar{x}^2}$.

For the classical theory there are two kinds of conditions: a loading type and a geometric type. The SSG boundary condition follows the similar principle. At $\bar{x} = 0$, the possible force produced by the fixed attachment is only classical force, so the higher order forces $\bar{P}_2$ and $\bar{P}_3$ should be set to zero. At $\bar{x} = 1$, $\bar{P}_0$ follows the force equilibrium on that section, and the higher order force $\bar{P}_2$ and $\bar{P}_3$ are set to zero because there is not external higher order force applied on that section.

Following the boundary conditions, six equilibrium with the amplitudes of each progressive and retrograde wave ($\mathcal{A}$, $\mathcal{B}$, $\mathcal{C}$, $\mathcal{D}$, $\mathcal{E}$, $\mathcal{F}$) as unknown variables are established. With some numerical calculation, the amplitude at observation point on each frequency can be obtained.

2.4.1 FRF result of analytical method

The investigation of frequency response is proceed with the amplitude of excitation force $q_0 = 0.05\mu A$ at $x = L$. Figure 2.17 displays the normalized displacement magnitude at observation point $x = 0.78L$ in complex structure based on SSG theory model and in homogeneous structure with classical theory model.

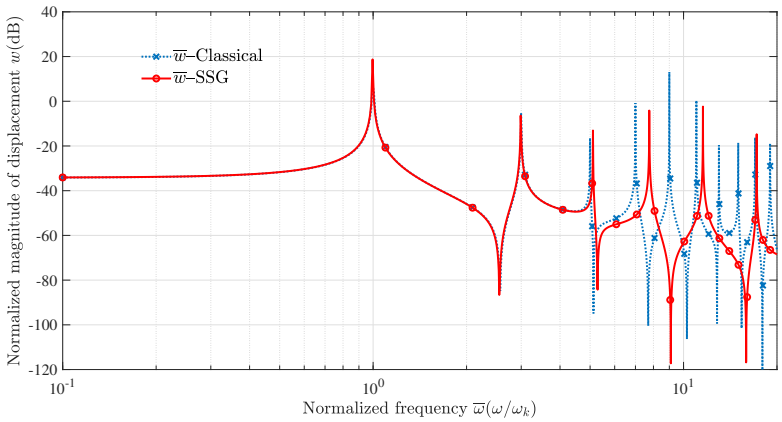

Figure 2.17: Frequency response function at $x = 0.78L$

We notice that resonances can be predicted by both models, but the corresponding values of SSG theory-based model shift to higher frequencies compared to classical ones from 3th order, and less resonances are observed in the same frequency

range $0.1 \leq \bar{\omega} \leq 10$ (6 for SSG theory model and 10 for classical theory model). Due to the long range interactions between micro-structure, wave propagation is significantly affected. vibration energy is not only conserved in the propagating non-classical longitudinal wave, but also converted into the other two evanescent modes. In higher frequency, micro-structure effects cause more energy conversion into the extra evanescent waves, which decay rapidly in near field instead of being transmitted to the far field and contribute to wave mode. This can be the explanation for the reduction of resonance numbers.

2.4.2 Frequency response analysis in COMSOL

To verify the analytical FRF results with wave approach, the same case of frequency response analysis in Sec. 2.4.1 is implemented in COMSOL, which is a finite element analysis, solver and multi-physics simulation software.

The modelling start with establishing one 1-D component by inserting interval of length '1' and selecting weak form PDE as the 'Physics'. To solve the governing equation of 6-order partial differential and describing the boundary conditions of 5-order partial differential, the number of dependent variables is set to be 6 for complex rod structure and the dependent variables include the longitudinal displacement u, its first derivative u_1, second derivative u_2, the regular axis force P_0 and two higher order force P_1 and P_2. To be specific, governing equation of six order partial difference is input in weak form in 'weak form PDE interface', and the boundary conditions are applied in from of 'Dirichlet boundary condition' or in form of 'Flux'. COMSOL can only solve the second order derivation, so the highest differential order of the weak form expression would be one. The shape function used for discretization is six-tic Hermite polynomials to guarantee the higher order derivative continuous condition. The component is meshed with maximum element size as 0.02, and the relative tolerance in solver is 10^{-5}.

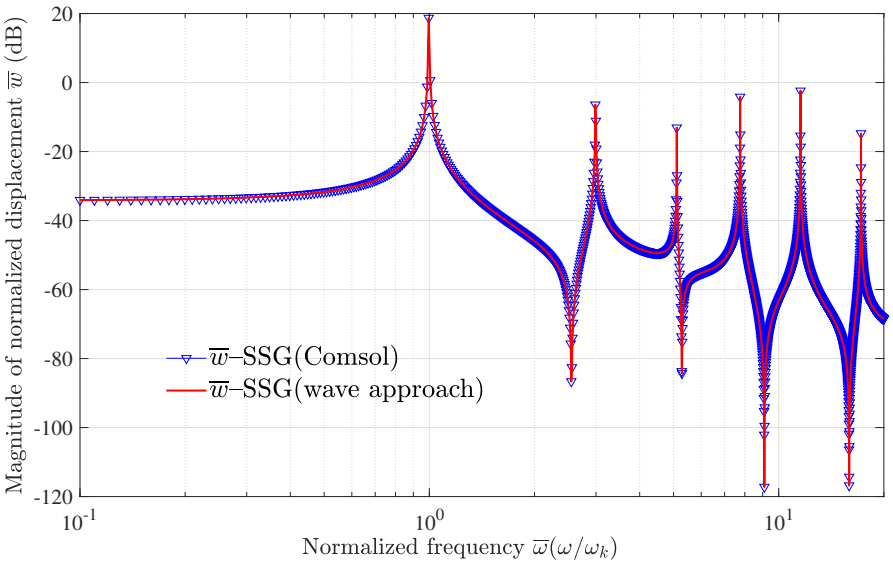

Figure 2.18: Frequency response at $x = 0.78L$ in COMSOL

Figure 2.18 displays the frequency response of the studied complex rod in frequency range $0.1 \leq \bar{\omega} \leq 100$. As we can see the response resulting from COMSOL matches well with response with wave approach in frequency range $0.1 \leq \bar{\omega} \leq 10$. The previous formulation is rigorous and the result are validated. With the analytical equations deduced based on non-classical theory and proper input in forms of weak form, COMSOL can be employed to calculate the structural response of complex rod with less computational effort and wider frequency range. The utilization of COMSOL can significantly simplify the dynamic behavior investigation of complex media.

2.5 One-dimensional lattice model for second strain gradient rod theory

Non-local continuum theory is based on the assumption that the forces between material points are a long-range type, thus the lattice model for the SSG theory should be capable of reflecting the long-range character of inter-atomic forces. In this section, one new lattice model is developed to have a discrete micro-structural basis for the SSG theory-based continuum model. For the studied 1D SSG theory-based rod, the lattice equation of motion is proposed with coupling particles describing the long range interactions as

$$M\frac{\partial^2 u_n(t)}{\partial t^2} = g_2\left(u_{n+1} - 2u_n + u_{n-1}\right) + g_4\left(u_{n+2} - 2u_n + u_{n-2}\right) + g_6\left(u_{n+3} - 2u_n + u_{n-3}\right) + F(n) \tag{2.41}$$

where M denotes particle mass, $u_n(t)$ are the displacements from the equilibrium. g_2, g_4 and g_6 represent coupling constants for the three different types of interac-

tion, the nearest-neighbor, the next-nearest-neighbor and the next-next neighbor interactions. F_n indicates the external force applied on the particles. One discrete mass-spring system that corresponds to the suggested lattice model is given in Figure 2.19

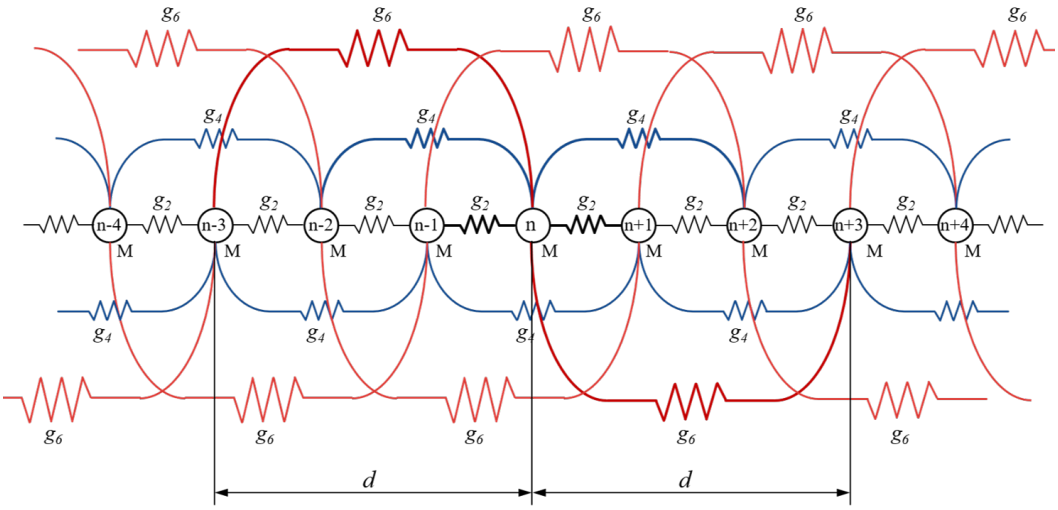

Figure 2.19: lattice model with nearest-neighbor and next-nearest-neighbor and next-next-neighbor interactions for SSG theory

In the lattice model, all the particles have the same mass M, and the infinite lattice possess the cross-section area A. The three types of interactions between particles are separately modeled by springs with stiffness coefficients $k_2 = g_2$, $k_4 = g_4$ and $k_6 = g_6$.

To achieve a continuum equation from the suggested lattice model, one map operation is utilized that transforms the equations of motion for $u_n(t)$ of lattice model into continuum equation for $u(x,t)$ that describes one-dimensional displacement field. In order to explain deducing process clearly, the map operation [116, 117] is briefly introduced. To obtain the continuum equation from a lattice equation, firstly, $u_n(t)$ are defined as Fourier coefficients of function $\hat{u}(k,t)$ on $[-K_0/2, K_0/2]$ by the equation

$$\hat{u}(k,t) = \sum_{n=-\infty}^{+\infty} u_n(t)\, e^{-ikx_n} = \mathcal{F}_\Delta\{u_n(t)\}, \tag{2.42}$$

where $x_n = nd$ and $d = 2\pi/K_0$ is the distance between equilibrium positions of the lattice particles. The inverse Fourier series transform is defined by

$$u_n(t) = \frac{1}{K_0}\int_{-K_0/2}^{K_0/2} dk\, \hat{u}(k,t)\, e^{-ikx_n} = \mathcal{F}_\Delta{}^{-1}\{\hat{u}(k,t)\}. \tag{2.43}$$

Equations (2.42) and (2.43) are the basis for the Fourier transform, which is obtained by transforming from lattice variable to a continuum one in the limit $d \to 0$ ($K_0 =$

$\frac{2\pi}{d} \to \infty$). The Fourier transform are derived from (2.42) and (2.43) with limit $d \to 0$. We replace the lattice function

$$u_n(t) = \frac{2\pi}{K_0} u(x_n, t)$$

with continuous $u(x,t)$ while letting

$$x_n = nd = \frac{2\pi n}{K_0} \to x.$$

Then the sum in Eq. (2.42) can be changed to an integral with $(d \to \infty)$, and Eq. (2.42), (2.43) become

$$\tilde{u}(k,t) = \int_{-\infty}^{+\infty} dx e^{-ikx} u(x,t) = \mathcal{F}\{u(x,t)\}, \tag{2.44a}$$

$$u(x,t) = \frac{1}{2\pi} \int_{-\infty}^{+\infty} dk e^{-ikx} \tilde{u}(k,t) = \mathcal{F}^{-1}\{u(x,t)\}. \tag{2.44b}$$

We assume that

$$\tilde{u}(k,t) = \lim \hat{u}(k,t),$$

where limit denotes the passage to the limit $d \to 0$ ($K_0 = \frac{2\pi}{d} \to \infty$). As we can see, $\tilde{u}(k,t)$ is a Fourier transform of the field $u(x,t)$, and $\hat{u}(k,t)$ is a Fourier series transform of $u_n(t)$, where we can use $u_n(t) = \frac{2\pi}{K_0} u(nd,t)$, and the function $u(x,t)$ can be derived in the limit $d \to 0$. As a result, the map operation from a lattice model into a continuum model is defined by the following steps [118]

(1) The Fourier series transform:

$$F_\Delta : \qquad u_n(t) \to F_\Delta\{u_n(t)\} \to \hat{u}(k,t)$$

(2) The passage to the limit $d \to 0$:

$$Limit : \qquad \hat{u}(k,t) \to \lim\{\hat{u}(k,t)\} = \tilde{u}(k,t)$$

(3)The inverse Fourier transform:

$$F^{-1} : \qquad \tilde{u}(k,t) \to F^{-1}\{\tilde{u}(k,t)\} = u(x,t)$$

The similar transformations can be performed for different equations to map the lattice equation into an equation for the elastic continuum. In the following, the transformations is proceeded based on the introduced map operation. The first step is transforming the discreet lattice equation of motion $u_n(t)$ to the field $\hat{u}(k,t)$. We multiply Eq. (2.41) by e^{-iknd}, and summing over n from $-\infty$ to $+\infty$. Then

$$\begin{aligned} M \sum_{n=-\infty}^{+\infty} e^{-iknd} \frac{d^2 u_n}{dt^2} =& g_2 \cdot \sum_{n=-\infty}^{+\infty} e^{-iknd} (u_{n+1} - 2u_n + u_{n-1}) + g_4 \cdot \sum_{n=-\infty}^{+\infty} e^{-iknd} (u_{n+2} - 2u_n + u_{n-2}) \\ &+ g_6 \cdot \sum_{n=-\infty}^{+\infty} e^{-iknd} (u_{n+3} - 2u_n + u_{n-3}) + \sum_{n=-\infty}^{+\infty} e^{-iknd} F(n). \end{aligned} \tag{2.45}$$

The first three terms on the right-hand of Eq. (2.45) equals

$$
\begin{aligned}
& g_2 \cdot \sum_{n=-\infty}^{+\infty} e^{-iknd}\left(u_{n+1}-2u_n+u_{n-1}\right)+g_4 \cdot \sum_{n=-\infty}^{+\infty} e^{-iknd}\left(u_{n+2}-2u_n+u_{n-2}\right) \\
& +g_6 \cdot \sum_{n=-\infty}^{+\infty} e^{-iknd}\left(u_{n+3}-2u_n+u_{n-3}\right) \\
= & g_2 \cdot\left(\sum_{n=-\infty}^{+\infty} e^{-iknd} u_{n+1}-2 \sum_{n=-\infty}^{+\infty} e^{-iknd} u_n+\sum_{n=-\infty}^{+\infty} e^{-iknd} u_{n-1}\right) \\
& +g_4 \cdot\left(\sum_{n=-\infty}^{+\infty} e^{-iknd} u_{n+2}-2 \sum_{n=-\infty}^{+\infty} e^{-iknd} u_n+\sum_{n=-\infty}^{+\infty} e^{-iknd} u_{n-2}\right) \\
& +g_6 \cdot\left(\sum_{n=-\infty}^{+\infty} e^{-iknd} u_{n+3}-2 \sum_{n=-\infty}^{+\infty} e^{-iknd} u_n+\sum_{n=-\infty}^{+\infty} e^{-iknd} u_{n-3}\right) \\
= & g_2 \cdot\left(e^{ikd} \sum_{m=-\infty}^{+\infty} e^{-ikmd} u_m-2 \sum_{n=-\infty}^{+\infty} e^{-iknd} u_n+e^{-ikd} \sum_{j=-\infty}^{+\infty} e^{-ikjd} u_j\right) \\
& +g_4 \cdot\left(e^{2ikd} \sum_{m=-\infty}^{+\infty} e^{-ikmd} u_m-2 \sum_{n=-\infty}^{+\infty} e^{-iknd} u_n+e^{-2ikd} \sum_{j=-\infty}^{+\infty} e^{-ikjd} u_j\right) \\
& +g_6 \cdot\left(e^{3ikd} \sum_{m=-\infty}^{+\infty} e^{-ikmd} u_m-2 \sum_{n=-\infty}^{+\infty} e^{-iknd} u_n+e^{-3ikd} \sum_{j=-\infty}^{+\infty} e^{-ikjd} u_j\right) .
\end{aligned}
\tag{2.46}
$$

Using the definition of $\hat{u}(k,t)$, Eq. (2.46) gives

$$
\begin{aligned}
& g_2 \cdot\left(e^{ikd} \hat{u}(k,t)-2 \hat{u}(k,t)+e^{-ikd} \hat{u}(k,t)\right)+g_4 \cdot\left(e^{2ikd} \hat{u}(k,t)-2 \hat{u}(k,t)+e^{-2ikd} \hat{u}(k,t)\right) \\
& +g_6 \cdot\left(e^{3ikd} \hat{u}(k,t)-2 \hat{u}(k,t)+e^{-3ikd} \hat{u}(k,t)\right) \\
& =g_2 \cdot\left(e^{ikd}+e^{-ikd}-2\right) \hat{u}(k,t)+g_4 \cdot\left(e^{2ikd}+e^{-2ikd}-2\right) \hat{u}(k,t) \\
& +g_6 \cdot\left(e^{3ikd}+e^{-3ikd}-2\right) \hat{u}(k,t) \\
& =2\left(g_2 \cdot(\cos(kd)-1)+g_4 \cdot(\cos(2kd)-1)+g_6 \cdot(\cos(3kd)-1)\right) \hat{u}(k,t) .
\end{aligned}
\tag{2.47}
$$

To further simplify Eq. (2.47), we have

$$\begin{aligned}
\cos(kd)-1 &= \cos\left(2\frac{kd}{2}\right)-1=\left(1-2\sin^2\left(\frac{kd}{2}\right)\right)-1=-2\sin^2\left(\frac{kd}{2}\right);\\
\cos(2kd)-1 &= \left(1-2\sin^2(kd)\right)-1=-2\sin^2(kd)\\
&= -2\sin^2\left(2\frac{kd}{2}\right)=-2\left(2\sin\left(\frac{kd}{2}\right)\cos\left(\frac{kd}{2}\right)\right)^2=-8\sin^2\left(\frac{kd}{2}\right)\cos^2\left(\frac{kd}{2}\right)\\
&= -8\sin^2\left(\frac{kd}{2}\right)\left(1-\sin^2\left(\frac{kd}{2}\right)\right)=-8\sin^2\left(\frac{kd}{2}\right)+8\sin^4\left(\frac{kd}{2}\right);\\
\cos(3kd)-1 &= -2\sin^2\left(3\frac{kd}{2}\right)=-2\left(-4\sin^3\left(\frac{kd}{2}\right)+3\sin\left(\frac{kd}{2}\right)\right)^2\\
&= -2\left(16\sin^6\left(\frac{kd}{2}\right)+9\sin^2\left(\frac{kd}{2}\right)-24\sin^4\left(\frac{kd}{2}\right)\right)\\
&= -32\sin^6\left(\frac{kd}{2}\right)-18\sin^2\left(\frac{kd}{2}\right)+48\sin^4\left(\frac{kd}{2}\right).
\end{aligned} \tag{2.48}$$

Substitution of Eq. (2.48) into Eq. (2.47) gives

$$\begin{aligned}
&2\begin{pmatrix} -2g_2\cdot\sin^2\left(\frac{kd}{2}\right)-8g_4\cdot\left(\sin^2\left(\frac{kd}{2}\right)-\sin^4\left(\frac{kd}{2}\right)\right)\\ -2g_6\cdot\left(9\sin^2\left(\frac{kd}{2}\right)-24\sin^4\left(\frac{kd}{2}\right)+16\sin^6\left(\frac{kd}{2}\right)\right)\end{pmatrix}\hat{u}(k,t)\\
&=-4\left(g_2+4g_4+9g_6\right)\sin^2\left(\frac{kd}{2}\right)\hat{u}(k,t)+16\left(g_4+6g_6\right)\sin^4\left(\frac{kd}{2}\right)\hat{u}(k,t)\\
&\quad-64g_6\sin^6\left(\frac{kd}{2}\right)\hat{u}(k,t).
\end{aligned} \tag{2.49}$$

With the obtained first three term equation and using the definition of $\hat{u}(k,t)$ for the other two terms, (2.45) becomes

$$\begin{aligned}
M\frac{\partial^2\hat{u}(k,t)}{\partial t^2} &= -4\left(g_2+4g_4+9g_6\right)\sin^2\left(\frac{kd}{2}\right)\hat{u}(k,t)+16\left(g_4+6g_6\right)\sin^4\left(\frac{kd}{2}\right)\hat{u}(k,t)\\
&\quad-64g_6\sin^6\left(\frac{kd}{2}\right)\hat{u}(k,t)+F\left\{F(x)\right\}.
\end{aligned} \tag{2.50}$$

Using the asymptotic behavior of the sine in the form

$$\sin\left(\frac{kd}{2}\right)=\frac{kd}{2}-\frac{1}{6}\left(\frac{kd}{2}\right)^3+\frac{1}{5!}\left(\frac{kd}{2}\right)^5+O\left((kd)^7\right),$$

we have

$$\begin{aligned}
\sin^2\left(\frac{kd}{2}\right) =& \left(\frac{kd}{2}\right)^2 + \frac{1}{36}\left(\frac{kd}{2}\right)^6 - 2\frac{kd}{2}\frac{1}{6}\left(\frac{kd}{2}\right)^3 + 2\frac{kd}{2}\frac{1}{5!}\left(\frac{kd}{2}\right)^5 + O\left((kd)^7\right) \\
=& \frac{(kd)^2}{4} - \frac{(kd)^4}{48} + \frac{(kd)^6}{1440} + O\left((kd)^7\right); \\
\sin^4\left(\frac{kd}{2}\right) =& \left(\sin^4\left(\frac{kd}{2}\right)\right)^2 = \left(\frac{(kd)^2}{4} - \frac{(kd)^4}{48}\right)^2 + O\left((kd)^7\right) \\
=& \frac{(kd)^4}{16} - 2\frac{(kd)^2}{4}\frac{(kd)^4}{48} + O\left((kd)^7\right) = \frac{(kd)^4}{16} - \frac{(kd)^6}{96} + O\left((kd)^7\right); \\
\sin^6\left(\frac{kd}{2}\right) =& \left(\frac{kd}{2} - \frac{1}{6}\left(\frac{kd}{2}\right)^3 + \frac{1}{5!}\left(\frac{kd}{2}\right)^5 + O\left((kd)^7\right)\right)^6 = \left(\frac{kd}{2}\right)^6 + O\left((kd)^7\right).
\end{aligned} \tag{2.51}$$

Replacing the terms of $\sin^2\left(\frac{kd}{2}\right)$, $\sin^4\left(\frac{kd}{2}\right)$ and $\sin^6\left(\frac{kd}{2}\right)$ in Eq. (2.49) with the simplified expressions in Eq. (2.51), we have

$$\begin{aligned}
&-4\left(g_2+4g_4+9g_6\right)\sin^2\left(\frac{kd}{2}\right) + 16\left(g_4+6g_6\right)\sin^4\left(\frac{kd}{2}\right) - 64g_6\sin^6\left(\frac{kd}{2}\right) \\
&= -4\left(g_2+4g_4+9g_6\right)\left(\frac{(kd)^2}{4} - \frac{(kd)^4}{48} + \frac{(kd)^6}{1440}\right) + 16\left(g_4+6g_6\right)\left(\frac{(kd)^4}{16} - \frac{(kd)^6}{96}\right) + 64g_6\left(\frac{kd}{2}\right)^6 \\
&= -4\left(g_2+4g_4+9g_6\right)(kd)^2 + \frac{1}{12}\left(g_2+16g_4+81g_6\right)(kd)^4 - \frac{1}{360}\left(g_2+64g_4+729g_6\right)(kd)^6.
\end{aligned} \tag{2.52}$$

The transition to the limit $d \to 0$ in Eq. (2.49) gives

$$\frac{\partial^2 \tilde{u}(k,t)}{\partial t^2} = -G_2 k^2 \tilde{u}(k,t) + G_4 k^4 \tilde{u}(k,t) - G_6 k^6 \tilde{u}(k,t) + \mathcal{F}\left\{F(x)\right\}, \tag{2.53}$$

where

$$G_2 = \frac{\left(g_2+4g_4+9g_6\right)d^2}{M}, \qquad G_4 = \frac{\left(g_2+16g_4+81g_6\right)d^4}{12M},$$
$$G_6 = \frac{\left(g_2+64g_4+729g_6\right)d^6}{360M}.$$

The inverse Fourier transform $\mathcal{F}^{-1}$ of Eq. (2.53) has the form

$$\frac{\partial^2 \mathcal{F}^{-1}\left\{\tilde{u}(k,t)\right\}}{\partial t^2} = -G_2\mathcal{F}^{-1}\left\{k^2\tilde{u}(k,t)\right\} + G_4\mathcal{F}^{-1}\left\{k^4\tilde{u}(k,t)\right\} - G_6\mathcal{F}^{-1}\left\{k^6\tilde{u}(k,t)\right\} + F(x). \tag{2.54}$$

Then we can use the relation $\mathcal{F}^{-1}\left\{\tilde{u}(k,t)\right\} = u(x,t)$ and the connection between

the derivatives and its Fourier transforms as

$$F^{-1}\left\{k^2\tilde{u}\left(k,t\right)\right\}=-\frac{\partial^2 u\left(x,t\right)}{\partial x^2},\qquad F^{-1}\left\{k^4\tilde{u}\left(k,t\right)\right\}=+\frac{\partial^4 u\left(x,t\right)}{\partial x^4},$$
$$F^{-1}\left\{k^6\tilde{u}\left(k,t\right)\right\}=-\frac{\partial^6 u\left(x,t\right)}{\partial x^6}.$$

Then the continuum equation can be achieved as

$$\frac{\partial^2 u\left(x,t\right)}{\partial t^2}=G_2\frac{\partial^2 u\left(x,t\right)}{\partial x^2}+G_4\frac{\partial^4 u\left(x,t\right)}{\partial x^4}+G_6\frac{\partial^6 u\left(x,t\right)}{\partial x^6}+F\left(x\right),\tag{2.55}$$

where

$$G_2=\frac{\left(g_2+4g_4+9g_6\right)d^2}{M},G_4=\frac{\left(g_2+16g_4+81g_6\right)d^4}{12M},G_6=\frac{\left(g_2+64g_4+729g_6\right)d^4}{360M}$$

The one-dimension continuum equation of motion deduced with Hamilton principle is as follows,

$$\frac{\partial^2 u\left(x,t\right)}{\partial t^2}=\frac{E}{\rho}\frac{\partial^2 u\left(x,t\right)}{\partial x^2}+\frac{B_4-B_2}{\rho}\frac{\partial^4 u\left(x,t\right)}{\partial x^4}+\frac{B_3}{\rho}\frac{\partial^6 u\left(x,t\right)}{\partial x^6}+F\left(x\right),\tag{2.56}$$

where

$$\begin{aligned}B_1&=2A\left(a_1+a_2+a_3+a_4+a_5\right),\\B_2&=2A\left(b_1+b_2+b_3+b_4+b_5+b_6+b_7\right),\\B_3&=2A\left(c_1+c_2+c_3\right).\end{aligned}$$

The corresponding coefficients of each terms should be identify with the other ones, thus we have

$$\begin{aligned}G_2&=\frac{\left(g_2+4g_4+9g_6\right)d^2}{M}=\frac{E}{\rho},\\G_4&=\frac{\left(g_2+16g_4+81g_6\right)d^4}{12M}=\frac{B_3-B_1}{\rho},\\G_6&=\frac{\left(g_2+64g_4+729g_6\right)d^4}{360M}=\frac{B_2}{\rho}.\end{aligned}\tag{2.57}$$

And the stiffness coefficients of the three types of interactions between particles are connected with the Young's modulus higher order material.

$$\begin{aligned}g_2&=\frac{\left(3Ed^4+13\left(B_1-B_3\right)d^2+30B_2\right)A}{2d^5},\\g_4&=-\frac{\left(3Ed^4+40\left(B_1-B_3\right)d^2+120B_2\right)A}{20d^5},\\g_6&=\frac{\left(Ed^4+15\left(B_1-B_3\right)d^2+90B_2\right)A}{90d^5}.\end{aligned}\tag{2.58}$$

we can see the proposed 1D lattice model can be transform to SSG theory-based continuous model. The higher order material constants are directly connected with the stiffness of long range interactions along with the Young's modulus, the inner-particle distance and area of cross sections. Therefore the local behavior of heterogeneity caused by the complex interactions of internal structures can be captured by the SSG theory-based model.

The other statement that the three type coupling interactions determine the material constants in continuous models is also valid. In the presented work, the higher-order material constants of different material refer to the results in research by Shodja et al. (2012) [109] with atomistic approach, and these constants can be applied in complex structure with internal structures in atomic-scale. On the other hand, considering one complex media in macro-scale is designed with micro-scale internal structures, the long range coupling within different components will play a major role to structural global behavior under some circumstance. The SSG theory-based model as well as other generalized continuum elasticity theory also applies in this case, merely the higher order material constants should be determined corresponding to the long range interaction coefficients. The proposed lattice model as well as the SSG theory-based continuum model can be employed to study the distinct behavior of complex rod structure as the local behavior of heterogeneity governed by both short range interaction and long range interactions are considered in both models.

2.6 Conclusions

Wave propagation in complex rod structure is different from the conventional one with consideration of local behaviors caused by internal micro-structure interaction. In order to analyze this special behavior, we established an enriched model based on Mindlin's SSG theory. This formulation allows the micro-structure's effects to be captured, by considering the higher order strains into strain energy density, meanwhile the heterogeneity to be described in the frame of continuum mechanics. From the numerical calculations, one can see that the proposed SSG theory-based rod model is effective in predicting the non-classical dispersive behaviors in complex media. Apart from the dispersion characteristics, this research also highlighted a number of interesting features including the modal density, the energy flux and the resulting frequency response of the rod. Some conclusions can be drawn from the numerical calculation and discussions as follows:

(1) There are three wave modes that can be generated in complex rod based on second strain gradient theory, one is the propagating non-classical longitudinal wave k_1 which exhibits dispersive feature, and the dispersive behavior become more prominent in higher frequency. The other two waves k_2 and k_3 are both evanescent. In higher frequency, energy dissipation through viscous damping for wave k_1 become negligible compared with classical result. As dimension goes up, micro-structural effect is weaken due to the increasing of structural characteristic length, and wave

k_1 become less dispersive.

(2) The proposed formulation of the energy flux is validated as the energy velocity V_e and group c_g velocity of conservative wave k_1 are proved to be identical in the whole frequency range. Energy flux is coupled with one classical force and two higher order forces, which are resultants of classical and higher-order stresses generated on the surface of the observed section.

(3) The complex rod structure with considering the long range interactions between micro-structures shows more resistance to the driving force and the net energy transmitted into the structure diminish distinctly compared with the classical one even without damping dissipation.

(4) The generated disturbance propagate away with transfer mobility modulus $|\overline{Y}_t|$ as well as reactive power $\overline{Q}$-SSG decaying significantly in the near field of force excitation point. The decrease in near field becomes significant in higher frequency as the micro-structure interaction is more prominent. The greater the distance between the points of observation and force application, the smaller the near-field effect.

(5) The statistical value of the modal density for the non-classical longitudinal wave k_1 is lower than the classical results, and this phenomenon becomes more serious as the structure's size decreases. From the FRF analysis, the locations of the first few resonances resulting from SSG theory-based model shift to higher frequencies compared to classical ones from 3th order. These unusual behaviors can be explained with different energy transfer through the extra evanescent waves k_2 and k_3 especially in higher frequency range when the wavelength and the structural characteristic length are in the same order. The frequency response resulting from wave approach is validated by FEM results in COMSOL

(6) One lattice model is proposed to establish a micro-structure basis for the SSG theory continuum model. The proposed lattice model is capable of reflecting the long range character of the inner particles forces. With the map operation approach, the proposed lattice model can be transformed to SSG theory-based continuum model in limit $d \to 0$, and the long range interaction coefficients can be associated with the material constants.

Chapter 3

Wave propagation analysis of SSG theory-based beam

Contents

3.1 Introduction

In this chapter, the proposed SSG theory-based Timoshenko beam model is developed to study the free wave propagation features and forced vibration of the structure with considering the micro-structure interactions. The governing equation and associated boundary conditions are derived based on Hamilton's principle, based on which the dispersion relation of non-classical bending wave, shear wave together with the extra-waves appearing exclusively in SSG theory model are investigated, then the modal density and energy flow are also analyzed. Based on the free wave propagation features, the structural mobility and impedance are investigated along with the forced vibration of bounded structure. The results of the SSG theory-based model are well interpreted by comparing with the classical theory results, and some useful conclusions are derived on the SSG theory-based model in the wave propagation characterization.

3.2 The formulation of SSG theory beam and wave propagation features

The multi-scale modeling begins with establishing the motion equation of the Timoshenko beam. Considering a Timoshenko beam with a rectangular section, the coordinate system $x-y-z$ and kinematic parameters of the model are illustrated as in Figure 3.1 with its x-axis along the axial direction of the beam, and its origin on the left-end section. The plane $x-y$ of the coordinate system is coincident with the mid-plane of the beam. The beam is assumed to be uniform, homogeneous and initially straight along the x-direction with length L, and its the cross sections are assumed to remain plane after deformation. $q(x,t)$ denotes the distributed loads acting on the beam in transverse direction as force per unit axial length.

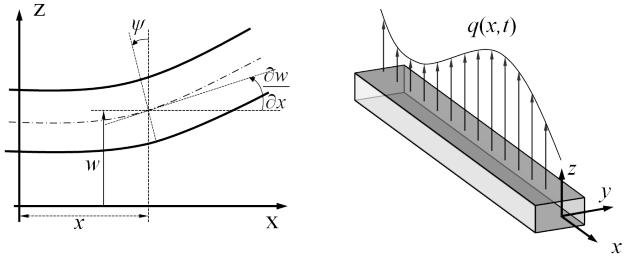

Figure 3.1: Coordinate system and kinematic parameters of the beam

3.2.1 The derivation of governing equation and boundary conditions

The components of the displacement field in the Timoshenko beam model in an in-plane motion are written as Eq. (3.1)

$$\begin{aligned} u_x(x,y,z,t) &= -z\psi(x,t), \\ u_y(x,y,z,t) &= 0, \\ u_z(x,y,z,t) &= w(x,t), \end{aligned} \tag{3.1}$$

where u_x, u_y, and u_z denote the displacement of the beam particles along x, y, and z directions respectively. As shown in Figure 3.1, $w(x,t)$ represents the flexural deformation of the beam. The cross sections are not assumed to remain perpendicular to the deformed axial line of the beam , instead $\psi(x,t)$ represents the rotation angle of the cross-sections after deformation with respect with the perpendicular section.

According to the definition in Sec. 1.4.2.3, the nonzero components of the strain tensor $\boldsymbol{\varepsilon}$, the strain gradient tensor $\boldsymbol{\eta}$, and the second strain gradient tensor $\boldsymbol{\xi}$ for

the presented Timoshenko beam are depicted as,

$$\begin{aligned}
&\varepsilon_{11} = -z\frac{\partial \psi}{\partial x}, \qquad \varepsilon_{13} = \varepsilon_{31} = \frac{1}{2}\left(\frac{\partial w}{\partial x} - \psi\right), \\
&\eta_{111} = -z\frac{\partial^2 \psi}{\partial x^2}, \quad \eta_{311} = \eta_{131} = -\frac{\partial \psi}{\partial x}, \quad \eta_{113} = \frac{\partial^2 w}{\partial x^2}, \\
&\xi_{1111} = -z\frac{\partial^3 \psi}{\partial x^3}, \quad \xi_{1311} = \xi_{3111} = \xi_{1131} = -\frac{\partial^2 \psi}{\partial x^2}, \quad \xi_{1113} = \frac{\partial^3 w}{\partial x^3}.
\end{aligned} \tag{3.2}$$

Considering these nonzero components only, the general form of the strain energy density $\overline{u}$ for the SSG theory is simplified as Eq. (3.3),

$$\begin{aligned}
\overline{u} =& \frac{1}{2}\lambda {\varepsilon_{11}}^2 + \mu\left({\varepsilon_{11}}^2 + 2{\varepsilon_{13}}^2\right) + a_1\left({\eta_{111}}^2 + {\eta_{311}}^2\right) + a_2\left({\eta_{111}}^2 + \eta_{113}\eta_{311}\right) + a_3\left({\eta_{111}}^2 + {\eta_{113}}^2\right) \\
&+ a_4\left({\eta_{111}}^2 + {\eta_{113}}^2 + {\eta_{131}}^2 + {\eta_{311}}^2\right) + a_5\left({\eta_{111}}^2 + 2\eta_{113}\eta_{311} + {\eta_{131}}^2\right) + b_1{\xi_{1111}}^2 \\
&+ b_2\left({\xi_{1111}}^2 + {\xi_{1311}}^2 + {\xi_{3111}}^2\right) + b_3\left({\xi_{1111}}^2 + \xi_{1113}\xi_{1311} + \xi_{1131}\xi_{3111}\right) + b_4\left({\xi_{1111}}^2\right. \\
&\left.+\xi_{1113}\xi_{1131} + \xi_{1131}\xi_{1113}\right) + b_5\left({\xi_{1111}}^2 + {\xi_{1113}}^2 + {\xi_{1131}}^2\right) + b_6\left({\xi_{1111}}^2 + {\xi_{1113}}^2\right. \\
&\left.+{\xi_{1131}}^2 + {\xi_{1311}}^2 + {\xi_{3111}}^2\right) + b_7\left({\xi_{1111}}^2 + \xi_{1131}\xi_{1311} + \xi_{1113}\xi_{1131} + \xi_{3111}\xi_{1113} + \xi_{1311}\xi_{3111}\right) \\
&+ c_1\varepsilon_{11}\xi_{1111} + c_2\left(\varepsilon_{11}\xi_{1111} + \varepsilon_{13}\xi_{1311} + \varepsilon_{31}\xi_{3111}\right) + c_3\left(\varepsilon_{11}\xi_{1111} + \varepsilon_{13}\xi_{1113} + \varepsilon_{31}\xi_{1131}\right)
\end{aligned} \tag{3.3}$$

As has been discussed, lame's constants λ and μ in Eq. (3.3) are related to the the Young's modulus E and the Poisson's ratio ν which can be tested with experimental method. The higher-order material constants a_i, b_i, and c_i still refer to the data tested in the work by Shodja et al. (2012) [109]. The strain energy of the beam can be calculated by integrating Eq. (3.3) over the volume of the beam, and the obtained expression can be simplified by the combination of Eqs. (3.2) and (3.3) as,

$$\begin{aligned}
U =& \int_0^L \int_A \overline{u}\, dA dx = \frac{1}{2}\int_0^L B_1\left(\frac{\partial \psi}{\partial x}\right)^2 + B_2\left(\frac{\partial^2 \psi}{\partial x^2}\right)^2 + B_3\left(\frac{\partial^3 \psi}{\partial x^3}\right)^2 + B_4\left(\frac{\partial \psi}{\partial x}\right)\frac{\partial^3 \psi}{\partial x^3} \\
&+ B_5\left(\frac{\partial^2 w}{\partial x^2}\right)^2 + B_6\left(\frac{\partial^3 w}{\partial x^3}\right)^2 + B_7\left(\frac{\partial \psi}{\partial x}\right)\frac{\partial^2 w}{\partial x^2} + B_8\left(\frac{\partial^2 \psi}{\partial x^2}\right)\frac{\partial^3 w}{\partial x^3} + \mu A\left(\frac{\partial w}{\partial x} - \psi\right)^2 \\
&- 2c_2 A\left(\frac{\partial w}{\partial x} - \psi\right)\frac{\partial^2 \psi}{\partial x^2} + c_3 A\left(\frac{\partial w}{\partial x} - \psi\right)\left(\frac{\partial^3 w}{\partial x^3} - \frac{\partial^2 \psi}{\partial x^2}\right) dx
\end{aligned} \tag{3.4}$$

in which,

$$\begin{aligned}
&B_1 = \zeta EI + 2A(a_1 + 2a_4 + a_5), \\
&B_2 = 2I(a_1 + a_2 + a_3 + a_4 + a_5) + 2A(2b_2 + b_3 + b_5 + 3b_6 + 2b_7), \\
&B_3 = 2I(b_1 + b_2 + b_3 + b_4 + b_5 + b_6 + b_7)
\end{aligned}$$

$$\begin{aligned}
&B_4 = 2I(c_1 + c_2 + c_3), \\
&B_5 = 2A(a_3 + a_4), \qquad B_6 = 2A(b_5 + b_6), \\
&B_7 = -2A(a_2 + 2a_5), \qquad B_8 = -2A(b_3 + 2b_4 + 2b_7),
\end{aligned}$$

with the term $\chi = (1-\upsilon)/(1+\upsilon)\,(1-2\upsilon)$, parameter A as the area of the beam cross section, and $I = \int_A z^2 dA$ as the area moment of inertia for the beam cross section around y axis. The analysis in the present work will be proceeded with setting $\upsilon = 0$ to avoid Poisson effect, namely $\chi = 1$ is set.

To apply the Hamilton principle, the expression for the kinetic energy is also needed. From the displacement field represented in Eq. (3.1), the kinetic energy of the beam can be written as,

$$T = \frac{1}{2}\int_0^L \int_A \rho \left[\left(\frac{\partial w}{\partial t} \right)^2 + \left(-z \frac{\partial \psi}{\partial t} \right)^2 \right] dA dx; \tag{3.5}$$

in which ρ represents the mass density of the beam, and this expression can be simplified to

$$T = \frac{1}{2}\int_0^L m_0 \left(\frac{\partial w}{\partial t} \right)^2 + m_2 \left(\frac{\partial \psi}{\partial t} \right)^2 dx \tag{3.6}$$

with $m_0 = \rho A$, and $m_2 = \rho \int_A z^2 dA$.

Considering the distributed transverse loads $q\,(x,t)$ and end-sectional loads, the virtual work done by external loads can be expressed as,

$$\delta W = \int_0^L (q \cdot \delta w) dx + \left[\begin{array}{l} V_0 \delta w + V_1 \delta \left(\dfrac{\partial w}{\partial x} \right) + V_2 \delta \left(\dfrac{\partial^2 w}{\partial x^2} \right) \\ + M_0 \delta \psi + M_1 \delta \left(\dfrac{\partial \psi}{\partial x} \right) + M_2 \delta \left(\dfrac{\partial^2 \psi}{\partial x^2} \right) \end{array} \right] \Bigg| \begin{array}{l} x = L \\ \\ x = 0 \end{array} \tag{3.7}$$

where V_0, V_1, V_2 and M_0, M_1, M_2 are end-sectional loads dual to corresponding kinematic variables w, $\frac{\partial w}{\partial x}$, $\frac{\partial^2 w}{\partial x^2}$ and ψ, $\frac{\partial \psi}{\partial x}$, $\frac{\partial^2 \psi}{\partial x^2}$. These loads are resultants of not only classical stresses but also higher-order stresses on the end-sectional surface. V_0 and M_0 are respectively referred as shear force and bending moment acting on the end sections. V_1 and M_1 denote the first higher order loads with unit of $\mathrm{N} \cdot \mathrm{m}$ and $\mathrm{N} \cdot \mathrm{m}^2$, and V_2 and M_2 denote the second higher order loads with unit of $\mathrm{N} \cdot \mathrm{m}^2$ and $\mathrm{N} \cdot m^3$. Indeed, these four higher order loads V_1, V_2, M_1 and M_2 are the resultants of higher-order stress components on the end-sectional surface. Physically speaking, the extra kinematic parameters $\frac{\partial w}{\partial x}$, $\frac{\partial^2 w}{\partial x^2}$ and $\frac{\partial \psi}{\partial x}$, $\frac{\partial^2 \psi}{\partial x^2}$ represent the inner relative movement of the adjacent micro-structures, and the corresponding higher order generalized loads represent the inner interactions of the adjacent micro-structures.

The Hamilton principle in time interval $[t_1, t_2]$ is employed as,

$$\int_{t_1}^{t_2} (\delta T - \delta U + \delta W) dt = 0 \tag{3.8}$$

where δT and δU are the variation of kinetic energy and strain energy. By substitution of Eqs. (3.4) (3.5) and (3.7) into Eq. (3.8), and then doing some mathematical operations in accordance with the variational calculus, the two coupled governing

differential equations of motion, one describing the flexural motion and the other describing the shear motion are obtained as,

$$\begin{aligned}\delta w : &-\mu A\left(\frac{\partial \psi}{\partial x}\right)-\left(\frac{B_7}{2}+(c_3+c_2)\,A\right)\left(\frac{\partial^3 \psi}{\partial x^3}\right)+\frac{B_8}{2}\left(\frac{\partial^5 \psi}{\partial x^5}\right)\\ &+\mu A\left(\frac{\partial^2 w}{\partial x^2}\right)+(c_3A-B_5)\left(\frac{\partial^4 w}{\partial x^4}\right)+B_6\left(\frac{\partial^6 w}{\partial x^6}\right)+q=m_0\left(\frac{\partial^2 w}{\partial t^2}\right),\end{aligned} \tag{3.9a}$$

$$\begin{aligned}\delta \psi : &-\mu A\psi+(B_1-c_3A-2c_2A)\left(\frac{\partial^2 \psi}{\partial x^2}\right)+(B_4-B_2)\left(\frac{\partial^4 \psi}{\partial x^4}\right)+B_3\left(\frac{\partial^6 \psi}{\partial x^6}\right)\\ &+\mu A\left(\frac{\partial w}{\partial x}\right)+\left(\frac{B_7}{2}+(c_3+c_2)\,A\right)\left(\frac{\partial^3 w}{\partial x^3}\right)-\frac{B_8}{2}\left(\frac{\partial^5 w}{\partial x^5}\right)=m_2\left(\frac{\partial^2 \psi}{\partial t^2}\right).\end{aligned} \tag{3.9b}$$

And the associated essential and natural boundary conditions at each end (i.e.$x = 0, L$) are derived as

$$\begin{aligned}M_0 =&\left(B_1-A\left(c_2+\frac{c_3}{2}\right)\right)\left(\frac{\partial \psi}{\partial x}\right)+(B_4-B_2)\left(\frac{\partial^3 \psi}{\partial x^3}\right)+B_3\left(\frac{\partial^5 \psi}{\partial x^5}\right)\\ &+\left(\frac{B_7}{2}+A\left(c_2+\frac{c_3}{2}\right)\right)\left(\frac{\partial^2 w}{\partial x^2}\right)-\frac{B_8}{2}\left(\frac{\partial^4 w}{\partial x^4}\right) \qquad or \quad \delta\psi=0\\ M_1 =&A\left(c_2+\frac{c_3}{2}\right)\psi+\left(B_2-\frac{B_4}{2}\right)\left(\frac{\partial^2 \psi}{\partial x^2}\right)-B_3\left(\frac{\partial^4 \psi}{\partial x^4}\right)\\ &-A\left(\frac{c_3}{2}+c_2\right)\left(\frac{\partial w}{\partial x}\right)+\frac{B_8}{2}\left(\frac{\partial^3 w}{\partial x^3}\right) \qquad or \quad \delta\left(\frac{\partial \psi}{\partial x}\right)=0\\ M_2 =&\frac{B_4}{2}\left(\frac{\partial \psi}{\partial x}\right)+B_3\left(\frac{\partial^3 \psi}{\partial x^3}\right) \qquad or \quad \delta\left(\frac{\partial^2 \psi}{\partial x^2}\right)=0\\ V_0 =&-\mu A\psi-\left(\frac{B_7}{2}+(c_3+c_2)\,A\right)\left(\frac{\partial^2 \psi}{\partial x^2}\right)+\frac{B_8}{2}\left(\frac{\partial^4 \psi}{\partial x^4}\right)\\ &+\mu A\left(\frac{\partial w}{\partial x}\right)+(c_3A-B_5)\left(\frac{\partial^3 w}{\partial x^3}\right)+B_6\left(\frac{\partial^5 w}{\partial x^5}\right) \qquad or \quad \delta w=0\\ V_1 =&\left(\frac{B_7+c_3A}{2}\right)\left(\frac{\partial \psi}{\partial x}\right)-\frac{B_8}{2}\left(\frac{\partial^3 \psi}{\partial x^3}\right)\\ &+\left(B_5-\frac{c_3A}{2}\right)\left(\frac{\partial^2 w}{\partial x^2}\right)-B_6\left(\frac{\partial^4 w}{\partial x^4}\right) \qquad or \quad \delta\left(\frac{\partial w}{\partial x}\right)=0\\ V_2 =&-\frac{c_3A}{2}\psi+\frac{B_8}{2}\left(\frac{\partial^2 \psi}{\partial x^2}\right)+\frac{c_3A}{2}\left(\frac{\partial w}{\partial x}\right)+B_6\left(\frac{\partial^3 w}{\partial x^3}\right) \qquad or \quad \delta\left(\frac{\partial w}{\partial x}\right)=0\end{aligned} \tag{3.10}$$

At each end-section of the beam, only one type of boundary condition need to be considered. In the special case when the beam is classical continua, parameters a_i, b_i and c_i vanish. Consequently, the two differential equations of motion degenerate to classical theory ones, and only classical parameters V_0 and M_0 stick in the natural boundary conditions.

For parametric study of the complex mechanical behavior, the following dimensionless variables are defined as,

$$\overline{x} = \frac{x}{L}, \quad \overline{w} = \frac{w}{L}, \quad \overline{\omega} = \frac{\omega}{\omega_k}, \quad \tau = \frac{t}{t_k} \tag{3.11}$$

in which, the term

$$\omega_k = \sqrt{\frac{Ak'\mu}{I\rho}}$$

represents the cut-on frequency of the shear wave in the classical theory Timoshenko beam model, k' is the shear constant depending on the shape of cross sections. The normalization parameter for time t is expressed as

$$t_k = \frac{1}{\omega_k} = \sqrt{\frac{I\rho}{Ak'\mu}}$$

With the newly defined variables, the normalized equations of motion can be derived as,

$$\begin{aligned} -\psi + \left(\frac{B_1 - 2c_2A - Ac_3}{\mu AL^2}\right)\left(\frac{\partial^2\psi}{\partial\overline{x}^2}\right) + \left(\frac{B_4 - B_2}{\mu AL^4}\right)\left(\frac{\partial^4\psi}{\partial\overline{x}^4}\right) + \frac{B_3}{\mu AL^6}\frac{\partial^6\psi}{\partial\overline{x}^6} \\ + \frac{\partial\overline{w}}{\partial\overline{x}} + \left(\frac{B_7 + 2\left(c_2 + c_3\right)A}{2\mu AL^2}\right)\left(\frac{\partial^3\overline{w}}{\partial\overline{x}^3}\right) - \frac{B_8}{2\mu AL^4}\frac{\partial^5\overline{w}}{\partial\overline{x}^5} = \frac{m_2}{\mu A{t_k}^2}\frac{\partial^2\psi}{\partial\tau^2} \end{aligned} \tag{3.12a}$$

$$\begin{aligned} -\left(\frac{\partial\psi}{\partial\overline{x}}\right) - \left(\frac{B_7 + 2\left(c_3 + c_2\right)A}{2\mu AL^2}\right)\left(\frac{\partial^3\psi}{\partial\overline{x}^3}\right) + \frac{B_8}{2\mu AL^4}\left(\frac{\partial^5\psi}{\partial\overline{x}^5}\right) + \left(\frac{\partial^2\overline{w}}{\partial\overline{x}^2}\right) \\ + \left(\frac{c_3A - B_5}{\mu AL^2}\right)\left(\frac{\partial^4\overline{w}}{\partial\overline{x}^4}\right) + \frac{B_6}{\mu AL^4}\left(\frac{\partial^6\overline{w}}{\partial\overline{x}^6}\right) + \overline{q} = \frac{m_0L^2}{\mu A{t_k}^2}\left(\frac{\partial^2\overline{w}}{\partial t^2}\right) \end{aligned} \tag{3.12b}$$

in which $\overline{q} = qL/\mu A$ is the dimensionless body load intensity. With the same method, we can obtain the dimensionless boundary conditions as,

$$\begin{aligned} \overline{M}_0 =& \frac{\left(B_1 - A\left(c_2 + \frac{c_3}{2}\right)\right)}{\mu AL^2}\left(\frac{\partial\psi}{\partial\overline{x}}\right) + \frac{\left(B_4 - B_2\right)}{\mu AL^4}\left(\frac{\partial^3\psi}{\partial\overline{x}^3}\right) + \frac{B_3}{\mu AL^6}\left(\frac{\partial^5\psi}{\partial\overline{x}^5}\right) \\ &+ \frac{\left(\frac{B_7}{2} + A\left(c_2 + \frac{c_3}{2}\right)\right)}{\mu AL^2}\left(\frac{\partial^2\overline{w}}{\partial\overline{x}^2}\right) - \frac{B_8}{2\mu AL^4}\left(\frac{\partial^4\overline{w}}{\partial\overline{x}^4}\right) \qquad or \quad \delta\overline{\psi} = 0 \\ \overline{M}_1 =& \frac{A}{\mu AL^2}\left(c_2 + \frac{c_3}{2}\right)\psi + \frac{\left(B_2 - \frac{B_4}{2}\right)}{\mu AL^4}\left(\frac{\partial^2\psi}{\partial\overline{x}^2}\right) - \frac{B_3}{\mu AL^6}\left(\frac{\partial^4\psi}{\partial\overline{x}^4}\right) \\ &- \left(\frac{c_3}{2} + c_2\right)\frac{A}{\mu AL^2}\left(\frac{\partial\overline{w}}{\partial\overline{x}}\right) + \frac{B_8}{2\mu AL^4}\left(\frac{\partial^3\overline{w}}{\partial\overline{x}^3}\right) \qquad or \quad \delta\left(\frac{\partial^2\overline{\psi}}{\partial\overline{x}^2}\right) = 0 \\ \overline{M}_2 =& \frac{B_4}{2\mu AL^4}\left(\frac{\partial\psi}{\partial\overline{x}}\right) + \frac{B_3}{\mu AL^6}\left(\frac{\partial^3\psi}{\partial\overline{x}^3}\right) \qquad or \quad \delta\left(\frac{\partial^2\overline{\psi}}{\partial\overline{x}^2}\right) = 0 \end{aligned}$$

$$
\begin{aligned}
\overline{V}_0 =& -\psi - \frac{\left(\frac{B_7}{2} + (c_3 + c_2)\, A\right)}{\mu A L^2}\left(\frac{\partial^2 \overline{w}}{\partial \overline{x}^2}\right) + \frac{B_8}{2\mu A L^4}\left(\frac{\partial^4 \psi}{\partial \overline{x}^4}\right) + \left(\frac{\partial \overline{w}}{\partial \overline{x}}\right) \\
&+ \frac{(c_3 A - B_5)}{\mu A L^2}\left(\frac{\partial^3 \overline{w}}{\partial \overline{x}^3}\right) + \frac{B_6}{\mu A L^4}\left(\frac{\partial^5 \overline{w}}{\partial \overline{x}^5}\right) \qquad\qquad or \quad \delta \overline{w} = 0 \\
\overline{V}_1 =& \left(\frac{B_7 + c_3 A}{2\mu A L^2}\right)\left(\frac{\partial \psi}{\partial \overline{x}}\right) - \frac{B_8}{2\mu A L^4}\left(\frac{\partial^3 \psi}{\partial \overline{x}^3}\right) + \frac{(B_5 - c_3 A)}{\mu A L^2}\left(\frac{\partial^2 \overline{w}}{\partial \overline{x}^2}\right) \\
&- \frac{B_6}{\mu A L^4}\left(\frac{\partial^4 \overline{w}}{\partial \overline{x}^4}\right) \qquad\qquad or \quad \delta\left(\frac{\partial \overline{w}}{\partial \overline{x}}\right) = 0 \\
\overline{V}_2 =& -\frac{c_3 A}{2\mu A L^2}\psi + \frac{B_8}{2\mu A L^4}\left(\frac{\partial^2 \psi}{\partial \overline{x}^2}\right) + \frac{c_3 A}{2\mu A L^2}\left(\frac{\partial \overline{w}}{\partial \overline{x}}\right) + \frac{B_6}{\mu A L^4}\left(\frac{\partial^3 \overline{w}}{\partial \overline{x}^3}\right) \\
&\qquad\qquad or \quad \delta\left(\frac{\partial^2 \overline{w}}{\partial \overline{x}^2}\right) = 0
\end{aligned}
\tag{3.13}
$$

3.2.2 Dispersion relation

For the material with heterogeneity due to micro-structures effects, the classical elasticity theory is not capable of describing their deformation behaviour and capturing their wave dispersion properties especially when the wavelength is of the same order with the heterogeneity. In this section, the dispersion relation of the waves propagating in complex Timoshenko beam is investigated based on the proposed SSG theory-based model.

Assuming the external loading $\overline{q} = 0$, the free wave propagation modes in the proposed model can be achieved by substituting the general exponential form of wave propagation solution:

$$
\begin{aligned}
w(x,t) &= \widetilde{w}_0 e^{i(\omega t - kx)} \\
\psi(x,t) &= \widetilde{\psi}_0 e^{i(\omega t - kx)}
\end{aligned}
\tag{3.14}
$$

into the governing equations, then we obtain

$$
\begin{aligned}
\mathcal{R}\widetilde{\psi}_0 + \mathcal{S}\widetilde{w}_0 &= 0, \\
\mathcal{S}\widetilde{\psi}_0 + \mathcal{T}\widetilde{w}_0 &= 0,
\end{aligned}
\tag{3.15}
$$

in which,

$$
\begin{aligned}
\mathcal{R} &= -B_3 k^6 + (-B_2 + B_4)\, k^4 + (2\, Ac_2 + Ac_3 - B_1)\, k^2 + m_2 \omega^2 - \mu A, \\
\mathcal{S} &= \frac{B_8}{2} i k^5 + \left(\frac{B_7}{2} + Ac_2 + Ac_3\right) i k^3 - i \mu A k, \\
\mathcal{T} &= B_6 k^6 + (-Ac_3 + B_5)\, k^4 + \mu A k^2 - m_0 \omega^2.
\end{aligned}
$$

In order to have nontrivial solutions for $\widetilde{\psi}_0$ and $\widetilde{w}_0$ in Eq. (3.15), the determinant of coefficients must be zero. Therefore, one $12th$-order function of k is obtained as the dispersion relation for the SSG theory-based Timoshenko beam model in Eq. 3.16,

$$
k_{12} k^{12} + k_{10} k^{10} + k_8 k^8 + k_6 k^6 + k_4 k^4 + k_2 k^2 + k_0 = 0 \tag{3.16}
$$

in which,

$$
\begin{aligned}
k_{12} &= -B_3 B_6, \\
k_{10} &= \frac{{B_8}^2}{4} - B_3 B_5 + (B_4 - B_2) B_6 + c_3 A B_3, \\
k_8 &= B_4 B_5 - B_2 B_5 - B_1 B_6 + \frac{B_7 B_8}{2} + c_3 A (B_2 - B_4 + B_6 + B_8) + 2c_2 A B_6 + c_2 A B_8 - \mu A B_3, \\
k_6 &= \frac{{B_7}^2}{4} + A^2 {c_2}^2 - B_1 B_5 + c_2 A (2B_5 + B_7) + c_3 A (B_1 + B_5 + B_7) - \mu A (B_2 - B_4 + B_6 - B_8) \\
&\quad + \omega^2 (B_3 m_0 + B_6 m_2), \\
k_4 &= m_0 \omega^2 (B_2 - B_4) + m_2 \omega^2 (B_5 - c_3 A) - \mu A (B_5 + B_7 + B_1), \\
k_2 &= m_0 \omega^2 \left(B_1 - 2c_2 A - c_3 A + \frac{m_2}{m_0} \mu A \right), \\
k_0 &= m_0 \omega^2 \left(\mu A - m_2 \omega^2 \right).
\end{aligned}
$$

For parametric study, wavenumber should be normalized with $\overline{k} = kL$, then the normalized dispersion relation can be displayed as,

$$\overline{k}_{12} \overline{k}^{12} + \overline{k}_{10} \overline{k}^{10} + \overline{k}_8 \overline{k}^8 + \overline{k}_6 \overline{k}^6 + \overline{k}_4 k^4 + \overline{k}_2 \overline{k}^2 + \overline{k}_0 = 0 \tag{3.17}$$

in which,

$$
\begin{aligned}
\overline{k}_{12} &= -\frac{1}{L^{10}} B_3 B_6 \\
\overline{k}_{10} &= \frac{1}{L^8} \left(\tfrac{{B_8}^2}{4} + B_4 B_6 + c_3 A B_3 - B_3 B_5 - B_2 B_6 \right) \\
\overline{k}_8 &= \frac{1}{L^6} \left[B_4 B_5 - B_2 B_5 - B_1 B_6 + \frac{B_7 B_8}{2} + c_3 A (B_2 - B_4 + B_6 + B_8) + 2c_2 A B_6 + c_2 A B_8 - \mu A B_3 \right] \\
\overline{k}_6 &= \frac{1}{L^4} \left[\frac{{B_7}^2}{4} + A^2 {c_2}^2 - B_1 B_5 + 2c_2 A B_5 + c_2 A B_7 + c_3 A (B_1 + B_5 + B_7) \right] \\
&\quad - \frac{\mu A}{L^4} (B_2 - B_4 + B_6 - B_8) + \frac{\omega^2}{{t_k}^2 L^4} (B_3 m_0 + B_6 m_2) \\
\overline{k}_4 &= \frac{m_0 \omega^2}{{t_k}^2 L^2} (B_2 - B_4) + \frac{m_2 \omega^2}{{t_k}^2 L^2} (B_5 - c_3 A) - \frac{\mu A}{L^2} (B_5 + B_7 + B_1) \\
\overline{k}_2 &= \frac{m_0 \omega^2}{{t_k}^2} \left(B_1 - 2c_2 A - c_3 A + \mu A \frac{m_2}{m_0} \right), \\
\overline{k}_0 &= \frac{m_0 \omega^2 L^2}{{t_k}^2} \left(\mu A - m_2 \omega^2 \right)
\end{aligned}
$$

The dispersion relation of classical Timoshenko beam is 4th order, and 4 modes (2 positive going and 2 negative going) can be generated for the free wave propagation in structure. On contrast, SSG theory dispersion relation is 12th order, which indicates 12 wave modes (k_i) can be generated on each frequency (ω), 6 positive going modes and 6 negative going modes.

In the following, one case is studied to investigate the complex wave propagation behaviours in Timoshenko beam based on SSG theory model. The structure of the beam is shown as in Figure 3.1. The material is assumed to be aluminum with

$\mu = 26\,\text{GPa}$, and the higher-order material constant values are given in Table 2.1. The beam's cross section is considered to be rectangular with width $b = 3h$, length $L = 5h$, and height of the section $h = 10a_0$, with the lattice parameter $a_0 = 4.04\text{Å}$.

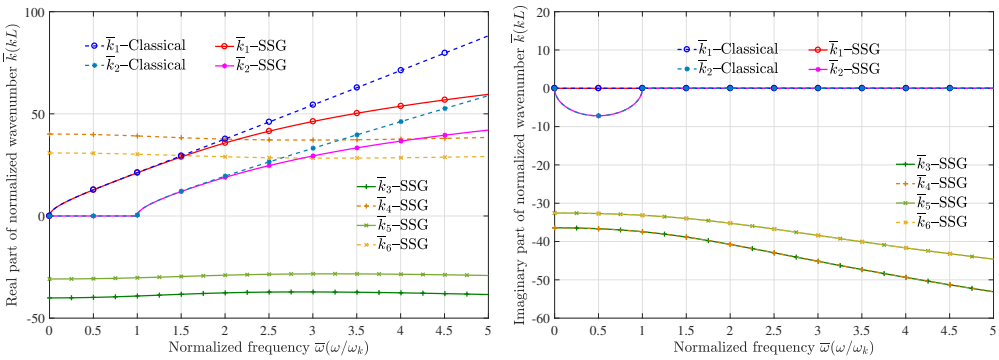

(a) Real part (b) Imaginary part

Figure 3.2: Dispersion relation of positive going waves k^+

Figure 3.2 display the comparison of dispersion curves of the positive going waves resulting from SSG theory model and classical model. As been noted before, the positive- or negative-going waves can have arbitrary Real (k) sign. The direction of propagation is defined by the Imag (k), which corresponds to the wave attenuation. Thus wave k_3 and k_5, with negative imaginary part and negative real part are considered as positive-going waves.

Figure 3.2 has two subfigures, fig. 3.2(a) and fig. 3.2(b), which respectively show the real parts and imaginary parts of the dimensionless wavenumbers positive-going waves in frequency range $0 \leq \varpi \leq 5$. Different from the dispersion relation of classical theory beam, 6 wave modes $(k_1, k_2, k_3, k_4, k_6, k_6)$ are generated in complex beam with the SSG theory model. k_1-SSG is non-classical bending wave, k_2-SSG is non-classical shear waves. k_3, k_4, k_5 and k_6 are the evanescent waves which exist exclusively in SSG theory model. The non-classical bending wave k_1-SSG and shear wave k_2–SSG propagate in dispersive manners. Compared with k_1-Classical and k_2-Classical, wavenumber of k_1-SSG and k_2-SSG are less on each frequency especially in higher frequency, thus in higher frequency range, waves propagation in complex media exhibits longer spatial periodicity character on the same frequency. In addition, the other 4 evanescent waves k_3, k_4, k_5 and k_6 are predicted exclusively in SSG theory model. k_3 and k_4 are real part conjugate, so do k_5 and k_6. These four waves decay to zero in a very close range. They do not transport energy to far field but they do affect energy transfer in the near field.

In order to confirm the size-effect of the dispersive feature, dispersion curves of non-classical bending wave k_1-SSG in Timoshenko beams of different size and same geometrical shape are investigated. The results are illustrated in Figure 3.3

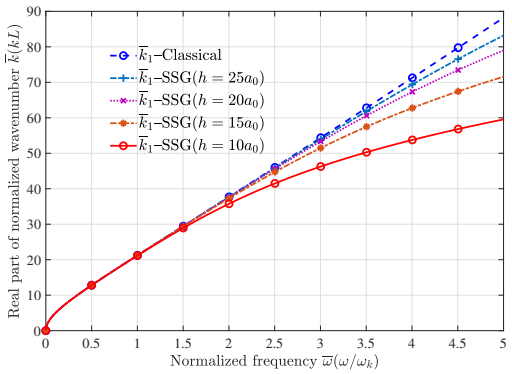

Figure 3.3: Bending wave dispersion curves changing with dimension

Figure 3.3 displays the comparison of the dispersion curves for classical bending wave k_1-Classical and non-classical bending wave k_1-SSG in Timoshenko beams with section height h increasing from $10a_0$ to $25a_0$. Since the geometrical shape of the structure is unchanged, the resulting classical dispersion curve is size independent. Whereas the non-classical dispersion curves are observed to exhibit size dependent feature as the dimension increase.As the structural characteristic length increase and external wavelength being invariant, the influence of long range micro-structure interaction diminish evidently, so we can predict that the non-classical dispersion curve will converge to the classical one in structure with fairly large dimension.

The above wave propagation features are calculated without damping in the system. In practical applications, energy dissipation by damping effect can affect wave propagation features significantly. In the case of hysteretic damping, $E = 52\,(1 + i\zeta)$ GPa is assumed with ζ indicating the loss factor of the system. The real part of the resulting dispersion curves will not be influenced, while the imaginary part representing energy dissipation will be affected significantly. To analyze the damping effect on wave propagation feature in complex Timoshenko beam, the imaginary parts of bending wave k_1 and shear wave k_2 with $\zeta = 0.01$ are shown in Figure 3.4.

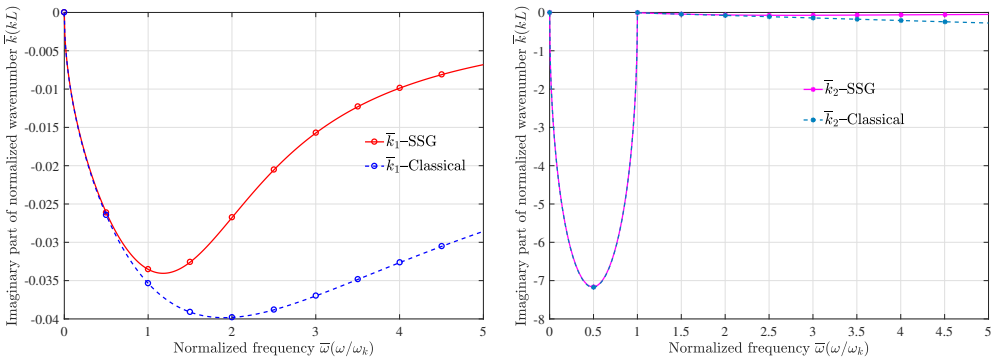

(a) Bending wave (b) Shear wave

Figure 3.4: Dispersion curves influenced by damping

In lower frequency range $0 \leq \bar{\omega} \leq 1$, the result of Im($k_i$)-Classical and Im($k_i$)-SSG match well for both bending wave and shear wave. In higher frequency range $[1 \leq \overline{\omega} \leq 5]$, |Im($k_i$)|-SSG shows great difference by decreasing distinctly compared with |Im(k_i)|-Classical. If only consider these two waves, energy dissipation through viscous damping become negligible compared with the classical model.

3.2.3 Modal density

The definition and physical meaning of modal density has been described in Sec.2.2.3, here no longer details. In the proposed Timoshenko beam model, only non-classical bending wave k_1-SSG and shear wave k_2-SSG can travel in long distance and transfer energy in the media. Hence in this section, modal density of these two waves are analyzed to study the statistic distribution of resonances of complex Timoshenko beam in higher frequency range. As has been shown in Sec. 2.2.3, modal density can be expressed as

$$n(\omega) = \frac{dN}{d\omega} = \frac{dN}{dk}\frac{dk}{d\omega} = \frac{L}{\pi}\frac{1}{c_g}. \tag{3.18}$$

in which, the term c_g denotes the group velocity of the studied wave mode

$$c_g = \frac{d\omega}{dk}.$$

In this case, modal density of bending wave and shear wave can be calculated separately based on the group velocity of each wave mode. With the normalizing variables defined in Eq. (3.11), the normalized modal density can be expressed as

$$\overline{n}(\overline{\omega}) = \frac{1}{\pi}\frac{d\overline{k}}{d\overline{\omega}} = \frac{1}{\pi}\frac{1}{\overline{c}_g}. \tag{3.19}$$

The result of the studied case is shown as follows.

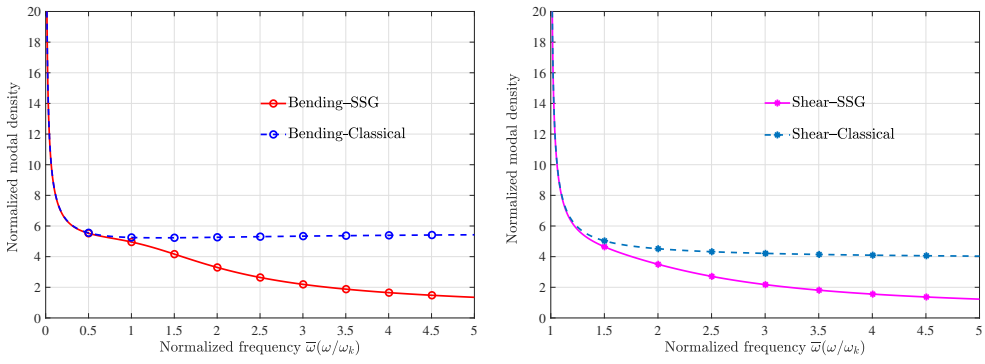

(a) Bending wave (b) Shear wave

Figure 3.5: Modal density of bending wave and shear wave

As shown in Figure 3.5, Fig.beam 3.5(a) and Fig.beam 3.5(b) respectively depict the modal density of non-classical bending wave and non-classical shear wave.

To be noted here, the studied frequency range of shear wave is $1 \leq \bar{\omega} \leq 5$ because the shear wave propagate only above the cut-on frequency ($\bar{\omega} > 1$). In higher frequency, the obtained modal density from SSG theory model declines distinctly compared with the classical one, which indicates the expected number of resonant frequencies is much less than classical result in the same frequency range. This difference is originated from the influence of long range interaction between underlying micro-structures. In higher frequency, wavelength becomes more comparable to the characteristic length of the structure, thus the influence of internal micro-structures will be more distinct.

3.2.4 Energy flux analysis

Based on Sec. 3.2.2, we known that the input energy flow can be transferred into all the six wave modes generated in complex Timoshenko beam. For further exploration, the expression of energy velocity at one point in the complex Timoshenko beam is presented in this section. Refer to Eq. (3.4), the time averaged kinetic energy and potential energy through the observed cross section A of SSG theory-based Timoshenko beam can be expressed as,

$$
\begin{aligned}
\langle \mathrm{T} \rangle &= \frac{\rho}{4} \int_A \left[\mathrm{Re}\left(\dot{w} \cdot \dot{w}^*\right) + z^2 \cdot \mathrm{Re}\left(\dot{\psi} \cdot \dot{\psi}^*\right) \right] dA, \\
\langle \mathrm{U} \rangle &= \frac{1}{4} \mathrm{Re} \left[B_1 \left(\frac{\partial \psi}{\partial x}\right) \left(\frac{\partial \psi}{\partial x}\right)^* + B_2 \left(\frac{\partial^2 \psi}{\partial x^2}\right) \left(\frac{\partial^2 \psi}{\partial x^2}\right)^* + B_3 \left(\frac{\partial^3 \psi}{\partial x^3}\right) \left(\frac{\partial^3 \psi}{\partial x^3}\right)^* \right. \\
&\quad + B_4 \left(\frac{\partial \psi}{\partial x}\right) \left(\frac{\partial^3 \psi}{\partial x^3}\right)^* + B_5 \left(\frac{\partial^2 w}{\partial x^2}\right) \left(\frac{\partial^2 w}{\partial x^2}\right)^* + B_6 \left(\frac{\partial^3 w}{\partial x^3}\right) \left(\frac{\partial^3 w}{\partial x^3}\right)^* \\
&\quad + B_7 \left(\frac{\partial \psi}{\partial x}\right) \left(\frac{\partial^2 w}{\partial x^2}\right)^* + B_8 \left(\frac{\partial^2 \psi}{\partial x^2}\right) \left(\frac{\partial^3 w}{\partial x^3}\right)^* + \mu A \left(\frac{\partial w}{\partial x} - \psi\right) \left(\frac{\partial w}{\partial x} - \psi\right)^* \\
&\quad \left. - 2c_2 A \left(\frac{\partial w}{\partial x} - \psi\right) \left(\frac{\partial^2 \psi}{\partial x^2}\right)^* + c_3 A \left(\frac{\partial w}{\partial x} - \psi\right) \left(\frac{\partial^3 w}{\partial x^3} - \frac{\partial^2 \psi}{\partial x^2}\right)^* \right].
\end{aligned}
\tag{3.20}
$$

The higher-order stress should also be taken into account when it comes to energy flow. Based on the definition of virtual work in Eq. (3.7), the expression of time averaged active and reactive energy flow through the observation section is assumed in form of Eq. (3.21)

$$
\langle \mathrm{P} \rangle = -\frac{1}{2} \mathrm{Re}\left[\mathbf{S}\right], \qquad \langle \mathrm{Q} \rangle = -\frac{1}{2} \mathrm{Im}\left[\mathbf{S}\right]. \tag{3.21}
$$

where $\mathbf{S}$ denotes the Poynting vector representing directional energy flux of the wave field and has the expression in Eq. (3.22)

$$
\mathbf{S} = V_0 \cdot \dot{w}^* + V_1 \cdot \left(\frac{\partial \dot{w}}{\partial x}\right)^* + V_2 \cdot \left(\frac{\partial^2 \dot{w}}{\partial x^2}\right)^* + M_0 \cdot \dot{\psi}^* + M_1 \cdot \left(\frac{\partial \dot{\psi}}{\partial x}\right)^* + M_2 \cdot \left(\frac{\partial^2 \dot{\psi}}{\partial x^2}\right)^*. \tag{3.22}
$$

V_0, V_1, V_2 and M_0, M_1, and M_2 are the loads dual to the corresponding kinematic parameters. Physically speaking, they share the same expression with the generalized end sectional forces in essential boundary condition, thus they are connected with the displacement field at M position as

$$
\begin{aligned}
V_0 &= -\mu A\psi - \left(\frac{B_7}{2} + (c_3+c_2)\,A\right)\left(\frac{\partial^2 w}{\partial x^2}\right) + \frac{B_8}{2}\left(\frac{\partial^4 \psi}{\partial x^4}\right) \\
&\quad + \mu A\left(\frac{\partial w}{\partial x}\right) + (c_3 A - B_5)\left(\frac{\partial^3 w}{\partial x^3}\right) + B_6\left(\frac{\partial^5 w}{\partial x^5}\right) \\
V_1 &= \left(\frac{B_7 + c_3 A}{2}\right)\left(\frac{\partial \psi}{\partial x}\right) - \frac{B_8}{2}\left(\frac{\partial^3 \psi}{\partial x^3}\right) + (B_5 - c_3 A)\left(\frac{\partial^2 w}{\partial x^2}\right) - B_6\left(\frac{\partial^4 w}{\partial x^4}\right) \\
V_2 &= -\frac{c_3 A}{2}\psi + \frac{B_8}{2}\left(\frac{\partial^2 \psi}{\partial x^2}\right) + \frac{c_3 A}{2}\left(\frac{\partial w}{\partial x}\right) + B_6\left(\frac{\partial^3 w}{\partial x^3}\right) \\
M_0 &= \left(B_1 - A\left(c_2 + \frac{c_3}{2}\right)\right)\left(\frac{\partial \psi}{\partial x}\right) + (B_4 - B_2)\left(\frac{\partial^3 \psi}{\partial x^3}\right) + B_3\left(\frac{\partial^5 \psi}{\partial x^5}\right) \\
&\quad - \frac{B_8}{2}\left(\frac{\partial^4 w}{\partial x^4}\right) + \left(\frac{B_7}{2} + A\,(c_3+c_2)\right)\left(\frac{\partial^2 w}{\partial x^2}\right) \\
M_1 &= A\left(c_2 + \frac{c_3}{2}\right)\psi + \left(B_2 - \frac{B_4}{2}\right)\left(\frac{\partial^2 \psi}{\partial x^2}\right) - B_3\left(\frac{\partial^4 \psi}{\partial x^4}\right) - A\left(\frac{c_3}{2} + c_2\right)\left(\frac{\partial w}{\partial x}\right) \\
&\quad + \frac{B_8}{2}\left(\frac{\partial^3 w}{\partial x^3}\right) \\
M_2 &= \frac{B_4}{2}\left(\frac{\partial \psi}{\partial x}\right) + B_3\left(\frac{\partial^3 \psi}{\partial x^3}\right),
\end{aligned}
$$

'$\dot{w}$' and '$\dot{\psi}$' in Eq. (3.22) denote the time derivative of w and ψ. The energy velocity of the wave propagation equals the time averaged active energy flow $\langle P\rangle$ over the time averaged total energy $\langle W_{total}\rangle$, which can be expressed as

$$
\mathrm{V}_e = \frac{\langle \mathrm{P}\rangle}{\langle W_{total}\rangle} = \frac{\langle \mathrm{P}\rangle}{\langle U\rangle + \langle T\rangle}. \tag{3.23}
$$

With the normalizing variables defined in Eq. (3.11), the normalized energy density and power flow can be expressed as

$$
\langle \overline{\mathrm{T}}\rangle = \frac{\langle \mathrm{T}\rangle}{\mu A}, \quad \langle \overline{\mathrm{U}}\rangle = \frac{\langle \mathrm{U}\rangle}{\mu A}, \quad \langle \overline{\mathrm{P}}\rangle = \frac{\langle \mathrm{P}\rangle \cdot k_t}{\mu A L}, \quad \overline{\mathrm{V}}_e = \frac{\mathrm{V}_e \cdot k_t}{L}, \tag{3.24}
$$

In the following numerical application, the formulation of potential energy density and energy velocity will be validated with the non-classical bending wave and non-classical shear wave. When there is only one conservative wave propagating in the structure, energy velocity V_e obtained by the proposed formulation should be equal with the group velocity of that wave c_g. For the studied structure, the results are illustrated as follows,

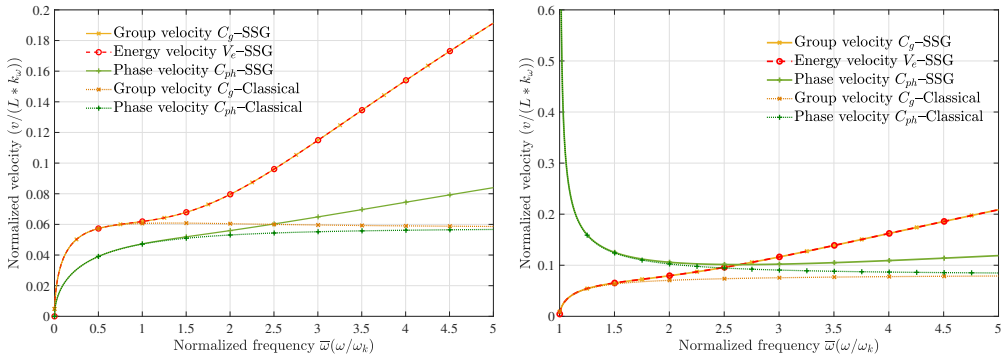

(a) Bending wave (b) Shear wave

Figure 3.6: Energy velocity of bending wave and shear wave

Figure 3.6 depicts the energy velocity V_e, group velocity c_g and phase velocity c_{ph} of SSG theory model and classical they model. ***The formulation of potential energy*** (3.20) ***and energy flux*** (3.21) ***in complex Timoshenko beam based on the SSG theory model are proved to be correct with*** $c_g = \mathrm{V}_e$ ***for both bending wave and shear wave in whole frequency range.***

In addition, we can see the results of this two models match well in low frequency range ($\overline{\omega} < 1$ for bending wave and $\overline{\omega} < 2$ for shear wave). As frequency increase, energy velocities V_e-Classical of both bending wave and shear wave approach to one constant value, whereas energy velocity V_e-SSG of non-classical waves keeps increasing. Therefore, energy velocities of non-classical waves V_e-SSG are larger than the classical ones in higher frequency. In the meantime, phase velocity c_{ph}-SSG is also increasing with frequency and larger than c_{ph}-Classical. The wider gap between C_g-SSG and c_{ph}-SSG in high frequency imply the more distinct dispersive character for both non-classical bending wave and non-classical shear wave propagating in complex beam structure.

3.3 Mobility and impedance of infinite Timoshenko beam

To reveal the dynamic behaviors of complex Timoshenko beam structure, frequency response of infinite beam structure to simple harmonic excitation is analyzed based on the proposed SSG theory model in this section. The impedance and mobility function of an infinite beam are derived using the wave formulation method. Energy input, transfer and dissipation are also studied to have a proper interpretation for the obtained dynamic behaviours.

As shown in Figure 3.7, dynamic response of one infinite beam which is subject to a transverse harmonic force $F = \mathrm{Re}\left\{q_0 e^{i\omega t}\right\}$ at $x = 0$ is studied. The harmonic force $F = q_0 \cdot e^{i\omega t}$ generates free waves in the beam structure, then all waves propagate away from the source to both $+x$ or $-x$ directions. Since the system is symmetrical about $x = 0$, we will concentrate on the positive going waves field which in Figure

3.7 is denoted as region $x > 0$.

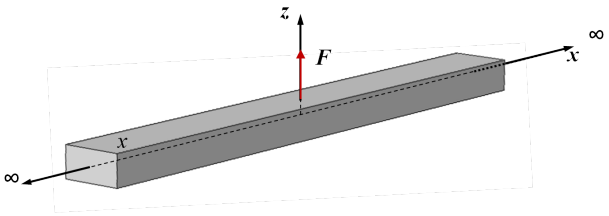

Figure 3.7: An infinite beam with harmonic force excitation.

3.3.1 Derivation of the displacement field based on SSG beam theory

According to section 3.2, the governing equation of free vibration 3.12 applies to all the points on the structure that are not subject to external forces, in this case the driving forces at $x = 0$. At the driving point, shear force suffers a step change equal to the applied harmonic transverse force $F(t)$. One Dirac delta function $\delta(x-0)$ is employed to represent the concentrated force F applied at $x = 0$, hence the governing equation of infinite SSG theory beam subject to harmonic point transverse force $F(t) = \mathrm{Re}(\mathrm{q}_0 \cdot \mathrm{e}^{\mathrm{i}\omega t})$ at $x = 0$ can be expressed as

$$\begin{aligned}\delta w : &- \mu A\left(\frac{\partial \psi}{\partial x}\right) - \left(\frac{B_7}{2} + (c_3 + c_2)\, A\right)\left(\frac{\partial^3 \psi}{\partial x^3}\right) + \frac{B_8}{2}\left(\frac{\partial^5 \psi}{\partial x^5}\right) + \mu A\left(\frac{\partial^2 w}{\partial x^2}\right) \\ &+ (c_3 A - B_5)\left(\frac{\partial^4 w}{\partial x^4}\right) + B_6\left(\frac{\partial^6 w}{\partial x^6}\right) + q_0 \cdot \delta(x) \cdot e^{i\omega t} = m_0\left(\frac{\partial^2 w}{\partial t^2}\right);\end{aligned} \tag{3.25a}$$

$$\begin{aligned}\delta \psi : &- \mu A \psi + (B_1 - c_3 A - 2c_2 A)\left(\frac{\partial^2 \psi}{\partial x^2}\right) + (B_4 - B_2)\left(\frac{\partial^4 \psi}{\partial x^4}\right) + B_3\left(\frac{\partial^6 \psi}{\partial x^6}\right) \\ &+ \mu A\left(\frac{\partial w}{\partial x}\right) + \left(\frac{B_7}{2} + (c_3 + c_2)\, A\right)\left(\frac{\partial^3 w}{\partial x^3}\right) - \frac{B_8}{2}\left(\frac{\partial^5 w}{\partial x^5}\right) = m_2\left(\frac{\partial^2 \psi}{\partial t^2}\right).\end{aligned} \tag{3.25b}$$

Based on the previous analysis, 12 wave modes $\pm k_1$, $\pm k_2$, $\pm k_3$, $\pm k_4$, $\pm k_5$, and $\pm k_6$ can be generated in complex beam structure with the proposed SSG theory model. The negative sign applies for $x < 0$ and the positive sign applies for $x > 0$. Consider that the beam is infinitely extended and the external force is applied at $x = 0$, Eq. (3.9) is valid at every point except that at which the force is applied, therefore solutions to the non-classical infinite continuous structure are employed to satisfy the governing equilibrium and boundary conditions. The general solutions of deflection and rotation in region $x > 0$ and $x < 0$ are given in forms of superposition

of positive going wave modes and negative going waves modes as in Eq. (3.26).

$$
\begin{aligned}
w\left(x^{+},t\right) &= \left(\mathcal{A}_1 e^{-ik_1 x} + \mathcal{B}_1 e^{-ik_2 x} + \mathcal{C}_1 e^{-ik_3 x} + \mathcal{D}_1 e^{-ik_4 x} + \mathcal{E}_1 e^{-ik_5 x} + \mathcal{F}_1 e^{-ik_6 x}\right)\cdot e^{i\omega t};\\
\psi\left(x^{+},t\right) &= \left(\mathcal{G}_1 e^{-ik_1 x} + \mathcal{H}_1 e^{-ik_2 x} + \mathcal{I}_1 e^{-ik_3 x} + \mathcal{J}_1 e^{-ik_4 x} + \mathcal{K}_1 e^{-ik_5 x} + \mathcal{L}_1 e^{-ik_6 x}\right)\cdot e^{i\omega t};
\end{aligned}
\tag{3.26a}
$$

$$
\begin{aligned}
w\left(x^{-},t\right) &= \left(\mathcal{A}_2 e^{ik_1 x} + \mathcal{B}_2 e^{ik_2 x} + \mathcal{C}_2 e^{ik_3 x} + \mathcal{D}_2 e^{ik_4 x} + \mathcal{E}_2 e^{ik_5 x} + \mathcal{F}_2 e^{ik_6 x}\right)\cdot e^{i\omega t}.\\
\psi\left(x^{-},t\right) &= \left(\mathcal{G}_2 e^{ik_1 x} + \mathcal{H}_2 e^{ik_2 x} + \mathcal{I}_2 e^{ik_3 x} + \mathcal{J}_2 e^{ik_4 x} + \mathcal{K}_2 e^{ik_5 x} + \mathcal{L}_2 e^{ik_6 x}\right)\cdot e^{i\omega t};
\end{aligned}
\tag{3.26b}
$$

The expressions of w^{+} and ψ^{+} represent the vibration of deflection and rotation in region $x > 0$, and w^{-}, ψ^{-} in $x < 0$. The subscripts 1 and 2 distinguish the amplitudes of waves propagating on the right of force excitation and on the left of force excitation. Since the system is symmetrical about the driving force position $x = 0$, for arbitrary point $x = x_0$, the transverse displacement $w(x_0, t)$ should equal $w\left(-x_0, t\right)$, and rotation angle $\psi(x_0, t)$ should be opposite to $\psi(-x_0, t)$ on the whole frequency range. Therefore the coefficient of each term $e^{-ik_i x+i\omega t}$ in expression (3.26a) and the coefficient of the term $e^{ik_i x+i\omega t}$ in expression (3.26b) should take the following relation

$$
\begin{aligned}
&\mathcal{A}_1 = \mathcal{A}_2, \quad \mathcal{B}_1 = \mathcal{B}_2, \quad \mathcal{C}_1 = \mathcal{C}_2, \quad \mathcal{D}_1 = \mathcal{D}_2, \quad \mathcal{E}_1 = \mathcal{E}_2, \quad \mathcal{F}_1 = \mathcal{F}_2,\\
&\mathcal{G}_1 = -\mathcal{G}_2,\ \mathcal{H}_1 = -\mathcal{H}_2,\ \mathcal{I}_1 = -\mathcal{I}_2,\ \mathcal{J}_1 = -\mathcal{J}_2,\ \mathcal{K}_1 = -\mathcal{K}_2,\ \mathcal{L}_1 = -\mathcal{L}_2,
\end{aligned}
$$

Then the solution given in 3.26b is simplified as

$$
\begin{aligned}
w\left(x^{-},t\right) &= \left(\mathcal{A}_1 e^{ik_1 x} + \mathcal{B}_1 e^{ik_2 x} + \mathcal{C}_1 e^{ik_3 x} + \mathcal{D}_1 e^{ik_4 x} + \mathcal{E}_1 e^{ik_5 x} + \mathcal{F}_1 e^{ik_6 x}\right)\cdot e^{i\omega t};\\
\psi\left(x^{-},t\right) &= \left(-\mathcal{G}_1 e^{ik_1 x} - \mathcal{H}_1 e^{ik_2 x} - \mathcal{I}_1 e^{ik_3 x} - \mathcal{J}_1 e^{ik_4 x} - \mathcal{K}_1 e^{ik_5 x} - \mathcal{L}_1 e^{ik_6 x}\right)\cdot e^{i\omega t};
\end{aligned}
\tag{3.27}
$$

The number of unknown variables are narrowed down to 12. From the dispersion relation, which is obtained by the governing equation in section 3.2.2, all the wavenumbers k_1, k_2, k_3, k_4, k_5, and k_6 on each frequency can be obtained. Then the value of the displacement w and rotation ψ on that frequency only depend on the unknown amplitudes of each wave mode. The general solution of w^{+} and ψ^{+} (3.26a) should be valid to the enriched governing equations 3.25 for any point $x > 0$ on the structure on any frequency. Substitute the solution in Eq. 3.26a into the governing equation, the coefficient of each term $e^{-ik_i x+i\omega t}$ should equal zero, which yields the amplitudes of each mode constituting w and ψ follows the principle in

Eq. (3.28)

$$\begin{aligned}
\mathcal{G}_1 &= \frac{-2i\left(-B_6{k_1}^6 + c_3A{k_1}^4 - B_5{k_1}^4 - \mu A{k_1}^2 + m_0\omega^2\right)}{k_1\left(B_8{k_1}^4 + 2c_2A{k_1}^2 + 2c_3A{k_1}^2 + B_7{k_1}^2 - 2\mu A\right)}\mathcal{A}_1;\\
\mathcal{H}_1 &= \frac{-2i\left(-B_6{k_2}^6 + c_3A{k_2}^4 - B_5{k_2}^4 - \mu A{k_2}^2 + m_0\omega^2\right)}{k_2\left(B_8{k_2}^4 + 2c_2A{k_2}^2 + 2c_3A{k_2}^2 + B_7{k_2}^2 - 2\mu A\right)}\mathcal{B}_1;\\
\mathcal{I}_1 &= \frac{-2i\left(-B_6{k_3}^6 + c_3A{k_3}^4 - B_5{k_3}^4 - \mu A{k_3}^2 + m_0\omega^2\right)}{k_3\left(B_8{k_3}^4 + 2c_2A{k_3}^2 + 2c_3A{k_3}^2 + B_7{k_3}^2 - 2\mu A\right)}\mathcal{C}_1;\\
\mathcal{J}_1 &= \frac{-2i\left(-B_6{k_4}^6 + c_3A{k_4}^4 - B_5{k_4}^4 - \mu A{k_4}^2 + m_0\omega^2\right)}{k_4\left(B_8{k_4}^4 + 2c_2A{k_4}^2 + 2c_3A{k_4}^2 + B_7{k_4}^2 - 2\mu A\right)}\mathcal{D}_1;\\
\mathcal{K}_1 &= \frac{-2i\left(-B_6{k_5}^6 + c_3A{k_5}^4 - B_5{k_5}^4 - \mu A{k_5}^2 + m_0\omega^2\right)}{k_5\left(B_8{k_5}^4 + 2c_2A{k_5}^2 + 2c_3A{k_5}^2 + B_7{k_5}^2 - 2\mu A\right)}\mathcal{E}_1;\\
\mathcal{L}_1 &= \frac{-2i\left(-B_6{k_6}^6 + c_3A{k_6}^4 - B_5{k_6}^4 - \mu A{k_6}^2 + m_0\omega^2\right)}{k_6\left(B_8{k_6}^4 + 2c_2A{k_6}^2 + 2c_3A{k_6}^2 + B_7{k_6}^2 - 2\mu A\right)}\mathcal{F}_1;
\end{aligned} \tag{3.28}$$

The governing equations and the above equilibrium are not sufficient to solve the described problem, boundary condition at $x = 0$ is required. Assuming the first order shear force produced on the left-hand end of an elemental beam section $x = 0^-$ is upward, and on the right-hand $x = 0^+$ is downward, if the applied force is considered to be positive, and the mass of the beam between $x = 0^+$ and $x = 0^-$ is infinitesimal, the general solution in Eqs. (3.26a) and (3.27) should satisfy the all the equilibrium conditions at infinitesimally small distances to the left and right of $x = 0$, at $x = 0^-$ and $x = 0^+$. Firstly, shear force equilibrium equations can be applied at $x = 0$ as,

$$V_0|_{x=0^-} - V_0|_{x=0^+} + F = 0 \tag{3.29}$$

in which the force ${V_0}^{0^+}$ and ${V_0}^{0^-}$ respectively equal the loads at the $x = 0$ section dual to the kinematic parameter δw generated by the right-hand end deformation and left-hand end deformation.

$$\begin{aligned}
{V_0}^{0^-} =& -\mu A\psi_{0^-} - \left(\frac{B_7}{2} + (c_3 + c_2)\,A\right)\left(\frac{\partial^2 w_{0^-}}{\partial x^2}\right) + \frac{B_8}{2}\left(\frac{\partial^4 \psi_{0^-}}{\partial x^4}\right) + \mu A\left(\frac{\partial w_{0^-}}{\partial x}\right)\\
&+ (c_3A - B_5)\left(\frac{\partial^3 w_{0^-}}{\partial x^3}\right) + B_6\left(\frac{\partial^5 w_{0^-}}{\partial x^5}\right)\\
{V_0}^{0^+} =& -\mu A\psi_{0^+} - \left(\frac{B_7}{2} + (c_3 + c_2)\,A\right)\left(\frac{\partial^2 w_{0^+}}{\partial x^2}\right) + \frac{B_8}{2}\left(\frac{\partial^4 \psi_{0^+}}{\partial x^4}\right) + \mu A\left(\frac{\partial w_{0^+}}{\partial x}\right)\\
&+ (c_3A - B_5)\left(\frac{\partial^3 w_{0^+}}{\partial x^3}\right) + B_6\left(\frac{\partial^5 w_{0^+}}{\partial x^5}\right)
\end{aligned}$$

Since the applied force affects neither first higher order force, nor the second higher order force, the higher order forces is continuous through $x = 0$ as,

$${V_1}^{0^-} = {V_1}^{0^+}, \quad {V_2}^{0^-} = {V_2}^{0^+}; \tag{3.30}$$

in which the force ${V_1}^{0^+}$, ${V_1}^{0^-}$ and ${V_2}^{0^+}$ ${V_2}^{0^-}$ respectively equal the loads at the $x = 0$ section dual to the kinematic parameter $\delta\left(\frac{\partial w}{\partial x}\right)$ and $\delta\left(\frac{\partial^2 w}{\partial x^2}\right)$ generated by the right-hand end deformation and left-hand end deformation.

$$
\begin{aligned}
{V_1}^{0^-} =& \left(\frac{B_7 + c_3 A}{2}\right)\left(\frac{\partial \psi_{0^-}}{\partial x}\right) - \frac{B_8}{2}\left(\frac{\partial^3 \psi_{0^-}}{\partial x^3}\right) + (B_5 - c_3 A)\left(\frac{\partial^2 w_{0^-}}{\partial x^2}\right) - B_6\left(\frac{\partial^4 w_{0^-}}{\partial x^4}\right) \\
{V_1}^{0^+} =& \left(\frac{B_7 + c_3 A}{2}\right)\left(\frac{\partial \psi_{0^+}}{\partial x}\right) - \frac{B_8}{2}\left(\frac{\partial^3 \psi_{0^+}}{\partial x^3}\right) + (B_5 - c_3 A)\left(\frac{\partial^2 w_{0^+}}{\partial x^2}\right) - B_6\left(\frac{\partial^4 w_{0^+}}{\partial x^4}\right) \\
{V_2}^{0^-} =& -\frac{c_3 A}{2}\psi_{0^-} + \frac{B_8}{2}\left(\frac{\partial^2 \psi_{0^-}}{\partial x^2}\right) + \frac{c_3 A}{2}\left(\frac{\partial w_{0^-}}{\partial x}\right) + B_6\left(\frac{\partial^3 w_{0^-}}{\partial x^3}\right) \\
{V_2}^{0^+} =& -\frac{c_3 A}{2}\psi_{0^+} + \frac{B_8}{2}\left(\frac{\partial^2 \psi_{0^+}}{\partial x^2}\right) + \frac{c_3 A}{2}\left(\frac{\partial w_{0^+}}{\partial x}\right) + B_6\left(\frac{\partial^3 w_{0^+}}{\partial x^3}\right).
\end{aligned}
$$

The moments continuity should also be valid for the moment M_0, the first higher order moment M_1 and the second higher order moment M_2 through $x = 0$ as,

$$
{M_0}^{0^-} = {M_0}^{0^+},\ {M_1}^{0^+} = {M_1}^{0^+},\ {M_2}^{0^+} = {M_2}^{0^+}. \tag{3.31}
$$

and the moments and higher order moments can be expressed by $w_{0^\pm}$ and $\psi_{0^\pm}$ as

$$
\begin{aligned}
{M_0}^{0^-} =& \left(B_1 - A\left(c_2 + \frac{c_3}{2}\right)\right)\left(\frac{\partial \psi_{0^-}}{\partial x}\right) + (B_4 - B_2)\left(\frac{\partial^3 \psi_{0^-}}{\partial x^3}\right) + B_3\left(\frac{\partial^5 \psi_{0^-}}{\partial x^5}\right) \\
&+ \left(\frac{B_7}{2} + A\left(c_3 + c_2\right)\right)\left(\frac{\partial^2 w_{0^-}}{\partial x^2}\right) - \frac{B_8}{2}\left(\frac{\partial^4 w_{0^-}}{\partial x^4}\right) \\
{M_0}^{0^+} =& \left(B_1 - A\left(c_2 + \frac{c_3}{2}\right)\right)\left(\frac{\partial \psi_{0^+}}{\partial x}\right) + (B_4 - B_2)\left(\frac{\partial^3 \psi_{0^+}}{\partial x^3}\right) + B_3\left(\frac{\partial^5 \psi_{0^+}}{\partial x^5}\right) \\
&+ \left(\frac{B_7}{2} + A\left(c_3 + c_2\right)\right)\left(\frac{\partial^2 w_{0^+}}{\partial x^2}\right) - \frac{B_8}{2}\left(\frac{\partial^4 w_{0^+}}{\partial x^4}\right) \\
{M_1}^{0^-} =& A\left(c_2 + \frac{c_3}{2}\right)\psi_{0^-} + \left(B_2 - \frac{B_4}{2}\right)\left(\frac{\partial^2 \psi_{0^-}}{\partial x^2}\right) - B_3\left(\frac{\partial^4 \psi_{0^-}}{\partial x^4}\right) \\
&- A\left(\frac{c_3}{2} + c_2\right)\left(\frac{\partial w_{0^-}}{\partial x}\right) + \frac{B_8}{2}\left(\frac{\partial^3 w_{0^-}}{\partial x^3}\right) \\
{M_1}^{0^+} =& A\left(c_2 + \frac{c_3}{2}\right)\psi_{0^+} + \left(B_2 - \frac{B_4}{2}\right)\left(\frac{\partial^2 \psi_{0^+}}{\partial x^2}\right) - B_3\left(\frac{\partial^4 \psi_{0^+}}{\partial x^4}\right) \\
&- A\left(\frac{c_3}{2} + c_2\right)\left(\frac{\partial w_{0^+}}{\partial x}\right) + \frac{B_8}{2}\left(\frac{\partial^3 w_{0^+}}{\partial x^3}\right) \\
{M_2}^{0^-} =& \frac{B_4}{2}\left(\frac{\partial \psi_{0^-}}{\partial x}\right) + B_3\left(\frac{\partial^3 \psi_{0^-}}{\partial x^3}\right) \\
{M_2}^{0^+} =& \frac{B_4}{2}\left(\frac{\partial \psi_{0^+}}{\partial x}\right) + B_3\left(\frac{\partial^3 \psi_{0^+}}{\partial x^3}\right)
\end{aligned}
$$

All the coefficients in Eq. (3.26) must also take values that satisfy all kinetic parameters continuous conditions at $x = 0$, which includes not only the displacements

and rotation continuity, but also the extra kinetic parameters defined in the SSG theory-based model as,

$$\begin{aligned} w_{0^-} &= w_{0^+},\ \frac{\partial w_{0^-}}{\partial x} = \frac{\partial w_{0^+}}{\partial x},\ \frac{\partial^2 w_{0^-}}{\partial x^2} = \frac{\partial^2 w_{0^+}}{\partial x^2}; \\ \psi_{0^-} &= \psi_{0^+},\ \frac{\partial \psi_{0^-}}{\partial x} = \frac{\partial \psi_{0^+}}{\partial x},\ \frac{\partial^2 \psi_{0^-}}{\partial x^2} = \frac{\partial^2 \psi_{0^+}}{\partial x^2}; \end{aligned} \tag{3.32}$$

Substitute solutions in Eqs. (3.26a) and (3.27) into the boundary conditions Eqs. (3.29)– (3.32), we find that half of the conditions are naturally satisfied because of the symmetrical property, and the combination of the other 6 equilibrium equations along with Eq. (3.28) are sufficient to calculate the unknown variables $\mathcal{A}_1$, $\mathcal{B}_1$, $\mathcal{C}_1$, $\mathcal{D}_1$, $\mathcal{E}_1$, $\mathcal{F}_1$, $\mathcal{G}_1$, $\mathcal{H}_1$, $\mathcal{I}_1$, $\mathcal{J}_1$, $\mathcal{K}_1$, $\mathcal{L}_1$ in solution (3.26a) and (3.27). Then amplitudes of wave k_1, k_2, k_3, k_4, k_5 and k_6 are obtained on each frequency, and we can easily find the complex amplitude of deflection $\widetilde{w}$ and rotation $\widetilde{\psi}$ on each frequency at arbitrary position by wave superposition.

3.3.2 Input mobility and transfer mobility

As one important structural property describing the frequency-dependent relationship between forces and motions, mechanical mobility measures the velocity generated by a unit force at the point of interest. In this section, input mobility and transfer mobility function of one infinite complex Timoshenko beam are derived with the previous SSG theory-based formulation. The complex mobility of the structure at any interface can expressed as the quotient of the complex amplitude of velocity (or rotational velocity) response and the complex amplitude of a harmonic force (or moment) that generates the response for a given frequency. For the studied case, the mobility between the driving force and the transverse velocity as well as the rotation velocity can be expressed as in Eq. (3.33)

$$Y_w(x,\omega) = \frac{\dot{w}(x,\omega)}{F(\omega)} = \frac{i\omega \cdot \widetilde{w}_x}{q_0}; \tag{3.33a}$$

$$Y_\omega(x,\omega) = \frac{\dot{\psi}(x,\omega)}{F(\omega)} = \frac{i\omega \cdot \widetilde{\psi}_x}{q_0}; \tag{3.33b}$$

Since the vibration is symmetrical about point $x = 0$, we will concentrate on the positive going waves field. For the studied complex Timoshenko beam, the amplitudes of deflection $\widetilde{w}$ and rotation $\widetilde{\psi}$ in the field of $x > 0$ have been evaluated in Sec. 3.3.1 as

$$\begin{aligned} \widetilde{w}_{x^+} &= \mathcal{A}_1 \cdot e^{-ik_1 x} + \mathcal{B}_1 \cdot e^{-ik_2 x} + \mathcal{C}_1 \cdot e^{-ik_3 x} + \mathcal{D}_1 \cdot e^{-ik_4 x} + \mathcal{E}_1 \cdot e^{-ik_5 x} + \mathcal{F}_1 \cdot e^{-ik_6 x}, \\ \widetilde{\psi}_{x^+} &= \mathcal{G}_1 \cdot e^{-ik_1 x} + \mathcal{H}_1 \cdot e^{-ik_2 x} + \mathcal{I}_1 \cdot e^{-ik_3 x} + \mathcal{J}_1 \cdot e^{-ik_4 x} + \mathcal{K}_1 \cdot e^{-ik_5 x} + \mathcal{L}_1 \cdot e^{-ik_6 x}. \end{aligned} \tag{3.34}$$

With the normalizing variables defined in Eq. (3.11), the normalized mobility can be expressed as

$$\overline{Y} = \frac{\overline{\dot{w}}_x}{\overline{F}} = \frac{Y \cdot \mu A k_t}{L} \tag{3.35}$$

Then the numerical investigation of input mobility and transfer mobility is proceeded for Timoshenko beam with the SSG theory-based formulation in section 3.3.1. Assuming no hysteretic damping in the system with $E = 52\,\text{GPa}$, and the amplitude of the harmonic axial force $q_0 = 0.1\mu A$ at $x = 0$ in Figure 3.7. The resulting 'driving point mobility' is obtained with the velocity response at $x = 0$.

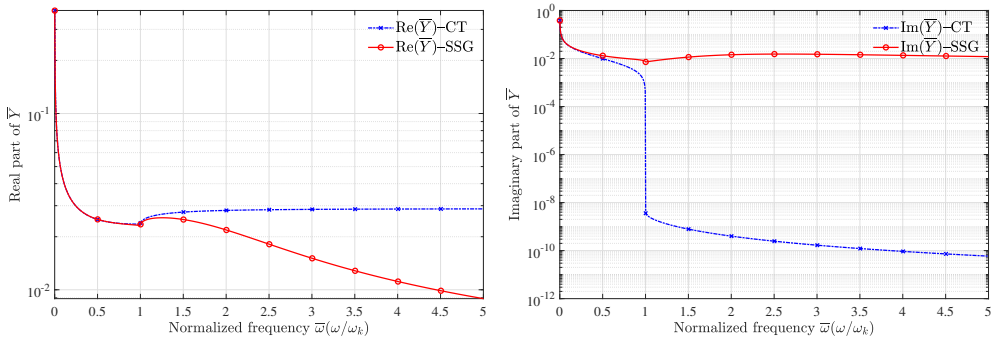

(a) Real part (b) Imaginary part

Figure 3.8: Force driving mobility of infinite beam

Figure 3.8 illustrates the compassion of input mobility $\overline{Y}$-SSG for complex Timoshenko beam resulting from SSG theory model and the input mobility $\overline{Y}$-CT of classical model. To be noted here, the responded rotation angle at point $x = 0$ equals zero, so the force driving mobility only relates the transverse velocity and the applied force.

Below the cut-on frequency ($\overline{\omega} \leq 1$), $\overline{Y}$-SSG and $\overline{Y}$-CT are both complex. The real parts match well by both decreasing from infinite high. The imaginary parts also decrease, but Im($\overline{Y}$)-SSG is higher which imply more phase difference between force the responded transverse velocity. Since the investigation is proceed without hysteretic damping, classical shear wave become pure real above cut-on frequency, then Im($\overline{Y}$)-CT become zero when $\overline{\omega} \geq 1$ as shown in Figure 3.8(b). Energy input will be carried away without dissipation and the response is always in the same phase with the excitation. In contrast, the SSG theory mobility is still complex even above the cut-on frequency, moreover the Im($\overline{Y}$)-SSG indeed increase slightly with frequency. As frequency goes up from cut-on frequency, Re($\overline{Y}$)-CT increases slightly and approaches to one constant, by contrast Re($\overline{Y}$)-SSG decrease significantly and become lower than classical one. The complex beam with considering micro-structure effect exhibit more resistance to the force excitation.

To study more details of the complex dynamic properties, we illustrate the absolute value and the phase changing of the input mobility as in Figure 3.9,

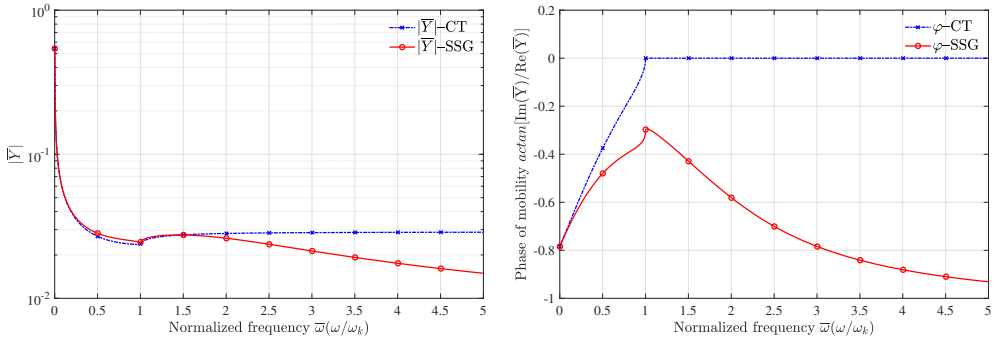

(a) Absolute value (b) Phase

Figure 3.9: Modulus and phase of driving mobility of infinite beam

As shown in Figure 3.9, the modulus of driving point mobility keeps dropping down in higher frequency and the phase difference ϕ enlarge as frequency goes up. The more phase difference, the less proportion of input power can be transferred from the force to the structure.

The transfer mobility $\overline{Y}_{\mathrm{w}}$ relates the complex amplitude of transverse velocity at point of $x > 0$ or $x < 0$ and the amplitude of the exciting force. The transfer mobility $\overline{Y}_{\psi}$ relates the complex amplitude of rotation velocity at point of $x > 0$ or $x < 0$ and the amplitude of the exciting force. In the following, $\overline{Y}_{\mathrm{w}}$ and $\overline{Y}_{\psi}$ in interval $0 < \overline{x} < 1$ are analyzed on different frequency ($\overline{\omega}_1 = 0.5$ is below the cut-on frequency, and $\overline{\omega}_2 = 1.5, \overline{\omega}_3 = 2.5$ are above the cut-on frequency).

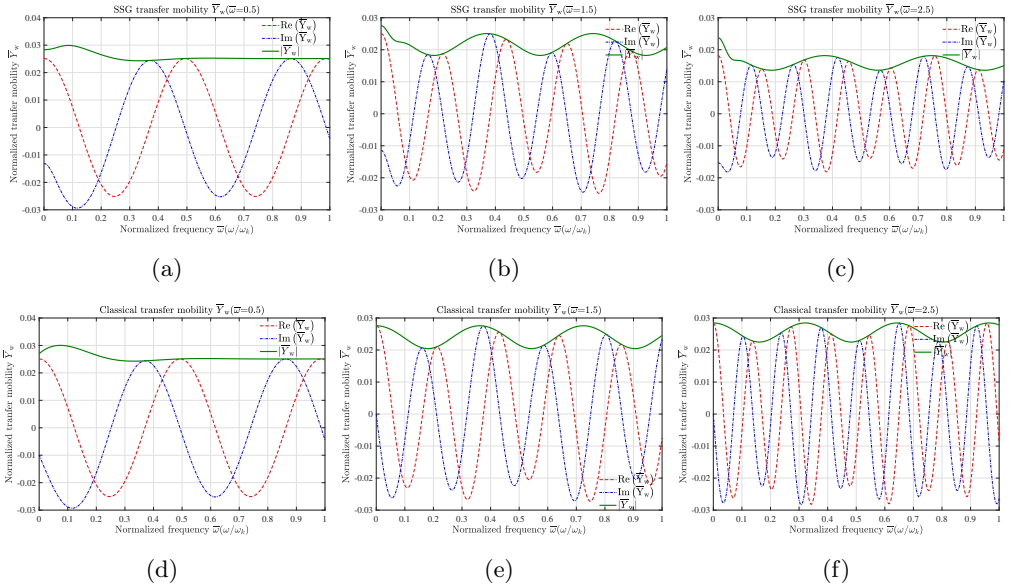

(a) (b) (c)

(d) (e) (f)

Figure 3.10: Comparison of transfer mobility $\overline{Y}_{\mathrm{w}}$

Figure 3.10 illustrate the transfer mobility $\overline{Y}_{\mathrm{w}}$ of SSG theory model (3.10(a),

3.10(b), 3.10(c)) and of classical model (3.10(d), 3.10(e), 3.10(f)) on different frequency. In general, the modulus of classical mobility is higher than the enriched result on each frequency. The classical wave propagation field consist of two waves, the propagating bending wave and the shear wave which only propagate above the cut-on frequency. When $\overline{\omega} = 0.5$, the classical $|\overline{Y}_{\mathrm{w}}|$ decays distinctly local to the disturbance as the generated shear wave is pure evanescent. When $\overline{\omega} = 1.5$ and 2.5, the harmonic disturbance generated at $\overline{x} = 0$ propagate away to infinity in space in the form defined by the two propagating waves.

The complex wave propagation field consist of six waves, and four of them are evanescent waves in whole frequency range. For the enriched $\overline{Y}_{\mathrm{w}}$, as we can see in Figure 3.10(a), 3.10(b), 3.10(c), the disturbance propagate away in a different manner with $|\overline{Y}_{\mathrm{w}}|$ decaying obviously in close range from the excitation point. In higher frequency, the decrease in near field becomes more distinct. This phenomenon can be interpreted with the near field effect generated by the inner force interaction. The higher the frequency, the more micro-structure effect, the more obvious the near field effect. For a given frequency, the spatial period is longer with the classical result.

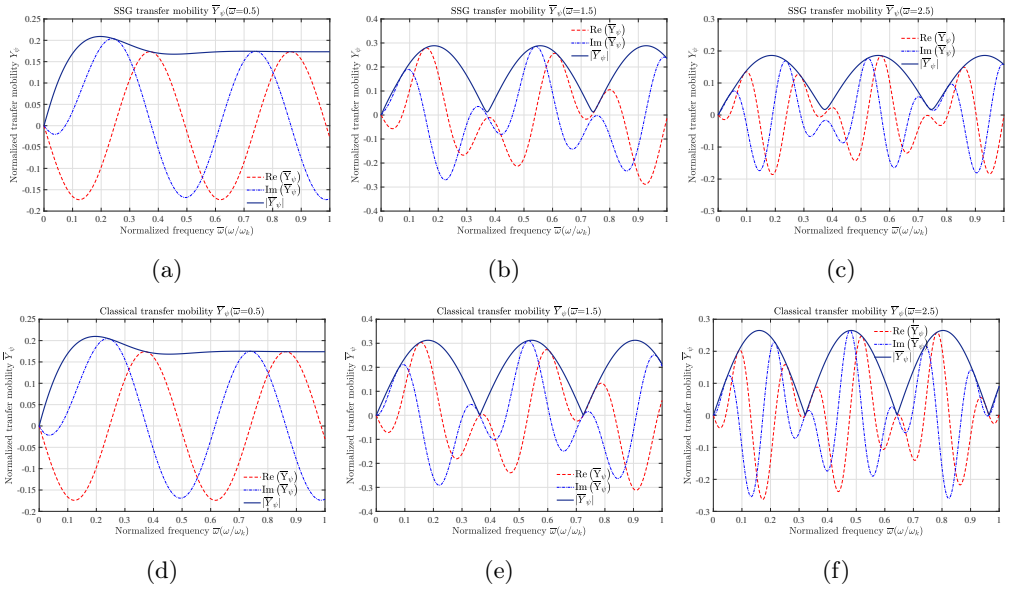

Figure 3.11: Comparison of transfer mobility $\overline{Y}_{\psi}$

Figure 3.11 illustrate the transfer mobility $\overline{Y}_{\psi}$ on different frequency of SSG theory model (3.11(a), 3.11(b), 3.11(c)) and of classical model (3.11(d), 3.11(e), 3.11(f)). As can be seen, the transfer mobility from the driving force to the rotation velocity are both zero at the origin point since the $\dot{\psi} = 0$. In higher frequency, classical $|\overline{Y}_{\psi}|$ is higher than that of the SSG result. The complex beam structure shows more resistance to the force excitation in terms of rotation. The near field effect shown in Figure 3.10(b) and 3.10(c) does not appear in rotation related transfer

mobility $\overline{Y}_{\psi}$. As the rotation angle at $x = 0$ in case of transverse excitation force equals zero, it cannot generate energy conversion from regular rotation deformation to higher order rotation deformation.

3.3.3 Input power and transfer power

As shown in Figure 3.7, only one transverse force apply on the studied Timsoshenko beam, therefore the input active and reactive power are governed by the driving point mobility at load application point. The active power is proportional to the real part of the direct mobility, while the reactive power is proportional to the imaginary part of the direct mobility [115]. To explore the influence of long range interaction on energy input and energy transfer through the complex structure, input active flow and reactive flow are analyzed based on the proposed SSG theory model. Time averaged input active power and reactive power are given as

$$P_{in} = \frac{1}{2}\mathrm{Re}\left[q_0 \cdot (\dot{w})^*\right], \tag{3.36a}$$

$$Q_{in} = \frac{1}{2}\mathrm{Im}\left[q_0 \cdot (\dot{w})^*\right]. \tag{3.36b}$$

With the complex amplitude $\widetilde{w}$ at $x = 0$ expressed in (3.34) and $\dot{w} = i\omega \cdot \widetilde{w}$, input power flow can be easily obtained. Then power flow are normalized by the normalizing expression in (3.24) and shown as follows,

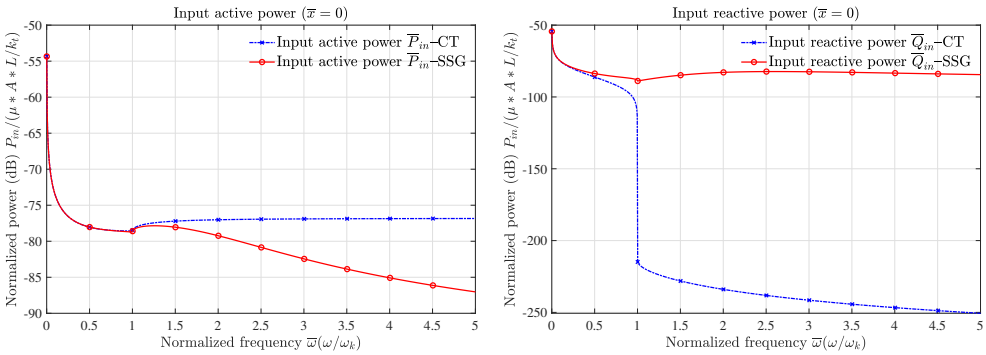

(a) Active power (b) Reactive power

Figure 3.12: Input active power and reactive power

Figure 3.12 display the dimensionless input active and reactive power flow. The active power represents the energy that can be carried away to infinity, and the reactive power does not transform power from force or dissipate power. For the homogeneous beam structure with classical theory model, input active power $\overline{P}_{in}$-CT increases and approaches to one constant as frequency goes up. Whereas the SSG theory result $\overline{P}_{in}$-SSG decrease and clearly lower than the classical one especilly in higher frequency. On the other hand, reactive power $\overline{Q}_{in}$-SSG input into the complex beam keeps increasing by small amount above the cut-on frequency as $\overline{Q}_{in}$-CT decrease to zero, which makes physical sense because the beam has been

assumed to possess no damping. For the complex media, as the frequency goes up, a larger proportion of energy will be transformed into reactive energy, and less energy can be converted into propagating waves and propagate to far field. This can be one of the physic interpretation for the decreasing input mobility for complex media.

According to the presented result, it is obvious that the micro-structure effect have great influence on energy transfer form source to far field vibration, and the influence mostly exists in the near field of the excitation force. To explore the energy transfer in near-field, active power and reactive power transferred spatially require to be analyzed. As shown in section 3.2.4, time averaged energy flow in complex beam structure based on SSG theory model are expressed in Eq. (3.37)

$$\langle \mathrm{P} \rangle = -\frac{1}{2}\mathrm{Re}\left[\mathbf{S}\right], \qquad \langle \mathrm{Q} \rangle = -\frac{1}{2}\mathrm{Im}\left[\mathbf{S}\right]. \tag{3.37}$$

$\mathbf{S}$ represents directional energy flux of the wave field through the observed section, and the expression has been deduced and validated as in Eq. (3.38)

$$\mathbf{S} = V_0 \cdot \dot{w}^* + V_1 \cdot \left(\frac{\partial \dot{w}}{\partial x}\right)^* + V_2 \cdot \left(\frac{\partial^2 \dot{w}}{\partial x^2}\right)^* + M_0 \cdot \dot{\psi}^* + M_1 \cdot \left(\frac{\partial \dot{\psi}}{\partial x}\right)^* + M_2 \cdot \left(\frac{\partial^2 \dot{\psi}}{\partial x^2}\right)^*. \tag{3.38}$$

For the studied case in Figure 3.7, the normalized spatial variation of transfer power flow between $\overline{x} = 0$ and $\overline{x} = 1$ on different frequency are illustrated as follows,

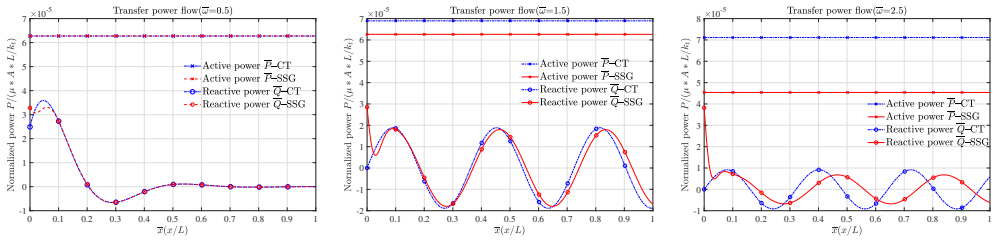

(a) (b) (c)

Figure 3.13: Transfer active power and reactive power

As shown in Figure 3.13, transfer active power of classical model $\overline{P}$-CT as well as SSG model $\overline{P}$-SSG are both space independent, energy can be transmitted to infinity without dissipation. Their values in interval $[0, 1]$ constantly equals half of the input active power at $\overline{x} = 0$, thus $\overline{P}$-SSG is less than $\overline{P}$-CT, and the higher the frequency, the wider the gap. Long range interaction between underlying micro-structures affect transfer reactive power significantly in the near field. The reactive power $\overline{Q}$-SSG at $x = 0$ is not zero, instead it equals half of the input reactive power as shown in Figure 3.12. $\overline{Q}$-SSG decrease rapidly in the near field from the excitation force. The higher the frequency, the more rapidly the reactive power decay. For a given frequency, the greater the distance between the points of observation and force application, the smaller the near-field effect.

For the complex Timoshenko beam, there are six components included in the expression of Poynting vector (3.38) corresponding to six types of kinetic parameters along with the generalized forces. To analyze the influence of long range interaction on reactive energy flow transferred by different types of generalized forces, the six components are divide into two group, $\overline{\mathbf{S}}_V$ represents the power transferred by generalized shear force, namely, the power flow associated with kinetic parameters w, $\frac{\partial w}{\partial x}$, and $\frac{\partial^2 w}{\partial x^2}$. $\overline{\mathbf{S}}_M$ represents the power transferred by generalized bending moment, namely, the power flow associated with kinetic parameters ψ, $\frac{\partial \psi}{\partial x}$ and $\frac{\partial^2 \psi}{\partial x^2}$. Based on the definition, two directional energy flux can be defined as

$$\begin{aligned} \mathbf{S}_V &= V_0 \cdot \dot{w}^* + V_1 \cdot \left(\frac{\partial \dot{w}}{\partial x}\right)^* + V_2 \cdot \left(\frac{\partial^2 \dot{w}}{\partial x^2}\right)^* \\ \mathbf{S}_M &= M_0 \cdot \dot{\psi}^* + M_1 \cdot \left(\frac{\partial \dot{\psi}}{\partial x}\right)^* + M_2 \cdot \left(\frac{\partial^2 \dot{\psi}}{\partial x^2}\right)^* . \end{aligned} \tag{3.39}$$

Then the transferred reactive power by generalized shear force and by generalized bending moment can be obtained as,

$$\langle Q_V \rangle = -\frac{1}{2}\mathrm{Im}\left[\mathbf{S}_V\right], \qquad \langle Q_M \rangle = -\frac{1}{2}\mathrm{Im}\left[\mathbf{S}_M\right]. \tag{3.40}$$

For a given frequency (i.e. $\overline{\omega} = 2.5$), results of transferred active and reactive energy by generalized shear force and generalized bending moment are illustrated as in Figure 3.14

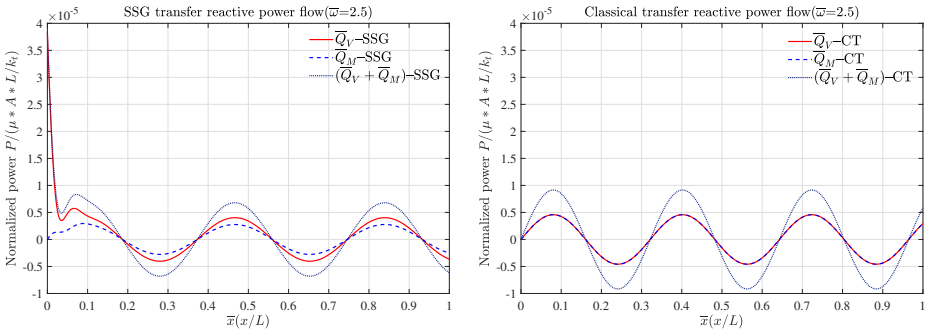

(a) (b)

Figure 3.14: Comparision of transfer reactive power

As shown in Figure 3.14, the near field effect exhibited by transfer reactive power mostly attribute to the decreasing of the shear component $\overline{Q}_V$-SSG, by contrast bending component $\overline{Q}_M$-SSG is of less importance. All the reactive power is transferred to the shear component Q_V-SSG, which is not zero at the origin, then the shear component decrease rapidly from the origin, which clearly interpret the reactive power attenuation through inner micro-interactions in the near field. On the other hand, if the beam is excited by harmonic moment at $x = 0$, this near field effect should contribute to the decreasing of bending moment component.

To be noted, energy dissipation mechanism through damping in complex media based on the SSG theory model is more complicated than the classical model due to the existence of the long range force interactions. Therefore no damping is assumed in the system. However, the most interesting phenomenon, namely, the reactive power decreasing in the near field of the force excitation, still should be validated for reactive power flow balance. According to reference [113], in a region which is not loaded, the reactive energy flow balance should follow the equilibrium as

$$\nabla \cdot \langle Q \rangle + 2\omega \left(\langle T \rangle - \langle U \rangle \right) = 0. \tag{3.41}$$

This expression shows the net reactive flow is proportional to the time averaged Lagrangian energy density which equals the difference between time averaged kinetic energy and potential energy. To confirm that, values of $-\nabla \cdot \langle Q \rangle$ and $2\omega \left(\langle T \rangle - \langle U \rangle \right)$ are calculated on one arbitrary frequency $\overline{\omega} = 3$, and the result is shown as follows,

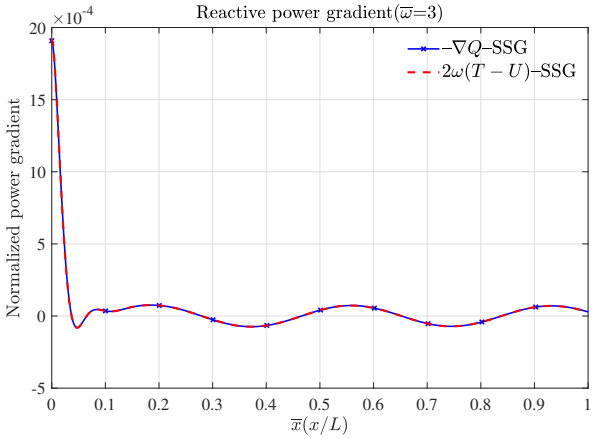

Figure 3.15: Reactive power flow balance

According to Figure 3.15, reactive power balance (2.38) is validated of for the proposed SSG theory model. In complex Timoshenko beam structure, the net reactive flow is proportional to the difference between time averaged kinetic energy and potential energy. At force excitation point, near field effect is significant because time averaged potential energy has great difference with time averaged kinetic energy due to the existence of higher order potential energy. As wave propagate to the far field, the internal force interactions are weaken, evanescent waves decay to zero and near field effect become less obvious.

3.4 Frequency response of finite Timoshenko beam based on SSG theory model

In this section, frequency response analysis of complex Timoshenko beam subject to a harmonic excitation with certain boundary condition will be implemented based

on the proposed SSG theory formulation. As shown in Figure 3.16, a cantilever bean subject to a harmonic force $q = q_0 e^{i\omega t}$ at the free end is considered. The height of cross-section $h = 10a_0$, and with $b = 3h$, and length of beam $L = 5h$. The observation point can be at any position, in this case it is set to be at $x = 0.7L$.

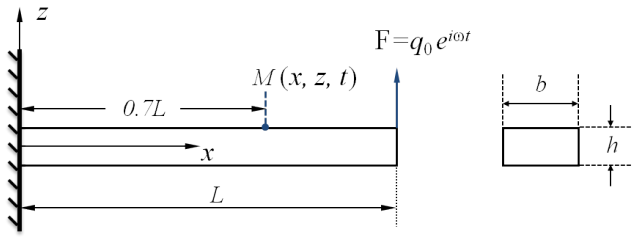

Figure 3.16: A fixed-free beam with loading in free end

The solution for the displacement can be given by the superposition of all the progressive and retrograde waves ($\pm\overline{k}_1$, $\pm\overline{k}_2$, $\pm\overline{k}_3$, $\pm\overline{k}_4$, $\pm\overline{k}_5$, $\pm\overline{k}_6$). Therefore the general expressions of the dimensionless displacement $\overline{w}$ and $\overline{\psi}$ can be expressed as

$$\begin{aligned} w(\overline{x},\tau) = &\Big(\mathcal{A}_1 e^{-i\overline{k}_1\overline{x}} + \mathcal{B}_1 e^{i\overline{k}_1\overline{x}} + \mathcal{C}_1 e^{-i\overline{k}_2\overline{x}} + \mathcal{D}_1 e^{i\overline{k}_2\overline{x}} + \mathcal{E}_1 e^{-i\overline{k}_3\overline{x}} + \mathcal{F}_1 e^{i\overline{k}_3\overline{x}} \\ &+\mathcal{G}_1 e^{-i\overline{k}_4\overline{x}} + \mathcal{H}_1 e^{i\overline{k}_4\overline{x}} + \mathcal{I}_1 e^{-i\overline{k}_5\overline{x}} + \mathcal{J}_1 e^{i\overline{k}_5\overline{x}} + \mathcal{K}_1 e^{-i\overline{k}_6\overline{x}} + \mathcal{L}_1 e^{i\overline{k}_6\overline{x}}\Big) e^{i\overline{\omega}\tau}, \\ \psi(\overline{x},\tau) = &\Big(\mathcal{A}_2 e^{-i\overline{k}_1\overline{x}} + \mathcal{B}_2 e^{i\overline{k}_1\overline{x}} + \mathcal{C}_2 e^{-i\overline{k}_2\overline{x}} + \mathcal{D}_2 e^{i\overline{k}_2\overline{x}} + \mathcal{E}_2 e^{-i\overline{k}_3\overline{x}} + \mathcal{F}_2 e^{i\overline{k}_3\overline{x}} \\ &+\mathcal{G}_2 e^{-i\overline{k}_4\overline{x}} + \mathcal{H}_2 e^{i\overline{k}_4\overline{x}} + \mathcal{I}_2 e^{-i\overline{k}_5\overline{x}} + \mathcal{J}_2 e^{i\overline{k}_5\overline{x}} + \mathcal{K}_2 e^{-i\overline{k}_6\overline{x}} + \mathcal{L}_2 e^{i\overline{k}_6\overline{x}}\Big) e^{i\overline{\omega}\tau}. \end{aligned} \tag{3.42}$$

From the normalized dispersion relation, which is obtained by the governing equation in section 3.2.2, values of all wavenumbers $\overline{k}_1$, $\overline{k}_2$, $\overline{k}_3$, $\overline{k}_4$, $\overline{k}_5$, and $\overline{k}_6$ on each frequency can be calculated out. Then the value of the displacement $\overline{w}$ and rotation ψ on that frequency only depend on the amplitudes of each wave mode. The general solution form of $\overline{w}$ and ψ should be valid to the governing equations 3.12 on any frequency $\overline{\omega}$ for all the point $\overline{x}$ on the structure except the boundary points. Hence when substitute the solution of Eq. 3.42 into the governing equations, the coefficient of each term $e^{\pm i\overline{k}_i\overline{x}+i\overline{\omega}\tau}$ should equal zero, which yields the normalized amplitudes of $\overline{w}$ and ψ for each mode follows the principle in Eq. (3.43)

$$\mathcal{A}_2 = \frac{-2i\left(-B_6\overline{k}_t^2\overline{k}_1^{\,6} + c_3AL^2\overline{k}_t^{\,2}\overline{k}_1^{\,4} - B_5L^2\overline{k}_t^{\,2}\overline{k}_1^{\,4} - \mu AL^4\overline{k}_t^{\,2}\overline{k}_1^{\,2} + m_0\omega^2L^6\right)}{\overline{k}_1\overline{k}_t^{\,2}\left(B_8\overline{k}_1^{\,4} + 2c_2AL^2\overline{k}_1^{\,2} + 2c_3AL^2\overline{k}_1^{\,2} + B_7L^2\overline{k}_1^{\,2} - 2\mu AL^4\right)}\mathcal{A}_1;$$

$$\mathcal{B}_2 = \frac{2i\left(-B_6\overline{k}_t^2\overline{k}_1^{\,6} + c_3AL^2\overline{k}_t^{\,2}\overline{k}_1^{\,4} - B_5L^2\overline{k}_t^{\,2}\overline{k}_1^{\,4} - \mu AL^4\overline{k}_t^{\,2}\overline{k}_1^{\,2} + m_0\omega^2L^6\right)}{\overline{k}_1\overline{k}_t^{\,2}\left(B_8\overline{k}_1^{\,4} + 2c_2AL^2\overline{k}_1^{\,2} + 2c_3AL^2\overline{k}_1^{\,2} + B_7L^2\overline{k}_1^{\,2} - 2\mu AL^4\right)}\mathcal{B}_1;$$

$$
\begin{aligned}
\mathcal{C}_2 &= \frac{-2i\left(-B_6\overline{k}_t^2\overline{k}_2{}^6 + c_3AL^2\overline{k}_t{}^2\overline{k}_2{}^4 - B_5L^2\overline{k}_t{}^2\overline{k}_2{}^4 - \mu AL^4\overline{k}_t{}^2\overline{k}_2{}^2 + m_0\omega^2L^6\right)}{\overline{k}_2\overline{k}_t{}^2\left(B_8\overline{k}_2{}^4 + 2c_2AL^2\overline{k}_2{}^2 + 2c_3AL^2\overline{k}_2{}^2 + B_7L^2\overline{k}_2{}^2 - 2\mu AL^4\right)}\mathcal{C}_1;\\
\mathcal{D}_2 &= \frac{2i\left(-B_6\overline{k}_t^2\overline{k}_2{}^6 + c_3AL^2\overline{k}_t{}^2\overline{k}_2{}^4 - B_5L^2\overline{k}_t{}^2\overline{k}_2{}^4 - \mu AL^4\overline{k}_t{}^2\overline{k}_2{}^2 + m_0\omega^2L^6\right)}{\overline{k}_2\overline{k}_t{}^2\left(B_8\overline{k}_2{}^4 + 2c_2AL^2\overline{k}_2{}^2 + 2c_3AL^2\overline{k}_2{}^2 + B_7L^2\overline{k}_2{}^2 - 2\mu AL^4\right)}\mathcal{D}_1;\\
\mathcal{E}_2 &= \frac{-2i\left(-B_6\overline{k}_t^2\overline{k}_3{}^6 + c_3AL^2\overline{k}_t{}^2\overline{k}_3{}^4 - B_5L^2\overline{k}_t{}^2\overline{k}_3{}^4 - \mu AL^4\overline{k}_t{}^2\overline{k}_3{}^2 + m_0\omega^2L^6\right)}{\overline{k}_3\overline{k}_t{}^2\left(B_8\overline{k}_3{}^4 + 2c_2AL^2\overline{k}_3{}^2 + 2c_3AL^2\overline{k}_3{}^2 + B_7L^2\overline{k}_3{}^2 - 2\mu AL^4\right)}\mathcal{E}_1;\\
\mathcal{F}_2 &= \frac{2i\left(-B_6\overline{k}_t^2\overline{k}_3{}^6 + c_3AL^2\overline{k}_t{}^2\overline{k}_3{}^4 - B_5L^2\overline{k}_t{}^2\overline{k}_3{}^4 - \mu AL^4\overline{k}_t{}^2\overline{k}_3{}^2 + m_0\omega^2L^6\right)}{\overline{k}_3\overline{k}_t{}^2\left(B_8\overline{k}_3{}^4 + 2c_2AL^2\overline{k}_3{}^2 + 2c_3AL^2\overline{k}_3{}^2 + B_7L^2\overline{k}_3{}^2 - 2\mu AL^4\right)}\mathcal{F}_1;\\
\mathcal{G}_2 &= \frac{-2i\left(-B_6\overline{k}_t^2\overline{k}_4{}^6 + c_3AL^2\overline{k}_t{}^2\overline{k}_4{}^4 - B_5L^2\overline{k}_t{}^2\overline{k}_4{}^4 - \mu AL^4\overline{k}_t{}^2\overline{k}_4{}^2 + m_0\omega^2L^6\right)}{\overline{k}_4\overline{k}_t{}^2\left(B_8\overline{k}_4{}^4 + 2c_2AL^2\overline{k}_4{}^2 + 2c_3AL^2\overline{k}_4{}^2 + B_7L^2\overline{k}_4{}^2 - 2\mu AL^4\right)}\mathcal{G}_1;\\
\mathcal{H}_2 &= \frac{2i\left(-B_6\overline{k}_t^2\overline{k}_4{}^6 + c_3AL^2\overline{k}_t{}^2\overline{k}_4{}^4 - B_5L^2\overline{k}_t{}^2\overline{k}_4{}^4 - \mu AL^4\overline{k}_t{}^2\overline{k}_4{}^2 + m_0\omega^2L^6\right)}{\overline{k}_4\overline{k}_t{}^2\left(B_8\overline{k}_4{}^4 + 2c_2AL^2\overline{k}_4{}^2 + 2c_3AL^2\overline{k}_4{}^2 + B_7L^2\overline{k}_4{}^2 - 2\mu AL^4\right)}\mathcal{H}_1;\\
\mathcal{I}_2 &= \frac{-2i\left(-B_6\overline{k}_t^2\overline{k}_5{}^6 + c_3AL^2\overline{k}_t{}^2\overline{k}_5{}^4 - B_5L^2\overline{k}_t{}^2\overline{k}_5{}^4 - \mu AL^4\overline{k}_t{}^2\overline{k}_5{}^2 + m_0\omega^2L^6\right)}{\overline{k}_5\overline{k}_t{}^2\left(B_8\overline{k}_5{}^4 + 2c_2AL^2\overline{k}_5{}^2 + 2c_3AL^2\overline{k}_5{}^2 + B_7L^2\overline{k}_5{}^2 - 2\mu AL^4\right)}\mathcal{I}_1;\\
\mathcal{J}_2 &= \frac{2i\left(-B_6\overline{k}_t^2\overline{k}_5{}^6 + c_3AL^2\overline{k}_t{}^2\overline{k}_5{}^4 - B_5L^2\overline{k}_t{}^2\overline{k}_5{}^4 - \mu AL^4\overline{k}_t{}^2\overline{k}_5{}^2 + m_0\omega^2L^6\right)}{\overline{k}_5\overline{k}_t{}^2\left(B_8\overline{k}_5{}^4 + 2c_2AL^2\overline{k}_5{}^2 + 2c_3AL^2\overline{k}_5{}^2 + B_7L^2\overline{k}_5{}^2 - 2\mu AL^4\right)}\mathcal{J}_1;\\
\mathcal{K}_2 &= \frac{-2i\left(-B_6\overline{k}_t^2\overline{k}_6{}^6 + c_3AL^2\overline{k}_t{}^2\overline{k}_6{}^4 - B_5L^2\overline{k}_t{}^2\overline{k}_6{}^4 - \mu AL^4\overline{k}_t{}^2\overline{k}_6{}^2 + m_0\omega^2L^6\right)}{\overline{k}_6\overline{k}_t{}^2\left(B_8\overline{k}_6{}^4 + 2c_2AL^2\overline{k}_6{}^2 + 2c_3AL^2\overline{k}_6{}^2 + B_7L^2\overline{k}_6{}^2 - 2\mu AL^4\right)}\mathcal{K}_1;\\
\mathcal{L}_2 &= \frac{2i\left(-B_6\overline{k}_t^2\overline{k}_6{}^6 + c_3AL^2\overline{k}_t{}^2\overline{k}_6{}^4 - B_5L^2\overline{k}_t{}^2\overline{k}_6{}^4 - \mu AL^4\overline{k}_t{}^2\overline{k}_6{}^2 + m_0\omega^2L^6\right)}{\overline{k}_6\overline{k}_t{}^2\left(B_8\overline{k}_6{}^4 + 2c_2AL^2\overline{k}_6{}^2 + 2c_3AL^2\overline{k}_6{}^2 + B_7L^2\overline{k}_6{}^2 - 2\mu AL^4\right)}\mathcal{L}_1;
\end{aligned}
\tag{3.43}
$$

The above equations are not sufficient to calculate the 24 variables in the solution Eq. (3.42), boundary conditions at each ends are required. For the classical theory model, there are two kinds of conditions: a loading type and a geometric type, and only one kind need to be satisfied for each kinetic parameter. The boundary conditions for the SSG based model follows the similar principle. For the case in Figure 3.16, at the fixed end $\overline{x} = 0$, transverse displacement $\overline{w}$ and rotation angle ψ equal zero; The higher order generalized forces $\overline{V}_1$, $\overline{V}_2$ and $\overline{M}_1$, $\overline{M}_2$ are set to be zero as the possible produced forces by the fixed base are only classical shear force and bending moment. At the force excitation end $\overline{x} = 1$, the produced classical

force and moment $\overline{V}_0$ and $\overline{M}_0$ follow the equilibrium for shear force and bending moment. The higher order forces $\overline{V}_1$, $\overline{V}_2$ and $\overline{M}_1$, $\overline{M}_2$ are also set to be zero. Then the generalized loading type or geometric type boundary conditions for Figure 3.16 are expressed in Eq. (3.44)

$$
\begin{aligned}
&\overline{w}\,(0,\tau)=0;\\
&\psi\,(0,\tau)=0;\\
&\overline{V}_1\,(0,\tau)=\left(\frac{B_7+c_3A}{2\mu AL^2}\right)\left(\frac{\partial\psi}{\partial\overline{x}}\right)-\frac{B_8}{2\mu AL^4}\left(\frac{\partial^3\psi}{\partial\overline{x}^3}\right)+\frac{(B_5-c_3A)}{\mu AL^2}\left(\frac{\partial^2\overline{w}}{\partial\overline{x}^2}\right)-\frac{B_6}{\mu AL^4}\left(\frac{\partial^4\overline{w}}{\partial\overline{x}^4}\right)=0;\\
&\overline{V}_2\,(0,\tau)=-\frac{c_3A}{2\mu AL^2}\psi+\frac{B_8}{2\mu AL^4}\left(\frac{\partial^2\psi}{\partial\overline{x}^2}\right)+\frac{c_3A}{2\mu AL^2}\left(\frac{\partial\overline{w}}{\partial\overline{x}}\right)+\frac{B_6}{\mu AL^4}\left(\frac{\partial^3\overline{w}}{\partial\overline{x}^3}\right)=0;\\
&\overline{M}_1\,(0,\tau)=\frac{A}{\mu AL^2}\left(c_2+\frac{c_3}{2}\right)\psi+\frac{\left(B_2-\frac{B_4}{2}\right)}{\mu AL^4}\left(\frac{\partial^2\psi}{\partial\overline{x}^2}\right)-\frac{B_3}{\mu AL^6}\left(\frac{\partial^4\psi}{\partial\overline{x}^4}\right)\\
&\qquad\qquad-\left(\frac{c_3}{2}+c_2\right)\frac{A}{\mu AL^2}\left(\frac{\partial\overline{w}}{\partial\overline{x}}\right)+\frac{B_8}{2\mu AL^4}\left(\frac{\partial^3\overline{w}}{\partial\overline{x}^3}\right)=0;\\
&\overline{M}_2\,(0,\tau)=\frac{B_4}{2\mu AL^4}\left(\frac{\partial\psi}{\partial\overline{x}}\right)+\frac{B_3}{\mu AL^6}\left(\frac{\partial^3\psi}{\partial\overline{x}^3}\right)=0;\\
&\overline{V}_0\,(1,\tau)=-\psi-\frac{\left(\frac{B_7}{2}+(c_3+c_2)\,A\right)}{\mu AL^2}\left(\frac{\partial^2\overline{w}}{\partial\overline{x}^2}\right)+\frac{B_8}{2\mu AL^4}\left(\frac{\partial^4\psi}{\partial\overline{x}^4}\right)+\left(\frac{\partial\overline{w}}{\partial\overline{x}}\right)\\
&\qquad\qquad+\frac{(c_3A-B_5)}{\mu AL^2}\left(\frac{\partial^3\overline{w}}{\partial\overline{x}^3}\right)+\frac{B_6}{\mu AL^4}\left(\frac{\partial^5\overline{w}}{\partial\overline{x}^5}\right)+\overline{q}_0=0\\
&\overline{M}_0\,(1,\tau)=\frac{\left(B_1-A\left(c_2+\frac{c_3}{2}\right)\right)}{\mu AL^2}\left(\frac{\partial\psi}{\partial\overline{x}}\right)+\frac{(B_4-B_2)}{\mu AL^4}\left(\frac{\partial^3\psi}{\partial\overline{x}^3}\right)+\frac{B_3}{\mu AL^6}\left(\frac{\partial^5\psi}{\partial\overline{x}^5}\right)\\
&\qquad\qquad+\frac{\left(\frac{B_7}{2}+A\left(c_2+\frac{c_3}{2}\right)\right)}{\mu AL^2}\left(\frac{\partial^2\overline{w}}{\partial\overline{x}^2}\right)-\frac{B_8}{2\mu AL^4}\left(\frac{\partial^4\overline{w}}{\partial\overline{x}^4}\right)=0\\
&\overline{V}_1\,(1,\tau)=\left(\frac{B_7+c_3A}{2\mu AL^2}\right)\left(\frac{\partial\psi}{\partial\overline{x}}\right)-\frac{B_8}{2\mu AL^4}\left(\frac{\partial^3\psi}{\partial\overline{x}^3}\right)+\frac{(B_5-c_3A)}{\mu AL^2}\left(\frac{\partial^2\overline{w}}{\partial\overline{x}^2}\right)-\frac{B_6}{\mu AL^4}\left(\frac{\partial^4\overline{w}}{\partial\overline{x}^4}\right)=0;\\
&\overline{V}_2\,(1,\tau)=-\frac{c_3A}{2\mu AL^2}\psi+\frac{B_8}{2\mu AL^4}\left(\frac{\partial^2\psi}{\partial\overline{x}^2}\right)+\frac{c_3A}{2\mu AL^2}\left(\frac{\partial\overline{w}}{\partial\overline{x}}\right)+\frac{B_6}{\mu AL^4}\left(\frac{\partial^3\overline{w}}{\partial\overline{x}^3}\right)=0;\\
&\overline{M}_1\,(1,\tau)=\frac{A}{\mu AL^2}\left(c_2+\frac{c_3}{2}\right)\psi+\frac{\left(B_2-\frac{B_4}{2}\right)}{\mu AL^4}\left(\frac{\partial^2\psi}{\partial\overline{x}^2}\right)-\frac{B_3}{\mu AL^6}\left(\frac{\partial^4\psi}{\partial\overline{x}^4}\right)\\
&\qquad\qquad-\left(\frac{c_3}{2}+c_2\right)\frac{A}{\mu AL^2}\left(\frac{\partial\overline{w}}{\partial\overline{x}}\right)+\frac{B_8}{2\mu AL^4}\left(\frac{\partial^3\overline{w}}{\partial\overline{x}^3}\right)=0;\\
&\overline{M}_2\,(1,\tau)=\frac{B_4}{2\mu AL^4}\left(\frac{\partial\psi}{\partial\overline{x}}\right)+\frac{B_3}{\mu AL^6}\left(\frac{\partial^3\psi}{\partial\overline{x}^3}\right)=0;
\end{aligned}
\tag{3.44}
$$

where $\overline{q}=\dfrac{q_0}{\mu A}e^{i\omega t}$ denotes the normalized harmonic excitation force. The extra kinematic parameters $\dfrac{\partial\overline{w}}{\partial\overline{x}}$, $\dfrac{\partial^2\overline{w}}{\partial\overline{x}^2}$ and $\dfrac{\partial\psi}{\partial\overline{x}}$ and $\dfrac{\partial^2\psi}{\partial\overline{x}^2}$ represent the inner relative movement between the adjacent micro-structures, hence the corresponding generalized loads

$\overline{V}_1$, $\overline{V}_2$ and $\overline{M}_1$, $\overline{M}_2$ represent the internal generalized force interactions of the adjacent micro-structures. With (3.43) and (3.44), 24 equations with the amplitudes of each progressive and retrograde wave as variables can be established. With some numerical calculation, the amplitudes of transverse displacement $\overline{w}$ and rotation angle ψ at observation point on each frequency can be obtained.

3.4.1 FRF result of analytical method

The numerical investigation of frequency response is proceed with the amplitude of excitation force $q_0 = 0.05\mu A$ at $x = L$. Figure 3.17 displays the normalized deflection magnitude $\overline{w}$ and rotation magnitude $\overline{w}$ at observation point $x = 0.7L$ in complex beam structure based on SSG theory model and in homogeneous beam structure based on classical theory model.

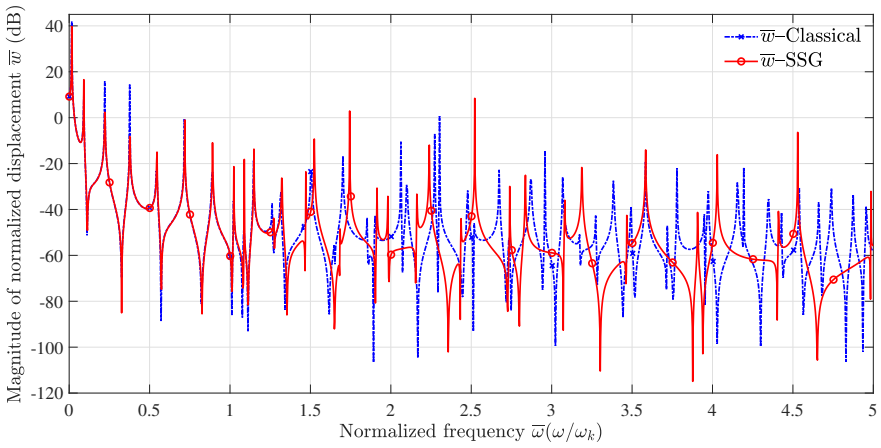

(a) Frequency response of $\overline{w}$

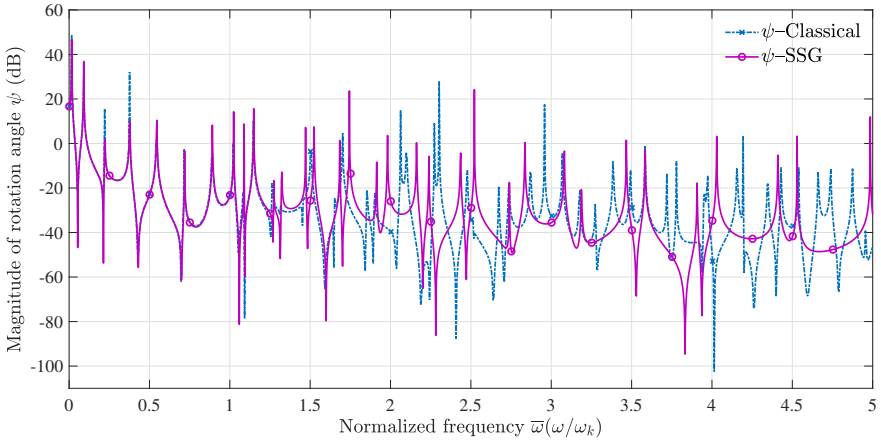

(b) Frequency response of ψ

Figure 3.17: Frequency response of $\overline{w}$ and ψ

As we can see, the resulting resonances of the SSG theory model match well with the classical results in frequency range $\overline{\omega} < 1$, when the wavelength generated by the excitation is much larger than the characteristic length of the beam. In higher frequency, less resonance peaks can be observed in complex beam structures. Due to the local behavior caused by complex micro-structure interactions, the input vibration energy can not only be transferred by the propagating waves, but also be converted into the other evanescent waves which decay rapidly in the near field of the excitation. The transfer power is distinctively less, and wave propagation feature as well as dynamic behavior of the complex structure is affected. This can be the interpretation for the reduction of resonance peaks. As frequency increase, wavelength generated by the excitation decrease and become more comparable with the characteristic length of the beam. Therefore micro-structure effects is more prominent, and the resulting frequency response shows more difference with the classical model.

3.4.2 Frequency response analysis in COMSOL

To verify the FRF results with wave approach, the frequency response analysis in section 3.4.1 is implemented in COMSOL. The modelling start with establishing one 1-D component by inserting interval of length '1' and selecting weak form PDE as the 'Physics'. To be specific, governing equations of six order partial difference is input in weak form in 'weak form PDE interface', and the boundary conditions are applied in from of 'Dirichlet boundary condition' or in form of 'Flux'. COMSOL can only solve the second order derivation, so two governing equations of 6-order partial differential are transformed into equations set with 12 variables including the transverse displacement $\overline{w}$ and rotation angle ψ, their first derivative u_1, ψ_1, second derivative u_2, ψ_2, the regular shear force $\overline{P}_0$ and moment $\overline{M}_0$ and four higher order

forces and moments $\overline{P}_1$, $\overline{P}_2$ and $\overline{M}_1$, $\overline{M}_2$.

$$
\begin{aligned}
&\frac{\partial}{\partial\bar{x}}\bar{V}_0+\bar{q}=m_0\frac{\partial^2\bar{w}}{\partial\tau^2}\\
&\bar{V}_0=-\psi-\left(\frac{(c_3+2c_2)\,A}{2\mu AL^2}\right)\left(\frac{\partial\psi_1}{\partial\bar{x}}\right)+\left(\frac{\partial\bar{w}}{\partial\bar{x}}\right)+\frac{c_3A}{2\mu AL^2}\left(\frac{\partial w_2}{\partial\bar{x}}\right)-\left(\frac{\partial\bar{V}_1}{\partial\bar{x}}\right)\\
&\bar{V}_1=\left(\frac{B_7}{2\mu AL^2}\right)\left(\frac{\partial\psi}{\partial\bar{x}}\right)+\frac{B_5}{\mu AL^2}\left(\frac{\partial w_1}{\partial\bar{x}}\right)-\left(\frac{\partial\bar{V}_2}{\partial\bar{x}}\right)\\
&\bar{V}_2=-\frac{c_3A}{2\mu AL^2}\psi+\frac{B_8}{2\mu AL^4}\left(\frac{\partial\psi_1}{\partial\bar{x}}\right)+\left(\frac{c_3A}{2\mu AL^2}\right)\left(\frac{\partial\bar{w}}{\partial\bar{x}}\right)+\frac{B_6}{\mu AL^4}\left(\frac{\partial w_2}{\partial\bar{x}}\right)\\
&w_1=\frac{\partial\bar{w}}{\partial\bar{x}},\qquad\overline{w}_2=\frac{\partial^2\bar{w}}{\partial\bar{x}^2}.\\
&-\psi+\frac{\partial}{\partial\bar{x}}\left(\bar{M}_0-\frac{(2c_2+c_3)\,A}{2\mu AL^2}\left(\frac{\partial\psi}{\partial\bar{x}}\right)+\bar{w}+\frac{c_3A}{2\mu AL^2}\left(\frac{\partial w_1}{\partial\bar{x}}\right)\right)=m_2\left(\frac{\partial^2\psi}{\partial\tau^2}\right);\\
&\bar{M}_0=\frac{B_1}{\mu AL^2}\left(\frac{\partial\psi}{\partial\bar{x}}\right)+\frac{B_4}{2\mu AL^4}\left(\frac{\partial\psi_2}{\partial\bar{x}}\right)+\frac{B_7}{2\mu AL^2}\left(\frac{\partial w_1}{\partial\bar{x}}\right)-\frac{\partial\bar{M}_1}{\partial\bar{x}},\\
&\bar{M}_1=\frac{(2c_2+c_3)\,A}{2\mu AL^2}\psi+\frac{B_2}{\mu AL^4}\left(\frac{\partial\psi_1}{\partial\bar{x}}\right)-\frac{(c_3+2c_2)\,A}{2\mu AL^2}\left(\frac{\partial\bar{w}}{\partial\bar{x}}\right)+\frac{B_8}{2\mu AL^4}\left(\frac{\partial w_2}{\partial\bar{x}}\right)-\frac{\partial\bar{M}_2}{\partial\bar{x}}\\
&\bar{M}_2=\frac{B_4}{2\mu AL^4}\left(\frac{\partial\psi}{\partial\bar{x}}\right)+\frac{B_3}{\mu AL^6}\left(\frac{\partial\psi_2}{\partial\bar{x}}\right);\\
&\psi_1=\frac{\partial\psi}{\partial\bar{x}},\qquad\psi_2=\frac{\partial^2\psi}{\partial\bar{x}^2}.
\end{aligned}
\tag{3.45}
$$

The shape function used for discretization is six-tic Hermite polynomials to guarantee the higher order derivative continuous condition. The component is meshed with maximum element size as 0.02, and the relative tolerance in solver is 10^{-5}.

As we can see in Figure 3.18, the frequency response resulting from COMSOL match well with response with wave approach. The previous formulation is rigorous and the result are validated. With the analytical equations deduced based on non-classical theory and proper input in forms of weak form, COMSOL can be employed to calculate the structural response of complex beam with less computational effort and wider frequency range. The utilization of COMSOL can significantly simplify the dynamic behavior investigation of complex media.

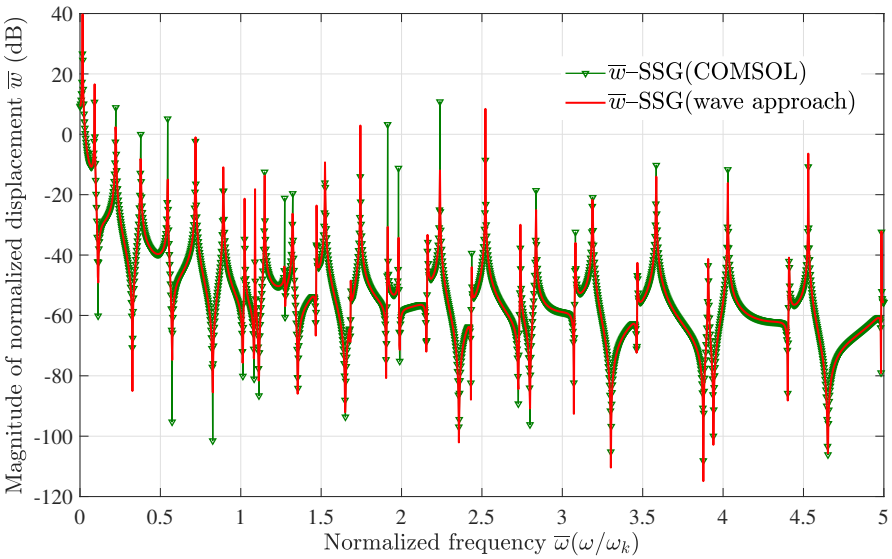

(a) Frequency response of $\overline{w}$

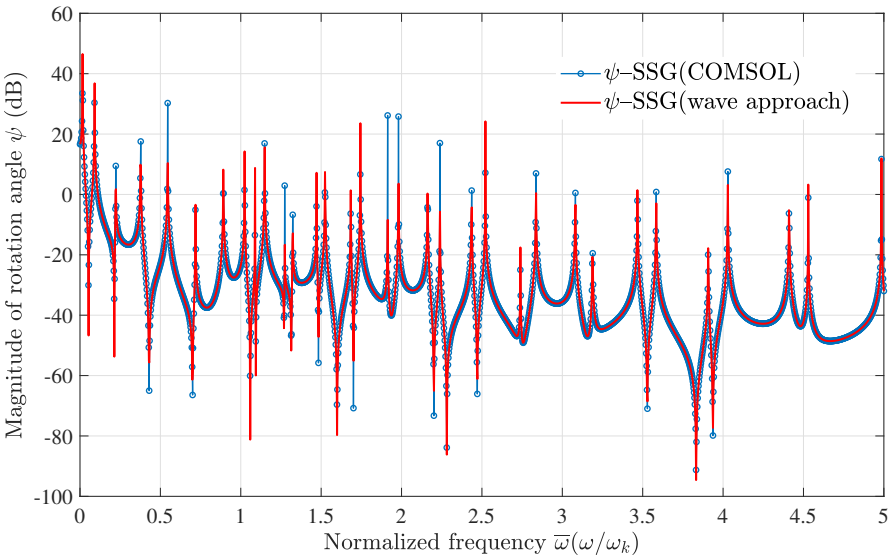

(b) Frequency response of ψ

Figure 3.18: Frequency response of $\overline{w}$ and ψ in COMSOL

3.5 Conclusions

Wave propagation in complex Timoshenko beam structure with consideration of local behaviors of heterogeneity is different from the classical one. In order to analyze this special behavior, one enriched model is established based on Mindlin's SSG theory. This formulation allows the micro-structure's effects to be captured, by considering the higher order strains into strain energy density, meanwhile the

heterogeneity to be described in the frame of continuum mechanics. From the numerical calculations, one can see that the proposed SSG theory-based beam model is effective in predicting the non-classical dispersive behaviors in complex media. Apart from the dispersion characteristics, this research also highlighted a number of interesting features of the modal density, the energy flux and the resulting frequency response of the complex beam. Some conclusions can be drawn from the numerical calculation and discussions as follows:

(1) There are six wave modes that can be generated in complex Timoshenko beam based on second strain gradient theory, of which the non-classical bending wave k_1 and non-classical shear wave k_2 are the propagating waves, and they both propagate in dispersive manner, and the dispersive behavior become more prominent in higher frequency.The other 4 waves are all evanescent waves (near field). In higher frequency, energy dissipation through viscous damping for wave k_1 and k_2 become negligible compared with classical result. As dimension goes up, micro-structural effect is weaken due to the increasing of structural characteristic length.

(2) The proposed formulation of the energy flux was validated, as the energy velocity V_e and group velocity c_g of conservative waves, the non-classical bending wave k_1 and shear wave k_2, are proved to be identical in the whole frequency range. Energy flux is coupled with one classical shear force, one bending moment and four higher order generalized forces, which are resultants of classical and higher-order stresses generated on the surface of the observed section.

(3) The complex beam structure with considering the long range interactions shows more resistance to the force excitation in terms of both deflection and rotation movement. The net power transmitted into the complex beam diminish distinctly compared with the classical result due to the complex force interaction on the point of harmonic force excitation. More proportion of work is in forms of reactive power which does not transform power from force or dissipate power.

(4) The generated disturbance propagate away in a different manner in the complex beam. Transfer mobility modulus $|\overline{Y}_{\mathrm{w}}|$ as well as reactive power $\overline{Q}$-SSG decay significantly in the near field of the excitation point, the latter is mostly caused by reduction of shear force component $\overline{Q}_V$-SSG. The decrease in near field becomes significant in higher frequency as the micro-structure interaction is more prominent. Near field effect has little influence on rotation related transfer mobility $\overline{Y}_{\psi}$ or moment related transfer reactive power $\overline{Q}_M$-SSG. As the rotation angle at $x = 0$ equals zero in transverse force excitation case, which cannot generate energy conversion from regular rotation deformation to higher order rotation deformation. The greater the distance between the points of observation and force application, the smaller the near-field effect.

(5) The statistical value of the modal density for the non-classical bending wave k_1 as well as the non-classical shear wave are lower than the classical results due to the influence of micro-structure effect. From the FRF analysis, the first few resonances match well with the classical result. In higher frequency range, when the wavelength generated by the excitation is comparable with the length of inner micro-structure, less resonance peaks can be observed in the same frequency range.

Due to the heterogeneity caused by micro-structure interactions, the input vibration energy can not only be transferred to far field by the propagating waves, but also be converted into the evanescent waves in the near field of the excitation which decay rapidly in the near field of the excitation. The transfer power is distinctively less, and wave propagation feature as well as dynamic behavior of the complex structure is affected.

Chapter 4

Wave transmission and reflection between complex structures based on SSG theory model

Contents

4.1 Introduction

Wave transmission and reflection analysis between different mediums is constructive for comprehension of vibrating transmission through sub-systems, and further more vibration active control of sub-structures. According to previous analysis, we can say that wave propagation field in complex media process different characteristics from the classical media due to complex micro-structure interactions, and that difference will lead to significant impact to vibration transmission and reflection. In this chapter, vibration transmission through a planar interface between two complex

mediums is evaluated based on the proposed SSG theory rod model and beam model. The analysis is proceed in respects of transmission and reflection coefficients along with the power flow. The formulation of wave transmission through a certain length of complex rod structure is derived, then one approach of vibration transmission control is introduced by controlling the geometrical and material property of the complex media based on the proposed formulation.

4.2 Analysis of wave transmission and reflection through planar interface between two complex rod structure

In this section, one investigation is implemented to describe the vibration transmission and reflection behavior between two complex rods on the basis of the proposed SSG theory-based rod. Transmission and reflection of non-classical longitudinal wave through one planar interface between two complex rods are analyzed in terms of transmission and reflection coefficients as well as transmitted and reflected power flow. Figure 4.1 illustrates the studied system consisting of rod 1 and rod 2, which are connected together with same circular cross section but different material properties. Young's modulus and material density are denoted with E and ρ for rod 1, E' and ρ' for rod 2. The coefficients associated with their higher order material constants are respectively denoted with B_1, B_2, B_3 for rod 1 and B_1', B_2', B_3' for rod 2.

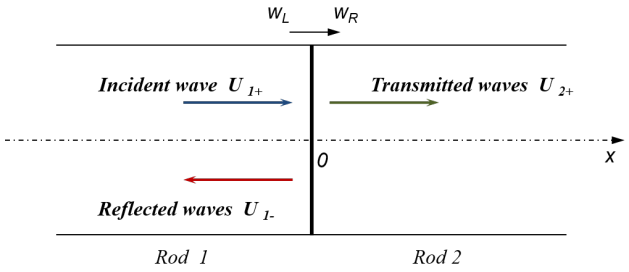

Figure 4.1: Reflection and transmission of longitudinal wave at normal incidence to a plane boundary

4.2.1 Reflection and transmission of non-classical longitudinal wave

From the formulation of non-classical dispersion relation in Sec. 1.2.1, we know that 3 types of wave modes can be generated in complex rod based on SSG theory model, let's say wave modes k_1, k_2, k_3 are generated in rod 1 while k_4, k_5, k_6 are generated in rod 2. Assuming the non-classical longitudinal wave k_1 with amplitude $\mathcal{A}_1$ propagates from negative infinity and vertically injects on the discontinuous surface at $x = 0$, the displacement contributed by incident longitudinal wave U_{1+}

can be expressed in Eq. (4.1)

$$w_{1+} = \mathcal{A}_1 \cdot e^{i(\omega t - k_1 x)}. \tag{4.1}$$

The mentioned six wave modes are generated by the incident wave k_1 on the discontinuous surface and propagate away respectively along $-x$ direction and $+x$ direction. Assuming the amplitudes of the reflected wave modes k_1, k_2, k_3 are denoted by $\mathcal{B}_1$, $\mathcal{C}_1$, $\mathcal{D}_1$, and the amplitudes of transmitted wave modes k_4, k_5, k_6 are denoted by $\mathcal{B}_2$, $\mathcal{C}_2$, $\mathcal{D}_2$, the displacement amplitude caused by reflected waves U_{1-} on the left hand of the interface and the displacement amplitude caused by transmitted waves U_{2+} on the right hand of the interface can be written as (omitting the time component $e^{i\omega t}$)

$$\begin{aligned} w_{1-} &= \mathcal{B}_1 \cdot e^{ik_1 x} + \mathcal{C}_1 \cdot e^{ik_2 x} + \mathcal{D}_1 \cdot e^{ik_3 x}, \\ w_{2+} &= \mathcal{B}_2 \cdot e^{-ik_4 x} + \mathcal{C}_2 \cdot e^{-ik_5 x} + \mathcal{D}_2 \cdot e^{-ik_6 x}, \end{aligned} \tag{4.2}$$

in which '1' '2' indicate the rod 1 and rod 2. '+', '–' indicate the positive and negative wave propagation direction. Then the displacement on the left hand of interface w_L and the displacement on the right hand of the interface w_R are given by the superposition of the contribution from all wave modes as

$$\begin{aligned} w_L &= \mathcal{A}_1 \cdot e^{-ik_1 x} + \mathcal{B}_1 \cdot e^{ik_1 x} + \mathcal{C}_1 \cdot e^{ik_2 x} + \mathcal{D}_1 \cdot e^{ik_3 x}, \\ w_R &= \mathcal{B}_2 \cdot e^{-ik_4 x} + \mathcal{C}_2 \cdot e^{-ik_5 x} + \mathcal{D}_2 \cdot e^{-ik_6 x}, \end{aligned} \tag{4.3}$$

in which 'L', 'R' indicate the rod 1 and rod 2. The force and higher-order forces on the left hand of the interface produced in rod 1 can be expressed with the displacement w_L as

$$\begin{aligned} {P_0}^L &= EA\frac{\partial w_L}{\partial x} + (B_3 - B_1)\frac{\partial^3 w_L}{\partial x^3} + \mathcal{B}_2\frac{\partial^5 w_L}{\partial x^5}, \\ {P_1}^L &= \left(B_1 - \frac{B_3}{2}\right)\frac{\partial^2 w_L}{\partial x^2} - B_2\frac{\partial^4 w_L}{\partial x^4}, \\ {P_2}^L &= \frac{B_3}{2}\frac{\partial w_L}{\partial x} + B_2\frac{\partial^3 w_L}{\partial x^3}. \end{aligned} \tag{4.4}$$

While the force and higher-order forces on the right hand of the interface produced in rod 2 can be also expressed with the displacement w_R as

$$\begin{aligned} {P_0}^R &= E'A\frac{\partial w_R}{\partial x} + \left(B_3' - B_1'\right)\frac{\partial^3 w_R}{\partial x^3} + B_2'\frac{\partial^5 w_R}{\partial x^5}, \\ {P_1}^R &= \left(B_1' - \frac{B_3'}{2}\right)\frac{\partial^2 w_R}{\partial x^2} - B_2'\frac{\partial^4 w_R}{\partial x^4}, \\ {P_2}^R &= \frac{B_3'}{2}\frac{\partial w_R}{\partial x} + B_2'\frac{\partial^3 w_R}{\partial x^3}. \end{aligned} \tag{4.5}$$

Assuming the interface does not dissipate energy, and the mass of the rod between $x = 0^+$ and $x = 0^-$ is infinitesimal, the force equilibrium can be developed at

$x = 0$. ***Amplitudes of each transmitted waves and reflected waves can be estimated based on the continuity of displacement, the first derivative of the displacement, and the second derivative of the displacement along with the equilibrium of the force and higher order forces*** as

$$\left[w, \frac{\partial w}{\partial x}, \frac{\partial^2 w}{\partial x^2}, P_0, P_1, P_1\right]\Big|_{w=w_L} = \left[w, \frac{\partial w}{\partial x}, \frac{\partial^2 w}{\partial x^2}, P_0, P_1, P_1\right]\Big|_{w=w_R}. \tag{4.6}$$

Reflection coefficients and transmission coefficients are respectively defined by the ratio of the complex amplitude of the reflected wave and the amplitude of the complex transmitted wave to that of the incident wave at a discontinuity. With the equilibrium in Eq. (4.6), amplitudes of all the reflected waves and transmitted waves in solution (4.2) can be achieved, then the reflection coefficients and transmission coefficients are presented in the form of amplitude ratios as follows.

$$R_1 = \frac{\mathcal{B}_1}{\mathcal{A}_1}, \quad R_2 = \frac{\mathcal{C}_1}{\mathcal{A}_1}, \quad R_3 = \frac{\mathcal{D}_1}{\mathcal{A}_1}, \quad T_1 = \frac{\mathcal{B}_2}{\mathcal{A}_1}, \quad T_2 = \frac{\mathcal{C}_2}{\mathcal{A}_1}, \quad T_3 = \frac{\mathcal{D}_2}{\mathcal{A}_1}. \tag{4.7}$$

R_1, R_2 and R_3 are the reflection coefficients for wave k_1, k_2 and k_3; T_1, T_2 and T_3 are the transmission coefficients for wave k_4, k_5 and k_6.

According to Sec. 2.2.4, energy flux in complex rod based on SSG theory model is a combination of work by the classical force and the higher order forces, then the incident wave power on the interface can be expressed as

$$E_{incident} = -\frac{1}{2}\mathrm{Re}\left[P_0 \cdot \dot{w}_{1+}^* + P_1 \cdot \left(\frac{\partial \dot{w}_{1+}}{\partial x}\right)^* + P_2 \cdot \left(\frac{\partial^2 \dot{w}_{1+}}{\partial x^2}\right)^*\right]\Big|_{w=w_{1+}}. \tag{4.8}$$

P_0, P_1 and P_2 in the Eq. (4.8) are only in dependence of w_{1+}, the displacement consisted by the incident wave modes, and derivatives of w_{1+}. Similarly, the energy flux reflected from the in-continuous interface can be expressed as

$$E_{reflection} = -\frac{1}{2}\mathrm{Re}\left[P_0 \cdot \dot{w}_{1-}^* + P_1 \cdot \left(\frac{\partial \dot{w}_{1-}}{\partial x}\right)^* + P_2 \cdot \left(\frac{\partial^2 \dot{w}_{1-}}{\partial x^2}\right)^*\right]\Big|_{w=w_{1-}}, \tag{4.9}$$

in which P_0, P_1 and P_2 are only in dependence of w_{1-}, the displacement consisted by the reflected wave modes, and derivatives of w_{1-}. And the transmitted energy flux is given as

$$E_{transmission} = -\frac{1}{2}\mathrm{Re}\left[P_0 \cdot \dot{w}_{2+}^* + P_1 \cdot \left(\frac{\partial \dot{w}_{2+}}{\partial x}\right)^* + P_2 \cdot \left(\frac{\partial^2 \dot{w}_{2+}}{\partial x^2}\right)^*\right]\Big|_{w=w_{2+}}. \tag{4.10}$$

in which P_0, P_1 and P_2 are only in dependence of w_{2+}, the displacement consisted by the transmitted wave modes, and derivatives of w_{2+}. The transmitted energy ratio and reflected flux ratio can be evaluated by normalizing the transmitted energy flux and the reflected energy flux with the incident power as

$$J_r = \frac{E_{reflection}}{E_{incident}}; \qquad J_t = \frac{E_{transmission}}{E_{incident}};$$

Table 4.1: High-order material constants for copper(Shodja et al.,2012).

a_1(eV/Å)	a_2(eV/Å)	a_3(eV/Å)	a_4(eV/Å)	a_5(eV/Å)		
0.1833	0.0103	0.0010	0.0717	0.1891		
b_1(eV/Å)	b_2(eV/Å)	b_3(eV/Å)	b_4(eV/Å)	b_5(eV/Å)	b_6(eV/Å)	b_7(eV/Å)
0.6612	0.0663	−0.2062	−0.0015	−0.0015	12.6254	37.9402
c_1(eV/Å)	c_2(eV/Å)	c_3(eV/Å)				
0.8448	0.5732	0.3465				

4.2.2 Numerical calculation of reflection and transmission characteristics

Numerical calculation for reflection and transmission characteristics at the discontinuous surface through different complex rods is conducted in this section based on the formulation. As shown in Figure 4.1, rod 1 and rod 2 are connected with same cross section radius $r = 3a_0$. Rod 1 is made of aluminum and the material constants have been illustrated in Sec.2.2.2. Rod 2 is made of copper with $\mu' = 40$GPa and $\rho' = 8.96 \times 10^3 \text{kg/m}^3$, and the higher-order material constants are shown in Table 4.1. Substitute these values into the formulation in Sec. 4.2.1, we can easily achieved the reflection and transmission coefficients as well as the energy transmitted ratio.

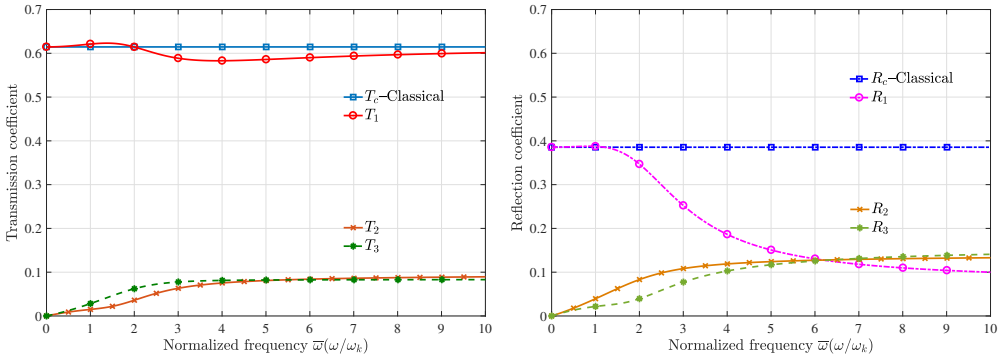

(a) Transmission coefficients (b) Reflection coefficients

Figure 4.2: Transmission and reflection coefficients

Figure 4.2 depicts the transmission and reflection coefficients based on SSG theory and classical theory. Compared with the classical transmission coefficient T_c and reflection coefficients R_c which keep constant in whole frequency range, the SSG theory results are frequency dependent and change significantly especially for R_1. In higher frequency, R_1 decreases dramatically compared with the classical result R_c, while T_1 changes slightly. Transmission and reflection coefficients T_2, T_3, R_2 and R_3 all grow up as frequency goes up.

In order to verify the size effect for the wave reflection behavior, reflection coefficients of wave k_1 propagating in complex rods with increasing dimensions are analyzed and the results are illustrated in Figure 4.3. We can see the reflection

coefficient of k_1 increase and approach to the classical result as the cross section radius r increasing from $5a_0$ to $15a_0$.

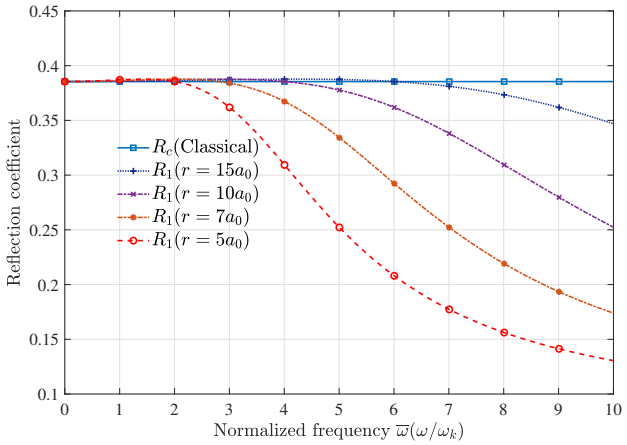

Figure 4.3: Size effect of reflection coefficients

Based on the previous formulation, it is admitted that energy conversion to the extra evanescent waves k_2 and k_3 leads to great differences in energy transmission. To achieve more information, we intended to calculate the energy conserved in all three modes separately, but it is impossible due to the strong coupling between these three modes in terms of energy flux. Therefore, in order to investigate the energy transmitted ratio in SSG theory model, Figure 4.4 is displayed.

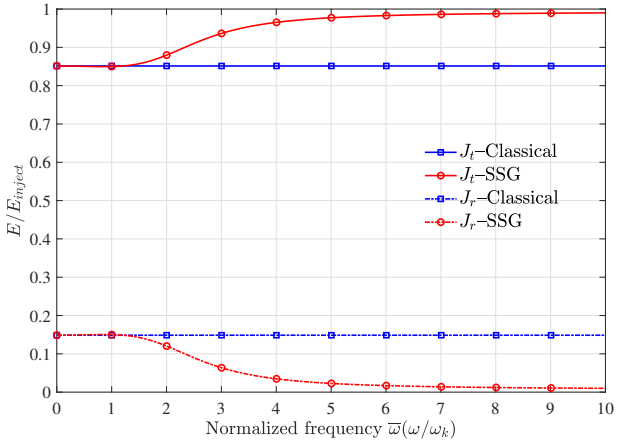

Figure 4.4: Energy transmission and reflection

Figure 4.4 shows the distribution of transmitted energy and reflected energy conserved in all diffused wave modes. We notice that even though energy transmitted ratio between complex rods increase and meanwhile the energy reflected ratio decrease, the summation of these two values is still '1', which indicates the previous SSG theory-based formulations are valid. Thus the incident energy is predicted to

transmit more and reflect less. Combined with Figure 4.2(a), we noted that the transmitted energy diffuse quite large percentage to wave modes k_2 and k_3, so T_1, the transmission coefficient of non-classical longitudinal wave k_1 is actually decreasing. Conversely, the total reflected energy decreases slightly, but with considering the energy diffusion into k_2 and k_3, the reflection coefficient for wave k_1 decrease dramatically.

4.3 Analysis of wave transmission and reflection through planar interface between two complex beam structures

In this section, one investigation is implemented to describe vibration transmission and reflection behavior between two complex beams with considering the microstructure effect based on the proposed SSG theory beam model. Transmission and reflection of the non-classical bending wave through one planar interface between two complex Timoshenko beam are analyzed in terms of transmission and reflection coefficients as well as transmitted and reflected power flow. Figure 4.5 illustrates the studied system consisting of beam 1 and beam 2, which are connected together with same rectangular cross section but different material properties. Lamé's second parameter and material density are denoted with μ and ρ for beam 1, μ' and ρ' for beam 2. The higher order material constants are denoted with a_i, b_i, and c_i for beam 1 and a_i', b_i', c_i' for beam 2. The coefficients associated with material higher order constants are denoted with B_i for beam 1 and B_i' for beam 2.

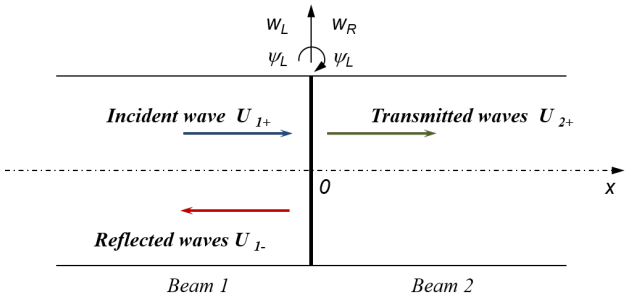

Figure 4.5: Wave reflection and transmission of bending wave

4.3.1 Reflection and transmission of non-classical bending wave

According to the formulation of non-classical dispersion relation in complex beam in Sec. 3.2.2, we know that 6 different wave modes can be generated in complex Timoshenko beam based on SSG theory model, let's say modes k_j $(j = 1, 2, ...6)$ can be generated in beam 1 while k_j' $(j = 1, 2, ...6)$ are generated in beam 2. Assuming bending wave k_1 with amplitude $\mathcal{A}_1$ propagates from negative infinity and vertically injects on the discontinuous surface at $x = 0$, then the transverse displacement w_{1+}

and rotation angle ψ_{1+} caused by the incident wave can be expressed as

$$\begin{aligned} w_{1+} &= \mathcal{A}_1 \cdot e^{i(\omega t - k_1 x)}, \\ \psi_{1+} &= \alpha_1 \cdot \mathcal{A}_1 \cdot e^{i(\omega t - k_1 x)}. \end{aligned} \tag{4.11}$$

in which, α_1 represents the relation between amplitude of transverse displacement and amplitude of rotation angle consisted by wave mode k_1 in form of

$$\alpha_1 = \frac{-2i\left(-B_6{k_1}^6 + c_3 A{k_1}^4 - B_5{k_1}^4 - \mu A{k_1}^2 + m_0\omega^2\right)}{k_1\left(B_8{k_1}^4 + 2c_2 A{k_1}^2 + 2c_3 A{k_1}^2 + B_7{k_1}^2 - 2\mu A\right)}; \tag{4.12}$$

For SSG theory-based beam model, not only bending wave, shear wave but also the extra evanescent waves can be diffused on the discontinuous interface, hence 12 wave modes will be diffused out at the discontinuity. Wave k_j $(j = 1, 2, ...6)$ are reflected and negative going waves, while k_j' $(j = 1, 2, ...6)$ are transmitted and positive going waves. The transverse displacement w_{1-} and rotation angle ψ_{1-} caused by the reflected wave group U_{1-} can be expressed respectively by the substitution of the reflected wave modes in beam 1 as

$$w_{1-} = \sum_{j=1}^{6} \mathcal{B}_j e^{ik_j x}, \qquad \psi_{1-} = \sum_{j=1}^{6} \beta_j \mathcal{B}_j e^{ik_j x} \tag{4.13}$$

where '1' indicates beam 1 and '–' indicates the negative going wave propagation direction. β_j represents the relation between amplitude of transverse displacement and amplitude of rotation angle consisted by each reflected wave mode $-k_j$ in beam 1 on difference frequency in form of

$$\beta_j = \frac{2i\left(-B_6{k_j}^6 + c_3 A{k_j}^4 - B_5{k_j}^4 - \mu A{k_j}^2 + m_0\omega^2\right)}{k_j\left(B_8{k_j}^4 + 2c_2 A{k_j}^2 + 2c_3 A{k_j}^2 + B_7{k_j}^2 - 2\mu A\right)}; (j = 1, 2...6)$$

The transverse displacement w_{2+} and rotation angle ψ_{2+} caused by the transmitted wave group U_{2+} can be expressed respectively by the superposition of the transmitted wave modes in beam 2 as

$$w_{2+} = \sum_{j=1}^{6} \mathcal{C}_j e^{-jk_j' x}, \qquad \psi_{2+} = \sum_{j=1}^{6} \alpha_j' \mathcal{C}_j e^{-jk_j' x} \tag{4.14}$$

in which '2' indicate beam 2 and '+' indicate the positive going wave propagation direction. α_j' represent the relation between amplitude of transverse displacement and amplitude of rotation angle consisted by each transmitted wave mode k_j' on difference frequency in form of

$$\alpha_j' = \frac{-2i\left(-B_6'{k_j'}^6 + c_3' A{k_j'}^4 - B_5'{k_j'}^4 - \mu' A{k_j'}^2 + m_0'\omega^2\right)}{k_j'\left(B_8'{k_j'}^4 + 2c_2' A{k_j'}^2 + 2c_3' A{k_j'}^2 + B_7{k_j'}^2 - 2\mu' A\right)}; (j = 1, 2...6) \tag{4.15}$$

Then the transverse displacement and rotation angle on the left hand of interface w_L, ψ_L and the transverse displacement and rotation angle on the right hand of the interface w_R, ψ_R are given as (omitting time component)

$$\begin{aligned} w_L &= \mathcal{A}_1 \cdot e^{-ik_1 x} + \sum_{j=1}^{6} \mathcal{B}_j e^{ik_j x}, \qquad \psi_L = \alpha_1 \mathcal{A}_1 \cdot e^{-ik_1 x} + \sum_{j=1}^{6} \beta_j \mathcal{B}_j e^{ik_j x}, \\ w_R &= \sum_{j=1}^{6} \mathcal{C}_j e^{-ik'_j x}, \qquad\qquad \psi_R = \sum_{j=1}^{6} \alpha'_j \mathcal{C}_j e^{-ik'_j x}, \end{aligned} \tag{4.16}$$

in which 'L', 'R' indicate displacement field on the left hand of interface and on the right hand of the interface. On basis of the solution form of transverse displacement w_L and rotation angle ψ_L in beam 1, the generalized force and higher-order forces as well as moment and higher order moments produced on the left hand of the interface $x = 0$ can be expressed as

$$\begin{aligned} {V_0}^L =& -\mu A \psi_L - \left(\frac{B_7}{2} + (c_3 + c_2)\, A\right)\left(\frac{\partial^2 w_L}{\partial x^2}\right) + \frac{B_8}{2}\left(\frac{\partial^4 \psi_L}{\partial x^4}\right) + \mu A \left(\frac{\partial w_L}{\partial x}\right) \\ &+ (c_3 A - B_5)\left(\frac{\partial^3 w_L}{\partial x^3}\right) + B_6 \left(\frac{\partial^5 w_L}{\partial x^5}\right) \\ {V_1}^L =& \left(\frac{B_7 + c_3 A}{2}\right)\left(\frac{\partial \psi_L}{\partial x}\right) - \frac{B_8}{2}\left(\frac{\partial^3 \psi_L}{\partial x^3}\right) + (B_5 - c_3 A)\left(\frac{\partial^2 w_L}{\partial x^2}\right) - B_6 \left(\frac{\partial^4 w_L}{\partial x^4}\right) \\ {V_2}^L =& -\frac{c_3 A}{2}\psi_L + \frac{B_8}{2}\left(\frac{\partial^2 \psi_L}{\partial x^2}\right) + \frac{c_3 A}{2}\left(\frac{\partial w_L}{\partial x}\right) + B_6 \left(\frac{\partial^3 w_L}{\partial x^3}\right). \\ {M_0}^L =& \left(B_1 - A\left(c_2 + \frac{c_3}{2}\right)\right)\left(\frac{\partial \psi_L}{\partial x}\right) + (B_4 - B_2)\left(\frac{\partial^3 \psi_L}{\partial x^3}\right) + B_3 \left(\frac{\partial^5 \psi_L}{\partial x^5}\right) \\ &+ \left(\frac{B_7}{2} + A\,(c_3 + c_2)\right)\left(\frac{\partial^2 w_L}{\partial x^2}\right) - \frac{B_8}{2}\left(\frac{\partial^4 w_L}{\partial x^4}\right) \\ {M_1}^L =& A\left(c_2 + \frac{c_3}{2}\right)\psi_L + \left(B_2 - \frac{B_4}{2}\right)\left(\frac{\partial^2 \psi_L}{\partial x^2}\right) - B_3 \left(\frac{\partial^4 \psi_L}{\partial x^4}\right) \\ &- A\left(\frac{c_3}{2} + c_2\right)\left(\frac{\partial w_L}{\partial x}\right) + \frac{B_8}{2}\left(\frac{\partial^3 w_L}{\partial x^3}\right) \\ {M_2}^L =& \frac{B_4}{2}\left(\frac{\partial \psi_L}{\partial x}\right) + B_3 \left(\frac{\partial^3 \psi_L}{\partial x^3}\right) \end{aligned}$$

On basis of the solution form of transverse displacement w_R and rotation angle ψ_R in beam 2, the generalized force and higher-order forces as well as moment and higher order moments produced on the right hand of the interface $x = 0$ can be

expressed as

$$
\begin{aligned}
{V_0}^R =& -\mu' A\psi_R - \left(\frac{{B_7}'}{2} + \left({c_3}' + {c_2}'\right) A\right)\left(\frac{\partial^2 w_R}{\partial x^2}\right) + \frac{{B_8}'}{2}\left(\frac{\partial^4 \psi_R}{\partial x^4}\right) + \mu' A\left(\frac{\partial w_R}{\partial x}\right) \\
&+ \left({c_3}' A - {B_5}'\right)\left(\frac{\partial^3 w_R}{\partial x^3}\right) + {B_6}'\left(\frac{\partial^5 w_R}{\partial x^5}\right) \\
{V_1}^R =& \left(\frac{{B_7}' + {c_3}' A}{2}\right)\left(\frac{\partial \psi_R}{\partial x}\right) - \frac{{B_8}'}{2}\left(\frac{\partial^3 \psi_R}{\partial x^3}\right) + \left({B_5}' - {c_3}' A\right)\left(\frac{\partial^2 w_R}{\partial x^2}\right) - {B_6}'\left(\frac{\partial^4 w_R}{\partial x^4}\right) \\
{V_2}^R =& -\frac{{c_3}' A}{2}\psi_R + \frac{{B_8}'}{2}\left(\frac{\partial^2 \psi_R}{\partial x^2}\right) + \frac{{c_3}' A}{2}\left(\frac{\partial w_R}{\partial x}\right) + {B_6}'\left(\frac{\partial^3 w_R}{\partial x^3}\right). \\
{M_0}^R =& \left({B_1}' - A\left({c_2}' + \frac{{c_3}'}{2}\right)\right)\left(\frac{\partial \psi_R}{\partial x}\right) + \left({B_4}' - {B_2}'\right)\left(\frac{\partial^3 \psi_R}{\partial x^3}\right) + {B_3}'\left(\frac{\partial^5 \psi_R}{\partial x^5}\right) \\
&+ \left(\frac{{B_7}'}{2} + A\left({c_3}' + {c_2}'\right)\right)\left(\frac{\partial^2 w_R}{\partial x^2}\right) - \frac{{B_8}'}{2}\left(\frac{\partial^4 w_R}{\partial x^4}\right) \\
{M_1}^R =& A\left({c_2}' + \frac{{c_3}'}{2}\right)\psi_R + \left({B_2}' - \frac{{B_4}'}{2}\right)\left(\frac{\partial^2 \psi_R}{\partial x^2}\right) - {B_3}'\left(\frac{\partial^4 \psi_R}{\partial x^4}\right) \\
&- A\left(\frac{{c_3}'}{2} + {c_2}'\right)\left(\frac{\partial w_R}{\partial x}\right) + \frac{{B_8}'}{2}\left(\frac{\partial^3 w_R}{\partial x^3}\right) \\
{M_2}^R =& \frac{{B_4}'}{2}\left(\frac{\partial \psi_R}{\partial x}\right) + {B_3}'\left(\frac{\partial^3 \psi_R}{\partial x^3}\right)
\end{aligned}
$$

To avoid the difficulty of establishing multiple equilibrium equations, one state vector is defined here. For the studied section $x = x_0$ in complex Timoshenko beam based on the SSG theory model, the state vector should includes all 12 components describing its state of motion and force condition as shown in Eq. (4.17),

$$
\mathbf{X} = \left[w, \frac{\partial w}{\partial x}, \frac{\partial^2 w}{\partial x^2}, \mathrm{V}_0, \mathrm{V}_1, \mathrm{V}_2, \psi, \frac{\partial \psi}{\partial x}, \frac{\partial^2 \psi}{\partial x^2}, \mathrm{M}_0, \mathrm{M}_1, \mathrm{M}_2\right]\Bigg|_{\ x = x_0}. \tag{4.17}
$$

Assuming the interface does not dissipate energy, and the mass of the beam between $x = 0^-$ and $x = 0^+$ is infinitesimal, the force equilibrium can be developed at $x = 0$. ***Amplitudes of each transmitted waves and reflected waves can be estimated based on the continuity of state vector*** as

$$
\mathbf{X}|_{\substack{w=w_L \\ \psi=\psi_L}} = \mathbf{X}|_{\substack{w=w_R \\ \psi=\psi_R}} \tag{4.18}
$$

Based on Eq. (4.18), 12 equations can be built and the amplitudes of all the reflected waves and transmitted waves can be calculated and expressed by $\mathcal{A}_1$. The reflection coefficients for wave k_j and and transmission coefficients for wave k_j' $(j = 1, 2, ...6)$ are presented in the form of amplitude ratios as follows,

$$
R_i = \frac{\mathcal{B}_j}{\mathcal{A}_1}, \qquad T_i = \frac{\mathcal{C}_j}{\mathcal{A}_1} \tag{4.19}
$$

According to analysis in Sec. 3.2.4, energy flux in complex Timoshenko beam based on SSG theory model is a combination of work by the classical force the classical

moment along with the higher order forces and higher order moments, hence the incident wave power on the interface can be expressed as

$$E_{incident} = -\frac{1}{2}\mathrm{Re}\left[\begin{array}{l} V_0 \cdot \dot{w}_{1+}^* + V_1 \cdot \left(\dfrac{\partial \dot{w}_{1+}}{\partial x}\right)^* + V_2 \cdot \left(\dfrac{\partial^2 \dot{w}_{1+}}{\partial x^2}\right)^* \\ +M_0 \cdot \dot{\psi}_{1+}^* + M_1 \cdot \left(\dfrac{\partial \dot{\psi}_{1+}}{\partial x}\right)^* + M_2 \cdot \left(\dfrac{\partial^2 \dot{\psi}_{1+}}{\partial x^2}\right)^* \end{array}\right]\Bigg|_{\substack{w=w_{1+} \\ \psi=\psi_{1+}}} \tag{4.20}$$

V_0, V_1, V_2 and M_0, M_1, M_2 in the Eq. (4.20) are generalized forces and moments produced in beam 1 in dependence of w_{1+} and ψ_{1+}, the transverse displacement and rotation angle caused by the incident wave, along with their derivatives. Similarly, the energy flux reflected from the in-continuous interface can be expressed as

$$E_{reflection} = -\frac{1}{2}\mathrm{Re}\left[\begin{array}{l} V_0 \cdot \dot{w}_{1-}^* + V_1 \cdot \left(\dfrac{\partial \dot{w}_{1-}}{\partial x}\right)^* + V_2 \cdot \left(\dfrac{\partial^2 \dot{w}_{1-}}{\partial x^2}\right)^* \\ +M_0 \cdot \dot{\psi}_{1-}^* + M_1 \cdot \left(\dfrac{\partial \dot{\psi}_{1-}}{\partial x}\right)^* + M_2 \cdot \left(\dfrac{\partial^2 \dot{\psi}_{1-}}{\partial x^2}\right)^* \end{array}\right]\Bigg|_{\substack{w=w_{1-} \\ \psi=\psi_{1-}}} \tag{4.21}$$

in which V_0, V_1, V_2 and M_0, M_1, M_2 are generalized forces and moments produced in beam 1 in dependence of w_{1-}, ψ_{1-}, the transverse displacement and rotation angle caused by the reflected wave modes, along with their derivatives. The transmitted energy flux can be expressed as

$$E_{transmission} = -\frac{1}{2}\mathrm{Re}\left[\begin{array}{l} V_0 \cdot \dot{w}_{2+}^* + V_1 \cdot \left(\dfrac{\partial \dot{w}_{2+}}{\partial x}\right)^* + V_2 \cdot \left(\dfrac{\partial^2 \dot{w}_{2+}}{\partial x^2}\right)^* \\ +M_0 \cdot \dot{\psi}_{2+}^* + M_1 \cdot \left(\dfrac{\partial \dot{\psi}_{2+}}{\partial x}\right)^* + M_2 \cdot \left(\dfrac{\partial^2 \dot{\psi}_{2+}}{\partial x^2}\right)^* \end{array}\right]\Bigg|_{\substack{w=w_{2+} \\ \psi=\psi_{2+}}} \tag{4.22}$$

V_0, V_1, V_2 and M_0, M_1, M_2 are the generalized forces and moments produced in beam 2 and contributed from w_{2+} and ψ_{2+}, the transverse displacement and rotation angle caused by the transmitted wave modes, along with their derivatives. Energy transmitted ratio J_t and reflected ratio J_r can be achieved by normalizing the transmitted energy as well as the reflected energy with the incident power as

$$J_r = \frac{E_{reflection}}{E_{incident}}; \qquad J_t = \frac{E_{transmission}}{E_{incident}}.$$

4.3.2 Numerical calculation of non-classical reflection and transmission characteristics

Numerical calculation is implemented for vibration transmission and reflection characteristics through one discontinuous planer interface between two complex beams based on the formulation. As shown in Figure 4.5, beam 1 and beam 2 are connected with cross section of the same rectangle geometrical shape. The height of

cross section $h = 10a_0$ and the width $b = 3h$. The normalization parameter for length is set as $L = 5h$. Beam 1 is made of aluminum and the material constants have been illustrated in Sec.2.2.2. Beam 2 is made of copper with $\mu' = 40\text{GPa}$ and $\rho' = 8.96 \times 10^3 \text{kg/m}^3$, and the higher-order material constants are shown in Table 4.1. Substitute these values into the formulations in section 4.3.1, we can easily achieved the reflection and transmission coefficients as well as the energy transmitted ratio.

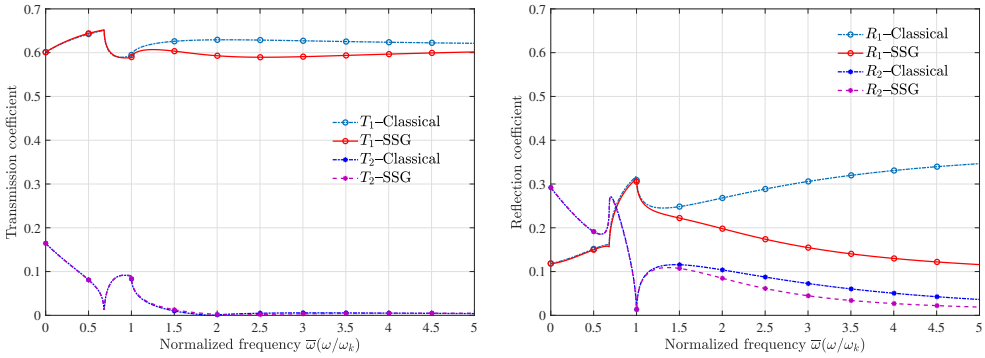

(a) Transmission coefficients (b) Reflection coefficients

Figure 4.6: Transmission and reflection coefficients

Figure 4.6 depicts the transmission coefficients T_1, T_2 for non-classical bending wave k_7 and shear wave k_8 (fig. 4.6(a)), and reflection coefficients R_1, R_2 for non-classical bending wave k_1 and shear wave k_2 (fig. 4.6(b)) based on SSG theory and classical theory. As we can see, both the transmission coefficients and reflection coefficients math well in low frequency range especially when $\overline{\omega} < 1$. In higher frequency range, vibration transmission between complex structures exhibits different characteristics.

Firstly, transmission coefficient T_1-SSG decreases slightly compared with the classical result T_1-Classical; transmission coefficient T_2−-SSG matches well with T_1-Classical in whole frequency range with both approaching to zero as frequency goes higher. These relation indicates that vibration transmission between complex structures through non-classical bending wave is less, meanwhile transmission through shear wave is close to zero in higher frequency for both models. Secondly, as reflection coefficient R_1-Classical increases with frequency, R_1-SSG decreases significantly with frequency and the difference between R_1-SSG and R_1-Classical is more and more obvious as frequency goes higher; Meanwhile non-classical reflection coefficient R_2-SSG share the similar changing trend with R_2-Classical but approach to zero more quickly as frequency goes up. Vibration reflections based on SSG theory formulation are less than the classical results through both bending wave and shear wave. Therefore we can conclude that vibration transmission and reflection from the discontinuous interface between complex structures are less than the classical results in homogeneous structures through both bending wave and shear wave.

Considering that energy balance should also be valid for the SSG theory-based

model, vibration reflection and transmission cannot be both decreased. The transmission or reflection coefficients for the other evanescent waves (k_3, k_4, k_5, k_6, k_9, k_{10}, k_{11}, k_{12}) are calculated, and the results are displayed in Figure 4.7

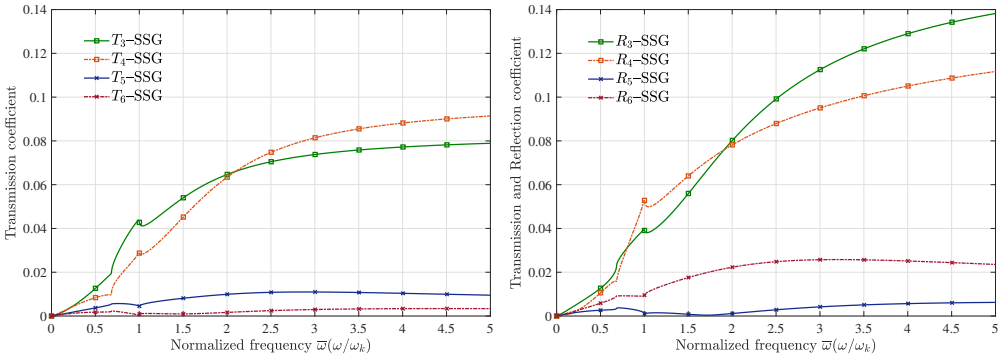

(a) Transmission coefficients (b) Reflection coefficients

Figure 4.7: Transmission and reflection coefficients for evanescent waves

Transmission coefficients T_3, T_4 and reflection coefficients R_3 and R_4 all grow up obviously as frequency goes up, but compared with the results of T_1, T_2 and R_1 R_2 (see the maximum coordinate values), their numerical value are smaller, and the values of T_5, T_6 and R_5 and R_6 are even more smaller.

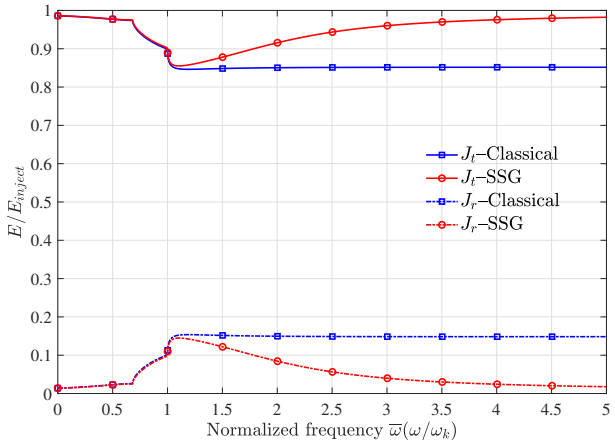

Figure 4.8: Energy transmission and reflection

Though the vibration transmissions and reflections through the evanescent waves are relatively slight, energy conversion to the evanescent waves and attenuation in near field leads to great differences to energy transmission features through discontinuous interface between complex Timoshenko beams. Figure 4.4 shows the proportional distribution of transmitted flux and reflected flux consisted by all possible wave modes diffused at the discontinuity. The summation of ratio is '1' for the SSG theory model just as the classical model, which indicates the SSG theory formu-

lations in terms of wave transmission and reflection are valid. Energy transmitted ratio J_t-SSG increase in higher frequency range compared with J_t-Classical, and energy reflected ratio J_r-SSG decrease, which means energy is predicted to transmit more and reflect less between complex structures with considering the long range interactions between underlying micro-structures.

Combined with Figure 4.6(a), the transmission coefficient of shear wave T_2-SSG does not change much, and the transmission coefficient of bending wave T_1-SSG is actually decreasing, we can interpret the results as follows: even the total transmitted energy between complex beams is predicted to be more than the homogeneous beams, quite a large percentage of transmitted energy is diffused into the evanescent wave modes k_9, k_{10}, k_{11} and k_{12}, and energy conserved in non-classical bending wave which can be effectively transmitted to far field is actually less. Meanwhile the total reflected energy decreases slightly, with considering the energy diffusion into the evanescent wave modes k_3, k_4, k_5 and k_6, the reflection coefficients of non-classical bending wave decrease dramatically.

4.4 Transmission and reflection of longitudinal wave through a certain length of complex rod

Vibration transmission and reflection through planer interface between complex structures based on SSG theory model exhibit different characteristics from that of between homogeneous structures based on classical model. The difference exists in forms of transmission and reflection characteristics of longitudinal wave and bending wave. To explore some potential applications of the complex structures, one investigation of longitudinal wave propagating through a certain length of complex rod is implemented based on SSG theory formulation in this section. The studied system is illustrated as in Figure 4.9.

As shown in Figure 4.9, rod 1 and rod 3 are both homogeneous rods, or rods with micro-structures whose size are much smaller than the external wavelength, thus rod 1 and rod 2 can be modeled with classical theory. Rod 2 is complex rod, namely size of its underlying micro-structures is comparable with the external wavelength, thus it should be model with SSG theory which can capture the local behavior of heterogeneity under long range interactions. Rod 2 of length d is connected with rod 1 with interface S_A, and connected with rod 3 with interface S_B.

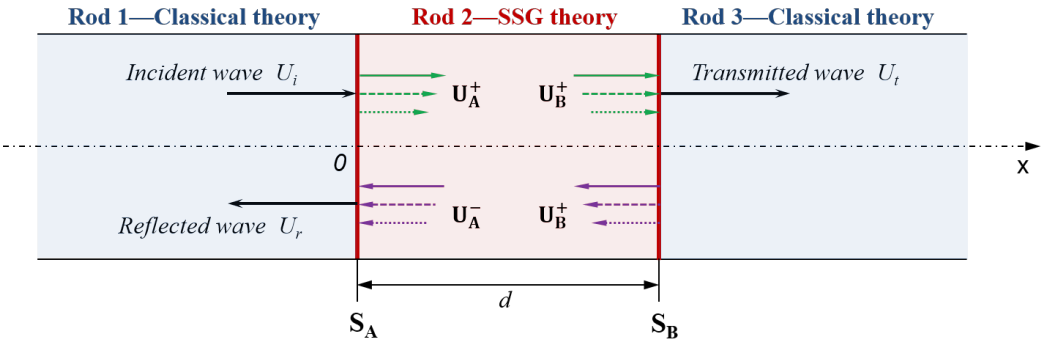

Figure 4.9: Reflection and transmission of longitudinal wave through complex rod of length d

Assuming one longitudinal wave U_i propagate from infinity towards $+x$ direction and normally inject on interface S_A at $x = 0$, a proportion of the incident energy are reflected and propagate away towards $-x$ direction in form of the reflected longitudinal wave U_r, and the remaining energy are transmitted to rod 2. Based on the previous analysis, 3 wave modes can be generated by the disturbance on the discontinuous interface S_A including the non-classical longitudinal wave k_1 and two evanescent waves k_2 and k_3, so the transmitted energy will continue propagate towards $+x$ direction in form of the generated wave group U_A^+. Assuming the length of rod 2 is short thus all generated wave modes on S_A can propagate through rod 2 and inject on interface S_B at $x = d$ in form of incident wave group U_B^+. Then part of the incident energy is transmitted to rod 3 in form of transmitted longitudinal wave U_t, and the other is reflected in form of wave group U_B^-. Then the reflected wave modes propagate along $-x$ direction until reach interface S_A and restart a new circular.

To describe the forces produced on interface S_A and S_B, some material constants and geometrical parameters are predefined. Rod 1 and rod 3 are of the same material with Young's modulus E_1 and mass density ρ_1. Rod 2 is of another type of material with Young's modulus E_2, mass density ρ_2, along with the higher order material constants a_i $(i = 1, 2, ...5)$, b_i $(i = 1, 2, ...7)$, and c_i $(i = 1, 2, 3)$. These three rod are assumed to share the same circular cross section with radius r and area A, and the coefficients associated with higher order material constants as well as cross section are denoted as B_i $(i = 1, 2, ...4)$.

4.4.1 Formulation of wave transmission through a certain length of complex rod

To characterize vibration transmission and reflection features for the studied case, transmission coefficient of incident wave U_i through Rod 2 (complex medium) to rod 3 and the reflection coefficient of wave U_i from rod 2 are derived in this section. Assuming the longitudinal wave that can propagate in rod 1 and rod 3 is denoted as k_c, the incident wave propagating along $+x$ direction with unit amplitude can be

expressed as

$$U_i = e^{i(\omega t - k_c x)}. \tag{4.23}$$

Due to the micro-structure effect, the generated kinetic motion and produced forces in rod 2 are more complicated. To clarify the transfer of motion and force form interface $\mathrm{S_A}$ to interface $\mathrm{S_B}$, one state vector $\mathbf{X}$ is defined with including all the kinetic parameters and force components generated on the interface of complex rod based on SSG theory. According to the analysis in Sec. 2.2.4, the state vector on the right hand of the studied interface $\mathrm{S_A}$ can be given as

$$\mathbf{X}_{A^+} = \left[u_{A^+}, \frac{\partial u_{A^+}}{\partial x}, \frac{\partial^2 u_{A^+}}{\partial x^2}, P_0, P_1, P_2\right]^{\mathrm{T}}\Big|_{\mathrm{S=S_{A^+}}}. \tag{4.24}$$

Assuming the amplitudes of the three positive going wave modes k_1, k_2 and k_3 generated on interface $\mathrm{S_A}$ are respectively $\mathcal{A}$, $\mathcal{C}$, $\mathcal{E}$, meanwhile the amplitudes of the negative going modes $-k_1$, $-k_2$ and $-k_3$ are $\mathcal{B}$, $\mathcal{D}$, $\mathcal{F}$, then the displacement on the right hand of the interface $\mathrm{S_A}$ can be given in form of the superposition of contributions from all the wave modes as (omitting the time component $e^{i\omega t}$)

$$u_{A^+} = \mathcal{A}e^{-ik_1 x} + \mathcal{B}e^{ik_1 x} + \mathcal{C}e^{-ik_2 x} + \mathcal{D}e^{ik_2 x} + \mathcal{E}e^{-ik_3 x} + \mathcal{F}e^{ik_3 x}; \tag{4.25}$$

The other two kinetic parameters, namely, the first derivative of displacement u_{A^+} and the second derivative of u_{A^+} can be given as

$$\begin{aligned}\frac{\partial u_{A^+}}{\partial x} =& -ik_1 \cdot \mathcal{A}e^{-ik_1 x} + ik_1 \cdot \mathcal{B}e^{ik_1 x} - ik_2 \cdot \mathcal{C}e^{-ik_2 x} + ik_2 \cdot \mathcal{D}e^{ik_2 x} \\ & - ik_3 \cdot \mathcal{E}e^{-ik_3 x} + ik_3 \cdot \mathcal{F}e^{ik_3 x};\end{aligned} \tag{4.26}$$

and

$$\begin{aligned}\frac{\partial^2 u_{A^+}}{\partial x^2} =& -{k_1}^2 \cdot \mathcal{A}e^{-ik_1 x} - {k_1}^2 \cdot \mathcal{B}e^{ik_1 x} - {k_2}^2 \cdot \mathcal{C}e^{-ik_2 x} - {k_2}^2 \cdot \mathcal{D}e^{ik_2 x} \\ & - {k_3}^2 \cdot \mathcal{E}e^{-ik_3 x} - {k_3}^2 \cdot \mathcal{F}e^{ik_3 x}.\end{aligned} \tag{4.27}$$

With the predefined material constants, amplitudes of the axis forces P_0, first higher order force P_1 and second higher order force P_2 produced on the right hand of interface $\mathrm{S_A}$ are given as

$$\begin{aligned}P_0|_{\mathrm{S_A}^+} &= E_2 A\frac{\partial u_{A^+}}{\partial x} + (B_3 - B_1)\frac{\partial^3 u_{A^+}}{\partial x^3} + B_2\frac{\partial^5 u_{A^+}}{\partial x^5}, \\ P_1|_{\mathrm{S_A}^+} &= \left(B_1 - \frac{B_3}{2}\right)\frac{\partial^2 u_{A^+}}{\partial x^2} - B_2\frac{\partial^4 u_{A^+}}{\partial x^4}, \\ P_2|_{\mathrm{S_A}^+} &= \frac{B_3}{2}\frac{\partial u_{A^+}}{\partial x} + B_2\frac{\partial^3 u_{A^+}}{\partial x^3}.\end{aligned} \tag{4.28}$$

Substitute the displacement form in expression (4.25) into the force expressions, we can achieve the state vector in form of

$$\mathbf{X}_{A^+} = \mathbf{M}_A \cdot \mathbf{U}_A \tag{4.29}$$

in which $\mathbf{U}_A$ represents the wave vector consisting of all wave modes as

$$\mathbf{U}_A = \left[\mathcal{A}e^{-ik_1x}, \mathcal{B}e^{ik_1x}, \mathcal{C}e^{-ik_2x}, \mathcal{D}e^{ik_2x}, \mathcal{E}e^{-ik_3x}, \mathcal{F}e^{ik_3x}\right]^{\mathbf{T}} \tag{4.30}$$

and $\mathbf{M}_A$ represents the coefficient matrix composed of the coefficients in front of each wave modes as

$$\mathbf{M}_A = \begin{bmatrix} 1 & 1 & 1 & \dots \\ -ik_1 & ik_1 & -ik_2 & \dots \\ -{k_1}^2 & -{k_1}^2 & -{k_2}^2 & \dots \\ \begin{pmatrix} -iE_2Ak_1 - iB_2{k_1}^5 \\ +i\left(B_3 - B_1\right){k_1}^3 \end{pmatrix} & \begin{pmatrix} iE_2Ak_1 + iB_2{k_1}^5 \\ -i\left(B_3 - B_1\right){k_1}^3 \end{pmatrix} & \begin{pmatrix} -iE_2Ak_2 - iB_2{k_2}^5 \\ +i\left(B_3 - B_1\right){k_2}^3 \end{pmatrix} & \dots \\ \left(\frac{B_3}{2} - B_1\right){k_1}^2 - B_2{k_1}^4 & \left(\frac{B_3}{2} - B_1\right){k_1}^2 - B_2{k_1}^4 & \left(\frac{B_3}{2} - B_1\right){k_2}^2 - B_2{k_2}^4 & \dots \\ -\frac{1}{2}iB_3k_1 + iB_2{k_1}^3 & \frac{1}{2}iB_3k_1 - iB_2{k_1}^3 & -\frac{1}{2}iB_3k_2 + iB_2{k_2}^3 & \dots \end{bmatrix}$$

$$\begin{bmatrix} \dots & 1 & 1 & 1 \\ \dots & ik_2 & -ik_3 & ik_3 \\ \dots & -{k_2}^2 & -{k_3}^2 & -{k_3}^2 \\ \dots & \begin{pmatrix} iE_2Ak_2 + iB_2{k_2}^5 \\ -i\left(B_3 - B_1\right){k_2}^3 \end{pmatrix} & \begin{pmatrix} -iE_2Ak_3 - iB_2{k_3}^5 \\ +i\left(B_3 - B_1\right){k_3}^3 \end{pmatrix} & \begin{pmatrix} iE_2Ak_3 + iB_2{k_3}^5 \\ -i\left(B_3 - B_1\right){k_3}^3 \end{pmatrix} \\ \dots & \left(\frac{B_3}{2} - B_1\right){k_2}^2 - B_2{k_2}^4 & \left(\frac{B_3}{2} - B_1\right){k_3}^2 - B_2{k_3}^4 & \left(\frac{B_3}{2} - B_1\right){k_3}^2 - B_2{k_3}^4 \\ \dots & \frac{1}{2}iB_3k_2 - iB_2{k_2}^3 & -\frac{1}{2}iB_3k_3 + iB_2{k_3}^3 & \frac{1}{2}iB_3k_3 - iB_2{k_3}^3 \end{bmatrix}.$$

Similarly, the state vector on the left hand of the studied interface $\mathrm{S_B}$ can be given as in Eq. (4.31)

$$\mathbf{X}_{B^-} = \left[u_{B^-}, \frac{\partial u_{B^-}}{\partial x}, \frac{\partial^2 u_{B^-}}{\partial x^2}, P_0, P_1, P_2\right]^{\mathrm{T}}\Big|_{\mathrm{S=S_{B^-}}}. \tag{4.31}$$

Due to the wave propagation distance along x direction, amplitude of each wave mode should be changed by $e^{\pm k_i d}$ to express the phase difference caused by propagation distance for wave mode $\pm k_i$. The displacement on the right hand of the interface $\mathrm{S_B}$ can be given in form of the superposition of contribution from all the wave modes as

$$u_{B^-} = \mathcal{A}e^{-ik_1(x+d)} + \mathcal{B}e^{ik_1(x+d)} + \mathcal{C}e^{-ik_2(x+d)} + \mathcal{D}e^{ik_2(x+d)} + \mathcal{E}e^{-ik_3(x+d)} + \mathcal{F}e^{ik_3(x+d)}; \tag{4.32}$$

The other two kinetic parameters, namely, the first derivative of u_{B^-} and the second

derivative of u_{B^-} can be given as

$$\begin{aligned}\frac{\partial u_{B^-}}{\partial x} =& -ik_1 \cdot \mathcal{A}e^{-ik_1(x+d)} + ik_1 \cdot \mathcal{B}e^{ik_1(x+d)} - ik_2 \cdot \mathcal{C}e^{-ik_2(x+d)} + ik_2 \cdot \mathcal{D}e^{ik_2(x+d)} \\ & - ik_3 \cdot \mathcal{E}e^{-ik_3(x+d)} + ik_3 \cdot \mathcal{F}e^{ik_3(x+d)};\end{aligned} \tag{4.33}$$

and

$$\begin{aligned}\frac{\partial^2 u_{B^-}}{\partial x^2} =& -{k_1}^2 \cdot \mathcal{A}e^{-ik_1(x+d)} - {k_1}^2 \cdot \mathcal{B}e^{ik_1(x+d)} - {k_2}^2 \cdot \mathcal{C}e^{-ik_2(x+d)} - {k_2}^2 \cdot \mathcal{D}e^{ik_2(x+d)} \\ & - {k_3}^2 \cdot \mathcal{E}e^{-ik_3(x+d)} - {k_3}^2 \cdot \mathcal{F}e^{ik_3(x+d)};\end{aligned} \tag{4.34}$$

The force P_0, first higher order force P_1 and second higher order force P_2 produced on the left hand of interface $\mathrm{S_B}$ are given as

$$\begin{aligned}P_0|_{\mathrm{S_B}^-} &= E_2 A\frac{\partial u_{B^-}}{\partial x} + (B_3 - B_1)\frac{\partial^3 u_{B^-}}{\partial x^3} + \mathcal{B}_2\frac{\partial^5 u_{B^-}}{\partial x^5}, \\ P_1|_{\mathrm{S_B}^-} &= \left(B_1 - \frac{B_3}{2}\right)\frac{\partial^2 u_{B^-}}{\partial x^2} - B_2\frac{\partial^4 u_{B^-}}{\partial x^4}, \\ P_2|_{\mathrm{S_B}^-} &= \frac{B_3}{2}\frac{\partial u_{B^-}}{\partial x} + B_2\frac{\partial^3 u_{B^-}}{\partial x^3}.\end{aligned} \tag{4.35}$$

Substitute the displacement form in expression (4.32) into the force expressions, we can achieve the state vector in form of

$$\mathbf{X}_{B^-} = \mathbf{M}_B \cdot \mathbf{U}_B \tag{4.36}$$

in which $\mathbf{U}_B$ represents the wave vector consisting of all modes as

$$\mathbf{U}_B = \left[\mathcal{A}e^{-ik_1 x}, \mathcal{B}e^{ik_1 x}, \mathcal{C}e^{-ik_2 x}, \mathcal{D}e^{ik_2 x}, \mathcal{E}e^{-ik_3 x}, \mathcal{F}e^{ik_3 x}\right]^{\mathbf{T}} \tag{4.37}$$

Comparing expression (4.30) and (4.37), the wave mode vectors $\mathbf{U}_B$ share the same form with wave mode vector $\mathbf{U}_A$. Moreover, $\mathbf{U}_A$ in Eq. (4.30) can be calculated by finding the inverse matrix of $\mathbf{M}_A$. Then we have

$$\mathbf{U}_B = \mathbf{U}_A = {\mathbf{M}_A}^{-1} \cdot \mathbf{X}_{A^+}. \tag{4.38}$$

Substitution of expression (4.38) into expression (4.36) yields

$$\mathbf{X}_{B^-} = \mathbf{M}_B \cdot \mathbf{U}_B = \mathbf{M}_B \cdot \mathbf{U}_A = \mathbf{M}_B \cdot {\mathbf{M}_A}^{-1} \cdot \mathbf{X}_{A^+}.$$

$\mathbf{M}_B$ in represents the coefficient matrix composed of the coefficients in front of each

wave modes as

$$\mathbf{M}_B = \begin{bmatrix} e^{-ik_1 d} & e^{ik_1 d} & \dots \\ -ik_1 \cdot e^{-ik_1 d} & ik_1 \cdot e^{ik_1 d} & \dots \\ -{k_1}^2 \cdot e^{-ik_1 d} & -{k_1}^2 \cdot e^{ik_1 d} & \dots \\ \begin{pmatrix} -iE_2 A k_1 - iB_2 {k_1}^5 \\ +i\left(B_3 - B_1\right){k_1}^3 \end{pmatrix} \cdot e^{-ik_1 d} & \begin{pmatrix} iE_2 A k_1 + iB_2 {k_1}^5 \\ -i\left(B_3 - B_1\right){k_1}^3 \end{pmatrix} \cdot e^{ik_1 d} & \dots \\ \left(\left(\frac{B_3}{2} - B_1\right){k_1}^2 - B_2 {k_1}^4\right) \cdot e^{-ik_1 d} & \left(\left(\frac{B_3}{2} - B_1\right){k_1}^2 - B_2 {k_1}^4\right) \cdot e^{ik_1 d} & \dots \\ \left(-\frac{B_3}{2} ik_1 + iB_2 {k_1}^3\right) \cdot e^{-ik_1 d} & \left(\frac{1}{2} iB_3 k_1 - iB_2 {k_1}^3\right) \cdot e^{ik_1 d} & \dots \end{bmatrix}$$

$$\begin{bmatrix} \dots & e^{-ik_2 d} & e^{ik_2 d} & \dots \\ \dots & -ik_2 \cdot e^{-ik_2 d} & ik_2 \cdot e^{ik_2 d} & \dots \\ \dots & -{k_2}^2 \cdot e^{-ik_2 d} & -{k_2}^2 \cdot e^{ik_2 d} & \dots \\ \dots & \begin{pmatrix} -iE_2 A k_2 - iB_2 {k_2}^5 \\ +i\left(B_3 - B_1\right){k_2}^3 \end{pmatrix} \cdot e^{-ik_2 d} & \begin{pmatrix} iE_2 A k_2 + iB_2 {k_2}^5 \\ -i\left(B_3 - B_1\right){k_2}^3 \end{pmatrix} \cdot e^{ik_2 d} & \dots \\ \dots & \left(\left(\frac{B_3}{2} - B_1\right){k_2}^2 - B_2 {k_2}^4\right) \cdot e^{-ik_2 d} & \left(\left(\frac{B_3}{2} - B_1\right){k_2}^2 - B_2 {k_2}^4\right) \cdot e^{ik_2 d} & \dots \\ \dots & \left(-\frac{1}{2} iB_3 k_2 + iB_2 {k_2}^3\right) \cdot e^{-ik_2 d} & \left(\frac{1}{2} iB_3 k_2 - iB_2 {k_2}^3\right) \cdot e^{-ik_2 d} & \dots \end{bmatrix}$$

$$\begin{bmatrix} \dots & e^{-ik_3 d} & e^{ik_3 d} \\ \dots & -ik_3 \cdot e^{-ik_3 d} & ik_3 \cdot e^{ik_3 d} \\ \dots & -{k_3}^2 \cdot e^{-ik_3 d} & -{k_3}^2 \cdot e^{ik_3 d} \\ \dots & \begin{pmatrix} -iE_2 A k_3 - iB_2 {k_3}^5 \\ +i\left(B_3 - B_1\right){k_3}^3 \end{pmatrix} \cdot e^{-ik_3 d} & \begin{pmatrix} iE_2 A k_3 + iB_2 {k_3}^5 \\ -i\left(B_3 - B_1\right){k_3}^3 \end{pmatrix} \cdot e^{ik_3 d} \\ \dots & \left(\left(\frac{B_3}{2} - B_1\right){k_3}^2 - B_2 {k_3}^4\right) \cdot e^{-ik_3 d} & \left(\left(\frac{B_3}{2} - B_1\right){k_3}^2 - B_2 {k_3}^4\right) \cdot e^{ik_3 d} \\ \dots & \left(-\frac{1}{2} iB_3 k_3 + iB_2 {k_3}^3\right) \cdot e^{-ik_3 d} & \left(\frac{1}{2} iB_3 k_3 - iB_2 {k_3}^3\right) \cdot e^{ik_3 d} \end{bmatrix}$$

Then we have the transfer relation between state vector of $\mathbf{X}_B$ for section $\mathbf{S_B}$ and state vector $\mathbf{X}_A$ for section $\mathbf{S_A}$ as

$$\mathbf{X_{B^-}} = \mathbf{M} \cdot \mathbf{X}_{A^+}, \tag{4.39}$$

in which $\mathbf{M}$ denotes the transfer matrix and $\mathbf{M} = \mathbf{M}_B \cdot {\mathbf{M}_A}^{-1}$.

Assuming the transmission coefficient of incident wave U_i through Rod 2 (complex medium) to rod 3 is C_t, and the reflection coefficient of wave U_i from rod 2 is C_r, transmitted wave U_t in rod 3 and reflected wave U_r in rod 1 can be expressed as

$$\begin{aligned} U_t &= C_t \cdot e^{i(\omega t - k_c x)} \\ U_r &= C_r \cdot e^{i(\omega t + k_c x)} \end{aligned} \tag{4.40}$$

Then the amplitudes of displacements caused by the classical longitudinal wave on the left hand of interface S_A and on the right hand of interface S_B can be expressed as (omitting the time component $e^{i\omega t}$),

$$\begin{aligned} u_{A^-} &= e^{-ik_c x} + C_r \cdot e^{ik_c x}; \\ u_{B^+} &= C_t \cdot e^{-ik_c x}. \end{aligned} \tag{4.41}$$

With the predefined material constants, amplitudes of the axis forces produced on the left hand of interface S_A and on the right hand of interface S_B can be expressed as (omitting the time component $e^{i\omega t}$),

$$\begin{aligned} F_{A^-} &= E_1 A\,(-ik_c) \cdot e^{-ik_c x} + E_1 A\,(ik_c)\, C_r \cdot e^{ik_c x}; \\ F_{B^+} &= C_t E_1 A\,(-ik_c) \cdot e^{-ik_c x}. \end{aligned} \tag{4.42}$$

Substitute $x = 0$ for interface S_A and $x = d$ for interface S_B into the expression of displacement (4.41) and force (4.42), the state vectors on the left hand of section S_A and right hand of section S_B are given as

$$\mathbf{X}_{A^-} = \begin{bmatrix} u_{A^-} \\ F_{A^-} \end{bmatrix} = \begin{bmatrix} 1 + C_r \\ -ik_c E_1 A + ik_c C_r E_1 A \end{bmatrix}; \tag{4.43a}$$

$$\mathbf{X}_{B^+} = \begin{bmatrix} u_{B^+} \\ F_{B^+} \end{bmatrix} = \begin{bmatrix} C_t e^{-ik_c d} \\ -ik_c C_t E_1 A e^{-ik_c d} \end{bmatrix}. \tag{4.43b}$$

To be noticed, the coordinate position where wave inject does not affect the vibration transmission characteristics of the complex rod. Section S_A is set at $x = 0$ to clarify the deducing process concisely.

Assuming the interface S_A does not dissipate energy, and the mass between $S = S_A^+$ and $S = S_A^-$ is infinitesimal, then the equilibrium describing continuity of state vector $\mathbf{X}_{A^-}$ and $\mathbf{X}_{A^+}$ can be developed. However, 4 more components specifying the higher order displacements and higher order forces appear in $\mathbf{X}_{A^+}$. As we know, only classical force is required to be considered in the force equilibrium for classical medium, meanwhile the higher order forces approximate to zero in classical media, in which case the long range interaction is approaching zero, thus the higher order force components are inserted into vector $\mathbf{X}_{A^-}$ with values equaling zero. Meanwhile the higher order kinetic component of the classical medium are not necessary to be zero, and they are set to be unknown variables u'_{A^-}, u''_{A^-}. In consequence, the equilibrium describing the continuity of state vector $\mathbf{X}_{A^-}$ and $\mathbf{X}_{A^+}$ is expressed as in Eq. (4.44)

$$\mathbf{X}_{A^+} = \mathbf{X}_{A^-} \Rightarrow \mathbf{X}_{A^+} = \left.\begin{bmatrix} u_{A^+} \\ \frac{\partial u_{A^+}}{\partial x} \\ \frac{\partial^2 u_{A^+}}{\partial x^2} \\ P_0 \\ P_1 \\ P_2 \end{bmatrix}\right|_{S=S_A{}^+} = \begin{bmatrix} 1 + C_r \\ u'_{A^-} \\ u''_{A^-} \\ -ik_c E_1 A + ik_c C_r E_1 A \\ 0 \\ 0 \end{bmatrix}; \tag{4.44}$$

The condition is the same when it comes to surface S_B. The higher order force components of vector $\mathbf{X}_{B^+}$ are also set to be zero, and the higher order kinetic component are set to be unknown variables ${u'}_{B^+}$ and ${u''}_{B^+}$. Then the equilibrium for the continuity of state vector $\mathbf{X}_{B^-}$ and $\mathbf{X}_{B^+}$ is given as

$$\mathbf{X}_{B^-} = \mathbf{X}_{B^+} \Rightarrow \mathbf{X}_{B^-} = \left[\begin{array}{c} u_{B^-} \\ \frac{\partial u_{B^-}}{\partial x} \\ \frac{\partial^2 u_{B^-}}{\partial x^2} \\ P_0 \\ P_1 \\ P_2 \end{array}\right]\Bigg|_{S=S_B{}^-} = \left[\begin{array}{c} C_t e^{-ik_c d} \\ {u'}_{B^+} \\ {u''}_{B^+} \\ -ik_c C_t E_1 A e^{-ik_c d} \\ 0 \\ 0 \end{array}\right] \tag{4.45}$$

Combination of Eq. (4.44), (4.45) and (4.39), the transformation from $\mathbf{X}_{A^+}$ to $\mathbf{X}_{B^-}$ is achieve as

$$\mathbf{X}_{B^-} = \mathbf{M} \cdot \mathbf{X}_{A^+}, \tag{4.46}$$

namely

$$\left[\begin{array}{c} C_t e^{-ik_c d} \\ {u'}_{B^+} \\ {u''}_{B^+} \\ -ik_c C_t E_1 A e^{-ik_c d} \\ 0 \\ 0 \end{array}\right] = \mathbf{M} \cdot \left[\begin{array}{c} 1 + C_r \\ {u'}_{A^-} \\ {u''}_{A^-} \\ -ik_c E_1 A + ik_c C_r E_1 A \\ 0 \\ 0 \end{array}\right], \tag{4.47}$$

in which $\mathbf{M}$ denotes the same transfer matrix in Eq. (4.39) with $\mathbf{M} = \mathbf{M}_B \cdot {\mathbf{M}_A}^{-1}$. Matrix $\mathbf{M}_B$ and $\mathbf{M}_A$ are governed by a group of variables including the wavenumber k_i, length d, Young's modulus E_2 and higher order material constants B_i. As long as the material constants are defined, wavenumbers of the generated waves in these two rods can be determined on any frequency. Combined with length d, the transfer matrix can be fully obtained. Then the six unknown variables including C_t and C_r can be achieved with the equilibrium established in Eq. (4.47). As the transfer matrix $\mathbf{M}$ is determined by the geometrical and material parameter of rod 2, the wave transmission coefficient C_t and reflection coefficient C_r are fully dominated by the second gradient property of the complex rod and wave transmission distance d.

4.4.2 Numerical calculation of wave transmission through SSG theory-based rod

In the numerical study, the transmission coefficient C_t and reflection coefficient C_r are calculated for the system shown in Figure 4.9. Assume the radius of the connecting interface $r = 3a_0$, and the normalization parameter for length $L = d$.

Material of the classical medium rod 1 and rod 3 is aluminum with Young's modulus $E_1 = 52\text{Gpa}$ and mass density $\rho_1 = 2700\text{kg/m}^3$. In the following analysis, C_r and C_t will be calculated in different cases when rod 2 is of different material and different length. Then influences of material properties and wave transmission distance on the C_r and C_t are investigated in frequency domain.

Firstly, if rod 2 is homogeneous and its material is the same with rod 1, the incident wave will be transmitted through rod 2 without any reflection, in that situation the transmission coefficient is 1 and reflection coefficient is 0 in the whole frequency range. If rod 2 is complex, and its material is also set to be aluminum, namely having the same Young's modulus and mass density with rod 1 along with higher order constants. The resulting C_t and C_r are illustrated in Figure 4.10

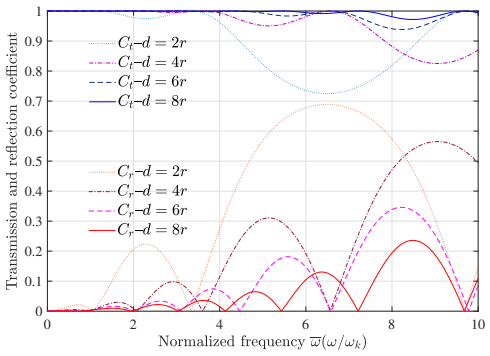

Figure 4.10: Transmission and reflection coefficients of longitudinal wave through complex rod made by Al

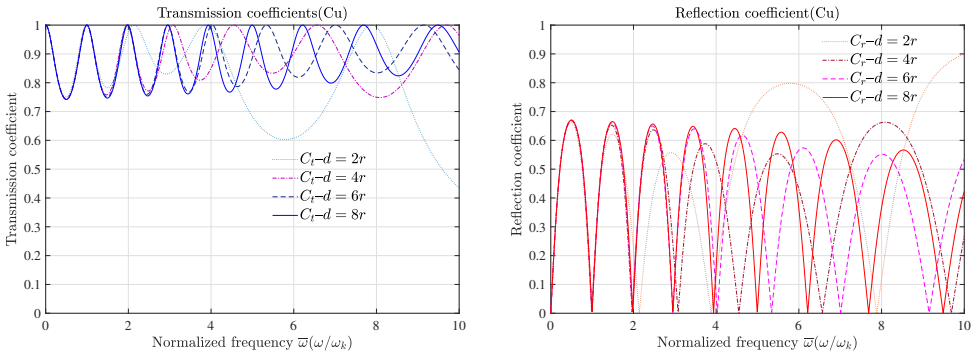

(a) (b)

Figure 4.11: Transmission and reflection coefficients of longitudinal wave through complex rod made by Cu

As shown in Figure 4.10, C_t is not constantly 1 anymore. In fact as shown in Figure 4.10, SSG theory-based C_t is less than '1', and C_r is more than '0', they both shows frequency dependent character and '$C_t^2 + C_r^2 = 1$'. As d increases from $2r$ to

$8r$, C_t and C_r are both approaching to degenerate to classical results. In addition, on some specific frequency, C_t regress to 1 and C_r to 0. As d becomes longer, the frequency gap between neighboring specific frequency also shows distinct difference.

Figure 4.11 illustrates transmission coefficient C_t and reflection coefficient C_r through complex rod made of copper based on SSG theory formulation, all the material constants have already be refereed before. As can be seen, C_t and C_r change significantly as length d increasing from $2r$ to $8r$, and the changing tendency is also approaching to the classical transmission and reflection coefficients. Compared with Figure 4.10. we can see the changing tendency is different from the previous case as the middle medium is different.

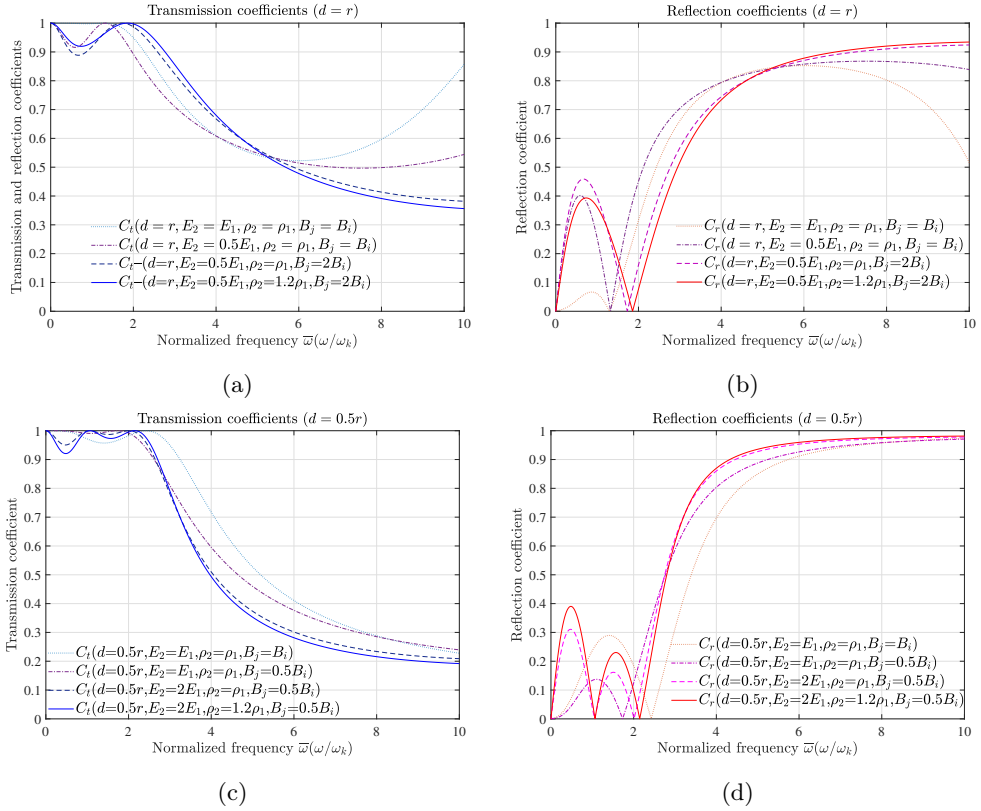

Figure 4.12: Transmission and reflection coefficients

Based on these two cases, We can conclude that C_t and C_r are affected by length d and all the material constants in SSG theory model, including the classical constants Young's modulus E_2 and mass density ρ_2, as well as the higher order material constants B_i. Combined with the lattice model proposed in Sec. 2.5, force interaction coefficient g_2 and long range force interaction coefficients g_4, g_6 can be determined by these material constants, namely these two groups of variables are equivalence under some conditions.Thus we can say that the structure behavior can be designed by adjusting the force interactions between inner structures, which can also be considered as adjusting the material constants. For the analyzed system,

wave transmission characteristics can be designed by adjusting all the material constants along with the length d of complex rod 2. To achieve some application, some cases with predefined material constants and and length d are implemented.

Figure 4.12 displays the transmission and reflection coefficients changing with material constants respectively when $d = r$ and $d = 0.5r$. As we can see, for complex rod 2 of different length d with some predefined Young's modulus, mass density and higher order material constants, reflection coefficient C_r can approach to '1' extremely in some frequency range. In that frequency range, all of the input energy will be reflected and the transmitted energy is close to zero. Thus the predefined complex rod shows great seismic isolation performance, and this phenomenon can be a start of enriching the inner micro-structure with utilization of SSG theory model to achieve better structural performance in acoustics.

4.5 Conclusions

In this chapter, vibration transmission through a planar interface between complex medias is investigated with employing the the proposed SSG theory-based rod model and SSG theory-based beam model. The investigation is proceed in terms of transmission and reflection coefficients along with energy transmitted ratio, then the impact of micro-structure effects on vibration transmission is evaluated. Afterwards, attention moves to wave transmission through a certain length of complex structure. The formulation is derived to calculate the transmission and reflection coefficient through complex rod, then one application of SSG theory formulation in active control of vibration transmission is introduced by adjusting properties of the complex rod structure.

(1)For vibration energy in form of longitudinal wave and bending wave, the incident energy is predicted to transmit more and reflect less in total. Duo to the dynamic behavior of heterogeneity caused by complex micro-structure interactions, a certain proportion of the transmitted and reflected energy is in forms of evanescent waves which are generated at the discontinuity, then energy in forms of the propagating waves (longitudinal wave for rod, bending wave and shear wave for beam) is less. Therefore, the transmission coefficient of the incident wave decrease slightly and the reflection coefficient decreases drastically for both the longitudinal wave and the bending wave, the higher the frequency becomes, the greater the impact of micro-structure. We can also conclude that energy that can be transmitted to far field is much more less because the generated evanescent waves decay rapidly in near field.

(2) Wave reflection and transmission characteristics through a certain length of complex rod is highly dependent on properties of the complex rod, length d and also frequency. As length d increase, the results approach to classical theory results. With some predefined Young's modulus, mass density and higher order material constants, reflection coefficient C_r can approach to '1' extremely in some frequency range, in that case all the input energy will be reflected while the transmitted energy

is close to zero. This phenomenon shows that the SSG theory model can be employed to optimize and to enrich the inner micro-structures of complex structure for better structural performance in acoustics.

Chapter 5

Sound radiation analysis from complex Timoshenko beam based on SSG theory model

Contents

5.1 Introduction

Sound radiation from vibrating structures is of great impact on the surrounding environment. Theoretically speaking, sound radiation is generated by interactions between the structure and the ambient fluid, and it depends on the structure dimensions, boundary conditions, material properties, external excitation, and ambient fluid properties, and so on. The dynamic structure model based on SSG theory enrich structural behavior with micro-structure characters, which will surely affect the resulting sound radiation. Therefore the intention of this chapter is to analyze the sound radiation from the vibrating Timoshenko beam with the proposed the SSG theory-based model. Sound radiation from an infinite complex beam is analyzed in regard to radiation impedance and radiated pressure field. Then sound radiation from finite-sized complex beam with proper boundary conditions is calculated based on Kirchhoff-Helmholtz integral equation. The impact of local behavior of heterogeneity will be discussed with comparing the results from SSG theory model and classical theory model.

5.2 Radiation from infinite beam

In this section, radiation from infinite complex Timoshenko beam excited by a simple harmonic transverse force is investigated based on the proposed SSG theory model. Radiation impedance and acoustic pressure are derived using the wave formulation method. The studied structure-fluid system is illustrated as in Figure 5.1.

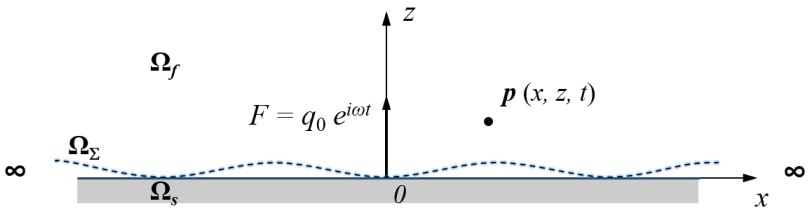

Figure 5.1: sound radiation from infinite Timoshenko beam

As shown in Figure5.1, the vibrating beam subject to a transverse harmonic force $\mathrm{F} = \mathrm{Re}\left\{\mathrm{q_0 e^{i\omega t}}\right\}$ at $x = 0$ is assumed to be infinitely extended along x direction, and the waves generated by the vibrating surface Ω_Σ in the fluid domain Ω_f will propagate away from the source at speed c_0.

5.2.1 Formulation of radiation from infinite SSG theory-based beam structure

Acoustic wave motion equation governing the propagation of small acoustic disturbances through a homogeneous, inviscid, isotropic, compressible fluid can be written in terms of the variation of pressure about the equilibrium pressure as

$$\frac{\partial^2 p}{\partial x^2} + \frac{\partial^2 p}{\partial y^2} + \frac{\partial^2 p}{\partial z^2} - \frac{1}{{c_0}^2}\frac{\partial^2 p}{\partial t^2} = 0. \tag{5.1}$$

where p is the radiated acoustic pressure in the field. c_0 represents the frequency-independent speed of sound govern by fluid medium by ${c_0}^2 = \gamma P_0/\rho_0$, where P_0 denotes the mean fluid pressure, ρ_0 is the mean density and γ is the adiabatic bulk modulus of the fluid. In studying of the wave radiation from beam structure to fluid, the vibration is uniform along y direction, so will the acoustic pressure field. Then the simplified two-dimensional wave propagation form is expressed in association with simple harmonic time dependence as,

$$\frac{\partial^2 p}{\partial x^2} + \frac{\partial^2 p}{\partial z^2} = -\left(\frac{\omega}{c_0}\right)^2 p = -k_0^2 p, \tag{5.2}$$

where $k_0 = \dfrac{\omega}{c_0}$. The general complex exponential form of the acoustic pressure $p\,(x, z, t)$ representing the propagation of sound pressure in the two-dimensional space is given as,

$$p\,(x, z, t) = \tilde{p} \cdot e^{-i(k_x x + k_z z)} \cdot e^{i\omega t}. \tag{5.3}$$

Substitution of this expression into Eq. (5.2) yields the following wavenumber relation:

$$k_x^2 + k_z^2 = {k_0}^2 = \frac{\omega^2}{c_0^2}. \tag{5.4}$$

In analysis of sound radiation from infinite beam, the vibrating beam is assumed to be infinitely extended along x direction and excited by one harmonic point force at $x = 0$. Since the vibration is symmetrical about the point $x = 0$, we will concentrate on the wave propagation field $x \geq 0$. According to the SSG theory-based formulation in chapter 3.3, the total transverse velocity of the vibrating surface in region $[0, +\infty)$ can be expressed in forms of the superposition of the contributions from all six wave modes as,

$$\begin{aligned} &v_n(x,t) = i\omega \cdot w(x,t) \\ &= i\omega \cdot \left(\mathcal{A}_1 \cdot e^{-ik_1 x} + \mathcal{B}_1 \cdot e^{-ik_2 x} + \mathcal{C}_1 \cdot e^{-ik_3 x} + \mathcal{D}_1 \cdot e^{-ik_4 x} + \mathcal{E}_1 \cdot e^{-ik_5 x} + \mathcal{F}_1 \cdot e^{-ik_6 x}\right) \cdot e^{i\omega t}. \end{aligned} \tag{5.5}$$

The complex solution given in Eq. (5.5) represents all the physically possible forms for transverse vibration velocity of the complex Timoshenko beam based on SSG theory. Generated by the harmonic acceleration disturbance at the structure-fluid interface, the solution of the radiated acoustic pressure may also be expressed by the superposition of six acoustic pressure field to physically represent the sound radiation from all the six wave modes generated by the source. The complex exponential form of the acoustic pressure $p(x,z,t)$ representing the propagation of sound pressure in the two-dimensional space $x \geq 0, z \geq 0$ is given as,

$$\begin{aligned} p(x,z,t) =& \mathcal{A}_3 \cdot e^{i\left(\omega t - k_{x_1} x - k_{z_1} z\right)} + \mathcal{B}_3 \cdot e^{i\left(\omega t - k_{x_2} x - k_{z_2} z\right)} + \mathcal{C}_3 \cdot e^{i\left(\omega t - k_{x_3} x - k_{z_3} z\right)} \\ &+ \mathcal{D}_3 \cdot e^{i\left(\omega t - k_{x_4} x - k_{z_4} z\right)} + \mathcal{E}_3 \cdot e^{i\left(\omega t - k_{x_5} x - k_{z_5} z\right)} + \mathcal{F}_3 \cdot e^{i\left(\omega t - k_{x_6} x - k_{z_6} z\right)}. \end{aligned} \tag{5.6}$$

Substitute the solution of acoustic pressure $p(x,z,t)$ into (5.1), the relation in Eq. (5.4) is valid for each mode constituting the radiated acoustic pressure field, then we have

$$\begin{aligned} &k_{x_1}^2 + k_{z_1}^2 = {k_0}^2; \quad k_{x_2}^2 + k_{z_2}^2 = {k_0}^2; \quad k_{x_3}^2 + k_{z_3}^2 = {k_0}^2; \\ &k_{x_4}^2 + k_{z_4}^2 = {k_0}^2; \quad k_{x_5}^2 + k_{z_5}^2 = {k_0}^2; \quad k_{x_6}^2 + k_{z_6}^2 = {k_0}^2; \end{aligned} \tag{5.7}$$

In deriving the wave equation, linearized form of Euler momentum equations are used as

$$\begin{aligned} &\frac{\partial p}{\partial x} + \rho_0 \cdot \frac{\partial \dot{u}_x}{\partial t} = 0; \\ &\frac{\partial p}{\partial y} + \rho_0 \cdot \frac{\partial \dot{u}_y}{\partial t} = 0; \\ &\frac{\partial p}{\partial z} + \rho_0 \cdot \frac{\partial \dot{u}_z}{\partial t} = 0. \end{aligned} \tag{5.8}$$

$\dot{u}_x$, $\dot{u}_y$ and $\dot{u}_z$ are the particle velocities in the x, y and z directions, respectively. In z direction, the vibration velocity u_z of a point on the interface in the fluid field equals the transverse vibration velocity $v_n(x,t)$ at that point on the beam surface. Then with Euler momentum equation, the pressure gradient in z direction in fluid domain can be connected with the particle acceleration of the structure normal to the interface between the two media as

$$\left.\frac{\partial p}{\partial z}\right|_{z=0} = -\rho_0 \cdot \left.\frac{\partial v_n}{\partial t}\right|_{z=0}. \tag{5.9}$$

Substitution of the solution form of acoustic pressure in the region $x \geq 0, z \geq 0$ in Eq. (5.6) and transverse displacement of the beam in the region $x \geq 0$ in Eq. (5.5) into Eq. (5.9) yields the following relation,

$$\begin{pmatrix} -ik_{z_1}\mathcal{A}_3 \cdot e^{-ik_{x_1}x} - ik_{z_2}\mathcal{B}_3 \cdot e^{-ik_{x_2}x} \\ -ik_{z_3}\mathcal{C}_3 \cdot e^{-ik_{x_3}x} - ik_{z_4}\mathcal{D}_3 \cdot e^{-ik_{x_4}x} \\ -ik_{z_5}\mathcal{E}_3 \cdot e^{-ik_{x_5}x} - ik_{z_6}\mathcal{F}_3 \cdot e^{-ik_{x_6}x} \end{pmatrix} = \rho_0 \cdot \omega^2 \cdot \begin{pmatrix} \mathcal{A}_1 \cdot e^{-ik_1x} + \mathcal{B}_1 \cdot e^{-ik_2x} \\ +\mathcal{C}_1 \cdot e^{-ik_3x} + \mathcal{D}_1 \cdot e^{-ik_4x} \\ +\mathcal{E}_1 \cdot e^{-ik_5x} + \mathcal{F}_1 \cdot e^{-ik_6x}. \end{pmatrix} \tag{5.10}$$

To have acoustic pressure solution for Eq. (5.10) on arbitrary frequency for arbitrary position, k_{x_i} should take the same value with k_i as

$$k_{x_1} = k_1,\ k_{x_2} = k_2,\ k_{x_3} = k_3,\ k_{x_4} = k_4,\ k_{x_5} = k_5,\ k_{x_6} = k_6. \tag{5.11}$$

Combined with the above relation (5.7), k_{z_i} should take the values as,

$$\begin{aligned} k_{z_1} &= \sqrt{{k_0}^2 - {k_1}^2}, \quad & k_{z_2} &= \sqrt{{k_0}^2 - {k_2}^2}, \quad & k_{z_3} &= \sqrt{{k_0}^2 - {k_3}^2}, \\ k_{z_4} &= \sqrt{{k_0}^2 - {k_4}^2}, \quad & k_{z_5} &= \sqrt{{k_0}^2 - {k_5}^2}, \quad & k_{z_6} &= \sqrt{{k_0}^2 - {k_6}^2}. \end{aligned} \tag{5.12}$$

In order to satisfy the Euler momentum Eq. (5.10), the corresponding coefficients in front of component of each wave mode on both sides of the equation should be identical to each other. Hence the coefficients in acoustic pressure solution are obtained as,

$$\begin{aligned} \mathcal{A}_3 &= \frac{i\rho_0\omega^2\mathcal{A}_1}{k_{z_1}}, \quad & \mathcal{B}_3 &= \frac{i\rho_0\omega^2\mathcal{B}_1}{k_{z_2}}, \quad & \mathcal{C}_3 &= \frac{i\rho_0\omega^2\mathcal{C}_1}{k_{z_3}} \\ \mathcal{D}_3 &= \frac{i\rho_0\omega^2\mathcal{D}_1}{k_{z_4}}, \quad & \mathcal{E}_3 &= \frac{i\rho_0\omega^2\mathcal{E}_1}{k_{z_5}}, \quad & \mathcal{F}_3 &= \frac{i\rho_0\omega^2\mathcal{F}_1}{k_{z_6}}. \end{aligned} \tag{5.13}$$

Substitution of the obtained wave vectors and amplitudes into Eq. (5.6) yields the acoustic pressure in the radiation field $x \geq 0, z \geq 0$ from the infinite beam as (omitting the time component $e^{i\omega t}$)

$$\begin{aligned} p(x,z,\omega) = &\frac{i\rho_0\omega^2\mathcal{A}_1}{k_{z_1}} \cdot e^{-i\left(k_1x + k_{z_1}z\right)} + \frac{i\rho_0\omega^2\mathcal{B}_1}{k_{z_2}} \cdot e^{-i\left(k_2x + k_{z_2}z\right)} + \frac{i\rho_0\omega^2\mathcal{C}_1}{k_{z_3}} \cdot e^{-i\left(k_3x + k_{z_3}z\right)} \\ &+ \frac{i\rho_0\omega^2\mathcal{D}_1}{k_{z_4}} \cdot e^{-i\left(k_4x + k_{z_4}z\right)} + \frac{i\rho_0\omega^2\mathcal{E}_1}{k_{z_5}} \cdot e^{-i\left(k_5x + k_{z_5}z\right)} + \frac{i\rho_0\omega^2\mathcal{F}_1}{k_{z_6}} \cdot e^{-i\left(k_6x + k_{z_6}z\right)} \end{aligned} \tag{5.14}$$

The similar process can be applied in deducing the coefficients in the solution of acoustic pressure in the region $x \leq 0, z \geq 0$, which is symmetric to the region $x \geq 0, z \geq 0$. Here no longer etc.

Amplitude of the pressure field is determined by the application of the condition of compatibility of normal velocities or displacements at the structure fluid interface. The specific acoustic impedance of the fluid at the interface $Z(x,\omega)$ describing the relationship between the oscillator velocity perpendicular to the vibrating surface and the resulting acoustic pressure at that point generated by that surface as shown in Eq. (5.15)

$$\begin{aligned} Z(x,\omega) &= \frac{p(x,0,\omega)}{v_n(x,\omega)} \\ &= \frac{\mathcal{A}_3 e^{-ik_1 x} + \mathcal{B}_3 e^{-ik_2 x} + C_3 \cdot e^{-ik_3 x} + \mathcal{D}_3 \cdot e^{-ik_4 x} + \mathcal{E}_3 \cdot e^{-ik_5 x} + \mathcal{F}_3 \cdot e^{-ik_6 x}}{i\omega \cdot (\mathcal{A}_1 e^{-ik_1 x} + \mathcal{B}_1 e^{-ik_2 x} + \mathcal{C}_1 \cdot e^{-ik_3 x} + \mathcal{D}_1 \cdot e^{-ik_4 x} + \mathcal{E}_1 \cdot e^{-ik_5 x} + \mathcal{F}_1 \cdot e^{-ik_6 x})} \end{aligned} \tag{5.15}$$

The real part of the impedance represents the energy that can be radiated into the ambient medium from surface S, while the imaginary part of the impedance represents the energy stored in the near field of the source, then we have the

$$\begin{aligned} P_\Sigma &= \frac{1}{2}\int_S \mathrm{Re}\left\{p(x,0,\omega)\cdot \tilde{v}_n^*(x,\omega)\right\} dS = \frac{1}{2}\int_S \mathrm{Re}\left\{Z(x,\omega)\right\}\cdot |v_n(x,\omega)|^2 dS \\ Q_\Sigma &= \frac{1}{2}\int_S \mathrm{Im}\left\{p(x,0,\omega)\cdot \tilde{v}_n^*(x,\omega)\right\} dS = \frac{1}{2}\int_S \mathrm{Im}\left\{Z(x,\omega)\right\}\cdot |v_n(x,\omega)|^2 dS \end{aligned} \tag{5.16}$$

We can see the square normal velocity of the vibrating surface can be regarded as an input to the energy radiation.

For simple harmonic vibration involving only one bending wave mode k, to follow Euler momentum in Eq. (5.9), component of wavenumber vector in x direction k_x should also be identical with the wavenumber k propagating in the structure as $k_x = k$, and component of wavenumber vector in z direction $k_z = \sqrt{{k_0}^2 - k^2}$, then the amplitude of the radiation pressure can be expressed as

$$\tilde{p} = \frac{i\rho_0\omega^2\tilde{w}}{k_z},$$

in which $\tilde{w}$ denotes the displacement amplitude of the propagating wave mode k in the structure. Therefore the resulting pressure field can be written as

$$p(x,z,\omega) = \tilde{p}\cdot e^{i(-k_x x - k_z z)} = \frac{i\rho_0\omega^2\tilde{w}}{k_z}\cdot e^{-i(kx+k_z z)}. \tag{5.17}$$

The radiation impedance at the structure fluid interface can be expressed as

$$Z(x,\omega) = \frac{p(x,0,\omega)}{v_n(x,\omega)} = \frac{\rho_0\omega}{k_z}. \tag{5.18}$$

Theoretically speaking, wavenumber vector $\mathbf{k}$ propagating in fluid domain can be decomposed with with $k_x = k$ and $k_z = \sqrt{{k_0}^2 - k^2}$, and it is generated by the transverse disturbance caused by wave mode k propagating in the vibrating structure. k_0 is frequency dependent with ${k_0}^2 = \left(\frac{\omega}{c_0}\right)^2$. When k is pure real and ${k_0}^2 < k^2$, k_z is pure imaginary and the generated sound wave will decay quickly in near field. When ${k_0}^2 > k^2$, k_z is pure real thus the generated sound wave will propagate to infinity. Although radiation field of complex Timoshenko beam is more complicated with consisting 6 wave vectors, the physical principle is similar with the radiation from single wave mode.

5.2.2 Numerical analysis of radiation from infinite complex Timoshenko beam based on SSG theory formulation

One numerical case is proceeded based on the formulation in section 5.2.1. The beam material is assumed to be aluminum with mu = 26 GPa, and the higher-order material constant values have been given in Table 2.1. Media in the fluid domain is set to be air with density $\rho_0 = 1.2\text{kg/m}^3$ and sound velocity $c_0 = 343\text{m/s}$. Cross section of the vibrating beam is considered to be rectangular with the height $h = 10a_0$ and width $b = 3h$, and the normalization parameter for length $L = 5h$. Amplitude of the harmonic transverse force $q_0 = 0.1\mu A$ at $x = 0$ in Figure 5.1. Then the transverse displacement as well as normal velocity of the vibrating surface can be obtained.

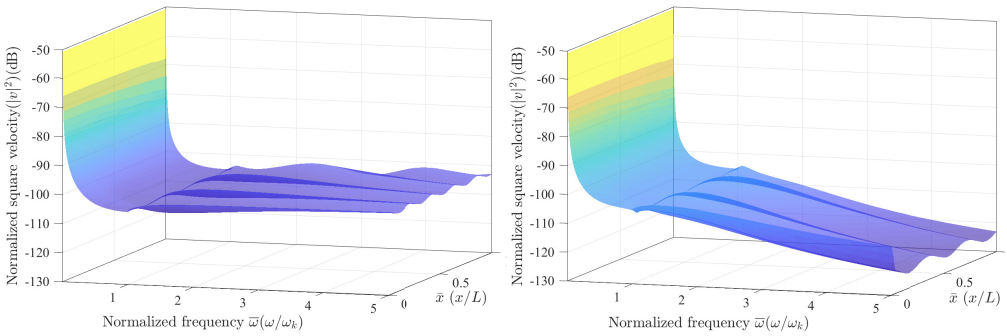

(a) Square velocity (CT) (b) Square velocity (SSG)

Figure 5.2: Transverse square velocity of the vibrating beam

Figure 5.2 illustrates the square normal velocity of the vibration surface of space interval $[0-1]$ in frequency range $0 < \overline{\omega} < 5$. As we can see, $|v_n|^2$ basically decreases as frequency $\overline{\omega}$ grows up from 0 to 1. In higher frequency range $1 < \overline{\omega} < 5$, $|v_n|^2$ is spatially dependent. According to classical theory result in Figure 5.2(a), $|v_n|^2$ varies spatially simply in sine form. In contrast, for SSG theory result in Figure 5.2(b), $|v_n|^2$ drops distinctly in the near field of excitation point $\overline{x} = 0$, then varies in sine form. The higher the frequency, the more distinct the decrease in near field. In the far field, $|v_n|^2$ of the SSG theory is lower than the classical result.

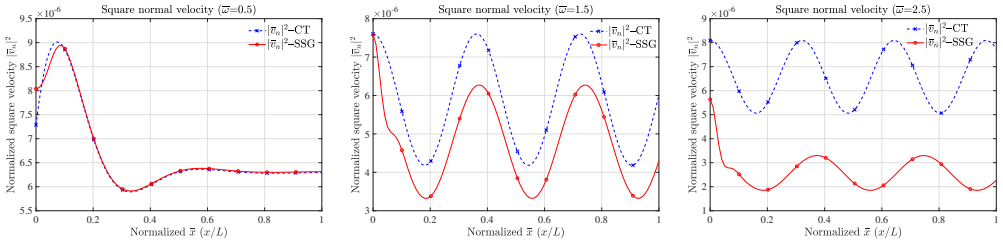

(a) (b) (c)

Figure 5.3: Transverse square velocity along x direction

To investigate the micro-structure effect on square velocity intuitively, a group of figures illustrating the surface square velocity of complex beam ($|v_n|^2$ – SSG) and classical beam ($|v_n|^2$ – CT) and on frequency $\overline{\omega} = 0.5$, $\overline{\omega} = 1.5$ and $\overline{\omega} = 2.5$ are displayed in Figure 5.3. As we can see, $|v_n|^2$ – SSG dose not differ much from the classical result on frequency $\overline{\omega} = 0.5$, but on higher frequency, $|v_n|^2$ – SSG at source point $\bar{x} = 0$ is lower and decrease obviously after being generated. In far field, $|v_n|^2$ – SSG is more lower than $|v_n|^2$ – CT and the difference becomes larger as frequency increase. Combined with the mobility analysis in Sec. 3.3, the lower generated square velocity results from the lower input structural mobility caused by energy converting to new wave modes, and the decrease of $|v_n|^2$ in near field can be interpreted with new evanescent waves decaying rapidly instead of propagating to infinity.

The input normal velocity determines the radiated energy along with radiation impedance, thus the decrease of normal velocity in the near field will significantly affects the acoustic radiation to the fluid domain. To display the resulting pressure field and radiation impedance systematically, firstly radiation impedance ($\overline{Z}$) on structure fluid interface Ω_Σ in region $0 < \overline{x} < 1$ is investigated.

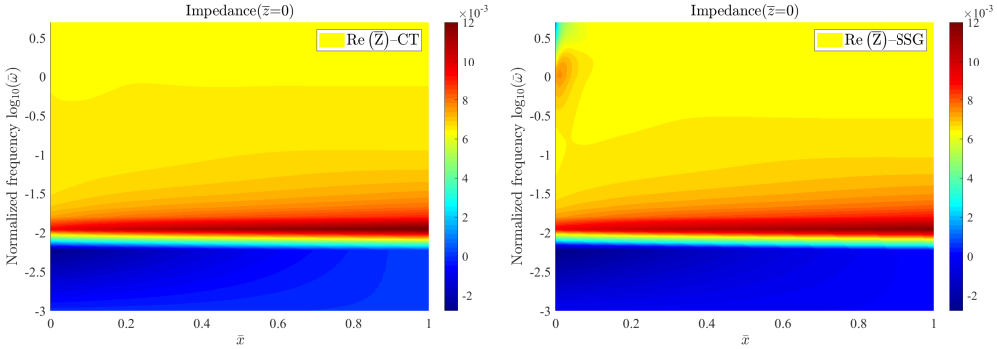

(a) Acoustic impedance (CT) (b) Acoustic impedance (SSG)

Figure 5.4: Acoustic radiation impedance

Figure 5.4 illustrates the real part of radiation impedance, which represents the energy that can be radiated into the fluid domain. As frequency goes up from zero, one clear line distinctly separate the figure, which indicate the radiation impedance

increase rapidly to one peak then drop off quickly. This phenomenon is caused by k_{z_1} (generated by bending wave) changing from pure imaginary value to pure real value on the critical frequency ω_r, then radiation of bending wave becoming effective. This peak arise for both classical beam and complex beam on the whole spatial position from 0 to 1. The different behavior between complex beam and classical beam is another relative small peak appearing in the near field of excitation on high frequency for radiation field of complex beam. This phenomenon is caused by k_{z_i} corresponding to the extra evanescent waves, and the small impedance peak appears exclusively in the near field of the force excitation as illustrated in Figure 5.5

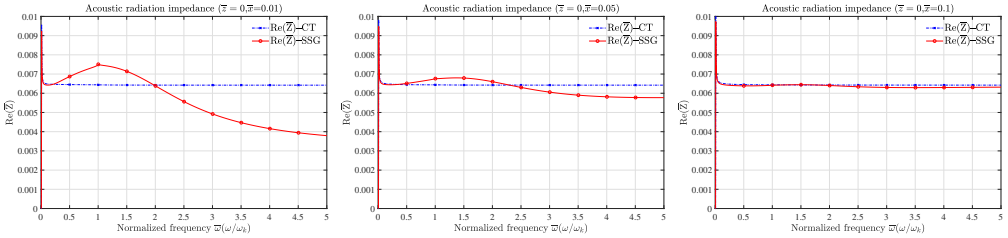

(a) (b) (c)

Figure 5.5: Acoustic radiation impedance changing with distance from force excitation

If the observation point is moving to the far field, from fig. 5.5(a) to fig. 5.5(c), the second peak becomes gentle and eventually disappear. One mathematical deducing process is provided in Appendix 6.2 to connect the second peak of impedance to the evanescent wave modes.

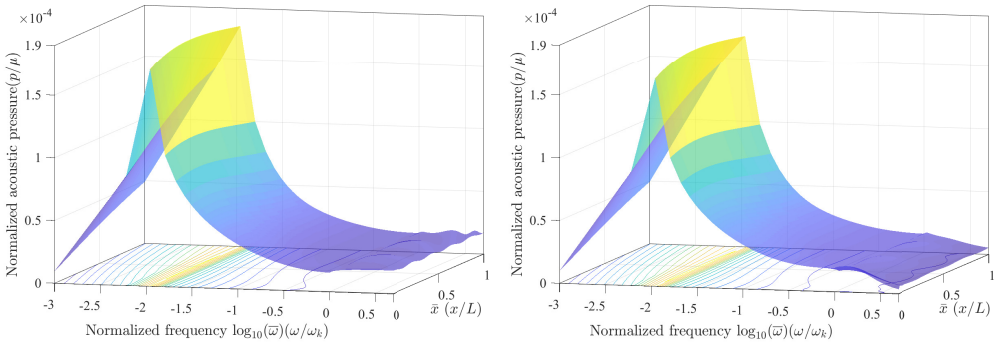

(a) Acoustic pressure (CT) (b) Acoustic pressure (SSG)

Figure 5.6: Acoustic pressure amplitude

Radiation pressure modulus $|\overline{p}|$ on the structure fluid interface Ω_Σ in region $0 < \overline{x} < 1$ is shown in Figure 5.6. There is one peak appearing in low frequency domain for both the classical model and the SSG theory model. This peak is governed by the critical frequency ω_r on which k_{z_1} transfers from pure imaginary to pure real value. In higher frequency range when $log10(\overline{\omega}) > 0$, namely $\overline{\omega} > 1$, $|\overline{p}| -$ SSG is obviously decreasing a little along with frequency increasing, the difference is caused

not only by the less input normal velocity but also the distinct radiation impedance character.

To mathematically demonstrate the resulting SSG theory acoustic pressure field, some interpretation are made as follows. For SSG theory-based Timoshenko beam, the pressure of point $(x_0, 0)$ on structure fluid interface can be expressed as

$$\begin{aligned} p\left(x_0,0,\omega\right) =& \frac{i\rho_0\omega^2\mathcal{A}_1}{k_{z_1}}\cdot e^{-ik_1x_0}+\frac{i\rho_0\omega^2\mathcal{B}_1}{k_{z_2}}\cdot e^{-ik_2x_0}+\frac{i\rho_0\omega^2\mathcal{C}_1}{k_{z_3}}\cdot e^{-ik_3x_0} \\ & \frac{i\rho_0\omega^2\mathcal{D}_1}{k_{z_4}}\cdot e^{-ik_4x_0}+\frac{i\rho_0\omega^2\mathcal{E}_1}{k_{z_5}}\cdot e^{-ik_5x_0}+\frac{i\rho_0\omega^2\mathcal{F}_1}{k_{z_6}}\cdot e^{-ik_6x_0} \end{aligned} \tag{5.19}$$

According to the above Figure 1, the bending wave component $k_{z_1}=\sqrt{{k_0}^2-{k_1}^2}$ is pure imaginary below the critical frequency ω_r, then become real as frequency exceeds ω_r. $k_{z_2}=\sqrt{{k_0}^2-{k_2}^2}$ is real in the whole frequency range, and the other k_{z_i} does not change significantly in lower frequency. Assuming the contribution of bending component to $|p|$ is $\frac{c+di}{x+yi}$ with $x+yi=k_{z_1}$, and the contribution form the other wave modes is $a+bi$ and then we have

$$\begin{aligned} |p| =& \left|a+bi+\frac{c+di}{x+yi}\right| = \left|a+\frac{cx+dy}{x^2+y^2}+\left(b+\frac{dx-cy}{x^2+y^2}\right)i\right| \\ =& \sqrt{\left(a+\frac{cx+dy}{x^2+y^2}\right)^2+\left(b+\frac{dx-cy}{x^2+y^2}\right)^2} \\ =& \sqrt{a^2+b^2+\left(c^2+d^2\right)\frac{x^2+y^2}{x^4+2x^2y^2+y^4}+2\frac{acx+ady+bdx-bcy}{x^2+y^2}} \end{aligned} \tag{5.20}$$

As ω increase to ω_r, $x=0$ and y is approaching to zero, thus p reach a peak at $\omega=\omega_r$, then ω exceed ω_r, $y=0$ and x is increasing with frequency, thus p decrease rapidly in frequency domain. In higher frequency range, $|\mathrm{Re}(k_{z_i})|$ $(i=3,4,5,6)$ increase significantly, and the $|\mathrm{Im}(k_{z_i})|$ decreases and approaches to zero. For one higher order wave, let's say k_3, assuming the contribution of k_3 to $|p|$ is $\frac{c+di}{x+yi}$ with $x+yi=k_{z_3}$, and the contribution form the other wave modes is $a+bi$, then Eq. (5.20) can also be utilized as the total expression of $\overline{p}$ with $x\neq 0, y\neq 0$. As frequency increase, x is continuously increasing and y is approaching to zero, $|\overline{p}|$-SSG will clearly decrease with frequency.

In order to investigate the radiation pressure field of complex Timoshenko beam structure changing in $x-z$ plan and study the influence of the evanescent wave caused by micro-structure effect in z direction, the radiation pressure field in region $\overline{x}\in[0-1], \overline{z}\in[0,10]$ on different frequency (ω=0.5, 1.5 and 2.5) are plotted in Figure 5.7

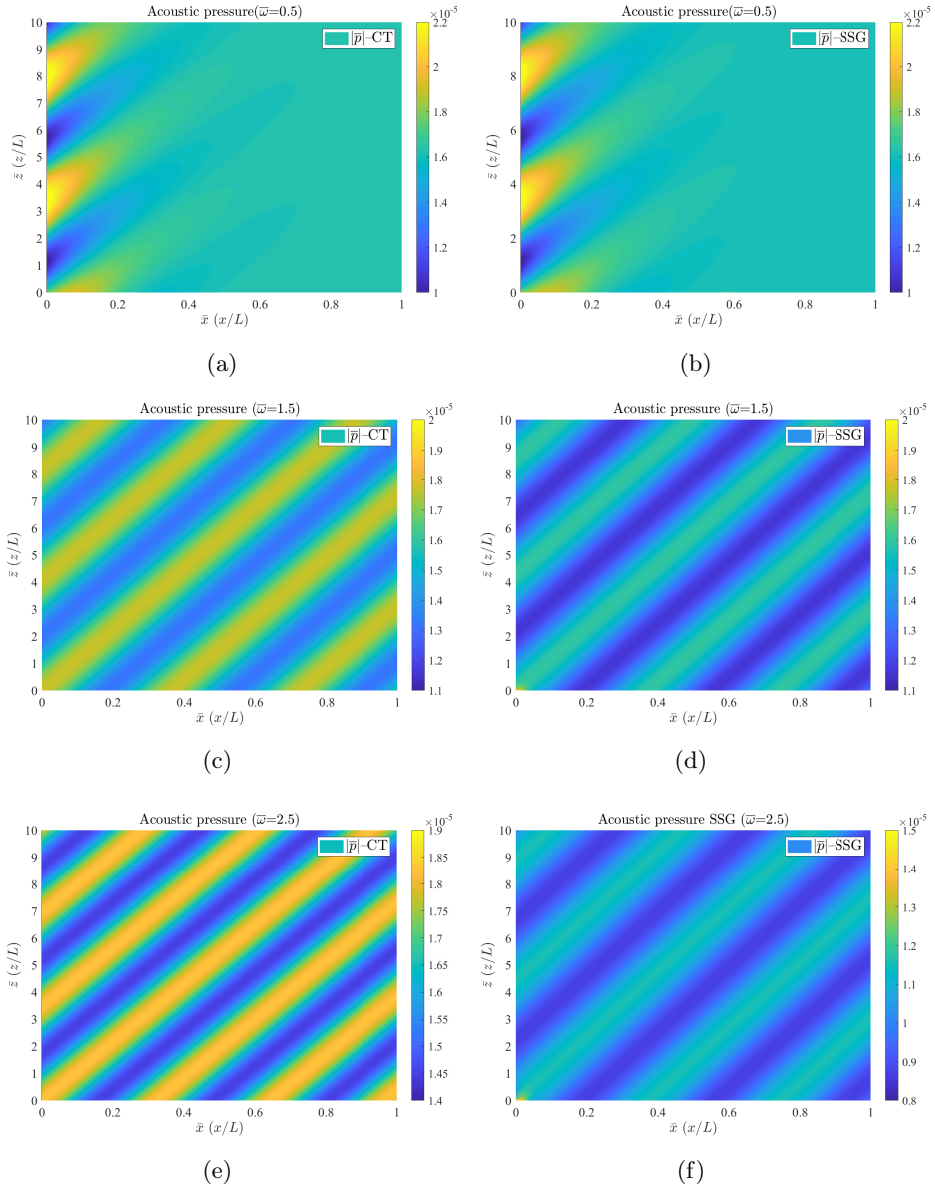

Figure 5.7: Acoustic pressure field in $x-z$ plane

Figure 5.7 illustrates the acoustic pressure field resulting from classical model and SSG theory-based mode on frequency ($\overline{\omega}=0.5$, 1.5 and 2.5) successively. Comparison of pressure field on each frequency yields the influence of the enrichment of micro-structure character on structural radiation behavior. Figure 5.7(a) and 5.7(b) shows results on frequency $\overline{\omega}=0.5$, we can see the pressure in the far field in x direction does not vary because $k_{x_2}=k_2$ is pure imaginary thus normal velocity amplitude v_n becomes a constant in the far field for both models. In addition, the results of these two models match well on on relative low frequency, it is reasonable because the influence of micro-structure is less prominent in low frequency range.

Radiation pressure field of complex beam on frequency $\overline{\omega} = 1.5$ in Figure 5.7(d) shows some differences with radiation of classical beam in Figure 5.7(c) as the pressure variation amplitude resulting from SSG theory model is lower than the classical one. This difference becomes more remarkable when frequency goes up to $\overline{\omega} = 2.5$. In higher frequency, wavelength is more comparable with the length of inner microstructures, therefore the resulting influence become more prominent. Moreover, the highest pressure can be observed near the force input source. Then the high pressure decrease rapidly with some slight fluctuation in the near field.

To study the drop of pressure in the near field of force excitation, SSG theory-based pressure fields in region $x \in [0 - 0.1], z \in [0 - 1]$ are respectively plotted on frequency $\overline{\omega}$ =0.5, 1.5, 2.5 and 3.5 in Figure 5.8.

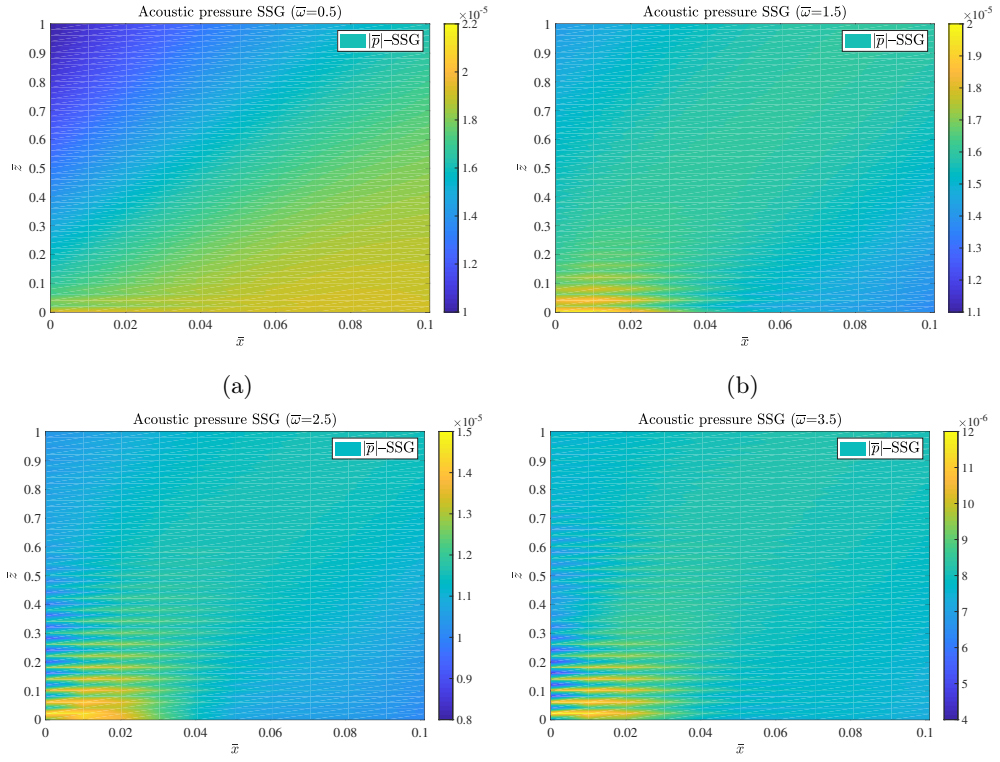

Figure 5.8: Near field of Radiation pressure field

As shown in Figure 5.8, decrease of radiation pressure in near field appears in the whole frequency range while more obvious for higher frequency. This phenomenon is caused by decay of short waves which are all generated by the evanescent waves in complex structure originating with the long range interaction between microstructures. After being radiated by the vibrating surface, sound pressure firstly decay rapidly to some extent in the near field then propagate away to infinity. Therefore we can conclude that the enrichment of micro-structure interaction character by SSG theory can successfully capture the distinct radiation behavior of complex

Timoshenko beam.

5.3 Radiation from finite beam

When the beam structure is in finite size with specified boundary condition, its vibration will have modal behaviors which governed by its material properties, geometrical shape, and boundary conditions. In this section, the formulation for the sound radiation of finite beam into an infinitely extended fluid domain Ω_f by vibrating surface S_a is developed, based on which numerical analysis of sound radiation from a simply supported beam in a rigid baffle is implemented. The resulting radiation pressure field of complex Timoshenko beam are illustrated and the influence of micro-structure interaction characters will be discussed by comparing the SSG theory model result and classical theory result.

5.3.1 Formulation of radiation from finite SSG theory-based beam structure

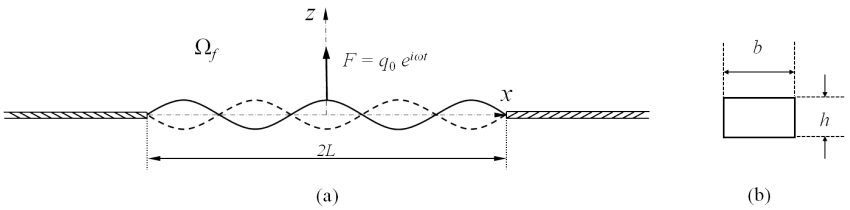

Figure 5.9: sound radiation from simply supported beam in a rigid baffle

As shown in Figure 5.9, one beam of length $2L$ in x direction embedded in an infinite rigid baffle is considered. The beam is simply supported at both ends and excited by one harmonic force in the middle. The cross section is the beam is of width b and height h. Theoretically, the vibration movement can be described by a superposition of all the vibrating modes in SSG theory model with different participation amplitudes, which determined by its boundary condition and external excitation. For the studied case, the transverse displacement can be expressed as

$$w(x,t) = \tilde{w}\,(x) \cdot e^{i\omega t}. \tag{5.21}$$

in which $\tilde{w}\,(x)$ represents the product of complex modal displacement amplitude and modes at each position on each frequency as

$$\begin{aligned}\tilde{w}\,(x) = \Big(&\mathcal{A}_1 e^{-ik_1 x} + \mathcal{B}_1 e^{ik_1 x} + \mathcal{C}_1 e^{-ik_2 x} + \mathcal{D}_1 e^{ik_2 x} + \mathcal{E}_1 e^{-ik_3 x} + \mathcal{F}_1 e^{ik_3 x} \\ &+\mathcal{G}_1 e^{-ik_4 x} + \mathcal{H}_1 e^{ik_4 x} + \mathcal{I}_1 e^{-ik_5 x} + \mathcal{J}_1 e^{ik_5 x} + \mathcal{K}_1 e^{-ik_6 x} + \mathcal{L}_1 e^{ik_6 x}\Big).\end{aligned} \tag{5.22}$$

Then the surface vibration velocity distribution $v_n\,(x,\omega)$ for the SSG theory-based Timoshenko beam model is given as

$$v_n(x,\omega) = i\omega \cdot \tilde{w}\,(x) \cdot e^{i\omega t} = \tilde{v}_n \cdot e^{i\omega t}. \tag{5.23}$$

$\tilde{v}_n(x)$ represents the product of complex modal velocity amplitude and modes at each position on each frequency.

The total sound radiation due to the surface vibration can be regarded as the superposition of all the progressive and retrograde modes, and each mode can be regarded as the superposition of a number of independent baffled piston cases. Therefore, the radiation from each mode could be estimated individually and then summed to give the total radiation pressure field. The principle of superposition is illustrated in Figure 5.3.1

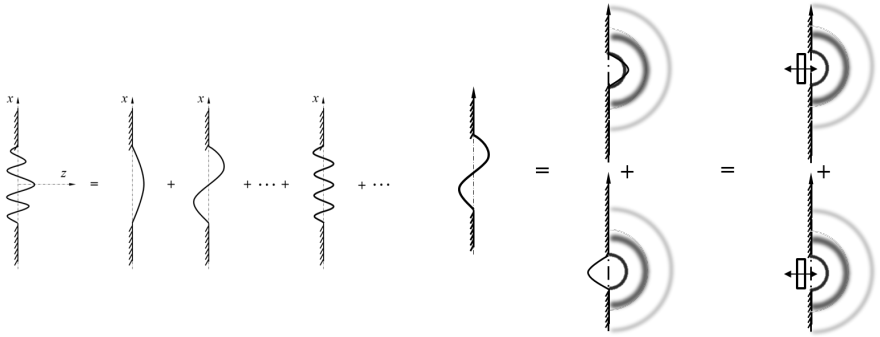

(a) Wave mode superposition (b) baffled piston radiation superposition

Figure 5.10: principle of superposition

To estimate the pressure field of each mode, the direct boundary integral formulation based on the Kirchhoff–Helmholtz integral theorem is given here. The pressure at a field point $\mathbf{r}$ in the interior or the exterior volume can be expressed in terms of the pressure $p(\mathbf{r})$ and the normal velocity $\tilde{v}_n$ at a boundary point $\mathbf{r}_a$ on the related closed boundary surface S_a as

$$c(\mathbf{r})p(\mathbf{r}) = \iint_{S_a} \left(p(\mathbf{r}) \frac{\partial G(\mathbf{r}, \mathbf{r}_a)}{\partial n} + i\rho_0 \omega G(\mathbf{r}, \mathbf{r_a}) \tilde{v}_n(\mathbf{r}_a) \right) dS_a; \tag{5.24}$$

where $c(\mathbf{r})$ is a coefficient dependent on the location of the field point. For the studied exterior problem, $c(\mathbf{r}) = -1$, -0.5 and 0 for points inside the volume Ω_f, on the surface S_a, and outside the volume Ω_f, respectively. n is the normal at the boundary surface directed to the fluid domain; G is a Green's function satisfying the Helmholtz equation. In the following analysis, the Green's function is applied to unbounded fluid. Without scattering boundaries, the Green's function must satisfy the Sommerfeld radiation condition that only waves travelling outward from the point source are allowed, and that the pressure tends to zero at an infinite distance from the source, one solution is

$$G(\mathbf{r}, \mathbf{r}_a, \omega) = \frac{e^{-ik|\mathbf{r}-\mathbf{r}_a|}}{4\pi |\mathbf{r} - \mathbf{r}_a|} \tag{5.25}$$

Therefore, the direct boundary integral formulation states that for the harmonic sound pressure field that satisfies the homogeneous Helmholtz equation and the Sommerfeld radiation condition, the acoustic pressure in any point $\mathbf{r}$ in the unbounded

fluid domain Ω_f is determined by the combination of the pressure distribution $p(\mathbf{r}_a)$ and normal velocity distribution related with $\frac{\partial G}{\partial n}$ on the vibrating boundary surface S_a.

For the studied beam structure, assuming the pressure on each vibrating surface of S_a^+ and S_a^- is $p(\mathbf{r})$, Green's function on S_a^+ and S_a^- is G_{S_a}, $\frac{\partial G}{\partial n}$ on S_a^+ and S_a^- will have the same magnitude but different sign. Then the contribution of the first term, pressure distribution, will be necessarily cancelled out. The only remaining term is the second term, the normal velocity distribution. The green's function propagate the normal velocity which related with $\frac{\partial p}{\partial n}$, from the surface. Then the pressure at any point in radiated field can be expressed purely in terms of the distribution of normal surface acceleration as

$$p(\mathbf{r}) = \iint_{S_a^+ + S_a^-} \left(-G(\mathbf{r}, \mathbf{r_a}) \frac{\partial p(\mathbf{r_a})}{\partial n} \right) dS_a = \iint_{S_a^+} \left(-2i\rho_0 \omega G(\mathbf{r}, \mathbf{r_a}) \tilde{v}_n(\mathbf{r_a}) \right) dS_a; \tag{5.26}$$

For the studied SSG theory-based Timoshenko beam, the pressure at point (x', z') in the radiated fluid domain can be obtained by substitute the normal velocity distribution (5.23) and form of Green's function into the Kirchhoff Helmholtz integral Eq. (5.26) as (omitting the time component $e^{i\omega t}$)

$$p(x', z', \omega) = \frac{-i\rho_0 \omega}{2\pi} \int_{-L}^{L} \frac{e^{-ikR}}{R} \tilde{v}_n(x)\, dx; \tag{5.27}$$

in which $R = \sqrt{(x' - x)^2 + z'^2}$ represents the distance between the observation point (x', z') and the source $(x, 0)$, and $\tilde{v}(x)$ is the product of modal velocity amplitude and mode shape as shown in Eq. (5.22).

5.3.2 Numerical calculation of radiation from simple supported complex Timoshenko beam

In this section, one numerical case is implemented based on the previous formulation. The beam cross section is assumed to be rectangular with height $h = 10a_0$ (lattice parameter $a_0 = 4.04$Å), width $b = 3h$, and half length $L = 5h$. The structure is made of aluminum and fluid is set to be air, material of these two media have been referred in section 5.2.2. The amplitude of the harmonic axial force $q_0 = 0.01\mu A$ at $x = 0$ in Figure 5.9. Substitute the above parameters into the formulation, the transverse displacement as well as normal velocity of the vibrating surface can be obtained, then the radiated pressure field can be obtained with the integral equation Eq. (5.27).

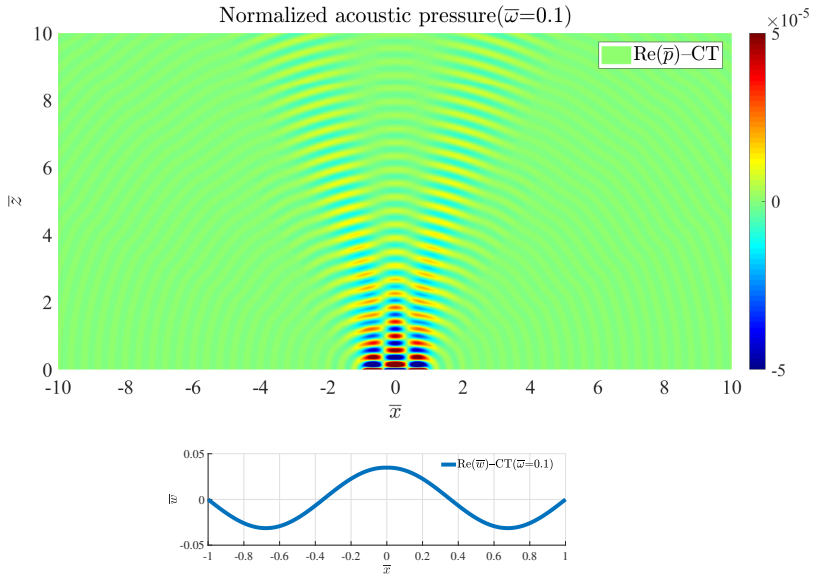

Figure 5.11: Classical acoustic pressure field and transverse displacement ($\overline{\omega} = 0.1$)

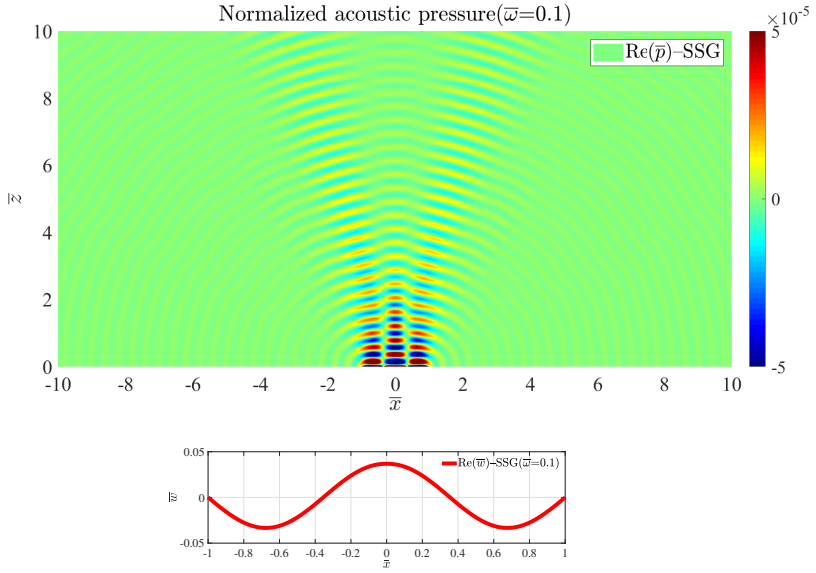

Figure 5.12: SSG acoustic pressure field and transverse displacement ($\overline{\omega} = 0.1$)

Figure 5.11 and 5.12 illustrate the radiated pressure field on frequency $\overline{\omega} = 0.1$ and the corresponding structure vibration shape of classical beam and complex beam. The frequency is in low frequency range, and the deformation wavelength is rather longer than the internal micro-structure, therefore the influence of micro-structure is negligible, and results of classical model and SSG theory model math well in terms of both structural vibration shape and radiation pressure.

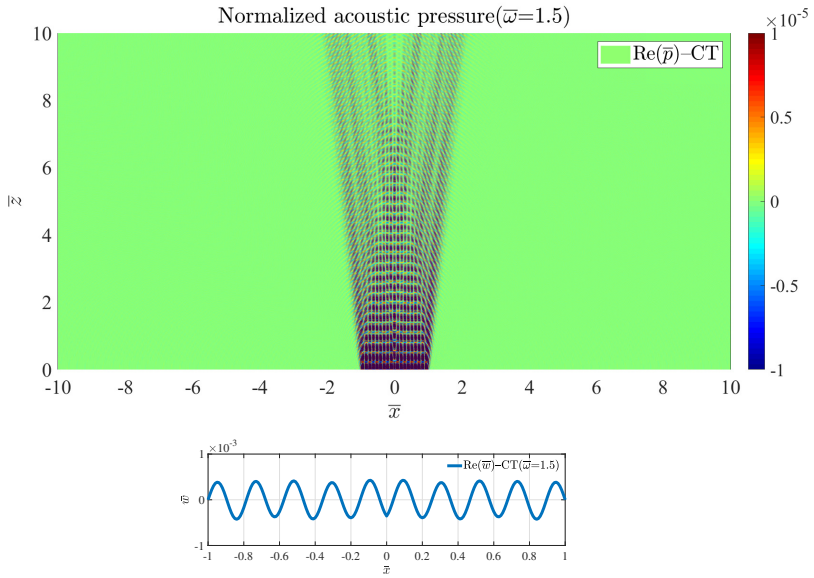

Figure 5.13: Classical acoustic pressure field and transverse displacement ($\overline{\omega} = 1.5$)

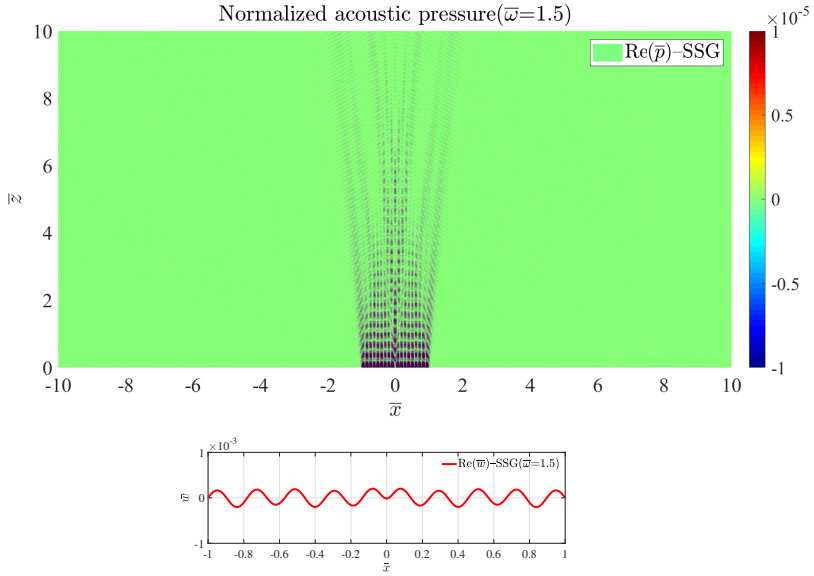

Figure 5.14: SSG acoustic pressure field and transverse displacement ($\overline{\omega} = 1.5$)

Figure 5.13 and 5.14 illustrate the radiated pressure field on frequency $\overline{\omega} = 1.5$ and the corresponding structure vibration shape for both classical beam and complex beam. The frequency is higher and deformation wavelength generated by excitation is comparable to the inner micro-structure, thus amplitudes of radiation pressure as well as structural vibration decrease distinctly.

To display more information on radiation pressure field in frequency domain, 4 special points are selected and investigated as shown in Figure 5.15.

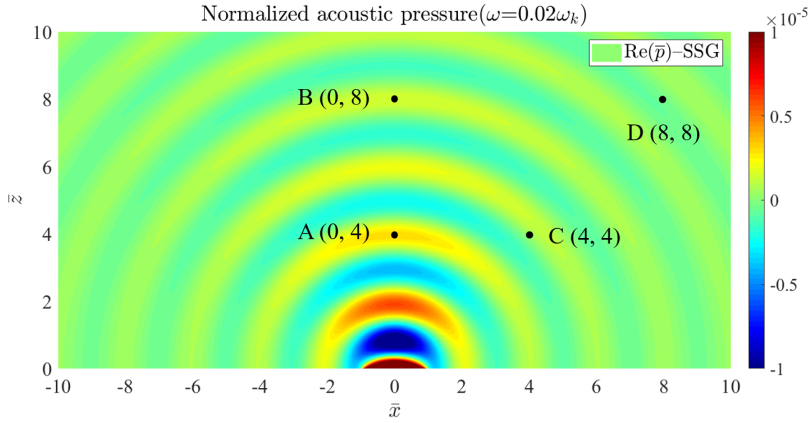

Figure 5.15: Points studied in frequency domain

As we can see, these four points are all located in the far field of the radiator. Pint A and B are right above the force excitation, meanwhile in the symmetrical line of the system, therefore the radiation form left-half and right-half of the beam can be self-cancelling. Point C and D are selected to be in general positions. The frequency-dependent radiation pressure modulus $|\overline{p}|$ of these four points are illustrated as follow,

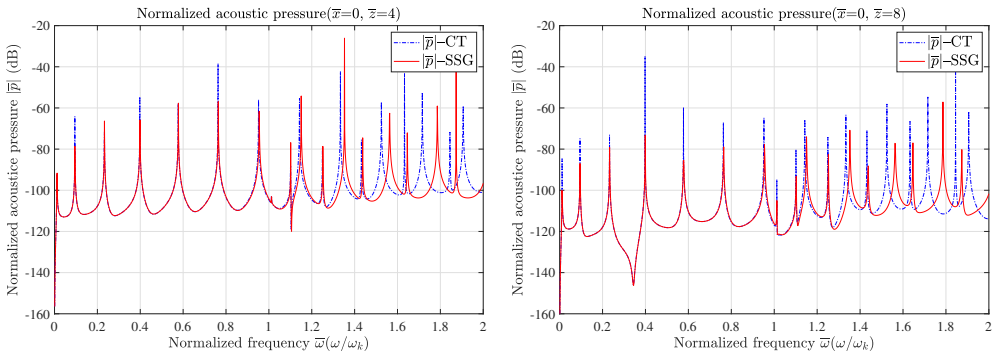

(a) Acoustic pressure at point A (b) Acoustic pressure at point B

Figure 5.16: Acoustic pressure at point A and B in frequency domain

Figure 5.16 illustrate comparison of normalized acoustic pressure modulus $|\overline{p}|$ at point A and B resulting from classical theory model and SSG theory-based model in frequency range $0 \leq \overline{\omega} \leq 2$. The results match well in lower frequency, and start to show slight difference when $\overline{\omega} > 0.8$. Starting from seventh order, peaking frequencies does not match well as the frequency value resulting from SSG theory model is higher. This phenomenon becomes more serious as frequency is higher. In that case the vibration amplitude shape of complex beam also shows great difference with the classical beam. The difference originates with distinct structural resonant behavior of complex beam (in Sec. 3.4) and pressure decay in the near field of excitation in fluid domain.

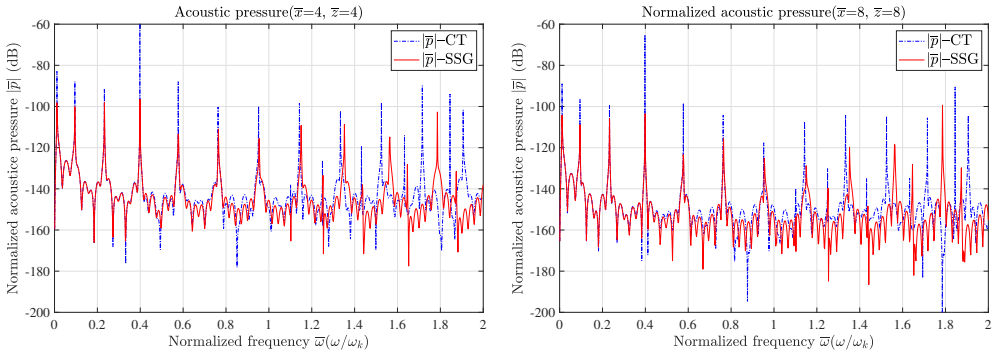

(a) Acoustic pressure at point C (b) Acoustic pressure at point D

Figure 5.17: Acoustic pressure at point C and D in frequency domain

Figure 5.16 illustrate the comparison of $|\overline{p}|$ at point C and D resulting from classical model and SSG theory model in frequency range $0 \leq \overline{\omega} \leq 2$. Compared with the above two figures, there are some small bumps arising between the neighboring resonant frequencies, which are caused by the integration of radiation from a mass of points on the radiator surface. The results match well in very lower frequency, and differences start to arise when $\overline{\omega} > 0.4$. As the pressures at point C and D are determined by the normal velocities of all the points on the beam surface, $|\overline{p}|$ is more sensitive to the enrichment of micor-structure character in SSG theory model. Therefore, the difference starts in lower frequency rang and appears not only in forms of higher resonant frequencies, but also different varying profile between the neighboring resonances.

5.4 Conclusion

In this chapter, sound radiation from complex Timoshenko beam is investigated with employing the proposed SSG theory-based beam model. The investigation is in terms of vibrating surface square velocity, radiation acoustic impedance and radiated pressure field. Then the influence of internal micro-structure on radiation is evaluated.

(1)For radiation from infinite complex Timoshenko beam, square velocity of vibrating surface as a whole is lower than classical result in high frequency range. The reduction can be interpreted by lower input structural mobility and velocity decreasing resulting from evanescent waves decaying in the near field of excitation point.

(2) The maximum point of non classical radiation impedance is located on the critical frequency for bending wave, besides that, one small peak appears in higher frequency range in the near field of excitation point. The second peak originates with wavevector corresponding to the evanescent waves in complex beam, therefore when the observation point is moving to the far field, the second peak becomes gentle and eventually disappear.

(3) Radiated pressure resulting from SSG theory model decrease distinctly in the far radiation field when the normalized frequency $\overline{\omega} > 1$. This decrease becomes more remarkable as frequency goes up. Another interesting phenomenon is that radiated pressure field decreases with fluctuation in the near field of force excitation. This phenomenon is caused by decay of short waves in fluid domain, which are generated by evanescent waves in complex structure. Therefore we can conclude that the radiation level from complex beam is lower resulting from firstly less transverse velocity input, then sound wave decay in the near field. The underlying physics lies in the distinct local behavior of heterogeneity governed by both near range and long range interactions.

(4) Radiation pressure from simply supported complex beam is determined by the normal velocity of all the points on the vibrating surface. The resulting radiation pressure from complex beam matches with classical one in low frequency, but it is much lower than the classical one in higher frequency. For radiation pressure analysis at specific points in frequency domain, points randomly distributed is more sensitive to the influence of local dynamic behavior of heterogeneity caused by complex inner micro-structures interactions, and starts exhibiting obvious differences as frequency $\overline{\omega} > 0.4$.

Chapter 6

Conclusion and perspectives

6.1 Conclusion

The main contributions of the conducted work are summarized below:

(1) In the first chapter, the investigations on failure of conventional continuum theory is given, upon which complex media is introduced for latter analysis. A review of numerous methods is given for periodic structure modelling. As an alternative approach to study the complex media with periodicity, the generalized continuum elasticity theory is introduced with detailed explanation of its historical development, fundamental equations and applications in different fields. Mindlin's second strain gradient theory is presented in detail and this theory is proven to be capable of capturing the complex interaction between micro-structures with its additional material constants. In the last part, length scale parameter existing in the generalized theory-based models are discussed, and different approaches to identify the length scale parameter are investigated.

(2) Enriched models respectively describing non-classical motion in complex rod and complex Timoshenko beam are developed based on Mindlin's Second Strain Gradient (SSG) theory, which can describe heterogeneity caused by complex microstructure interactions in the frame of continuum mechanics. The governing equations and associated boundary conditions are derived for complex rod in chapter 2, and for complex Timoshenko beam in chapter 3, based on Hamilton's principle. Non-classical longitudinal wave together with two evanescent waves appearing exclusively in SSG theory-based rod model are investigated in terms of the dispersion relation, sized effect, viscous damping effect and modal density. In the same manner, non-classical bending wave and shear wave together with the four extra evanescent waves appearing exclusively in SSG theory-based Timoshenko beam model are investigated. Compared with the results of classical theory model, non-classical longitudinal wave in complex rod, non-classical bending wave and non-classical shear wave in complex beam exhibit dispersive feature, the dispersive behavior become more prominent in higher frequency or for small size structure. In addition, the effect of viscous damping on these three kind of non-classical wave in complex media become negligible in higher frequency. Modal density of these three kind of non-classical propagating waves decreases drastically in frequency range compared with classical results. With employing the SSG theory-based models, long range interaction between underlying micro-structures can be described, thus the distinct structural behavior of complex media can be captured by incorporating with local behavior of

heterogeneity. The long range interaction description becomes more important when the deformation wavelength is comparable with the internal structural characteristic length, therefor the difference become more serious as the external wavelength decrease (higher frequency) or the structure internal size decreases (size effect).

(3) One lattice model is proposed in chapter 2 to establish a micro-structure basis for the SSG theory-based continuous structural model. The proposed lattice model is capable of reflecting the long range force interaction between inner particles. With the map operation, the proposed 1-D lattice model can be transformed to SSG theory-based rod model in limit $d \to 0$, and the long range interaction coefficients are connected with the material constants. Thus the proposed SSG theory continuous model can capture the co-dynamic behavior of local micro-character and global macro-structure in high frequency with higher order constants describing the long range interaction.

(4) The proposed formulation of the energy flux for SSG theory-based rod and SSG theory-based Timoshenko beam are validated in chapter 2 and chapter 3 as the resulting energy velocity V_e of conservative wave are proved to be identical with the group velocity C_g in the whole frequency range. Based on the proposed energy flux expression, infinite extended complex rod/beam excited by harmonic longitudinal/ transverse force are analyzed with respect to its input mobility and transfer mobility as well as the input power and transfer power. In general, the complex structure shows more resistance to the harmonic force excitation. The net power transmitted into the complex structure diminish distinctly compared with the classical result and more proportion of work is in forms of reactive power which does not transform power from force or dissipate power. The generated disturbance propagate away in a different manner in the complex beam. Transfer mobility modulus as well as reactive power decay significantly in the near field of the excitation point. The decrease in near field becomes significant in higher frequency as the micro-structure interaction is more prominent. The greater the distance between the points of observation and force application, the smaller the near-field effect. Due to the local behavior of heterogeneity caused by micro-structure interactions, the input vibration energy is in forms of not only the non-classical propagating waves, but also the evanescent wave modes which will decay rapidly in the near field, thus more energy attenuates in the system. For the FRF analysis of complex rod and complex beam, the resonant frequency of corresponding order resulting from SSG theory models is higher than classical model, and less resonances can be observed in the same frequency range for both rod and beam model. The frequency response resulting from analytical wave approach is validated by FEM in COMSOL

(5) Wave reflection and transmission in complex structures are investigated in chapter 4. For vibration energy in form of both longitudinal wave and bending wave, the incident energy is predicted to transmit more and reflect less in total. However, a proportion of transmitted and reflected energy is converted into evanescent waves

(k_2 and k_3 for rod, k_3, k_4, k_5 and k_6 for beam) duo to the local behavior of heterogeneity, thus the transmission coefficient of the incident wave decrease slightly and the reflection coefficient decreases drastically for both the longitudinal wave case and the bending wave case, the higher the frequency becomes, the greater the impact of micro-structure. Longitudinal wave reflection and transmission through a certain length of complex rod is highly dependent on material property constants and length of complex rod d. As length d increase, the result approach to classical theory result. With some predefined Young's modulus, density and higher order material constants, reflection coefficient C_r can approach '1' extremely in some frequency range, in that case all the input energy will be reflected while the transmitted energy is close to zero. This phenomenon shows that the SSG theory model can be employed to optimize and to enrich the complex structure for better structural performance in acoustics.

(6) Sound radiation characters form complex beam are investigated in chapter 5 based on the formulation in chapter 3. For sound radiation from infinite complex beam, square velocity, as the input to sound radiation, is lower than classical result in high frequency range due to lower force driving mobility and evanescent wave modes decaying in space. The maximum point of non-classical radiation impedance is located on the critical frequency for bending wave, besides that, one small peak appears in the near field of excitation point due to the variation of wave vector generated by evanescent waves in higher frequency. The radiated pressure field of complex beam is lower than classical one in the far field when $\overline{\omega} > 1$. Another interesting phenomenon is that the SSG theory-based pressure field decreases with fluctuation in the near field of excitation source, and this phenomenon is caused by decay of short waves in fluid domain, which are all generated by evanescent waves in the SSG theory structure. In short, the radiated pressure reduction is caused by the complex structural behavior and decay of short wave, both of which are arising form capturing the local behavior of heterogeneity. Thus the decrease in far field and in near field become more remarkable as frequency goes up. Radiation pressure from simply supported complex beam is determined by the normal velocity of all the points on the vibrating surface. The resulting radiation pressure from complex beam is much lower than the homogeneous beam in higher frequency. Points randomly distributed is more sensitive to the influence of local dynamic behavior of heterogeneity caused by complex inner micro-structure interactions.

6.2 Perspectives

Modelling and wave propagation analysis of complex media, especially the periodic media, has attracted much attentions from the researchers and the field is experiencing continued growth in research activities. Modelling of complex media based on generalized continuum elasticity theory provides another direction to investigate the distinct dynamic behavior of complex media which can only be described by incorporating with the local behavior of its inner heterogeneity. In the meantime,

the new model also offers much more possibilities for application of complex media. The perspectives of the presented research will be presented in terms of theoretical enrichment and potential application.

(1) Even though the proposed model is capable of capturing the local behavior of heterogeneity caused by complex interaction between micro-structures, this model can still be improved in dynamic behavior analysis. For example, the additional micro-inertia term introduced by Domenico [96] can also be introduced in the present SSG theory model. Then the higher-order stiffness terms can be accompanied by higher order inertia terms, the behavior predicted by the modified model can be more dynamic consistence.

(2) Combined with plate theory, the SSG theory-based plate model can be developed, upon which 2D wave propagation can be investigated with considering the local behavior of internal heterogeneity. All the relevant characteristics can be obtained, including 2D dispersion relation, wave propagation velocity, energy flux, wave reflection and transmission behavior through planer surface and wave radiation from vibrating surface. The influence of local behavior can be thoroughly analyzed and interpreted.

(3) There is still no specified physical meaning for the higher order material constants in SSG theory, but they has much influence on the behavior of complex media. The influence of higher order material constants on wave propagation characteristics can be studied in further research. Furthermore, the influence of structure parameter on wave propagation in complex media can be investigated, for example, the ratio effect, the Timoshenko shear coefficient, the ratio between the structure length and cross section dimension.

(4) With the discrete lattice modal, periodic structure with unite cells composed of non-classical medias can be modeled, that means heterogeneity in periodic media is not only in forms of periodic cell but also in form of internal structure that consist of the unit cell. With this model, the non-linearity at the edge of band gap could be captured. More complex behavior in short wave length can be investigated analytically.

(5) Investigation of wave propagation through a certain length of complex rod has been done in this research. With the same approach, wave transmission through a certain length of complex beam can be studied. The transmission coefficient should also be affected by the wave propagation distance and material constants of the complex beam. With this SSG theory-based wave transmission model, some potential application of complex media can be presented. For example, one periodic structure can be designed in forms of multiple layer. With some predefined material constants and certain internal length scale, this complex media can process high performance in absorbing the transmission energy and blocking some specific wave transmission.

(6) With the wave transmission formulation in Sec 4.4, another application is finding an appropriate SSG theory model by setting some specific material constants in order to achieve zero reflection through complex media, then the SSG theory model can be regarded as an equivalent model to the classical homogeneous rod but can capture the multi-scale behavior. The process to find the material constants by achieving zero reflection can be employed as an approach to find the appropriate higher order constants for meter-scale periodic structures with micro-scale unit cells.

(7) With the analytical motion equations deduced based on SSG theory and proper input in forms of weak form, COMSOL can be employed in many practical application to analyze the static behavior as well as the dynamic behavior of complex media. This process can significantly simplify the dynamic behavior investigation of complex medium. Most importantly, this procedure can not only apply to generalized rod and beam model, but also apply to plate model and wave radiation model. More related work will be done later.

Appendix A Mathematical justification of acoustic impedance variation

To have a mathematical comprehension of the second impedance peak, some detailed interpretation are made here. For a vibrating complex beam based on SSG theory model, there are six wave modes generated by force excitation, correspondingly, six wave vector and corresponding k_{z_i} in fluid domain. Based on the previous formulation, the radiation impedance of point $(x_0, 0)$ on structure fluid interface can be expressed as

$$Z(x_0,\omega) = \frac{p(x_0,0,\omega)}{v_n(x_0,\omega)} = \frac{i\rho_0\omega^2\mathcal{A}_1}{v_n\cdot k_{z_1}}e^{-ik_1x_0} + \frac{i\rho_0\omega^2\mathcal{B}_1}{v_n\cdot k_{z_2}}\cdot e^{-ik_2x_0} + \frac{i\rho_0\omega^2\mathcal{C}_1}{v_n\cdot k_{z_3}}\cdot e^{-ik_3x_0} + \frac{i\rho_0\omega^2\mathcal{D}_1}{v_n\cdot k_{z_4}}\cdot e^{-ik_4x_0} + \frac{i\rho_0\omega^2\mathcal{E}_1}{v_n\cdot k_{z_5}}\cdot e^{-ik_5x_0} + \frac{i\rho_0\omega^2\mathcal{F}_1}{v_n\cdot k_{z_6}}\cdot e^{-ik_6x_0} \tag{1}$$

We can see the resulting impedance is strongly affected by the wavenumber components in z direction k_{z_i} along with resulting normal velocity. In the following, k_{z_i} $(i = 1, 2, 3, 4, 5, 6)$ will be fully analyzed. Assuming the non-classical bending wave is denoted as k_1 (real), shear wave is k_2 ($\overline{\omega} < 1$ imaginary, $\overline{\omega} > 1$ real) and the other 4 evanescent waves are respectively k_3, k_4, k_5 and k_6, wavenumber vector components k_{z_i} are illustrated as follows

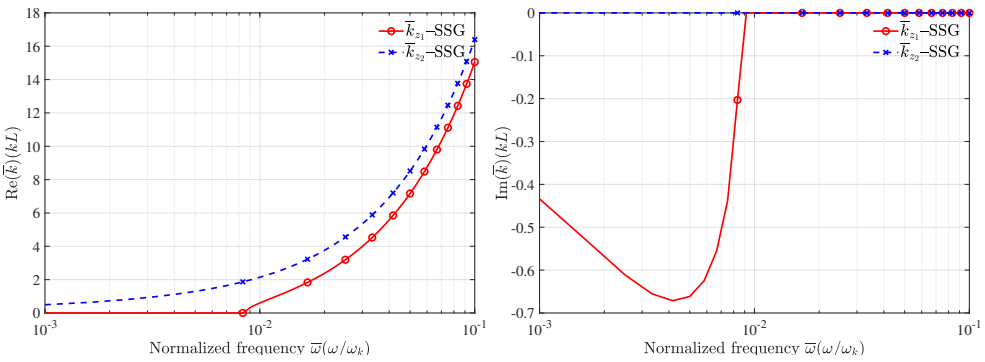

(a) Real part of k_{z_1} and k_{z_2} (b) Imaginary part of k_{z_1} and k_{z_2}

Figure 1: Real part and imaginary part of k_{z_1} and k_{z_2}

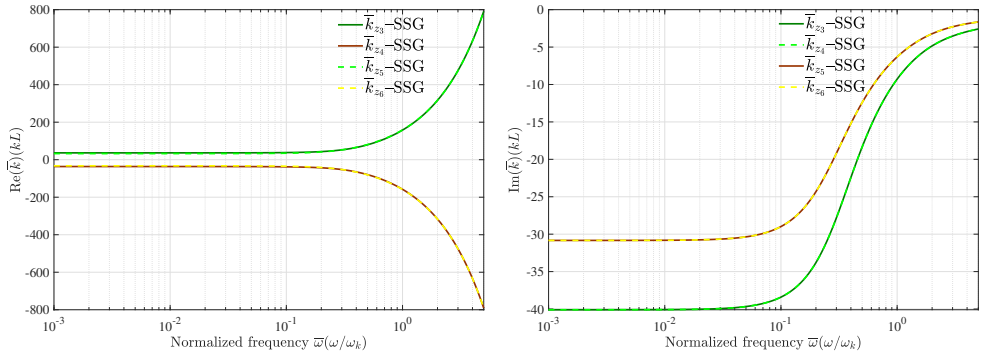

(a) Real part of k_{z_3}, k_{z_4}, k_{z_5} and k_{z_6} (b) Imaginary part of k_{z_3}, k_{z_4}, k_{z_5} and k_{z_6}

Figure 2: Real part and imaginary part of k_{z_3}, k_{z_4}, k_{z_5} and k_{z_6}

As shown in Figure 1, in lower frequency, wavenumber component $k_{z_1} = \sqrt{{k_0}^2 - {k_1}^2}$ corresponds to bending wave and is pure imaginary below the critical frequency ω_r, then become real as frequency exceeds ω_r. Wavenumber component $k_{z_2} = \sqrt{{k_0}^2 - {k_2}^2}$ is real in the whole frequency range. All the other k_{z_i} (i=3,4,5,6) are complex values and do not change obviously in low frequency range but change strongly in higher frequency as shown in Figure 2.

Since the changing trend of k_{z_i} in frequency domain is known, impedance peak should be able to prove mathematically. For the first peak around the critical frequency ω_r, assuming the contribution of bending component to Z is $\dfrac{c+di}{x+yi}$ with $x + yi = k_{z_1}$, and the contribution form the other wave modes is $a + bi$, then we have

$$Z = a + bi + \frac{c+di}{x+yi} = a + \frac{cx+dy}{x^2+y^2} + \left(b + \frac{dx-cy}{x^2+y^2}\right) i.$$

As ω increase from 0 to ω_r, $x = 0$ and $y \neq 0$, and $\mathrm{Re}\,(Z) = a + \frac{d}{y}$. As ω change from $\omega_r - o$ to $\omega_r + o$, $x \neq 0$ and $y = 0$, and $\mathrm{Re}\,(\mathrm{Z})$ change from $a + \frac{d}{y}$ to $a + \frac{c}{x}$ directly, and the rapid change is the reason for the first impedance peak. $\mathrm{Re}\,(\mathrm{Z})$ reach one maximum value at $\omega = \omega_r$, then decrease rapidly with increasing x, real part of k_{z_1}.

The small peak appearing exclusively in SSG theory result is caused by k_{z_i} $(i = 3, 4, 5, 6)$ corresponding to the extra evanescent waves. In higher frequency, assuming the contribution of one evanescent wave, let's say k_{z_3}, to Z is $\dfrac{c+di}{x+yi}$ with $\mathrm{Re}\,(k_{z_3}) = x$ and $\mathrm{Im}\,(k_{z_3}) = y$, and the contribution form the other wave modes is $a + bi$, then we have

$$\mathrm{Re}\,(Z) = \mathrm{Re}\left(a + bi + \frac{c+di}{x+yi}\right) = a + \frac{cx+dy}{x^2+y^2}$$

As shown in Figure 2, $x = \mathrm{Re}\,(k_{z_3})$ increase significantly in higher frequency and $y = \mathrm{Im}\,(k_{z_i})$ decreases in modulus. The increase of x is more efficient than the decrease of y. Certainly, the value of c and d will affect the resulting $\mathrm{Re}\,(Z)$, but

the rapid change of $\mathrm{Re}\,(k_{z_3})$ should plays a leading role to the changing trend of $\mathrm{Re}\,(Z)$. For example if c and d are set to be '1' or '-1', we have can easily plot the function dependent of k_{z_i}

$$f\,(k_{z_i}) = f\,(x, y) = \frac{x + y}{x^2 + y^2}$$

as

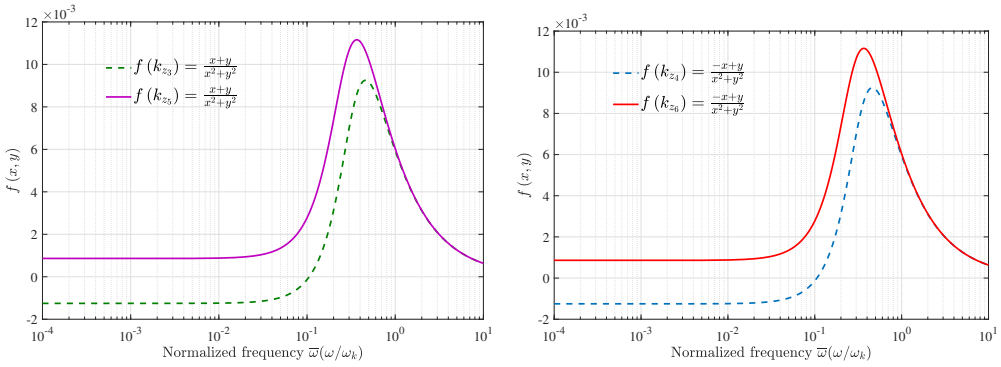

(a) (b)

Figure 3: Supplemented function for evanescent waves

Then it is obvious that the small peak of radiation impedance in near field of excitation on higher frequency is caused by the evanescent waves. As frequency goes increasingly higher, y is approaching to zero and x keeps increasing, then $\mathrm{Re}\,(Z)$ will continue decrease.

List of Figures

List of Tables

Bibliography

[1] D. A. Bonnell, R. Shao, Local behavior of complex materials: scanning probes and nano structure, Current Opinion in Solid State and Materials Science 7 (2) (2003) 161 – 171. doi:https://doi.org/10.1016/S1359-0286(03)00047-0. (Cited on pages 2 and 14.)

[2] W.-Y. Jang, A. M. Kraynik, S. Kyriakides, On the microstructure of open-cell foams and its effect on elastic properties, International Journal of Solids and Structures 45 (7) (2008) 1845 – 1875. doi:https://doi.org/10.1016/j.ijsolstr.2007.10.008.
URL http://www.sciencedirect.com/science/article/pii/S0020768307004118 (Cited on page 2.)

[3] A. S. J. Suiker et al., Micro-mechanical modelling of granular material. part 1: Derivation of a second-gradient micro-polar constitutive theory, Acta Mechanica 149 (1) (2001) 161–180. doi:10.1007/BF01261670. (Cited on pages 3, 4, 30 and 46.)

[4] L. Brillouin, Wave propagation in periodic structures: electric filters and crystal lattices 2nd ed., Dover, New York, NY, 1953.
URL http://cds.cern.ch/record/106186 (Cited on pages 5 and 7.)

[5] M. I. Hussein, M. J. Leamy, M. Ruzzene, Dynamics of Phononic Materials and Structures: Historical Origins, Recent Progress, and Future Outlook, Applied Mechanics Reviews 66 (4). doi:10.1115/1.4026911.
URL https://doi.org/10.1115/1.4026911 (Cited on pages 5, 6, 7, 13, 16, 17 and 165.)

[6] J. L. YARNELL, J. L. WARREN, S. H. KOENIG, Experimental dispersion curves for phonons in aluminum, in: R. WALLIS (Ed.), Lattice Dynamics, Pergamon, 1965, pp. 57 – 61. doi:https://doi.org/10.1016/B978-1-4831-9838-5.50014-5.
URL http://www.sciencedirect.com/science/article/pii/B9781483198385500145 (Cited on page 8.)

[7] M. Jirásek, Nonlocal theories in continuum mechanics, Acta Polytechnica 44 (5) (2004) 16 – 34.
URL https://ojs.cvut.cz/ojs/index.php/ap/article/viewFile/610/442 (Cited on page 8.)

[8] R. Di Sante, Fibre Optic Sensors for Structural Health Monitoring of Aircraft Composite Structures: Recent Advances and Applications (2015). doi:10.3390/s150818666. (Cited on page 10.)

[9] T. Murmu, S. Adhikari, M. McCarthy, Non-local Structural Mechanics, Wiley, Hoboken, USA, 2015. (Cited on pages 14, 15, 23, 24 and 165.)

[10] K. F. Graff, Wave motion in elastic solids, Dover books on physics, Dover, New York, NY, 1991.
URL http://cds.cern.ch/record/2019221 (Cited on page 15.)

[11] R. J. Talbot, J. Przemieniecki, Finite element analysis of frequency spectra for elastic waveguides, International Journal of Solids and Structures 11 (1) (1975) 115 – 138. doi:https://doi.org/10.1016/0020-7683(75)90106-7.
URL http://www.sciencedirect.com/science/article/pii/0020768375901067 (Cited on page 15.)

[12] M. Koshiba, S. Karakida, M. Suzuki, Finite-element analysis of lamb wave scattering in an elastic plate waveguide, IEEE Transactions on Sonics and Ultrasonics 31 (1) (1984) 18–24. doi:10.1109/T-SU.1984.31456. (Cited on page 15.)

[13] N. Nanda, S. Kapuria, S. Gopalakrishnan, Spectral finite element based on an efficient layerwise theory for wave propagation analysis of composite and sandwich beams, Journal of Sound and Vibration 333 (14) (2014) 3120 – 3137. doi:https://doi.org/10.1016/j.jsv.2014.02.036.
URL http://www.sciencedirect.com/science/article/pii/S0022460X14001771 (Cited on page 15.)

[14] P. Kudela, A. Żak, M. Krawczuk, W. Ostachowicz, Modelling of wave propagation in composite plates using the time domain spectral element method, Journal of Sound and Vibration 302 (4) (2007) 728 – 745. doi:https://doi.org/10.1016/j.jsv.2006.12.016.
URL http://www.sciencedirect.com/science/article/pii/S0022460X06009163 (Cited on page 15.)

[15] L. Houillon, M. Ichchou, L. Jezequel, Wave motion in thin-walled structures, Journal of Sound and Vibration 281 (3-5) (2005) 483–507. doi:10.1016/j.jsv.2004.01.020. (Cited on pages 15 and 16.)

[16] M. I. J.-M. Mencik, Wave finite elements in guided elastodynamics with internal fluid, International Journal of Solids and Structures 44 (7) (2007) 2148 – 2167. doi:https://doi.org/10.1016/j.ijsolstr.2006.06.048.
URL http://www.sciencedirect.com/science/article/pii/S002076830600271X (Cited on page 15.)

[17] E. Sapountzakis, J. Dourakopoulos, Shear deformation effect in flexural-torsional vibrations of composite beams by boundary element method (bem), Journal of Vibration and Control 16 (12) (2010) 1763–1789. doi:10.1177/1077546309341602.
URL https://doi.org/10.1177/1077546309341602 (Cited on page 16.)

[18] J. N. Reddy, A Simple Higher-Order Theory for Laminated Composite Plates, Journal of Applied Mechanics 51 (4) (1984) 745–752. doi:10.1115/1.3167719.
URL https://doi.org/10.1115/1.3167719 (Cited on page 16.)

[19] J. Reddy, N. Phan, Stability and vibration of isotropic, orthotropic and laminated plates according to a higher-order shear deformation theory, Journal of Sound and Vibration 98 (2) (1985) 157 – 170. doi:https://doi.org/10.1016/0022-460X(85)90383-9.
URL http://www.sciencedirect.com/science/article/pii/0022460X85903839 (Cited on page 16.)

[20] S. Ait Yahia, A. A. Hassen, M. Houari, A. Tounsi, Wave propagation in functionally graded plates with porosities using various higher-order shear deformation plate theories, Structural Engineering and Mechanics 53 (2015) 1143–1165. doi:10.12989/sem.2015.53.6.1143. (Cited on page 16.)

[21] J.-M. Mencik, M. Ichchou, A substructuring technique for finite element wave propagation in multi-layered systems, Computer Methods in Applied Mechanics and Engineering 197 (6) (2008) 505 – 523. doi:https://doi.org/10.1016/j.cma.2007.08.002.
URL http://www.sciencedirect.com/science/article/pii/S0045782507003398 (Cited on page 16.)

[22] W. Zhou, M. Ichchou, Wave propagation in mechanical waveguide with curved members using wave finite element solution, Computer Methods in Applied Mechanics and Engineering 199 (33) (2010) 2099 – 2109. doi:https://doi.org/10.1016/j.cma.2010.03.006.
URL http://www.sciencedirect.com/science/article/pii/S0045782510000824 (Cited on page 16.)

[23] C. Droz, Z. Zergoune, R. Boukadia, O. Bareille, M. Ichchou, Vibro-acoustic optimisation of sandwich panels using the wave/finite element method, Composite Structures 156 (2016) 108 – 114, 70th Anniversary of Professor J. N. Reddy. doi:https://doi.org/10.1016/j.compstruct.2016.01.025.
URL http://www.sciencedirect.com/science/article/pii/S0263822316000386 (Cited on page 16.)

[24] W. Zhong, F. Williams, On the direct solution of wave propagation for repetitive structures, Journal of Sound and Vibration 181 (3) (1995) 485 – 501. doi:https://doi.org/10.1006/jsvi.1995.0153.
URL http://www.sciencedirect.com/science/article/pii/S0022460X85701538 (Cited on page 17.)

[25] D. Duhamel, B. Mace, M. Brennan, Finite element analysis of the vibrations of waveguides and periodic structures, Journal of Sound and Vibration 294 (1)

(2006) 205 – 220. doi:https://doi.org/10.1016/j.jsv.2005.11.014.
URL http://www.sciencedirect.com/science/article/pii/S0022460X05007194 (Cited on page 17.)

[26] D. J. Mead, The forced vibration of one-dimensional multi-coupled periodic structures: An application to finite element analysis, Journal of Sound and Vibration 319 (1) (2009) 282 – 304. doi:https://doi.org/10.1016/j.jsv.2008.05.026.
URL http://www.sciencedirect.com/science/article/pii/S0022460X08004902 (Cited on page 17.)

[27] Y. Waki, B. Mace, M. Brennan, Numerical issues concerning the wave and finite element method for free and forced vibrations of waveguides, Journal of Sound and Vibration 327 (1) (2009) 92 – 108. doi:https://doi.org/10.1016/j.jsv.2009.06.005.
URL http://www.sciencedirect.com/science/article/pii/S0022460X09004908 (Cited on page 17.)

[28] D. C. Dobson, An efficient method for band structure calculations in 2d photonic crystals, Journal of Computational Physics 149 (2) (1999) 363 – 376. doi:https://doi.org/10.1006/jcph.1998.6157.
URL http://www.sciencedirect.com/science/article/pii/S0021999198961575 (Cited on page 17.)

[29] R.-L. Chern, C. Chang, C. Chang, R. Hwang, Large full band gaps for photonic crystals in two dimensions computed by an inverse method with multigrid acceleration, Physical review. E, Statistical, nonlinear, and soft matter physics 68 (2003) 026704. doi:10.1103/PhysRevE.68.026704. (Cited on page 17.)

[30] C. Droz, J.-P. Lainé, M. Ichchou, G. Inquiété, A reduced formulation for the free-wave propagation analysis in composite structures, Composite Structures 113 (2014) 134 – 144. doi:https://doi.org/10.1016/j.compstruct.2014.03.017.
URL http://www.sciencedirect.com/science/article/pii/S0263822314001202 (Cited on page 17.)

[31] J.-M. Mencik, A model reduction strategy for computing the forced response of elastic waveguides using the wave finite element method, Computer Methods in Applied Mechanics and Engineering 229-232 (2012) 68 – 86. doi:https://doi.org/10.1016/j.cma.2012.03.024.
URL http://www.sciencedirect.com/science/article/pii/S0045782512001004 (Cited on page 17.)

[32] C. Zhou, J. Lainé, M. Ichchou, A. Zine, Wave finite element method based on reduced model for one-dimensional periodic structures, International Journal of Applied Mechanics 07 (2015) 1550018. doi:10.1142/S1758825115500180. (Cited on page 17.)

[33] S. Nemat-Nasser, T. Iwakuma, M. Hejazi, On composites with periodic structure, Mechanics of Materials 1 (3) (1982) 239 – 267. doi:https://doi.org/10.1016/0167-6636(82)90017-5.
URL http://www.sciencedirect.com/science/article/pii/0167663682900175 (Cited on page 18.)

[34] W. Zhang, F. Wang, G. Dai, S. Sun, Topology optimal design of material microstructures using strain energy-based method, Chinese Journal of Aeronautics 20 (4) (2007) 320 – 326. doi:https://doi.org/10.1016/S1000-9361(07)60050-8.
URL http://www.sciencedirect.com/science/article/pii/S1000936107600508 (Cited on page 18.)

[35] G. Wang, S. Li, H.-N. Nguyen, N. Sitar, Effective elastic stiffness for periodic masonry structures via eigenstrain homogenization, Journal of Materials in Civil Engineering 19 (3) (2007) 269–277. doi:10.1061/(ASCE)0899-1561(2007)19:3(269). (Cited on page 18.)

[36] K. Challagulla, A. Georgiades, A. Kalamkarov, Asymptotic homogenization modeling of smart composite generally orthotropic grid-reinforced shells: Part i – theory, European Journal of Mechanics - A/Solids 29 (4) (2010) 530 – 540. doi:https://doi.org/10.1016/j.euromechsol.2010.03.007.
URL http://www.sciencedirect.com/science/article/pii/S0997753810000471 (Cited on page 18.)

[37] A. Georgiades, K. Challagulla, A. Kalamkarov, Asymptotic homogenization modeling of smart composite generally orthotropic grid-reinforced shells: Part ii– applications, European Journal of Mechanics - A/Solids 29 (4) (2010) 541 – 556. doi:https://doi.org/10.1016/j.euromechsol.2010.03.006.
URL http://www.sciencedirect.com/science/article/pii/S099775381000046X (Cited on page 18.)

[38] R. Craster, J. Kaplunov, E. Nolde, S. Guenneau, Bloch dispersion and high frequency homogenization for separable doubly-periodic structures, Wave Motion 49 (2) (2012) 333 – 346. doi:https://doi.org/10.1016/j.wavemoti.2011.11.005.
URL http://www.sciencedirect.com/science/article/pii/S0165212511001417 (Cited on page 18.)

[39] M. Jhung, J. Jo, Equivalent material properties of perforated plate with triangular or square penetration pattern for dynamic analysis, Nuclear Engineering and Technology 38 (2006) 689–696. (Cited on page 18.)

[40] D. Chronopoulos, B. Troclet, O. Bareille, M. Ichchou, Modeling the response of composite panels by a dynamic stiffness approach, Composite Structures 96 (2013) 111 – 120. doi:https://doi.org/10.1016/j.compstruct.2012.

08.047.
URL http://www.sciencedirect.com/science/article/pii/S0263822312004138 (Cited on pages 18 and 19.)

[41] M. Jhung, J. Jo, Equivalent material properties of perforated plate with triangular or square penetration pattern for dynamic analysis, Nuclear Engineering and Technology 38 (2006) 689–696. (Cited on page 19.)

[42] A. Kalamkarov, E. Hassan, A. Georgiades, M. Savi, Asymptotic homogenization model for 3d grid-reinforced composite structures with generally orthotropic reinforcements, Composite Structures 89 (2) (2009) 186 – 196. doi:https://doi.org/10.1016/j.compstruct.2008.07.026.
URL http://www.sciencedirect.com/science/article/pii/S026382230800250X (Cited on page 19.)

[43] E. Cosserat, F. Cosserat, Théorie des Corps déformables, Nature 81 (2072) (1909) 67. doi:10.1038/081067a0.
URL https://doi.org/10.1038/081067a0 (Cited on page 22.)

[44] C. Truesdell, R. A. Toupin, Principles of Classical Mechanics and Field Theory, Springer Berlin Heidelberg, Berlin, Heidelberg, 1960. doi:10.1007/978-3-642-45943-6_2. (Cited on page 22.)

[45] R. A. Toupin, Elastic materials with couple-stresses, Archive for Rational Mechanics and Analysis 11 (1) (1962) 385–414. (Cited on pages 22 and 26.)

[46] R. D. Mindlin, H. F. Tiersten, Effects of couple-stresses in linear elasticity, Archive for Rational Mechanics and Analysis 11 (1962) 415–448. doi:10.1007/BF00253946. (Cited on pages 22 and 26.)

[47] A. C. Eringen, E. S. Suhubi, Nonlinear theory of simple micro-elastic solids—i, International Journal of Engineering Science 2 (2) (1964) 189 – 203. doi:https://doi.org/10.1016/0020-7225(64)90004-7. (Cited on pages 22 and 23.)

[48] R. A. Toupin, Theories of elasticity with couple-stress, Archive for Rational Mechanics and Analysis 17 (2) (1964) 85–112. doi:10.1007/BF00253050. (Cited on page 22.)

[49] A. E. Green, R. S. Rivlin, Simple force and stress multipoles, Archive for Rational Mechanics and Analysis 16 (5) (1964) 325–353. doi:10.1007/BF00281725.
URL https://doi.org/10.1007/BF00281725 (Cited on page 22.)

[50] R. D. Mindlin, Second gradient of strain and surface-tension in linear elasticity, International Journal of Solids and Structures 1 (4) (1965) 417 – 438. doi:https://doi.org/10.1016/0020-7683(65)90006-5. (Cited on pages 22, 27, 32 and 49.)

[51] F. Yang et al., Couple stress based strain gradient theory for elasticity, International Journal of Solids and Structures 39 (10) (2002) 2731 – 2743. doi:https://doi.org/10.1016/S0020-7683(02)00152-X. (Cited on pages 23 and 26.)

[52] D. C. C. Lam et al., Experiments and theory in strain gradient elasticity, Journal of the Mechanics and Physics of Solids 51 (8) (2003) 1477 – 1508. doi:https://doi.org/10.1016/S0022-5096(03)00053-X. (Cited on page 23.)

[53] A. C. Eringen, Micromorphic Elasticity, Springer New York, New York, NY, 1999, Ch. 7, pp. 269–285. doi:10.1007/978-1-4612-0555-5_7. (Cited on page 23.)

[54] R. D. Mindlin, Micro-structure in linear elasticity, Archive for Rational Mechanics and Analysis 16 (1964) 51–78. doi:10.1007/BF00248490. (Cited on page 23.)

[55] A. C. Eringen, Theory of thermo-microstretch elastic solids, International Journal of Engineering Science 28 (12) (1990) 1291 – 1301. doi:https://doi.org/10.1016/0020-7225(90)90076-U. (Cited on page 23.)

[56] A. C. Eringen, Linear theory of micropolar elasticity, Journal of Mathematics and Mechanics 15 (6) (1966) 909–923.
URL http://www.jstor.org/stable/24901442 (Cited on page 23.)

[57] E. Kröner, Elasticity theory of materials with long range cohesive forces, International Journal of Solids and Structures 3 (5) (1967) 731 – 742. doi:https://doi.org/10.1016/0020-7683(67)90049-2.
URL http://www.sciencedirect.com/science/article/pii/0020768367900492 (Cited on page 23.)

[58] I. A. Kunin, The theory of elastic media with microstructure and the theory of dislocations, in: E. Kröner (Ed.), Mechanics of Generalized Continua, Springer Berlin Heidelberg, Berlin, Heidelberg, 1968, pp. 321–329. (Cited on page 23.)

[59] J. A. Krumhansl, Some considerations of the relation between solid state physics and generalized continuum mechanics, in: E. Kröner (Ed.), Mechanics of Generalized Continua, Springer Berlin Heidelberg, Berlin, Heidelberg, 1968, pp. 298–311. (Cited on page 23.)

[60] A. Eringen, A unified theory of thermomechanical materials, International Journal of Engineering Science 4 (2) (1966) 179 – 202. doi:https://doi.org/10.1016/0020-7225(66)90022-X.
URL http://www.sciencedirect.com/science/article/pii/002072256690022X (Cited on page 23.)

[61] A. Eringen, D. Edelen, On nonlocal elasticity, International Journal of Engineering Science 10 (3) (1972) 233 – 248. doi:https://doi.org/10.1016/0020-7225(72)90039-0.

URL http://www.sciencedirect.com/science/article/pii/0020722572900390 (Cited on page 23.)

[62] A. Eringen, Nonlocal polar elastic continua, International Journal of Engineering Science 10 (1) (1972) 1 – 16. doi:https://doi.org/10.1016/0020-7225(72)90070-5.
URL http://www.sciencedirect.com/science/article/pii/0020722572900705 (Cited on page 23.)

[63] A. Eringen, Linear theory of nonlocal elasticity and dispersion of plane waves, International Journal of Engineering Science 10 (5) (1972) 425 – 435. doi:https://doi.org/10.1016/0020-7225(72)90050-X.
URL http://www.sciencedirect.com/science/article/pii/002072257290050X (Cited on page 23.)

[64] J. Gao, An asymmetric theory of nonlocal elasticity—part 2. continuum field, International Journal of Solids and Structures 36 (20) (1999) 2959 – 2971. doi:https://doi.org/10.1016/S0020-7683(97)00322-3.
URL http://www.sciencedirect.com/science/article/pii/S0020768397003223 (Cited on page 23.)

[65] A. C. Eringen, On differential equations of nonlocal elasticity and solutions of screw dislocation and surface waves, Journal of Applied Physics 54 (9) (1983) 4703–4710. doi:10.1063/1.332803.
URL https://doi.org/10.1063/1.332803 (Cited on page 23.)

[66] E. C. Aifantis, On the gradient approach – relation to eringen's nonlocal theory, International Journal of Engineering Science 49 (12) (2011) 1367 – 1377, advances in generalized continuum mechanics. doi:https://doi.org/10.1016/j.ijengsci.2011.03.016.
URL http://www.sciencedirect.com/science/article/pii/S0020722511000723 (Cited on page 23.)

[67] C. W. Lim et al., A higher-order nonlocal elasticity and strain gradient theory and its applications in wave propagation, Journal of the Mechanics and Physics of Solids 78 (2015) 298 – 313. doi:https://doi.org/10.1016/j.jmps.2015.02.001.
URL http://www.sciencedirect.com/science/article/pii/S0022509615000320 (Cited on pages 23 and 30.)

[68] Y. Chen, J. D. Lee, A. Eskandarian, Atomistic viewpoint of the applicability of microcontinuum theories, International Journal of Solids and Structures 41 (8) (2004) 2085 – 2097, special Issue in Honour of Prof. Bruno Boley. doi:https://doi.org/10.1016/j.ijsolstr.2003.11.030.
URL http://www.sciencedirect.com/science/article/pii/S0020768303006796 (Cited on page 24.)

[69] Z. Zhang, C. Wang, N. Challamel, I. Elishakoff, Obtaining eringen's length scale coefficient for vibrating nonlocal beams via continualization method, Journal of Sound and Vibration 333 (20) (2014) 4977 – 4990. doi:https://doi.org/10.1016/j.jsv.2014.05.002.
URL http://www.sciencedirect.com/science/article/pii/S0022460X1400371X (Cited on page 25.)

[70] B. Arash, R. Ansari, Evaluation of nonlocal parameter in the vibrations of single-walled carbon nanotubes with initial strain, Physica E: Low-dimensional Systems and Nanostructures 42 (8) (2010) 2058 – 2064. doi:https://doi.org/10.1016/j.physe.2010.03.028.
URL http://www.sciencedirect.com/science/article/pii/S1386947710001797 (Cited on page 25.)

[71] R. Kaddour et al., Free vibration analysis of chiral double-walled carbon nanotube using non-local elasticity theory, Advances in nano research 4 (2016) 31–44. doi:10.12989/anr.2016.4.1.031. (Cited on page 25.)

[72] Y. Zhang, G. Liu, X. Xie, Free transverse vibrations of double-walled carbon nanotubes using a theory of nonlocal elasticity, Physical Review B - Condensed Matter and Materials Physics 71 (19). doi:10.1103/PhysRevB.71.195404. (Cited on page 26.)

[73] J. Reddy, Nonlocal theories for bending, buckling and vibration of beams, International Journal of Engineering Science 45 (2-8) (2007) 288–307. doi:10.1016/j.ijengsci.2007.04.004. (Cited on page 26.)

[74] J. N. Reddy, S. D. Pang, Nonlocal continuum theories of beams for the analysis of carbon nanotubes, Journal of Applied Physics 103 (2) (2008) 023511. doi:10.1063/1.2833431.
URL https://doi.org/10.1063/1.2833431 (Cited on page 26.)

[75] S. Silling, Reformulation of elasticity theory for discontinuities and long-range forces, Journal of the Mechanics and Physics of Solids 48 (1) (2000) 175–209. doi:10.1016/S0022-5096(99)00029-0. (Cited on page 26.)

[76] M. H. Kahrobaiyan et al., Nonlinear size-dependent forced vibrational behavior of microbeams based on a non-classical continuum theory, Journal of Vibration and Control 18 (5) (2012) 696–711. doi:10.1177/1077546311414600. (Cited on page 26.)

[77] L. C. Trinh et al., Size-dependent vibration of bi-directional functionally graded microbeams with arbitrary boundary conditions, Composites Part B: Engineering 134 (2018) 225 – 245. doi:https://doi.org/10.1016/j.compositesb.2017.09.054.
URL http://www.sciencedirect.com/science/article/pii/S1359836817325337 (Cited on page 27.)

[78] H. M. Ma, J. N. Reddy, A microstructure-dependent timoshenko beam model based on a modified couple stress theory, Journal of the Mechanics and Physics of Solids 56 (12) (2008) 3379 – 3391. doi:https://doi.org/10.1016/j.jmps.2008.09.007. (Cited on page 27.)

[79] G. Tsiatas, A new kirchhoff plate model based on a modified couple stress theory, International Journal of Solids and Structures 46 (13) (2009) 2757 – 2764. doi:https://doi.org/10.1016/j.ijsolstr.2009.03.004.
URL http://www.sciencedirect.com/science/article/pii/S0020768309001036 (Cited on page 27.)

[80] H. T. Thai, D. H. Choi, Size-dependent functionally graded kirchhoff and mindlin plate models based on a modified couple stress theory, Composite Structures 95 (2013) 142 – 153. doi:https://doi.org/10.1016/j.compstruct.2012.08.023.
URL http://www.sciencedirect.com/science/article/pii/S0263822312003893 (Cited on page 27.)

[81] M. Asghari, Geometrically nonlinear micro-plate formulation based on the modified couple stress theory, International Journal of Engineering Science 51 (2012) 292 – 309. doi:https://doi.org/10.1016/j.ijengsci.2011.08.013.
URL http://www.sciencedirect.com/science/article/pii/S0020722511001789 (Cited on page 28.)

[82] S. Karparvarfard et al., A geometrically nonlinear beam model based on the second strain gradient theory, International Journal of Engineering Science 91 (2015) 63 – 75. doi:https://doi.org/10.1016/j.ijengsci.2015.01.004.
URL http://www.sciencedirect.com/science/article/pii/S002072251500021X (Cited on page 28.)

[83] M. Asghari et al., The second strain gradient theory-based timoshenko beam model, Journal of Vibration and Control 23 (13) (2017) 2155–2166. doi:10.1177/1077546315611822. (Cited on pages 28 and 42.)

[84] S. Momeni, M. Asghari, The second strain gradient functionally graded beam formulation, Composite Structures 188 (2018) 15 – 24. doi:https://doi.org/10.1016/j.compstruct.2017.12.046.
URL http://www.sciencedirect.com/science/article/pii/S0263822317323516 (Cited on page 28.)

[85] S. Kong et al., Static and dynamic analysis of micro beams based on strain gradient elasticity theory, International Journal of Engineering Science 47 (4) (2009) 487 – 498. doi:https://doi.org/10.1016/j.ijengsci.2008.08.008.
URL http://www.sciencedirect.com/science/article/pii/S002072250800133X (Cited on page 29.)

[86] B. Wang et al., A micro scale timoshenko beam model based on strain gradient elasticity theory, European Journal of Mechanics - A/Solids 29 (4) (2010) 591 – 599. doi:https://doi.org/10.1016/j.euromechsol.2009.12.005.
URL http://www.sciencedirect.com/science/article/pii/S0997753809001430 (Cited on page 29.)

[87] R. P. Joseph et al., Size effects on double cantilever beam fracture mechanics specimen based on strain gradient theory, Engineering Fracture Mechanics 169 (2017) 309 – 320. doi:https://doi.org/10.1016/j.engfracmech.2016.10.013. (Cited on page 29.)

[88] R. P. Joseph et al., Fracture analysis of flexoelectric double cantilever beams based on the strain gradient theory, Composite Structures 202 (2018) 1322 – 1329. doi:https://doi.org/10.1016/j.compstruct.2018.06.067.
URL http://www.sciencedirect.com/science/article/pii/S0263822318307074 (Cited on page 29.)

[89] Y. Zhou et al., Improved incorporation of strain gradient elasticity in the flexoelectricity based energy harvesting from nanobeams, Physica E: Low-dimensional Systems and Nanostructures 98 (2018) 148 – 158. doi:https://doi.org/10.1016/j.physe.2017.12.037.
URL http://www.sciencedirect.com/science/article/pii/S1386947717317940 (Cited on page 29.)

[90] R. Ansari et al., Free vibration analysis of size-dependent functionally graded microbeams based on the strain gradient timoshenko beam theory, Composite Structures 94 (1) (2011) 221 – 228. doi:https://doi.org/10.1016/j.compstruct.2011.06.024.
URL http://www.sciencedirect.com/science/article/pii/S0263822311002443 (Cited on page 29.)

[91] A. W. McFarland, J. S. Colton, Role of material microstructure in plate stiffness with relevance to microcantilever sensors, Journal of Micromechanics and Microengineering 15 (5) (2005) 1060.
URL http://stacks.iop.org/0960-1317/15/i=5/a=024 (Cited on page 29.)

[92] M. Kandaz et al., Analysis of gold microbeams with higher order continuum theories, Proc. Appl. Math. Mech. 17 (1) (2017) 421–422. doi:10.1002/pamm.201710180.
URL https://onlinelibrary.wiley.com/doi/abs/10.1002/pamm.201710180 (Cited on pages 29 and 33.)

[93] A. S. J. Suiker et al., Micro-mechanical modelling of granular material. part 2: Plane wave propagation in infinite media, Acta Mechanica 149 (1) (2001) 181–200. doi:10.1007/BF01261671.
URL https://doi.org/10.1007/BF01261671 (Cited on pages 30 and 46.)

[94] L. Li et al., Flexural wave propagation in small-scaled functionally graded beams via a nonlocal strain gradient theory, Composite Structures 133 (2015) 1079 – 1092. doi:https://doi.org/10.1016/j.compstruct.2015.08.014. URL http://www.sciencedirect.com/science/article/pii/S0263822315006911 (Cited on page 30.)

[95] S. Gopalakrishnan, Propagation of elastic waves in nanostructures, in: Nanosensors, Biosensors, and Info-Tech Sensors and Systems 2016, Vol. 9802, 2016, p. 98020N. doi:10.1117/12.2218203. (Cited on page 30.)

[96] D. D. Domenico et al., Gradient elasticity and dispersive wave propagation: Model motivation and length scale identification procedures in concrete and composite laminates, International Journal of Solids and Structuresdoi:https://doi.org/10.1016/j.ijsolstr.2018.09.007. URL http://www.sciencedirect.com/science/article/pii/S0020768318303639 (Cited on pages 30, 34 and 158.)

[97] J. Fish, W. Chen, G. Nagai, Non-local dispersive model for wave propagation in heterogeneous media: one-dimensional case, International Journal for Numerical Methods in Engineering 54 (3) (2002) 331–346. arXiv:https://onlinelibrary.wiley.com/doi/pdf/10.1002/nme.423, doi:10.1002/nme.423. URL https://onlinelibrary.wiley.com/doi/abs/10.1002/nme.423 (Cited on page 30.)

[98] A. Berezovski et al., Waves in microstructured solids: a unified viewpoint of modeling, Acta Mechanica 220 (1) (2011) 349–363. doi:10.1007/s00707-011-0468-0. (Cited on page 30.)

[99] H. Askes, E. Aifantis, Gradient elasticity in statics and dynamics: An overview of formulations, length scale identification procedures, finite element implementations and new results, International Journal of Solids and Structures 48 (13) (2011) 1962–1990. doi:10.1016/j.ijsolstr.2011.03.006. (Cited on page 30.)

[100] A. V. Metrikine, H. Askes, One-dimensional dynamically consistent gradient elasticity models derived from a discrete microstructure: Part 1: Generic formulation, European Journal of Mechanics - A/Solids 21 (4) (2002) 555 – 572. doi:https://doi.org/10.1016/S0997-7538(02)01218-4. (Cited on pages 31 and 46.)

[101] H. Askes, A. V. Metrikine, One-dimensional dynamically consistent gradient elasticity models derived from a discrete microstructure: Part 2: Static and dynamic response, European Journal of Mechanics - A/Solids 21 (4) (2002) 573 – 588. doi:https://doi.org/10.1016/S0997-7538(02)01217-2. URL http://www.sciencedirect.com/science/article/pii/S0997753802012172 (Cited on pages 31 and 46.)

[102] Y. Li, P. Wei, Reflection and transmission of thermo-elastic waves without energy dissipation at the interface of two dipolar gradient elastic solids, Journal of the Acoustical Society of America 143 (1) (2018) 550–562. doi:10.1121/1.5020780.
URL https://www.scopus.com/inward/record.uri?eid=2-s2.0-85041445768 (Cited on page 31.)

[103] L. Placidi et al., Reflection and transmission of plane waves at surfaces carrying material properties and embedded in second-gradient materials, Mathematics and Mechanics of Solids 19 (5) (2014) 555–578. doi:10.1177/1081286512474016.
URL https://doi.org/10.1177/1081286512474016 (Cited on page 31.)

[104] F. Dell'Isola et al., Linear plane wave propagation and normal transmission and reflection at discontinuity surfaces in second gradient 3d continua, Journal of Applied Mathematics and Mechanics / Zeitschrift für Angewandte Mathematik und Mechanik 92 (1) (2012) 52–71. doi:https://doi.org/10.1002/zamm.201100022.
URL https://hal.archives-ouvertes.fr/hal-00602196 (Cited on page 31.)

[105] Y. Li et al., Reflection and transmission of elastic waves at the interface between two gradient-elastic solids with surface energy, European Journal of Mechanics, A/Solids 52 (2015) 54–71, cited By 7. doi:10.1016/j.euromechsol.2015.02.001.
URL https://www.scopus.com/inward/record.uri?eid=2-s2.0-84924626206&doi=10.1016 (Cited on page 31.)

[106] H. Espinosa, B. Prorok, M. Fischer, A methodology for determining mechanical properties of freestanding thin films and mems materials, Journal of the Mechanics and Physics of Solids 51 (1) (2003) 47 – 67. doi:https://doi.org/10.1016/S0022-5096(02)00062-5.
URL http://www.sciencedirect.com/science/article/pii/S0022509602000625 (Cited on page 33.)

[107] C. Liebold, W. Mueller, Applications of strain gradient theories to the size effect in submicrostructures incl. experimental analysis of elastic material parameters, Bull. TICMI 19 (2015) 45–55. (Cited on page 33.)

[108] R. Ansari, R. Gholami, H. Rouhi, Vibration analysis of single-walled carbon nanotubes using different gradient elasticity theories, Composites Part B: Engineering 43 (8) (2012) 2985 – 2989. doi:https://doi.org/10.1016/j.compositesb.2012.05.049.
URL http://www.sciencedirect.com/science/article/pii/S1359836812003782 (Cited on page 33.)

[109] M. Shodja et al., Calculation of the additional constants for fcc materials in second strain gradient elasticity: Behavior of a nano-size bernoulli-euler beam with surface effects, Journal of Applied Mechanics 79 (2) (2012) 1008–1016. doi:10.1115/1.4005535. (Cited on pages 34, 41, 70 and 75.)

[110] A. P. Sutton, J. Chen, Long-range finnis–sinclair potentials, Philosophical Magazine Letters 61 (3) (1990) 139–146. doi:10.1080/09500839008206493. URL https://doi.org/10.1080/09500839008206493 (Cited on page 34.)

[111] D. D. Domenico, H. Askes, A new multi-scale dispersive gradient elasticity model with micro-inertia: Formulation and -finite element implementation, International Journal for Numerical Methods in Engineering 108 (5) (2016) 485–512. doi:10.1002/nme.5222.
URL https://onlinelibrary.wiley.com/doi/abs/10.1002/nme.5222 (Cited on pages 35 and 165.)

[112] F. Fahy, P. Gardonio, 1 - waves in fluids and solid structures, in: F. Fahy, P. Gardonio (Eds.), Sound and Structural Vibration (Second Edition), second edition Edition, Academic Press, Oxford, 2007, pp. 1 – 73. doi:https://doi.org/10.1016/B978-012373633-8/50005-3.
URL http://www.sciencedirect.com/science/article/pii/B9780123736338500053 (Cited on page 43.)

[113] Y. Lase et al., Energy flow analysis of bars and beams: Theoretical formulations, Journal of Sound and Vibration 192 (1) (1996) 281 – 305. doi:https://doi.org/10.1006/jsvi.1996.0188.
URL http://www.sciencedirect.com/science/article/pii/S0022460X96901881 (Cited on pages 49, 59 and 98.)

[114] M. N. Ichchou et al., Energy models of one-dimensional multipropagative systems, Journal of Sound and Vibration 201 (5) (1997) 535 – 554. doi:https://doi.org/10.1006/jsvi.1996.0780. (Cited on page 49.)

[115] A. K. S., Active and reactive structural energy flow, Journal of Vibration and Acoustics 119 (1) (1997) 70–79. doi:http://dx.doi.org/10.1115/1.2889689. (Cited on pages 57 and 95.)

[116] V. E. Tarasov, Map of discrete system into continuous, Journal of Mathematical Physics 47 (9) (2006) 1–32. doi:10.1063/1.2337852. (Cited on page 64.)

[117] V. E. Tarasov, Lattice model with nearest-neighbor and next-nearest-neighbor interactions for gradient elasticity, Discontinuity, Nonlinearity, and Complexity 4 (1) (2015) 11–23. doi:10.5890/DNC.2015.03.002. (Cited on page 64.)

[118] V. E. Tarasov, Continuous limit of discrete systems with long-range interaction, Journal of Physics A: Mathematical and General 39 (48) (2006) 14895–14910. doi:10.1088/0305-4470/39/48/005. (Cited on page 65.)

dernière page de la thèse

AUTORISATION DE SOUTENANCE

Vu les dispositions de l'arrêté du 25 mai 2016,

Vu la demande des directeurs de thèse

Messieurs M. ICHCHOU et A. ZINE

et les rapports de

M. W. LARBI
Professeur - LMSSC - Laboratoire de Mécanique des Structures et des Systèmes Couplés
CNAM - 292 rue Saint-Martin - 75141 Paris cedex 03

et de

M. M-A. BENSOUF
Professeur - Laboratoire de Recherche de Mécanique, Modélisation et Productique (L2MP)
Ecole Nationale d'Ingénieurs de Sfax (ENIS) - Route de la Soukra km 4 - 3038 Sfax - Tunisie

Madame ZHU Guang

est autorisée à soutenir une thèse pour l'obtention du grade de **DOCTEUR**

Ecole doctorale MECANIQUE, ENERGETIQUE, GENIE CIVIL ET ACOUSTIQUE

Fait à Ecully, le 9 décembre 2019

P/Le directeur de l'E.C.L.
Le directeur des Etudes

ECOLE CENTRALE DE LYON
Service Scolarité
ECULLY

Grégory VIAL